COMBINED RADIATION, CONDUCTION AND/OR CONVECTION HEAT TRANSFER IN PARTICIPATING MEDIA

A Thesis Submitted

for the Award of the Degree of

Doctor of Philosophy

by

Prabal Talukdar

to the

DEPARTMENT OF MECHANICAL ENGINEERING

INDIAN INSTITUTE OF TECHNOLOGY GUWAHATI

August 2003

CERTIFICATE

It is certified that the work contained in the thesis entitled **Combined Radiation, Conduction and/or Convection Heat Transfer in Participating Media,** by **Prabal Talukdar**, a student in the Department of Mechanical Engineering, Indian Institute of Technology Guwahati, India, for the award of the degree of the Doctor of Philosophy has been carried out under my supervision and that this work has not been submitted elsewhere for a degree.

Dr Subhash C Mishra
Associate Professor
Department of Mechanical Engineering
Indian Institute of Technology Guwahati

August 2003

TH-1868_004301

Indian Institute of Technology Guwahati

Dedicated to

my parents

Mr. G. C. Talukdar

Mrs. C. Talukdar

TH-1868_004301

Acknowledgements

First of all, I would like to express my deepest gratitude to my supervisor, Dr. Subhash C. Mishra, for his invaluable inspiration, encouragement and support throughout my Ph.D. work. In the past few years I worked under his guidance to achieve this state of my work. He always provided me with invaluable guidance and insightful knowledge to lead me into critical thinking to keep the research work moving smoothly. As my supervisor, his personal character with great spirit and enthusiasm is an example for the rest of my life.

I would like to thank all my doctoral committee members, namely, Dr. A. Dewan, Dr. A. K. Dass and Dr. U. K. Saha for their valuable advice and encouragement.

I am thankful to Prof. A. D. Sahasrabudhe, Deputy Director, IIT Guwahati, for his help during the course of my Ph.D. work. I would also like to sincerely acknowledge all the faculty members of Mechanical Engineering Department for their help and advice in these years.

I am extremely grateful to Prof. Dr. Dr. h. c. Franz Durst, Institute of Fluid Mechanics (LSTM), University of Erlangen-Nuremberg, Germany for his support and guidance to carry out a part of my research work there. I spent 14 wonderful months along with my supervisor in LSTM and got a very good exposure in the area of heat transfer in porous media combustion. My sincere thanks are due to Dr.-ing D. Trimis, head of the combustion group of LSTM. Despite his busy schedule, he always helped me with insightful technical guidance. I also enjoyed a nice time

TH-1868_004301

with all my colleagues in that institute and would like to appreciate all of them for their kind cooperation and help during my stay. My thanks specially go to Sonja Hupfer, V. Stamatov, M. Steven and S. Nemoda for their invaluable cooperation.

I am extremely thankful to all my family members for their love and support. No words can express my deep appreciation to my parents for their love and encouragement. I am also grateful to the family of my in-laws for their help during my stay at Guwahati. Finally, I am very grateful to my wife Mitali and my son Sandeep for their love and support. They were always on my side to support me throughout the years in India and Germany wherever we lived.

And last, but not least, I am thankful to Dr. Pinakeswar Mahanta, Dr. Jiten Kalita, Mr. M. Pathak and Mr. A. Kalita for their kind help and encouragement.

Prabal Talukdar
IIT Guwahati

August 2003

TH-1868_004301

Indian Institute of Technology Guwahati

List of Publications from this Thesis Work

International Journal

1. P. Talukdar and S. C. Mishra, Transient Conduction and Radiation Heat Transfer with Heat Generation in a Participating Medium Using the Collapsed Dimension Method, *Numerical Heat Transfer-Part A*, 39(1):79-100, 2001.

2. P. Talukdar and S. C. Mishra, Transient Conduction and Radiation Heat Transfer with Variable Thermal Conductivity, *Numerical Heat Transfer-Part A*, 41:851-867, 2002.

3. S. C. Mishra, P. Talukdar, D. Trimis and F. Durst, Computational Efficiency Improvements of the Radiative Transfer Problem with or without Conduction - A Comparison of the Collapsed Dimension Method and the Discrete Transfer Method, *International Journal of Heat and Mass Transfer*, 46(16), 3083-3095, 2003.

4. P. Talukdar and S. C. Mishra, Transient Conduction-Radiation Interaction in a Planar Packed Bed with Variable Porosity, *Numerical Heat Transfer-Part A*, 44(3), 281-297, 2003.

5. P. Talukdar, S. C. Mishra, D. Trimis and F. Durst, Heat Transfer Characteristics of a Porous Radiant Burner under the Influence of a Two-Dimensional Radiation Field, *Journal of Quantitative Spectroscopy and Radiative Transfer*, 84(4), 527-537, 2004

6. P. Talukdar, S. C Mishra, D. Trimis and F. Durst, Combined Radiation and Convection Heat Transfer in a Porous Channel Bounded by Isothermal Parallel Plates, *International Journal of Heat and Mass Transfer*, 47(5), 1001-1013, 2004.

TH-1868_004301

7. S. C Mishra, P. Talukdar, D. Trimis and F. Durst, Two-Dimensional Transient Conduction and Radiation Heat Transfer with Temperature Dependent Thermal Conductivity , *International communications in Heat and Mass Transfer*, 2003 (submitted).

International Conferences

1. S. C. Mishra and P. Talukdar, Analysis of Conduction-Radiation Heat Transfer in a Participating Medium with flux Boundary, In *paper No. NHTC2001-20230, 35th National Heat Transfer Conference*, Anaheim, California, USA, 2001.

2. P. Talukdar and S. C. Mishra, Effect of Variable Thermal Conductivity on Transient Conduction-Radiation Heat Transfer, In *proceedings of the Sixteenth National Heat and Mass Transfer Conference and Fifth ISHMT/ASME Heat and Mass Transfer Conference*, January 3-5, 2002, Kolkata, India.

3. P. Talukdar and S. C. Mishra, Conduction-Radiation Interaction in a Plane-Parallel Packed Bed Using the Discrete Transfer Method, In *proceedings of the International Symposium on Recent Trends of Heat and Mass Transfer*, January 6-8, 2002, Indian Institute of Technology, Guwahati, India.

4. P. Talukdar, S. C Mishra, D. Trimis and F. Durst, Heat Transfer Characteristics of a Porous Radiant Burner under the Influence of a Two-Dimensional Radiation Field, *Eurotherm Seminar 73, Computational Thermal Radiation in Participating Media*, 15-17 April, 2003, Mons, Belgium.

5. S. C Mishra, P. Talukdar, D. Trimis and F. Durst, Effect of Temperature Dependent Thermal Conductivity on Two-Dimensional Conduction and Radiation Heat Transfer, *Eurotherm Seminar 73, Computational Thermal Radiation in Participating Media*, 15-17 April, 2003, Mons, Belgium.

TH-1868_004301

Synopsis

Name of Student: **Prabal Talukdar** Roll No. **004301**

Degree for which submitted: **Ph.D.** Department: **Mechanical Engineering**

Thesis Title:

Combined Radiation, Conduction and/or Convection Heat Transfer in Participating Media

Name of thesis supervisor: **Dr. Subhash C. Mishra**

Month and year of thesis submission: **August 2003**

Thermal radiation is one of the fundamental modes of heat transfer. It plays an important role in the design of high temperature engineering systems. The analysis and design of combustion chambers, porous burners and porous volumetric solar receivers, among many others, are some of the important application areas where consideration of thermal radiation is important.

Radiative heat transfer in a participating medium is a volumetric phenomenon. It is characterized by absorption, emission and scattering. The radiative transfer equation and the divergence of radiative heat flux are the two equations governing the radiative heat transfer in a participating medium. In a control volume, conservations of radiative energy in a given direction and over all directions are given by the radiative transfer equation and the divergence of radiative heat flux, respectively.

The equations governing the radiative heat transfer in a participating medium are integro-differential in nature and their solutions are difficult. The difficulty increases

TH-1868_004301

further if the thermophysical and the optical properties vary inside the medium and they are functions of temperature. Owing to the complexities in the solution, thermal radiation problems are solved using the approximate methods. In the literature more than 12 approximate methods exist, each of them having some advantages and disadvantages. All practical problems are solved using either of the methods.

The numerous advantages of the porous medium combustion over the free flame combustion have necessitated the need to perfect the design of appliances based on the porous medium combustion. The heat transfer analysis of the porous medium combustion is complex. It involves consideration of radiation along with conduction and convection. Among the three modes of heat transfer, radiation is the most difficult part to analyze. The detailed treatment of the porous medium combustion is laborious and time consuming. Among the three modes, the treatment of radiation is computationally the most expensive.

In the present work, with the final objective of doing the heat transfer analysis of the porous medium combustion, eight combined radiation, conduction and/or convection mode problems with varying degrees of complexities were considered. Radiative components in these problems were taken care of either by the collapsed dimension method (CDM) or the discrete transfer method (DTM). Further, these problems were chosen with an intention to extend the range of applications of the two methods. Finite difference based solvers were used to solve the energy equations.

The thesis is organized in 11 chapters. In the Introduction chapter, the need for analyzing heat transfer problems involving thermal radiation is justified and important works in this area are reviewed. In the second chapter, a general methodology is presented for the solution of any heat transfer problem involving thermal radiation. In such problems, how the radiative information required for the energy equation is computed using the CDM and the DTM is explained in some detail. Chapters 3 - 10 deal with eight different combined mode problems. Conclusions and recommendations are incorporated in Chapter 11. Problems considered in Chapters 3-10 are briefly described below.

TH-1868_004301

The problem considered in Chapter 3 analyses the steady state conduction and radiation heat transfer in a planar absorbing, emitting and scattering medium. The boundaries of the medium are gray. One of the boundaries is maintained at a constant flux while the temperature of the other boundary is prescribed. The selection of this problem was intended to test the application of the CDM to problems with known flux at one of the boundaries.

Porous medium combustion involves consideration of heat generation inside the medium. In Chapter 4, the analysis was carried out for the transient conduction and radiation heat transfer with heat generation in a planar absorbing, emitting and scattering medium. The boundaries of the medium were at the prescribed temperatures. This problem was also intended to test the applicability of the CDM to this type of problem.

In the porous medium, depending on the shape and the size of the voids, different scattering theories have been proposed. Researchers have been using either Kamiuto's correlated scattering theory or Kaviany's scaling factor. However, no study had been reported to compare the results of the two theories. The problem considered in Chapter 5 deals with the analysis of transient conduction and radiation heat transfer in a planar porous medium and compares the results of the two scattering theories. The effects of variable porosity as well as constant porosity are also studied. The DTM was used to find the radiative information.

In flow through a porous medium with relatively high porosity and permeability, the boundary and the inertia effects are important and the fully developed velocity field is not uniform. This non-uniform velocity field affects heat transfer to or from the porous medium. With radiation, this situation had not been analyzed so far. Therefore, Chapter 6 deals with the effects of radiation along with conduction and convection in porous channel bounded by isothermal parallel plates in which the boundary and the inertia effects are important. The analysis was carried out for a wide range of the porous medium shape parameter (which is a function of the porosity and the permeability) including the two limits of the Poiseuille flow and the slug flow. The problem was solved by considering both solid and the fluid phases

TH-1868_004301

as a single continuum. The radiative information was found using the DTM.

In heat transfer problems involving radiation, there are sharp temperature gradients in the medium. Because of a large temperature variations in the medium, thermal conductivity of the medium does not remain constant. In such problems, the assumption of constant thermal conductivity is not appropriate. Chapter 7, therefore, deals with the effects of the temperature dependent thermal conductivity on transient conduction and radiation heat transfer in a planar absorbing, emitting and scattering medium.

In 1-D planar medium problems, computational time is not a major concern. However, in 2-D conjugate mode problems, calculation of radiative information is expensive. To extend the application of the CDM to 2-D conjugate mode problems, and also to find which of the two methods is computationally efficient, three benchmark problems were considered in Chapter 8. The performances of the two methods were analyzed over the different ranges of the radiative parameters. The CDM was found to be computationally efficient and thus a preferred method for 2-D problems.

In Chapter 9, effects of the variable thermal conductivity were analyzed for combined conduction and radiation heat transfer in a 2-D rectangular enclosure. The CDM was used for the calculation of radiative information.

Chapter 10 deals with the heat transfer analysis of 2-D rectangular porous burners. The gas and the solid phase were considered in non-local thermal equilibrium, and separate energy equations were used for the two phases. The solid phase was assumed to be participating, while the gas was assumed to be transparent to radiation. Radiative part of the energy equation was solved using the CDM. Effects of various parameters such as the aspect ratio, the extinction coefficient, the scattering albedo, the boundary emissivity and interface heat transfer coupling were studied on the performance of the burner. These parameters were found to have significant bearings on the temperature and heat flux distributions.

****

TH-1868_004301

Contents

Synopsis xv

Contents xv

List of Figures xxi

List of Tables xxxi

Nomenclature xxxiii

Abbreviations xli

1 Introduction 1

1.1 Importance of Thermal Radiation 1

1.2 Radiation in a Participating Medium 3

1.3 Various Radiation Models in Participating Medium 4

1.4 Radiation Heat Transfer Combined with Other Modes 8

1.4.1 Radiation with Conduction 8

TH-1868_004301

1.4.2 Radiation-Conduction in Porous Media and Packed Beds . . . 10
1.4.3 Radiation-Convection in a Duct Flow 12
1.4.4 Radiation with Combustion 13
1.5 Organization of the Dissertation 14

2 Formulation **17**
2.1 Introduction 17
2.2 Energy Equation 18
2.3 Discrete Transfer Method 19
2.3.1 Introduction 19
2.3.2 Radiative Transfer Equation 21
2.3.3 Divergence of Radiative Heat Flux 26
2.3.4 Solution Methodology for the DTM 27
2.4 Collapsed Dimension Method 32
2.4.1 Introduction 32
2.4.2 The Methodology 33
2.4.3 Collapsing Coefficient 38
2.4.4 Radiative Transfer Equation 39
2.4.5 Divergence of Radiative Heat Flux 41
2.4.6 Solution Methodology for the CDM 43
2.5 Summary 45

TH-1868_004301

3 1-D Steady State Conduction-Radiation with Flux Boundary 47

3.1 Introduction 47

3.2 Formulation 49

3.3 Calculations and Results 51

3.4 Conclusions 60

4 1-D Transient Conduction-Radiation with Heat Generation 61

4.1 Introduction 61

4.2 Formulation 63

4.3 Results and Discussion 65

4.3.1 Transient Conduction-Radiation without Heat Generation 65

4.3.2 Transient Conduction-Radiation with Heat Generation 77

4.4 Conclusions 81

5 Effect of Variable Thermal Conductivity on 1-D Conduction-Radiation 83

5.1 Introduction 83

5.2 Formulation 85

5.3 Results and Discussion 88

5.3.1 Steady State Results 89

5.3.2 Unsteady State Results 96

5.4 Conclusions 103

TH-1868_004301

6 Conduction-Radiation Heat Transfer in Packed bed **105**

6.1 Introduction 105

6.2 Formulation 107

6.2.1 Radiative Transfer Equations 108

6.2.2 Porosity Distribution Function 109

6.2.3 Effective Thermal Conductivity 110

6.2.4 Radiative Properties 111

6.2.5 Heat Flux 111

6.2.6 Numerical Methods 112

6.3 Results and Discussion 112

6.4 Conclusions 126

7 Radiation-Convection Heat Transfer in a Porous Channel **127**

7.1 Introduction 127

7.2 Formulation 129

7.3 Results and Discussion 134

7.4 Conclusions 149

8 2-D Conduction-Radiation Heat Transfer **151**

8.1 Introduction 151

8.2 Formulation 154

8.3 Results and discussion 157

TH-1868_004301

8.3.1 Problem 1: Radiative equilibrium - Boundary emission case . 159

8.3.2 Problem 2: Non-radiative equilibrium - Isothermal medium emission case 160

8.3.3 Problem 3: Combined mode - Transient conduction and radiation 163

8.4 Conclusions 170

9 Effect of Variable Thermal Conductivity on 2-D Conduction-Radiation Interaction 173

9.1 Introduction 173

9.2 Formulation 174

9.3 Results and Discussion 177

9.4 Conclusions 186

10 Heat Transfer Characteristics of a Porous Radiant Burner 189

10.1 Introduction 189

10.2 Formulation 191

10.3 Results and Discussion 196

10.4 Conclusions 211

11 Conclusions and Recommendations 213

11.1 Summary 213

11.2 Recommendations and Future Works 217

Bibiliography 219

TH-1868_004301

Appendix **236**

TH-1868_004301

List of Figures

2.1 A hemisphere of south bound rays with intensities $i(\Theta, \Phi)$ focused at the center P of the infinitesimal area element dA. 20

2.2 Radiative energy balance over a control volume based on the DTM. . 23

2.3 2-D rectangular enclosure showing uniform grids and five sample intensities $i(\Theta, \Phi)$ focused at point $p(i, j)$. 28

2.4 A typical control volume for evaluation of source function 30

2.5 A flow chart showing the solution procedure 32

2.6 Discretization of hemisphere into longitudinal planes. 33

2.7 Solution plane and the 2-D control volume. 35

2.8 (a) Intensities $i(\Theta, \Phi)$ and EI $I(\alpha)$ in a representative discrete plane, (b) Discrete plane when viewed from Y axis towards $X - Z$ plane. . . 36

2.9 Some representative south bound EIs spanned over $0 \leq \alpha \leq \pi$ 37

3.1 1-D planar medium under consideration with physical/optical coordinates. 49

3.2 Variation of non-dimensional temperature θ with normalized optical depth τ/τ_L; comparison between the direct method and the inverse method. 53

TH-1868_004301

3.3 Variation of non-dimensional gas temperature θ with normalized optical depth τ/τ_L. 56

3.4 Variation of radiative heat flux Ψ_R, conductive heat flux Ψ_C with normalized optical depth τ/τ_L for various parameters. 58

3.5 Variation of radiative heat flux Ψ_R, conductive heat flux Ψ_C with normalized optical depth τ/τ_L for various parameters. 59

4.1 Variation of gas temperature θ with normalized optical depth τ/τ_L at different time ξ for N =0.01 and 0.1. 67

4.2 Variation of conductive heat flux Ψ_C, radiative heat flux Ψ_R and total heat flux Ψ_T with normalized optical depth τ/τ_L at different time ξ. . 69

4.3 Steady state temperature θ distributions with varying (a) τ/τ_L and N, (b) τ/τ_L and ω, and (c) τ/τ_L and τ_L; other radiative parameters fixed. 71

4.4 Steady state variations of (a) total heat flux Ψ_T, (b) conductive heat flux Ψ_C and (c) radiative heat flux Ψ_R with τ/τ_L and ω; $\tau_L = 1.0$ and $N = 0.01$. 73

4.5 Steady state variations of (a) total heat flux Ψ_T, (b) conductive heat flux Ψ_C and (c) radiative heat flux Ψ_R with τ/τ_L and τ_L; $N = 0.1$ and $\omega = 0$. 74

4.6 Variation of total heat flux Ψ_T, conductive heat flux Ψ_C and radiative heat flux Ψ_R at $\tau/\tau_L = 0.25$, 0.5 and 0.75 with non-dimensional time varying from unsteady to steady state for $N = 1.0$ and 0.01. 75

4.7 Effect of scattering on total heat flux Ψ_T at $\tau/\tau_L = 0.25$, 0.5 and 0.75 with ξ. (a) $N = 0.01$ and (b)$N = 0.1$ 76

4.8 Variation of temperature θ along optical depth τ/τ_L with and without heat generation at different time steps; (a) $N = 0.1$ (b) $N = 0.01$. . . 78

4.9 Variation of conductive heat flux Ψ_C, radiative heat flux Ψ_R and total heat flux Ψ_T with normalized optical depth τ/τ_L at steady state with and without heat generation. 79

TH-1868_004301

4.10 Variation of (a) conductive heat flux Ψ_C, (b) radiative heat flux Ψ_R and (c) total heat flux Ψ_T with non-dimensional time ξ. 80

5.1 Steady state variation of total heat flux Ψ_T with (a) variable thermal conductivity parameter γ, (b) conduction-radiation parameter N and (c) extinction coefficient β. 91

5.2 Steady state variation of total heat flux Ψ_T with scattering albedo ω for different values of γ with anisotropic effect. 92

5.3 Steady state variation of total heat flux Ψ_T with north boundary emissivity ϵ_N for different γ with anisotropic effect. 93

5.4 Effect of thermal conductivity parameter γ on steady state temperature θ variation with τ/τ_L for (a) $\beta = 0.1$, (b) $\beta = 1.0$ and (c) $\beta = 10.0$. 94

5.5 Effect of thermal conductivity parameter γ on steady state θ variation with τ/τ_L for conduction-radiation parameter (a) $N = 1.0$, (b) $N = 0.5$, (c) $N = 0.1$ and (d) $N = 0.01$. 95

5.6 Effect of thermal conductivity parameter γ on temperature θ variation with τ/τ_L at time (a) $\xi = 0.005$, (b) $\xi = 0.01$, and (c) $\xi = 0.05$. 96

5.7 Effect of thermal conductivity parameter γ on temperature θ variations with τ/τ_L for different scattering albedo ω at (a) $\xi = 0.1$ and (b)-(d) steady state. 97

5.8 Effect of thermal conductivity parameter γ on temperature θ variation with time ξ at locations $\tau/\tau_L = 0.1$ and 0.9 for different values of conduction-radiation parameter N. 98

5.9 Effect of thermal conductivity parameter γ on variation of radiative heat flux Ψ_R, conductive heat flux Ψ_C and total heat flux Ψ_T at the location $\tau/\tau_L = 0.75$. with the effect of anisotropy. 100

5.10 Effect of thermal conductivity parameter γ on conductive heat flux Ψ_C for different ω at time ξ (a) 0.01, (b) 0.05 and (c) 0.1. 101

5.11 Effect of thermal conductivity parameter γ on radiative heat flux Ψ_R for different ω at time ξ (a) 0.01, (b) 0.05 and (c) 0.1. 102

TH-1868_004301

6.1 Porosity distribution along the thickness for the four models (L/D_p = 10) 109

6.2 Comparison of dimensionless temperature θ with experimental results from reference [86] 113

6.3 Effects of κ on variations of (a) effective thermal conductivity λ_m, (b) total effective thermal conductivity K_{eff}, (c) radiative heat flux Ψ_R, (d) conductive heat flux Ψ_C and (e) total heat flux Ψ_T with η when $\omega = 0.5$, $N = 0.1$ and $L/D_p = 20$. 114

6.4 Effects of L/D_p ratio on variations of (a) conductive heat flux Ψ_C, (b) radiative heat flux Ψ_R, (c) total heat flux Ψ_T and (d) total effective thermal conductivity K_{eff} with η when $\omega = 0.5$, $N = 0.1$ and $\kappa = 100$. 115

6.5 Effects of conduction-radiation paramcter N on variations of (a) conductive heat flux Ψ_C, (b) radiative heat flux Ψ_R, and (c) total effective thermal conductivity K_{eff} with η when $\omega = 0.5$, $L/D_p = 20$. and $\kappa = 100$. 116

6.6 Effects of scaled scattering albedo ω on variations of (a) conductive heat flux Ψ_C, (b) radiative heat flux Ψ_R, and (c) total effective thermal conductivity K_{eff} with η when $N = 0.1$, $L/D_p = 20$ and $\kappa = 100$. 117

6.7 (a) Mean total effective thermal conductivity for different models with variation of κ when $\omega = 0.5$, $N = 0.1$ and $L/D_p = 20$ (b) Mean total effective thermal conductivity for different models with variation of L/D_p ratio when $\omega = 0.5$, $N = 0.1$ and $\kappa = 100$ (c) Mean total effective thermal conductivity for different models with variation of N when $\omega = 0.5$, $\kappa = 100$ and $L/D_p = 20$. 118

6.8 Variations of temperature θ with geometric depth η for different models with the effects of (a) L/D_p ratio when $\omega = 0.5$, $N = 0.1$ and $\kappa = 100$ and (b) κ when $\omega = 0.5$, $N = 0.1$ and $L/D_p = 20$. 120

6.9 Effects of (a) κ when $\omega = 0.5$, $N = 0.1$ and $L/D_p = 20$ and (b) L/D_p ratio when $\omega = 0.5$, $N = 0.1$ and $\kappa = 100$ on transient temperature θ distributions at locations $\eta = 0.25$ and 0.75. 122

TH-1868_004301

6.10 Effects of (a) κ when $\omega = 0.5$, $N = 0.1$ and $L/D_p = 20$, (b) L/D_p ratio when $\omega = 0.5$, $N = 0.1$ and $\kappa = 100$ and (c) N when $\omega = 0.5$, $L/D_p = 20$ and $\kappa = 100$ on transient total heat flux Ψ_T distributions at locations $\eta = 0.25$, 0.5 and 0.75. 123

6.11 Effects of (a) κ when $\omega = 0.5$, $N = 0.1$ and $L/D_p = 20$, (b) L/D_p ratio when $\omega = 0.5$, $N = 0.1$ and $\kappa = 100$ and (c) N when $\omega = 0.5$, $L/D_p = 20$ and $\kappa = 100$ on transient radiative heat flux Ψ_R distributions at locations $\eta = 0.25$, 0.5 and 0.75. 124

6.12 Effects of (a) κ when $\omega = 0.5$, $N = 0.1$ and $L/D_p = 20$, (b) L/D_p ratio when $\omega = 0.5$, $N = 0.1$ and $\kappa = 100$ and (c) N when $\omega = 0.5$, $L/D_p = 20$ and $\kappa = 100$ on transient conductive heat flux Ψ_C distributions at locations $\eta = 0.25$, 0.5 and 0.75. 125

7.1 Schematic diagram of the problem under consideration. 130

7.2 The fully-developed velocity distribution for several values of the porous media shape parameter. 132

7.3 Variation of the total Nusselt number Nu along the axial length η_x for various values of PMSP γ: (a) effect of the extinction coefficient β; (b) effect of the conduction-radiation parameter N. Results for Nu without radiation effect ($\beta = 0$) are also shown. 142

7.4 Similarity temperature profile $\frac{\theta_w - \theta}{\theta_w - \theta_m}$ at different axial locations, (a) $\gamma = 0.1$ and (b) $\gamma = 10$, corresponding to $\beta = 2$, ω =0.35, $N = 0.01$, $\epsilon = 1$ and $Pe = 8$ 143

7.5 Variation of the total Nusselt number Nu with PMSP γ, (a) without radiation ($\beta = 0.0$), (b) with radiation at axial location $\eta_x = 0.0001$ and (c) with radiation at axial location $\eta_x = 0.001$; $Pe = 0.08$ in both the figures 144

7.6 Effect of PMSP γ on variations of (a) convection Nusselt number Nu_C and radiation Nusselt number Nu_R, (b) total Nusselt number Nu and (c) bulk-mean temperature θ_m along the axial distance η_x; $\beta = 2.0, \omega = 0.35, \epsilon_w = 1.0, N = 0.01$ and $Pe = 8.0$. 145

TH-1868_004301

7.7 Effect of PMSP γ on variation of temperature θ normal to the flow direction at axial locations (a) $\eta_x = 0.005$, (b) $\eta_x = 0.0335$, (c) $\eta_x = 0.05$ and (d) $\eta_x = 0.08$ and 1.0; $\omega = 0.35, N = 0.01$, $\epsilon = 1$ and $Pe = 8.0$. Results without radiation effect ($\beta = 0$) are also shown. . 146

7.8 Variation of the total Nusselt number Nu along the axial length η_x for various values of PMSP γ: (a) effect of the extinction coefficient β and (b) effect of the conduction-radiation parameter N. Results for Nu without radiation effect ($\beta = 0$) are also shown. 147

7.9 Effects of PMSP γ on variations of (a) convection Nusselt number Nu_C and radiation Nusselt number Nu_R, (b) total Nusselt number Nu and (c) bulk-mean temperature θ_m along the axial distance η_x; $\beta = 2.0, \omega = 0.35, \epsilon_w = 1.0, N = 0.01$ and $Pe = 8.0$. 148

8.1 Geometry and the coordinates of the problems under consideration. . 154

8.2 Comparison of the CDM and the DTM results with the MCM results for the effects of extinction coefficient β on (a) heat flux Ψ_R along the hot (south) boundary and (b) the centerline emissive power $(T/T_S)^4$. 160

8.3 Comparison of the CDM and the DTM results for the effects of aspect ratio r on (a) heat flux Ψ_R along the hot (south) boundary and (b) the centerline emissive power $(T/T_S)^4$. 161

8.4 Comparison of the CDM and the DTM results for heat flux Ψ_R variations along the south boundary for the effects of (a) extinction coefficient β, (b) scattering albedo ω and (c) aspect ratio r. 162

8.5 Comparison of the 2-D CDM and the 2-D DTM results for the steady-state centerline temperature θ distribution for aspect ratio $r = 10$ with 1-D CDM results [29] for the effects of (a) extinction coefficient β, (b) conduction-radiation parameter N and (c) scattering albedo ω. 163

8.6 Comparison of the CDM and the DTM results for the centerline temperature θ distribution at time $\xi = 0.001, 0.005, 0.015, 0.04$ and steady state (SS) for conduction-radiation parameter $N =$ (a) 0.01, (b) 0.1 and (c) 1.0. 166

8.7 Comparison of the CDM and the DTM results for the centerline temperature θ distribution at time $\xi = 0.001, 0.005, 0.015, 0.04$ and steady state (SS) for extinction coefficient $\beta =$ (a) 0.1, (b) 1.0 and (c) 5.0. 168

TH-1868_004301

8.8 Comparison of the CDM and the DTM results for the centerline temperature θ distribution at time ξ = 0.001, 0.005, 0.015, 0.04 and steady state (SS) for scattering albedo ω = (a) 0.0, (b) 0.5 and (c) 0.9. 169

8.9 Comparison of the CDM and the DTM results for the centerline temperature θ distribution at time ξ = 0.001, 0.005, 0.015, 0.04 and steady state (SS) for the hot (south) boundary emissivity ϵ_S = (a) 1.0, (b) 0.5 and (c) 0.1. 170

9.1 Effect of γ on centerline temperature θ for different values of the aspect ratio r; $\beta = 1$, $N = 0.01$ and $\omega = 0.5$. 177

9.2 Effect of γ on total heat flux Ψ_T at (a) the bottom (hot) wall, (b) the top wall and (c) the side wall(s) for different values of the aspect ratio r; $\beta = 1$, $N = 0.01$ and $\omega = 0.5$. 178

9.3 Effect of γ on centerline temperature θ profile for the extinction coefficient β = (a) 0.1, (b) 1.0 and (c) 5.0; $r = 1$, $N = 0.5$ and ω = 0.5. 179

9.4 Effect of γ on total heat flux Ψ_T at the bottom (hot) wall for the extinction coefficient β = (a) 0.1, (b) 1.0 and (c) 5.0; $r = 1$, $N = 0.5$ and $\omega = 0.5$. 180

9.5 Effect of γ on centerline temperature θ profile for the conduction-radiation parameter N = (a) 1, (b) 0.1 and (c) 0.01; $r = 1$, $\beta = 1$ and $\omega = 0.5$. 181

9.6 Effect of γ on total heat flux Ψ_T at the bottom (hot) wall for the conduction-radiation parameter N = (a) 1, (b) 0.1 and (c) 0.01; r = 1, $\beta = 1$ and $\omega = 0.5$. 182

9.7 Percentage change in total heat flux Ψ_T due to the effect of γ for different values of the conduction-radiation parameter N; $r = 1$, β = 1 and $\omega = 0.5$. 183

9.8 Isotherms showing the effect of γ for N = (a) 0.01 and (b) 0.1; r = 1, $\beta = 1$ and $\omega = 0.5$. 184

9.9 Effect of γ on transient temperature θ along the centerline for the conduction-radiation parameter N = (a) 0.01, (b) 0.1 and (c) 1; r = 1, $\beta = 1$ and $\omega = 0.5$. 185

TH-1868_004301

9.10 Effect of γ on transient temperature at locations $y/L_y = 0.25$ and 0.75 along the centerline ($x/L_x = 0.5$) for the conduction-radiation parameter N = (a) 0.01, (b) 0.1 and (c) 1; $r = 1$, $\beta = 1$ and $\omega = 0.5$. 186

10.1 Schematic diagram of the problem under consideration. 192

10.2 Effect of aspect ratio r on centerline ($\eta_y = 0.5$) temperature for (a) $P_2 = 1$, $\beta = 10$ (b) $P_2 = 500$, $\beta = 10$, (c) $P_2 = 1$, $\beta = 0$ and (d) $P_2 = 500$, $\beta = 0$ for $\omega = 0.0$ and $\epsilon_S = \epsilon_N = 1$. 198

10.3 Isotherms of gas temperature for different aspect ratio r. (a) $r = 0.1$, (b) $r = 1$ and (c) $r = 5$ for $P_2 = 1$, $\beta = 10$, $\omega = 0.0$ and $\epsilon_S = \epsilon_N = 1$. 199

10.4 Isotherms of solid temperature for different aspect ratio r. (a) $r = 0.1$, (b) $r = 1$ and (c) $r = 5$ for $P_2 = 1$, $\beta = 10$, $\omega = 0.0$ and $\epsilon_S = \epsilon_N = 1$. 200

10.5 Effect of extinction coefficient β on centerline ($\eta_y = 0.5$) temperature for (a) black wall $\epsilon_S = \epsilon_N = 1$. (b) $\epsilon_S = \epsilon_N = 0.0$ for $r = 1$, $P_2 = 500$ and $\omega = 0.5$. 202

10.6 Effect of extinction coefficient β on radiative heat flux at exit for (a) black wall $\epsilon_S = \epsilon_N = 1$. (b) $\epsilon_S = \epsilon_N = 0.0$ for $r = 1$ $P_2 = 500$, $\omega = 0.5$. 203

10.7 Radiative flux at the exit ($\eta_x = 1.0$) with the effect of scattering albedo for (a) black wall , $\epsilon_S = \epsilon_N = 1$. (b) $\epsilon_S = \epsilon_N = 0.0$ for $P_2 = 500$, $r = 1.0$, $\beta = 100$ and $\omega = 0.5$. 205

10.8 (a) Different terms in gas energy equation for aspect ratio $r = 1$, (b) Different terms in solid energy equation for aspect ratio $r = 1$ (c) Centerline ($\eta_y = 0.5$) fluxes along x direction for different aspect ratio for $P_2 = 500$, $\beta = 100$ $\omega = 0.5$ and $\epsilon_S = \epsilon_N = 1$. 206

10.9 (a) Radiative flux at the exit ($\eta_x = 1.0$) with the effect of emissivity of the north and south boundaries and (b) Radiative efficiency at the exit for different aspect ratio r for $P_2 = 500$, $\beta = 100$ and $\omega = 0.5$. . . 208

10.10 Effect of emissivities of the south and the north boundaries on centerline ($\eta_y = 0.5$) temperature for different aspect ratio r (a) $r = 0.1$, (b) $r = 1$ and (c) $r = 5$ for $P_2 = 1$, $\beta = 100$ and $\omega = 0.5$. 209

TH-1868_004301

10.11 Transient centerline ($\eta_y = 0.5$) fluxes along x-direction (a) convective heat flux, (b) radiative heat flux, (c) gas conductive heat flux and (d) solid conductive heat flux for $r = 1$, $P_2 = 500$, $\beta = 100$ and $\omega = 0.5$. 211

TH-1868_004301

List of Tables

3.1 Comparison of temperature for isotropic scattering with $\omega = 0.5$ and $\tau_L = 1.0$, $\epsilon_N = \epsilon_S = 1.0$ and for $N = 0.5$, 0.1 and 0.05. 54

3.2 Comparison of radiative heat flux distribution for isotropic scattering with $\tau_L = 1.0$, $\theta_N = 0.1$, $\omega = 0.5$ and $\epsilon_N = \epsilon_S = 0.5$ for several values of N. 55

4.1 Comparison of transient temperature θ at time $\xi = 0.05$ for $\tau_L = 1.0$, $\omega = 0.5$ and $N = 0.1$ and two sets of boundary reflectivities. 65

4.2 Comparison of transient net radiative heat flux distributions with isotropic scattering at time $\xi = 0.05$ for $\tau_L = 1.0$, $\theta_N = 1.0$, $\theta_S = 0.0$, $\omega = 0.5$ and $N = 0.1$ and two sets of boundary reflectivities. 66

5.1 Steady state heat flux results of present work with a difference of ± 0.0001 with that of reference [60]; Here $N = 0.5$, $\epsilon_S = \epsilon_N = 1$, $\tau_L = 1.0$, $\theta_N = 0.5$. 90

7.1 Effect of the PMSP γ on Nu_C, Nu_R, Nu, Ψ_C and Ψ_R at various axial locations η_x corresponding to $\beta = 0.2, N = 0.01, \epsilon = 0.5$ and $\omega = 0.5$. Numbers in brackets are values from [96]. 133

7.2 Effect of the PMSP γ on Nu_C, Nu_R, Nu, Ψ_C and Ψ_R at various axial locations η_x corresponding to $\beta = 0.2, N = 0.1, \epsilon = 0.5$ and $\omega = 0.65$. Numbers in brackets are values from [96]. 134

7.3 Effect of the PMSP γ on Nu_C, Nu_R, Nu, Ψ_C and Ψ_R at various axial locations η_x corresponding to $\beta = 0.2, N = 0.5, \epsilon = 0.5$ and $\omega = 0.35$. Numbers in brackets are values from [96]. 135

TH-1868_004301

7.4 Effect of the PMSP γ on Nu_C, Nu_R, Nu, Ψ_C and Ψ_R at various axial locations η_x corresponding to $\beta = 2.0, N = 0.01, \epsilon = 0.5$ and $\omega = 0.65$. Numbers in brackets are values from [96]. 136

7.5 Effect of the PMSP γ on Nu_C, Nu_R, Nu, Ψ_C and Ψ_R at various axial locations η_x corresponding to $\beta = 2.0, N = 0.1, \epsilon = 0.5$ and $\omega = 0.65$. Numbers in brackets are values from [96]. 137

7.6 Effect of the PMSP γ on Nu_C, Nu_R, Nu, Ψ_C and Ψ_R at various axial locations η_x corresponding to $\beta = 2.0, N = 0.5, \epsilon = 0.5$ and $\omega = 0.65$. Numbers in brackets are values from [96]. 138

7.7 Effect of the PMSP γ on Nu_C, Nu_R, Nu, Ψ_C and Ψ_R at various axial locations η_x corresponding to $\beta = 10.0, N = 0.01, \epsilon = 0.5$ and $\omega = 0.65$. Numbers in brackets are values from [96]. 139

7.8 Effect of the PMSP γ on Nu_C, Nu_R, Nu, Ψ_C and Ψ_R at various axial locations η_x corresponding to $\beta = 10.0, N = 0.1, \epsilon = 0.5$ and $\omega = 0.65$. Numbers in brackets are values from [96]. 140

7.9 Effect of the PMSP γ on Nu_C, Nu_R, Nu, Ψ_C and Ψ_R at various axial locations η_x corresponding to $\beta = 10.0, N = 0.5, \epsilon = 0.5$ and $\omega = 0.65$. Numbers in brackets are values from [96]. 141

8.1 Comparison of the steady-state centerline ($x/L_x = 0.5$) temperature θ results from the CDM and the DTM at various locations along y/L_y with results in Refs. [76] and [65] for different values of the extinction coefficient β and conduction-radiation parameter N; $r = 1.0$, ω=0.0, all boundaries are black. 165

TH-1868_004301

Nomenclature

a_1 asymmetry factor, [-]

A surface area per unit volume of the solid, $[1/m]$

A constant, [-]

A_p projected area, $[m^2]$

c specific heat, $[J/kgK]$

C_p specific heat at constant pressure, $[J/kgK]$

ds small distance, $[m]$

D_h hydraulic diameter $= 2W$, $[m]$

D_p mean diameter of the packed bed, $[m]$

E_n exponential integral of order n

G incident radiant energy, $[W/m^2]$

G' effective incident radiant energy, $[W/m^2]$

h heat transfer coefficient, $[W/m^2K]$

i intensity/ray, $[W/m^2]$

TH-1868_004301

I effective intensity/ray, $[W/m^2]$

j indices, [-]

J radiosity, $[W/m^2]$

k thermal conductivity, $[W/mK]$

k_a thermal conductivity of the continuous phase, $[W/mK]$

k_m effective thermal conductivity, $[W/mK]$

k_o reference thermal conductivity,$[W/mK]$

k_s thermal conductivity of the dispersed phase, $[W/mK]$

K permeability of the porous medium, $[m^2]$

K_{eff} total effective thermal conductivity, $[W/mK]$

$\overline{K}_{\text{eff}}$ mean total effective thermal conductivity, $[W/mK]$

L thickness of the packed bed, $[m]$

L_x length of the enclosure in the x-direction, $[m]$

L_y length of the enclosure in the y-direction, $[m]$

m time step, [-]

M number of effective intensities/intensities/rays, [-]

n Number of control volumes, [-]

n_p number density of packed spheres, $[beads/m^3]$

TH-1868_004301

N conduction-radiation parameter, [-]

Nu Nusselt number, [-]

p Phase function, [-]

$P_1 - P_7$ dimensionless parameters, [-]

Pe Peclet number, [-]

Pr Prandtl number, [-]

Q''' volumetric heat generation rate, $[W/m^3]$

q heat flux, $[W/m^2]$

r aspect ratio, [-]

Re Reynolds number, [-]

S geometric path length, $[m]$

S source function, $[W/m^2]$

S' source function in the CDM formulation, $[W/m^2]$

S_r scaling factor, [-]

t time, [s]

T temperature, [K]

u, v velocity in x, y direction, $[m/s]$

U_m mean velocity, $[m/s]$

W width of the channel, $[m]$

TH-1868_004301

x, y, z coordinate direction

Greek symbols:

α planar angle in the CDM, [rad]

β extinction coefficient, [1/m]

β thermal coefficient of volume expansion, [1/m]

γ coefficient for thermal conductivity variation, [-]

γ porous medium shape parameter, [-]

γ' variable thermal conductivity parameter, $[W/mK^2]$

Γ collapsing coefficient, [-]

δ unit step function, [-]

δ delta function, [-]

δQ differential energy flow rate, $[W]$

$\Delta\alpha$ angular thickness of the discrete plane in the CDM, [rad]

$\Delta\Theta$ angular thickness of the discrete plane in the DTM, [rad]

$\Delta\Omega$ sub-solid angle, [sr]

$\Delta\xi$ non-dimensional time step, [-]

ϵ Emissivity, [-]

TH-1868_004301

η non-dimensional length, [-]

θ non-dimensional temperature, [-]

θ_m non-dimensional mean temperature, [-]

Θ polar angle, [rad]

κ absorption coefficient, $[1/m]$

λ wavelength, $[\mu m]$

μ direction cosine (of polar angle), [-]

μ dynamic viscosity, $[kg/ms]$

ξ non-dimensional time, [-]

ρ density, $[kg/m^3]$

σ Stefan-Boltzmann constant, $[= 5.670 \times 10^{-8} W/m^2K^4]$

σ_s scattering coefficient, $[1/m]$

τ optical thickness/depth, [-]

$\tilde{\tau}$ effective optical thickness/depth, [-]

ϕ porosity, [-]

Φ azimuthal angle, [rad]

Φ non-dimensional emissive power, [-]

Φ_d dissipation function, $[j/kgm^2]$

TH-1868_004301

ψ scattering angle, [rad]

Ψ non-dimensional heat flux, [-]

ω scattering albedo, [-]

Ω spherical solid angle, [sr]

Subscript:

0 reference value, or at length = 0

av average

b black body value

C conductive, convective

e exit

E East wall/boundary

g gas

i ith ray

i inlet

L at length = L

n nth ray

N north wall/boundary

R radiative

ref reference

TH-1868_004301

s	solid
S	south wall/boundary
T	total
w	wall value
W	west wall/boundary
x	x-direction
y	y-direction

Superscript:

$*$	non-dimensional quantities
$-$	negative direction
$'$	dummy variable

TH-1868_004301

Abbreviations

ADI	alternating direction implicit
CC	collapsing coefficient
CDM	collapsed dimension method
CPU	central processing unit
CVSCP	control volume surface central points
DTM	discrete transfer method
EI	effective intensity
LTE	local thermal equilibrium
MCM	Monte Carlo method
PMSP	porous media shape parameter
RTE	radtaive transfer equation
SS	steady state
1-D/2-D/3-D	one/two/three dimensional

TH-1868_004301

Chapter 1

Introduction

All bodies continuously emit energy by a process of electromagnetic radiation which is caused by the molecular and atomic agitation associated with their internal energy. The emitted radiant energy has a broad spectrum of wavelength ranging from 10^4 m for the radio waves to 10^{-14} m for the cosmic rays. The radiation which can be detected as heat or light is considered as thermal radiation. It falls in the wavelength range of 0.1 μm to 100 μm [1]. The electromagnetic radiation within the aforesaid range at which a medium emits energy only due to its temperature is called thermal radiation.

1.1 Importance of Thermal Radiation

Thermal radiation energy transfer between two bodies depends on the difference of their absolute temperatures, each raised to the fourth power in comparison to conduction and convection where energy transfer takes place at a power of temperature difference less than two. This makes thermal radiation more dominant in high temperature applications. This way radiation contributions become extremely

TH-1868_004301

important in furnaces, combustion chambers, fires, nuclear explosion, etc.

In contrast to the two other modes of heat transfer, viz. conduction and convection, thermal radiation is transferred by electromagnetic waves, or photons which does not require a medium for its propagation from one place to another. So, in the absence of a medium, radiation becomes the significant mode of heat transfer. This makes it important in vacuum and space applications.

The importance of radiation is even found in some low temperature phenomena. One example is that of the warming effect felt by a person outside in a cold weather [1]. In some cases, radiation interacts with the other modes by providing local heat sources to change the temperature profile of the medium. For example, radiation can heat the walls of an enclosure by acting from a distant place and can cause natural circulation which would have never occurred had there been no radiation. Another example is the effect of radiation in the boundary layer flow of a participating fluid. It has been seen that the convective heat transfer can significantly be affected by external radiation in a boundary layer type of flow [2].

Another important application of thermal radiation is in the collection of solar energy and the greenhouse effect [1]. For designing a solar receiver, the accurate modeling of radiation is found to be very important. The balance between the available solar energy, the useful energy transferred to a working fluid, and the various convective, conductive, and radiative losses are very sensitive, and presents a challenge in the design of an efficient collector [3]. Radiation is also important in the processing of glass, metals and fibrous and foam insulations [4–7].

Especially in combustion applications, either for power production or propulsion, consideration of thermal radiation becomes extremely important because combustion phenomenon as well as heat transfer rates are greatly influenced by radiation. In porous media combustion, radiation plays a vital role and the radiant output can be increased with a proper study of radiation inside such media [8, 9].

TH-1868_004301

1.2 Radiation in a Participating Medium

When two surfaces are exchanging heat by radiation, the intervening medium may or may not take part depending on the nature of the medium. Radiation can be grouped into two categories depending on the nature of the medium. When the medium is inactive to the radiation exchange, it is termed as surface radiation. In this situation, radiation from opaque bodies emanates only from 0.1 μm or less of the surface layers. Radiation intensities emanating from one surface hit another surface without any change of its magnitudes. Radiation in outer space, where there is no medium at all, and even on the earth, in many practical engineering applications in which medium is transparent to all wavelengths of thermal radiation, fall under the scope of surface radiation.

Radiation with participating medium,also known as gas radiation, on the other hand, is a complex phenomenon in comparison to surface radiation. In this case, in addition to the radiation from the boundary, the medium also takes part in the radiation. The intensity emanating from a boundary undergo changes inside the medium by absorption, emission and scattering before it reaches the other boundary. All problems involving combustion phenomenon fall under the purview of radiative transfer with participating medium.

The practical applications of radiation in a participating medium and the complexities associated with its computations, have been the source of motivations for the researchers. The importance of gas radiation in industry was recognized in the 1920s for heat transfer in furnaces. Combustion products such as carbon dioxide and water vapor were found to be significant emitters and absorbers of radiant energy. The energy emitted from flames arises not only from the gaseous emission but also from hot carbon (soot) particles within the flame and from suspended particulate material, as in the pulverized-coal combustion. Radiation can also be appreciable in engine combustion chambers, where temperatures can reach around 2000 K. Radiation transfer is very important in glass manufacturing. An example of radiation effects within an absorbing-emitting medium is in a glass-melting furnace.

TH-1868_004301

The modeling of thermal radiation in participating media continues to represent a significant challenge to the heat transfer community. Of particular interest has been to enhance the predictive capability of either homogeneous or heterogeneous combustion phenomena, including, among others, burning of pulverized coal, propellants for solid rockets and gun systems, and waste materials.

1.3 Various Radiation Models in Participating Medium

Although in high temperature applications consideration of thermal radiation is important, other modes of heat transfer can also not be ignored. For the evaluation of temperature and/or other heat transfer quantities of interest, energy equation has to be solved by taking into account the effect of radiation. In this case, the divergence of heat flux appearing in the energy equation is the contributions from the conductive and radiative modes of heat transfer. Calculation of the divergence of radiative flux requires solution of the radiative transfer equation. The radiative transfer equation is a third order integral equation and with its incorporation, the energy equation turns out to be an integro-differential equation whose solution is quite difficult. Further, complexities due to radiation increases due to the fact that radiative transfer deals with seven independent variables, viz., three space coordinates, the frequency of radiation, two coordinates for describing the direction of photon travel and time. On the other hand, conduction and convection involve a maximum of four independent variables, viz., three space coordinates and time. The combination of the above complexities make the complete solution of the problem, in real sense, a challenging task. Thus, there has been always the quest for the development of efficient and cost-effective methods for predicting radiative heat transfer rates in practical energy conversion systems.

Because of the aforementioned complexities, analytical solution of radiative transfer equation can be found only for some simple situations. On the other hand, a number of numerical methods have been found for calculating radiative transfer in

TH-1868_004301

participating media for different situations. All these approximate methods have their own merits and demerits. Some methods work very well for high optical thickness whereas the same show weakness for low optical thickness. Some are very accurate for pure radiation problems but the same do not work satisfactorily for combined mode heat transfer problems. So, depending upon the problems, one can opt for a particular method. On the other hand, to ascertain whether a particular method is appropriate for a given problem, comparisons have to be made against the benchmark results obtained either from experiments or exact analytical solutions.

Although, the Monte Carlo [10] method's applicability to conjugate radiation, conduction and/or convection mode problems is very restricted, for the majority of problems dealing purely with radiative transport, its solutions are considered benchmark. Monte Carlo method is a statistical method in which the history of bundles of photons is traced as they travel through the enclosure. While the statistical nature of the Monte Carlo method makes it difficult to couple it with other calculations, it is the only method that can satisfactorily deal with the effects of variable radiative properties (nonideal directional and/or nongray behavior). The zonal method solution is also considered exact and has been successfully applied to a large class of problems. This method was developed by Hottel [11] in his pioneering work on furnace heat transfer. Unlike the spherical harmonics or the P_N approximation [12–14] and the discrete ordinate method [15–18], the zonal method approximates spatial, rather than directional, behavior by breaking up an enclosure into finite, isothermal subvolumes. The P_N method and the discrete ordinate method, even being approximate methods, have the most diverse applications, in all types of simple and complex problems (conjugate problems). However, the P_N approximation do not perform well at low optical thickness situations. The finite element method [19–21] and the finite volume method [22,23] in radiative transport problems have the added advantage in conjugate problems as they can be easily coupled with the conductive and the convective part. On the other hand, most of the methods have difficulties in coupling the radiative part of the problem with the conductive and/or convective part. For example, Monte Carlo method is difficult to match it with other calculations because of its statistical nature. The discrete transfer method (DTM), proposed by Lockwood and Shah [24,25], is comparatively simple in formulation and

TH-1868_004301

has been tested for many situations in this work [26–28]. This method combines features of the discrete ordinate, the zonal and the Monte Carlo method. It works for low to high optical thickness and can handle any scattering phase function. It also works for conjugate mode problems. The collapsed dimension method (CDM) is one of the latest methods in this area. This is also a ray tracing method and has been successfully applied to many situations [29–33]. This method is computationally more efficient than the DTM [34]. However, the performance of the CDM for a 3-dimensional enclosure with complicated participating medium situation is yet to be established.

The different radiative transfer methods found in the literature are the following [1, 35–37]:

1. Exact analytical method
2. Diffusion approximation
3. Zonal method
4. Monte Carlo method
5. Multi-flux method
6. Moment method
7. Spherical harmonics method/P_N approximation
8. Discrete ordinate method
9. Discrete transfer method
10. Heat ray method
11. Discretized intensity method
12. Finite element method
13. Product integration method

TH-1868_004301

14. Boundary element method

15. Finite volume method

16. Collapsed dimension method

A survey of the literature over the past several years demonstrates that some solution methods have been used frequently, while others that appeared promising at one time are no longer employed on a regular basis. Apparently, some methods have been found to be more readily adapted to more difficult situations than others (such as multidimensionality, variable properties, anisotropic scattering and/or nongray effects). The majority of radiative heat transfer analyses today appears to use one of the five methods: (i) spherical harmonics method or a variation of it, (ii) the discrete ordinate method, (iii) the finite volume method, (iv) the Monte Carlo method and (v) the discrete transfer method. But, it is always very difficult to comment which is the best radiation model used so far. According to Howell [38] and Yang [39], any practical numerical radiation method should have the following features:

1. Capability to handle multi-dimensional and complex geometry.

2. Good accuracy under all conditions: non-scattering or anisotropic scattering, gray or non-gray, isothermal or non-isothermal participating media.

3. Ease of application.

4. Ease of generalization: flexibility in choosing the different order of approximations

5. Availability of the accurate intensity field and the integrated quantity.

6. Computational compatibility with conductive and/or convective heat transfer codes.

7. Low computation cost.

TH-1868_004301

But it is seen that most of the methods are not able to fulfil all the criteria listed above and they suffer from some discrepancies. As a result, the quest for the development of new methods still remains, and is the reason for development of a dozen of numerical methods in radiative heat transfer in participating media.

It has been mentioned before that the CDM is one of the latest approximate radiative heat transfer methods. This method, although still in the process of development, has been successfully implemented for pure radiation [40–42] problems. It gives good accuracy for all optical thicknesses, works for different geometries [30, 31, 43], is able to handle non-homogeneous medium [44] and also works for the conjugate mode problems [29,45,46]. The CDM is simple in formulation and is also economical [34]. Looking at these features, the current research also aims to extend the range of applications of this method. As far as the methodology and formulations are considered, the CDM is similar to the DTM. The main difference between the two methods is that in the DTM, radiation is a 3-D phenomenon, whereas in the CDM, it is always a 2-D one. The methodologies of the two methods are briefly described in the next chapter.

1.4 Radiation Heat Transfer Combined with Other Modes

A brief but a general review of different class of problems considered in the present work is presented in the following sections. Specific reviews of particulars problems considered in this work are provided in the respective chapters.

1.4.1 Radiation with Conduction

Radiation combined with conduction has many practical applications. In case of a solid or highly viscous media, convection in the medium is negligible and heat transfer usually takes place either by conduction/radiation or both. Glass has the

TH-1868_004301

property of absorbing radiation in certain wavelength regions and also it can emit a significant amount of energy at high temperatures. Glass is optically dense in the infrared region and hence radiative transport takes place through it layer by layer by absorption and emission. In an optically dense material molecular energy conduction is thus augmented by radiative conduction [1]. Therefore, for the process of drawing optical fibers and for the heat treatment of glass plates [47,48], radiation effects become quite important in calculating the temperature distribution within the molten glass in a furnace.

The behavior of radiative transfer within translucent coating is another application in this direction. To protect the interiors of a body from high external temperatures, glassy materials are used as a sacrificial ablating coating. The process of radiation-conduction interaction becomes important in this cases in determining the temperature distribution within the ablating coating [49,50]. The knowledge of temperature distribution thus helps to make the coating more and more efficient for protecting the surfaces.

Radiation can be a significant part of the energy transfer in fibrous insulation materials [6,7], foam insulations [5], high temperature porous insulating materials [51], silica aerogels [52] and in glass-fluidized beds [53]. Initially it was thought that radiation is negligible in the heat transfer through the fibrous materials used for building insulations due to the moderate temperature range. However, it was found that for the temperature range of 300-400 K, both conduction and radiation are significant modes of heat transfer. The consideration of radiation can also become important in case of polyurethane foam as the cell walls are partially transparent to infrared radiation. Low-density, high temperature insulations such as hafnia, thoria, and zirconia are used for high-technology applications such as the space shuttle, re-entry vehicles, and solar central receivers. Since these materials are semitransparent to infrared and visible radiation, radiative transfer through them become comparable to conduction in these applications.

The work towards the coupling of radiation with conduction started in the early 1960s. The solution given by Viskanta and Grosh [54,55] long remained as a bench-

TH-1868_004301

mark solution for 1-D planar medium with consideration of both conduction and radiation. Numerous articles have been found during that time associated with simple combined conduction and radiation problem in a 1-D planar medium. Some of these investigations dealt with the effect of scattering in a 1-D slab [17, 55 60]. A pertaining amount of literature has been found which deals with transient conduction and radiation [4, 60–67]. It has been seen that most of the works deal with 1-D planar medium, whereas works towards 1-D spherical geometry [60, 63, 68, 69], 1-D cylindrical geometry [70 73], 2-D rectangular geometry [74 80] and other 2-D or 3-D geometries are not much. Throughout the 1970s and up to present, the search has continued for methods that could be applied broadly to multidimensional radiative transfer in enclosures, with the additional capability of handling spectral and anisotropic characteristics in absorbing-emitting-scattering media.

1.4.2 Radiation-Conduction in Porous Media and Packed Beds

Radiative heat transfer combined with other modes in porous media is emerging as a topic of major interests in the recent days. Its applications are found in combustion, high-temperature heat exchangers, regenerators and recuperators, insulation systems, packed and circulating bed combustors and reactors, and energy storage and energy conversion devices [1]. A porous medium is defined as a heterogeneous system made up of a solid matrix with its voids filled with fluids. At high temperatures the fluid is usually a gas, which can often be assumed as transparent to radiation because the dimensions between the elements of the solid structure in the porous medium are usually much less than the radiative mean free path for absorption or scattering in the fluid. So, only the solid matrix serves as an absorbing, scattering, and emitting medium in which radiative heat transfer is often coupled with other modes of heat transfer. The porosity of the medium can be very low, as in consolidated particle systems, to intermediate, as in closely packed spheres ($\phi = 0.26$) to greater than 0.98 for some foam-type structures [81]. The solution of radiative transfer in porous media can be based on either continuum or noncontinuum treatment. In a noncontinuum treatment, radiative heat transfer analysis is

TH-1868_004301

carried out based on every single particle, whereas in a continuum approach, radiation is analyzed based on volume averaged properties. Since, the complexity and computational cost is less in case of a continuum treatment, most of the works are based on it. However, if the volume averaged properties are not known, continuum treatment can not be used.

The continuum treatment can be carried out if the elements of the system (solid matrix) are arranged in some regular pattern. For example, a fibrous media can be modeled as an array of cylinders with infinite length or a system made up of arbitrary convex-surfaced particles can be represented by packed bed of spheres. If the system is considered to be made up of elements, it is important to determine whether they can be treated as independent or dependent [82]. In theory, all systems are dependent, but if they do not deviate much from the independent theory, the assumption of independent theory should be done. The criteria for choosing the independent theory can be approximately set at $C/\lambda > 0.5$ and $\phi > 0.95$. Here C is the average particle clearance, λ is the wavelength and ϕ is the porosity. In case of an independent scattering, it is easier to calculate the properties of the bed. On the other hand, some modeling has to be carried out for calculating the properties of the bed with dependent scattering. Models for particles in the Rayleigh range and the geometric range are available. However, no approach is yet available for particles of arbitrary size, and experimental determination of properties is again necessary.

On the other hand, direct simulation technique is very limited. Except for the Monte Carlo technique for large particles, direct simulation techniques have not been developed to solve any but the simplest of problems [81].

The importance of combined conductive and radiative heat transfer in a packed bed is increasing day by day. It has wide applications in thermal insulation systems designs, pebble-bed-type gas-cooled reactors, catalytic converters and so on. Radiative transfer in porous and dispersed media is reviewed in [81, 83–85]. Kamiuto et al. [86,87] solved combined conduction-radiation heat transfer in packed bed with dependent scattering. They assumed the packed bed to be made of opaque diffuse gray spheres and solved it for pure radiation [88], conduction-radiation in 1-D Cartesian

TH-1868_004301

geometry [86] and also in conduction-radiation in cylindrical geometry [87]. Tien [83] gave an overview of existing knowledge on radiative heat transfer on packed beds. Kaviany and Singh [81] have also discussed the different characteristics of radiative heat transfer in a packed bed.

1.4.3 Radiation-Convection in a Duct Flow

Radiation combined with convection and conduction can be found in combustion chambers, atmospheric phenomena, shock-wave problems, rocket nozzles, high-temperature heat exchangers, radiation devices for outer space applications, and industrial furnaces. A number of review papers and books are available in this area [36, 89, 90]. Combined radiation-convection heat transfer for flow of a participating gas in a duct is of engineering interests in some high-temperature heat exchange devices.

Starting from 1960s, there has been a lot of work with the interaction of radiation and convection for a radiatively participating fluid flowing through a duct. The flow through a parallel plate channel, commonly known as a Poiseuille flow, was investigated by Viskanta [91] considering an absorbing-emitting medium. His solution was approximate as he considered thermally developed conditions to obtain relatively simple results. He introduced a new parameter Nusselt number which differs from the usual convective Nusselt number. That new Nusselt number included the contribution from radiation also. Kurosaki [92] solved the same problem without considering the thermally developed approximations. He used the exact integral relations for the calculations of radiative heat flux. Echigo and coworkers [93] also solved the same problem but for high temperatures. Similar problem was introduced earlier by Timofeyev and coworkers [94] using the two flux method. Lii and Ozisik [95] solved the slug flow between two parallel plates with rigorous modeling of the radiative heat flux. The effect of scattering on Poiseuille flow has been discussed by a number of investigators [96, 97]. Chawla and Chen [96] studied the effect of scattering using the method of collocation. The same type of problem was solved by Yener and coworkers [98] for turbulent flow conditions. In all of these works, axial

TH-1868_004301

radiation was neglected.

The effect of two-dimensional radiation was included in the work of Einstein [99] without considering scattering. The effect of scattering was included in the work of Kassemi and Chung [100]. They studied the combined effect of laminar convective heat transfer from an absorbing, emitting, isotropically scattering and uniformly heat generating medium subjected to two-dimensional radiation.

The laminar flow through a porous channel have also been investigated by many researchers [101–103]. Wang and Tien [102] have considered the effect of combined radiation and convection considering uniform velocity across the channel. Kaviany [103] introduced a porous media shape parameter which determines the velocity distribution and calculated the temperature field and Nusselt number without the consideration of radiation.

1.4.4 Radiation with Combustion

Radiation plays an important role in combustion. During combustion, thermal radiation carries energy directly from the combustion products to the burner walls, often at higher rates than convection. In the case of liquid and solid fuels, thermal radiation also plays an important role in the preheating of the fuel and its ignition. A review of importance of radiative heat transfer in combustion systems has been given by Sarofim and Hottel [104]. Viskanta and Menguc [8] discussed the treatment of thermal radiation for the mathematical model of a combustion process or to design of a combustion system. They discussed the radiative properties of combustion products, their modeling and methods of solving the radiative transfer equations.

The treatment of radiation is important in case of porous medium combustion. It is worthwhile to mention here that porous medium combustion has come out to be an emerging field in the recent decades. It offers exceptional advantages compared to techniques of free flame burners [105]. Porous medium burners are characterized by higher burning rates, increased flame stability and lower combustion zone tempera-

TH-1868_004301

tures which lead to a reduction in NO_x formation. They also show a very high turn down ratio, low emissions of CO and are relatively smaller in sizes. Due to these outstanding properties, the porous burner technology is advantageously applied to many different industrial branches. Some of its applications are found in household and air heating systems, in gas turbine combustion chambers, in independent vehicle heating systems, in steam generators etc [105] . Radiation plays a very important role in this type of porous medium combustion. The generally used porous structures made of ceramic foam [106] has excellent properties to convert the energy produced due to combustion into radiant energy. The accurate modeling of radiative transfer is very important to analyze the heat transfer characteristics of such burners. Most of the numerical modeling deals with one dimensional planar medium [107–111]. For calculating the radiative transfer in such a media, different radiation properties like absorption and scattering coefficients become important. For an irregular foam structure, it is numerically difficult to calculate the extinction coefficient. Some researchers do inverse analysis for calculating this radiative properties [112, 113]. But in most of the cases, for calculating these properties experiments remain as the only option.

1.5 Organization of the Dissertation

This thesis is organized in eleven chapters. A brief description of each chapter is discussed here.

In the Introduction chapter, a brief discussion of the definition of thermal radiation in participating media is discussed. The different areas of the application of thermal radiation is reviewed. An overall literature review of thermal radiation with other modes is presented.

In the second chapter, a general discussion is presented for the solution of radiative heat transfer problem combined with other modes of heat transfer. In such problems, coupling of radiation with the energy equation using the CDM and the DTM is

TH-1868_004301

explained in some detail. The solution procedure in a 2-D rectangular enclosure for the DTM is presented. The CDM is also discussed briefly in this chapter.

Chapters 3 - 10 deal with eight different class of combined mode problems. Conclusions and recommendations are incorporated in Chapter 11. Brief discussions of these 8 problems are presented below.

The steady combined conduction-radiation interaction in a planar medium is analyzed in Chapter 1. The medium is considered to be absorbing, emitting and anisotropically scattering. Flux boundary condition is assumed in one of the boundaries. The applicability of the CDM is tested here in case of a problem with the flux boundary.

The internal heat generation is important in many problems. The transient conduction and radiation heat transfer with heat generation in a planar absorbing, emitting and scattering medium is discussed in Chapter 4. The boundaries of the medium are at the prescribed temperatures. Effect of heat generation on temperature and heat flux distributions is investigated. This problem is also intended to test the applicability of the CDM to a new situation.

In Chapter 5, transient conduction-radiation interaction in a planar porous medium is discussed. The porous medium is considered to be a packed bed of opaque spheres. Both Kamiuto's correlated scattering theory and Kaviany's scaling factor is used for calculating the optical thickness. Effect of variable porosity is also introduced. The comparison between different models are analyzed. The DTM is used for calculating the radiative information.

Heat transfer through combined convection-radiation in a porous channel is investigated in Chapter 6. The non-uniform velocity field due to boundary and inertia effects is considered and effect of the same is discussed. The analysis is done for a wide range of the porous medium shape parameter (which is a function of the porosity and the permeability) including the two limits of the Poiseuille flow and the slug flow. The problem is solved considering solid and the fluid phases in the

TH-1868_004301

local thermal equilibrium. The radiative information is found using the DTM.

There are many situations in which sharp temperature gradient is found in the medium. The assumption of constant thermal conductivity is not appropriate in those cases. The effect of temperature dependent thermal conductivity on transient conduction and radiation heat transfer in a planar medium is investigated in Chapter 7. The DTM is used for evaluating the radiative calculations in an absorbing, emitting and scattering medium.

The computational efficiency of the CDM and the DTM are compared in Chapter 8. Three different benchmark problems are considered. The performances of the two methods are analyzed over the different ranges of the radiative parameters. The CDM is found to be computationally efficient and thus a preferred method for 2-D problems.

In Chapter 9, effects of the variable thermal conductivity are analyzed for combined conduction and radiation heat transfer in a 2-D rectangular enclosure. The CDM is used for the calculation of radiative information.

The heat transfer analysis of 2-D rectangular porous burners is carried out in Chapter 10. The gas and the solid phase are considered to be in non-local thermal equilibrium, and separate energy equations are used for the two phases. The solid phase consisting of the porous matrix is assumed to be participating, while the gas is assumed to be transparent to radiation. Radiative part of the energy equation is solved using the CDM. Effects of various parameters such as the aspect ratio, the extinction coefficient, the scattering albedo, the boundary emissivity and interface heat transfer coupling are studied on the performance of the burner. These parameters are found to have significant bearings on the temperature and heat flux distributions.

Chapter 11 gives a summary of this research work. The future prospect of this research are highlighted there.

TH-1868_004301

Indian Institute of Technology Guwahati

Chapter 2

Formulation

2.1 Introduction

Continuity, momentum, species conservation and energy equations are the governing equations required to solve any fluid flow and heat transfer problems. These equations are coupled and have to be solved simultaneously. If the temperature is high and the enclosed medium is radiatively participating, the energy equation contains an additional term because of radiation. Radiation from the medium is a volumetric phenomenon and it is characterized by absorption, emission and scattering. In the presence of radiation, therefore, the solution of the energy equation becomes complicated.

The equation governing radiative transfer is an integro-differential one and except for very idealized conditions, its analytic solutions are very difficult. To solve the practical problems, therefore, approximate methods are used. Over the years, owing to limitations of the existing methods, various new methods have been developed.

TH-1868_004301

In the combined radiation, conduction and/or convection mode problems considered in the present work, radiation from the participating medium is very significant. In this chapter, a general procedure to solve a heat transfer problem involving thermal radiation has been described. The basic equations for radiative heat transfer are discussed. The discrete transfer and the collapsed dimension methods are described briefly. The solution procedures for both the methods are also explained.

2.2 Energy Equation

In heat transfer problems involving thermal radiation, apart from the thermo physical and optical properties of the medium, the radiation intensity depends on the temperature field, and is thus coupled with the overall energy equation that incorporates all three modes of heat transfer. The general form of the overall energy equation for a single component radiatively participating compressible fluid may be written as [1, 35]

$$\rho c_v \left(\frac{\partial T}{\partial t} + \mathbf{v} \cdot \nabla T \right) = \nabla \cdot (k \nabla T) - p \nabla \cdot \mathbf{v} + \Phi_d + Q''' - \nabla \cdot q_R \qquad (2.1)$$

where ρ is the density, c_v is the specific heat, k is the thermal conductivity, p is the pressure term, $\mathbf{v}$ is the velocity vector, Φ_d is the energy production by viscous dissipation, Q''' is the local energy source (electrical, chemical, nuclear) per unit volume and time and q_R is the radiative heat flux.

In a general problem which involves all three modes of heat transfer, the energy equation (Eq. (2.1)) is simultaneously solved with the continuity and the momentum equations. At any solution steps, with the velocity field $\mathbf{v}$, the pressure field p, and the terms Φ_d and Q''' known, the solution of Eq. (2.1) requires information about the divergence of radiative heat flux $\nabla \cdot q_R$. This can be calculated by many methods found in the literatures as mentioned in the 1st chapter. In the subsequent sections, the phenomena of radiative heat transfer in participating media are discussed and the governing equations are explained with the collapsed dimension and the discrete transfer method leading to the evaluation of $\nabla \cdot q_R$

TH-1868_004301

2.3 Discrete Transfer Method

2.3.1 Introduction

The discrete transfer method (DTM) was proposed by Shah [24] and Lockwood and Shah [25]. It is a ray-tracing method and exhibits the feature of the zone method [1,35], flux method [1,35] and the Monte Carlo method [1,10]. This method is also similar to the discrete ordinate method [15–18] as far as the discrete directions are chosen. In the following sections, the definition of an intensity/ray in case of the DTM is described. The energy balance of an infinitesimal pencil of ray is discussed leading to the derivation of the radiative transfer equation (RTE) and the divergence of radiative heat flux.

2.3.1.1 Intensity

In this section, we will discuss how intensity is described in case of the DTM.

Consider an area element dA in the $X-Y$ plane, as shown in Fig. 2.1. The point P of this element will be receiving the radiation rays/intensities from all the directions constituting the hemisphere shown in the figure. Base of the hemisphere is also in the $X-Y$ plane. One such ray QP is shown with a thick arrow in the figure. Let an elemental solid angle $d\Omega$ be constructed around the ray QP.

If Θ and Φ are polar and azimuthal angles, respectively, of the ray QP, then the solid angle, $d\Omega$, is equal to $\sin\Theta\, d\Theta\, d\Phi$. The intensity, $i(\Theta,\Phi)$, is defined as the radiative energy flow rate per unit area normal to the ray direction per unit differential solid angle or, [35]

$$i(\Theta,\Phi) = \frac{\delta Q}{dA_p\, d\Omega} = \frac{\delta Q}{(dA\cos\Theta)\sin\Theta\, d\Theta\, d\Phi} \tag{2.2}$$

where δQ is the differential energy flow through the elemental area dA and dA_p is the projection of this area on a plane normal to the ray direction (Θ,Φ).

TH-1868_004301

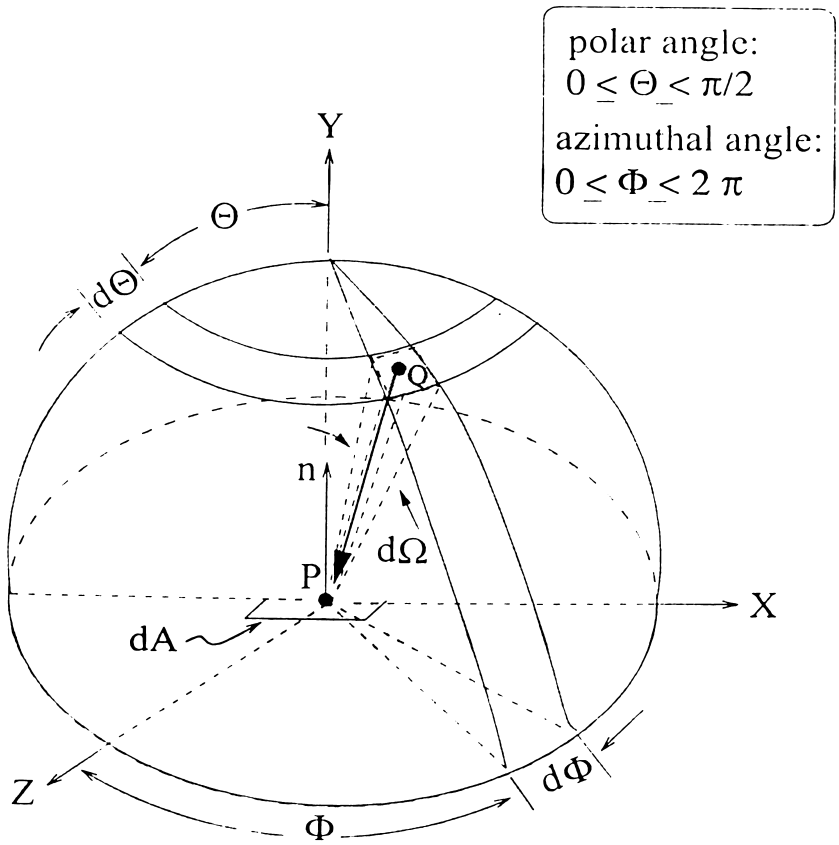


Figure 2.1: A hemisphere of south bound rays with intensities $i(\Theta, \Phi)$ focused at the center P of the infinitesimal area element dA.

In the present discussion, for the sake of convenience, we will associate terms like south bound, north bound, east bound, and west bound with the radiation rays, hemisphere, heat flux, etc. If an elemental surface is facing north direction (as depicted in the Fig. 2.1) and is receiving radiation from the entire hemisphere above it, then all the rays in the hemisphere converging at a point on the elemental surface will be identified as south bound rays. Such a hemisphere will be referred to as the south bound hemisphere and the heat flux due to all such south bound rays will be known as south bound heat flux. Likewise, depending upon the orientation of the surface receiving the radiation, the rays can be east bound, west bound or north bound.

In the DTM, if we need to find, say the south bound radiative heat flux, $q_{s,p}$, at

TH-1868_004301

the center, P, of the area element dA of Fig. 2.1, we have to integrate a hemisphere of south bound rays with intensity, $i(\Theta, \Phi)$, over the solid angle, $\Omega = 2\pi$, as per the following equation

$$q_{S,P} = \int_{\Phi=0}^{2\pi} \int_{\Theta=0}^{\frac{\pi}{2}} i(\Theta, \Phi) \cos\Theta \sin\Theta \, d\Theta \, d\Phi \tag{2.3}$$

Here, the subscript S in $q_{S,P}$ denotes the south bound nature of the heat flux and P denotes the point at which the heat flux is being computed.

2.3.2 Radiative Transfer Equation

As discussed earlier, for determination of radiative quantities, viz., heat flux, emissive power, etc., at a point in a participating media, the values of all the radiation intensities focused at that point are required. To know the magnitude of radiation intensity at a point in the participating media, solution of radiative transfer equation (RTE) is required. For real 3-D intensities, the RTE and its solution methodology are well established. Before, we proceed with the above, we list the important assumptions made in the present study. These assumptions are equally valid for both the methods CDM and the DTM. It should be noted that the assumptions presented herein are the general assumptions on which most practical thermal radiation methods are evolved.

2.3.2.1 Important Assumptions

Participating medium has been assumed to be in local thermodynamic equilibrium (LTE). Physically, LTE implies that the emission of radiant energy is independent of the characteristics of the incident radiation. This is true in many engineering applications where incident radiation is rapidly redirected into internal energy states in an equilibrium distribution at the local temperature of the medium [1]. But, if LTE cannot be assumed, the emission term in the RTE will become much more complex. Cases in which LTE does not prevail (for example, rarefied gases), are rarely encountered in thermal radiation, and hence these cases will not be considered

TH-1868_004301

in the present work. Radiative heat transfer has been assumed a steady state process, which is generally the case, since radiation travels at the speed of light [35].

Another major assumption, in this study, is the diffuse-gray assumption which eliminates all spectral effects and directional characteristics of emission, absorption, and reflection of radiation. The state of polarisation has been neglected and participating medium has been assumed to have constant refractive index, i.e., medium through which electromagnetic waves travel along straight lines.

2.3.2.2 Derivation of RTE Based on the DTM

In the radiative transfer equation, intensity of radiation is the primary variable. It is a function of space and direction. Note that direction Ω is designated by the polar angle, Θ, and the azimuthal angle, Φ. Consider the radiative energy with real intensity $i(s_w, \Omega)$ travelling along a line of sight from s to $s + ds$ at an angle Ω through an absorbing, emitting, and anisotropically scattering medium bounded by an arbitrary enclosure, as shown in Fig. 2.2.

In this figure, energy balance over a small control volume has been shown. Derivation of the radiative transfer equation can easily be done by identifying each of the terms contributing to the radiation, as it travels from s to $s + ds$. By referring to Fig. 2.2, a list of the intensity components encountered during this transfer process can be summarized as [1]

(i) Differential change in radiation intensity through ds:

$$\frac{\partial i(s, \Omega)}{\partial s}\, ds\, dA$$

(ii) Loss by absorption:

$$-\kappa\, i(s, \Omega)\, ds\, dA$$

(iii) Loss by out-scattering of the radiative intensity through the control volume:

$$-\sigma_s\, i(s, \Omega)\, ds\, dA$$

TH-1868_004301

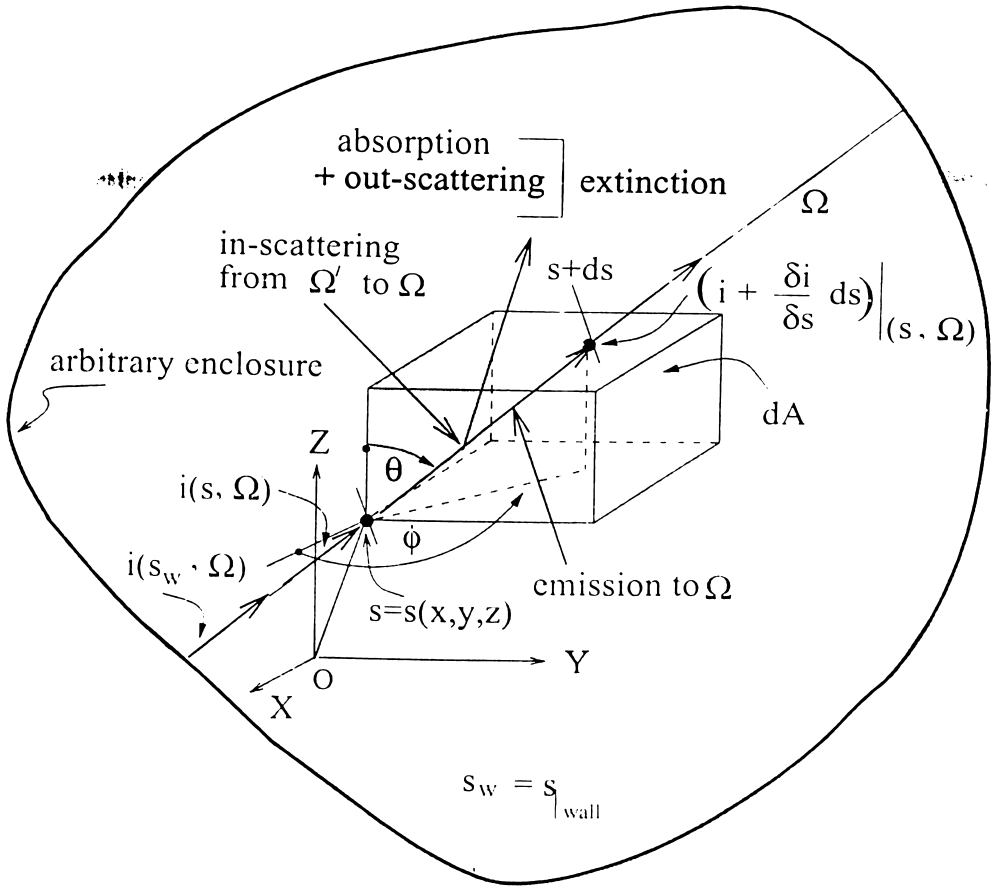


Figure 2.2: Radiative energy balance over a control volume based on the DTM.

(iv) Gain by emission from the medium in Ω direction :

$$\kappa\, i_b(s)\, ds\, dA$$

(v) Gain by in-scattering radiation - energy scattered into the direction Ω from rays traversing the elemental volume from all other directions Ω':

$$\left(\frac{1}{4\pi}\right) \int_{\Omega'} p(\Omega' \rightarrow \Omega)\, i(s, \Omega')\, d\Omega'\, ds\, dA$$

In the above expressions, κ and σ_s are absorption and scattering coefficients of the medium, respectively. The blackbody intensity, i_b, is the Planck's intensity function.

TH-1868_004301

and it depends explicitly upon the local temperature, T, of the medium. This Planck's blackbody intensity is related to blackbody emissive power as $E_b = \pi i_b$, where

$$i_b = \frac{\sigma T^4}{\pi} \tag{2.4}$$

The function $p(\Omega' \rightarrow \Omega)$ is called scattering phase function. This directional distribution function represents the probability distribution of the energy scattered into the direction Ω from the rays traversing the elemental volume from all other directions, Ω'. To be more explicit, $p(\Omega' \rightarrow \Omega)\, d\Omega/4\pi$ represents the probability that a ray propagating in the direction Ω' confined within the solid angle $d\Omega'$ will get scattered into the solid angle $d\Omega$ around by the direction Ω. Since the sum of the probability over all directions must be unity, we have

$$\frac{1}{4\pi} \int_{\Omega'=4\pi} p(\Omega' \rightarrow \Omega)\, d\Omega' = 1 \tag{2.5}$$

which implies that the phase function is normalized to unity.

The change in the magnitude of intensity from the location s to $s + ds$, in Fig. 2.2, is found by summing the contributions from emission, absorption, out-scattering, and in-scattering, along the path ds, as follows

$$i(s+ds,\Omega) - i(s,\Omega) \equiv \frac{\partial i}{\partial s} ds = \overbrace{\kappa\, i_b(s)\, ds}^{\text{emission}} - \overbrace{\overbrace{\kappa\, i(s,\Omega)\, ds}^{\text{absorption}} - \overbrace{\sigma_s\, i(s,\Omega)\, ds}^{\text{out-scattering}}}^{\text{extinction as per Bouger-Beer's law}} + \underbrace{\left(\frac{\sigma_s}{4\pi}\right) \int_{\Omega'=4\pi} i(s,\Omega')\, p(\Omega' \rightarrow \Omega)\, d\Omega'}_{\text{in-scattering}} \tag{2.6}$$

Equation (2.6) can be written in the form

$$\frac{di(s,\Omega)}{ds} = \kappa\, i_b(s) - \beta\, i(s,\Omega) + \left(\frac{\sigma_s}{4\pi}\right) \int_{\Omega'=4\pi} i(s,\Omega')\, p(\Omega' \rightarrow \Omega)\, d\Omega' \tag{2.7}$$

The coefficient β, in the above equation, represents the extinction coefficient of the medium, in accordance with Bouger-Beer relation, and is equal to $\kappa + \sigma_s$. In gas radiation, it is common to express intensity, heat flux, etc., as functions of a dimensionless parameter, called optical thickness which is defined as

$$\tau = \int_0^s (\kappa + \sigma_s)\, ds' = \int_0^s \beta\, ds' \tag{2.8}$$

TH-1868_004301

This parameter is a measure of the extent to which the medium participates in the radiative heat transfer process.

Equation (2.7) may be written in terms of optical thickness, τ, as

$$\frac{di(\tau,\Omega)}{d\tau} = -i(\tau,\Omega) + (1-\omega)\, i_b(\tau) + \left(\frac{\omega}{4\pi}\right) \int_{\Omega'=4\pi} i(\tau,\Omega')\, p(\Omega' \rightarrow \Omega)\, d\Omega' \qquad (2.9)$$

Here, in equation (2.9), ω is scattering albedo and is equal to $\frac{\sigma_s}{\kappa+\sigma_s}$. Value of $\omega = 0.0$ indicates no scattering by the medium, whereas its limiting value 1.0 implies only scattering and no absorption-emission by the medium.

Equation (2.9) can be written in a more compact and convenient form as

$$\frac{di(\tau,\Omega)}{d\tau} + i(\tau,\Omega) = S(\tau,\Omega) \qquad (2.10)$$

where the source function

$$S(\tau,\Omega) = (1-\omega)\, i_b(\tau) + \left(\frac{\omega}{4\pi}\right) \int_{\Omega'=4\pi} i(\tau,\Omega')\, p(\Omega' \rightarrow \Omega)\, d\Omega' \qquad (2.11)$$

Writing equation (2.11) in terms of Θ and Φ gives:

$$S(\tau,\Theta,\Phi) = (1-\omega)\, i_b(\tau) + \left(\frac{\omega}{4\pi}\right) \int_{\Phi'=0}^{2\pi} \int_{\Theta'=0}^{\pi} i(\tau,\Theta',\Phi')\, p\left((\Theta',\Phi') \rightarrow (\Theta,\Phi)\right) \sin\Theta'\, d\Theta'\, d\Phi' \qquad (2.12)$$

Equation (2.10) is the differential form of the RTE. It is an integro-partial differential equation, because the directional derivative $d/d\tau$ involves partial derivatives with respect to spatial variables when it is written explicitly for a specific coordinate system, and intensity appears under the integral sign of the source function (Eq. (2.12)). Therefore, the solution of equation (2.10) is very complex, even for 1-D case. If the source function is known or assumed to be known, then equation (2.10) can be integrated from the point of origin of the ray, $\tau' = 0$ at the wall, to a point $\tau' = \tau$ inside the enclosure to yield an integral form of the RTE given as

$$i(\tau,\Theta,\Phi) = i(0,\Theta,\Phi)\exp(-\tau) + \int_0^{\tau} S(\tau',\Theta',\Phi')\, \exp(-(\tau-\tau'))\, d\tau' \qquad (2.13)$$

TH-1868_004301

It should be noted that equation (2.13) is a third-order integral equation in intensity, $i(\tau, \Theta, \Phi)$. For its evaluation, the integral over the source function must be carried out over the optical thickness. But the source function itself is an unknown function of intensity (Eq. (2.12)) which has to be integrated over two directions, Θ and Φ. Furthermore, usually the temperature and, therefore, the blackbody intensity terms in the source function are not known, and these must be found in conjunction with the equation of the overall conservation of energy, Eq. (2.1), thus further **complicating the situation.**

In equation (2.13), $i(0, \Theta, \Phi) = i(0)$ (for diffuse boundary emission), is the intensity emanating from the boundary of the enclosure. If the enclosure wall is assumed diffuse-gray, then intensity, $i(0)$, emanating from the boundary wall having temperature T_w and emissivity ϵ_w is given by

$$i(0, \theta, \phi) = \underbrace{\epsilon_w \frac{\sigma T_w^4}{\pi}}_{\text{emitted}} + \underbrace{\frac{1 - \epsilon_w}{\pi} \int_{\Phi=0}^{2\pi} \int_{\Theta=0}^{\frac{\pi}{2}} i(\Theta, \Phi) \cos\Theta \sin\Theta \, d\Theta \, d\Phi}_{\text{diffusely reflected}} \tag{2.14}$$

2.3.3 Divergence of Radiative Heat Flux

In a given control volume, RTE gives the conservation of radiative energy along a given ray direction. However, the equation for conservation of total energy (Eq. 2.1) is based on net energy balance in a control volume. Radiation, being 3-D phenomena, RTE can not fully describe radiative component in energy equation. To accommodate conservation of radiative energy in a control volume, it is necessary to integrate RTE over the control volume. This results in divergence of radiative heat flux. How the divergence of radiative heat flux enters in calculation in overall energy equation is already mentioned section 2.2. Divergence of radiative flux gives a measure of net radiative energy absorbed or emitted in a control volume. Important phenomena such as radiative and non-radiative equilibrium situations are perfectly described by divergence of radiative heat flux.

In the DTM as well as for other methods also, divergence of radiative heat flux can be

TH-1868_004301

found from the RTE. The RTE is a energy balance for radiation for an infinitesimal pencil of rays. Thus, in order to get a volume balance which is the divergence of radiative heat flux, we have to integrate this equation over all solid angles. This derivation of divergence of radiative heat flux $\nabla \cdot q_R$ for the DTM is same as for the most of the methods and is available in many of the text books [1, 35] and hence is not derived here. The expression for $\nabla \cdot q_R$ for the DTM is given by,

$$\nabla \cdot q_R = \kappa \left[4\pi\, i_b - G\right] \tag{2.15}$$

or,

$$\nabla \cdot q_R = \kappa \left[4\sigma\, T^4 - G\right] \tag{2.16}$$

where G is the incident radiation given by

$$G = \int_{\phi=0}^{2\pi} \int_{\Theta=0}^{\pi} i(\Theta, \Phi)\, d\Theta\, d\Phi \tag{2.17}$$

The divergence of radiative heat flux can also be expressed in terms of optical coordinate by dividing Eq. (2.16) with extinction coefficient β as

$$\nabla \cdot q_R = \frac{\kappa}{\beta} \left[4\sigma\, T^4 - G\right] = (1 - \omega) \left[4\sigma\, T^4 - G\right] \tag{2.18}$$

It is to be noted that in Eq. (2.16), $\nabla = \frac{\partial}{\partial s}$ and in Eq. (2.18), $\nabla = \frac{\partial}{\partial \tau}$

2.3.4 Solution Methodology for the DTM

Numerical integration of Eqs. (2.17) require that a finite number of directions (Θ, Φ) be considered and the intensity at the point of interest be known in all these finite directions. Since intensity depends on the source function which itself is a function of the intensity (Eq. (2.12)) and also the unknown temperature, an intensity at the point of interest can not be calculated in one step. The DTM considers a finite number of discrete directions and in each direction it finds intensity in a number of discrete steps. In the following paragraphs, the methodology of the DTM is described for a 2-D rectangular enclosure. Details about the DTM can be found in [18, 24, 29, 114–116].

TH-1868_004301

Shown in Fig. 2.3 is a 2-D rectangular enclosure with dimensions L_x and L_y in the x and y directions, respectively. The temperatures T and emissivities ϵ of the four boundaries are shown in the figure. Temperature and/or emissivity may vary along the boundaries. However, within a control surface, at a given time level, they are constant.

Since radiative heat transfer is coupled with conduction and/or convection, the computational grids used in the radiative transfer module are the same as those for the conduction and/or convection modes of heat transfer. In Fig. 2.3, for the sake of explanation, uniform rectangular grids have been shown.

To find out the radiative information $\nabla \cdot q_R$ required for the energy equation (Eq. (2.1)), intensity distributions are to be found at all the grid points including those at the boundaries. For this, at every grid point, over the spherical space ($0 \leq \Theta \leq \pi, 0 \leq \Phi \leq 2\pi$), intensities are considered in some finite number of discrete (Θ, Φ) directions. In Fig. 2.3, five token intensities are shown. Over a hemispherical space

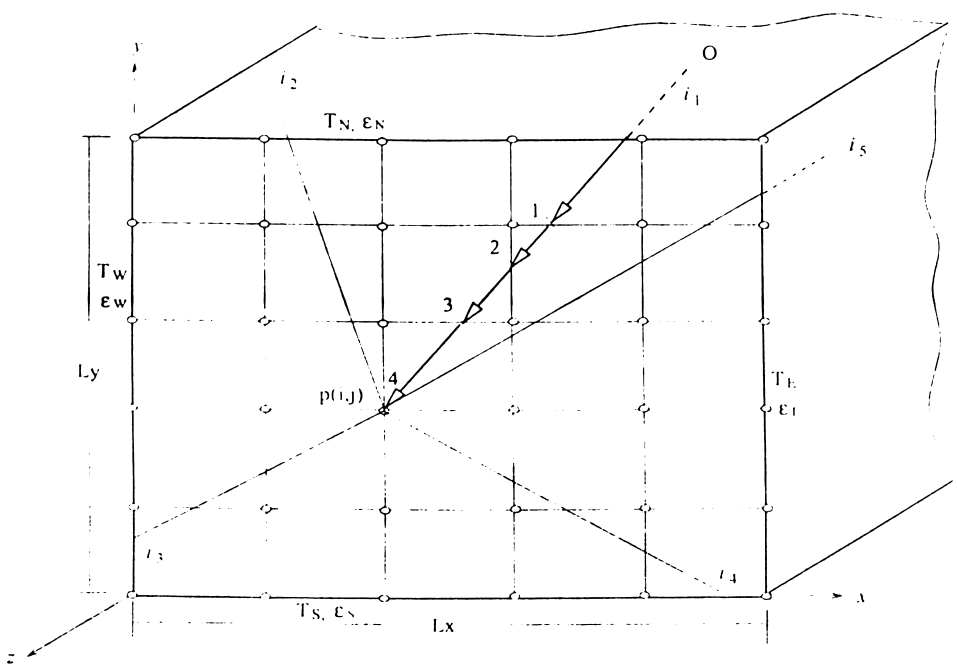


Figure 2.3: 2-D rectangular enclosure showing uniform grids and five sample intensities $i(\Theta, \Phi)$ focused at point $p(i, j)$.

TH-1868_004301

$(0 \leq \Theta \leq \pi/2, 0 \leq \Phi \leq 2\pi)$, for grid point $p(i,j)$, a typical intensity in the direction (Θ, Φ) can be seen from Fig. 2.3. Every intensity is considered centered in the sub-solid angle $\Delta\Omega$. Intensities are assumed uniformly distributed over the spherical space.

At any grid point $p(i,j)$ in the direction (Θ, Φ), an intensity is assumed to originate from the boundary. Since from the point of origin to the grid-point $p(i,j)$ of interest, the distribution of the source function over the length is unknown (Eq. (2.12)), intensity can not be calculated in one step. Intensity at point $p(i,j)$ is found in the finite number of steps by dividing the entire geometric length. For a typical intensity i_1, how this is done has been shown in Fig. 2.3.

To arrive at the destination grid-point $p(i,j)$ from its origin 0 at the north boundary, intensity is crossing many control volumes. In one step, the intensity is assumed to travel length equal to the distance between the two faces of a control volume. The number of control volumes are chosen in such a way that the distance between the control volume faces are small enough and the source function over this length can be assumed to be constant. With this assumption, for a given direction (Θ, Φ), Eq. (2.13) can be written as

$$i_{n+1}(\tau) = i_n \exp(-\tau) + S[1 - \exp(-\tau)] \tag{2.19}$$

where in the direction of travel, $(n+1)$ is the downstream point and n is the upstream point. Both these points always lie on the faces of same control volume. In a control volume, for a particular intensity, the source function S given by Eq. (2.12) is constant over the path-leg between the points $(n+1)$ and n. It should be noted that within a control volume, the source function S is different for different rays.

As shown in Fig. 2.3, intensity i_1 crosses four control volumes to reach the destination point $p(i,j)$. The locations at which it crosses the control volume faces are shown in the figure. Therefore, to get the intensity value i_i at $p(i,j)$, Eq. (2.19) has to be recursively used four times. The optical path-leg τ between any two points $(0,1)$, $(1,2)$, $(2,3)$ and $(3,4)$ are assumed small enough so that the source function

TH-1868_004301

given by Eq. (2.12) is constant over the path. For a particular ray, over the length

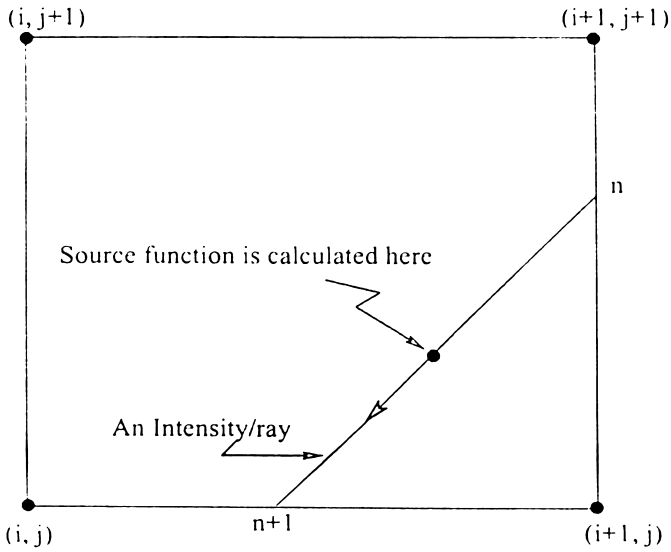


Figure 2.4: A typical control volume for evaluation of source function

τ between the points $(n+1)$ and n, the constant value of the S is assumed to be its value at the middle of the path-length τ. Angular distributions of intensities are known at the grid points only. Thus with known angular distributions of the intensities, the source functions S are computed at the four corners of the control volume of interest. With S values known at the corner points, its value at the middle point is found using the bilinear interpolation as shown in Fig. 2.4. The first iteration starts with the guess value of the S.

With S known at all the grid points from the previous iteration, Eq. (2.19) is recursively used to compute the intensity at $p(i,j)$. Equation (2.19) is used for all the selected directions.

For a particular intensity, when Eq. (2.19) is used for the first time, the upstream point n lies on the boundary. This requires information about the intensity i_0 in Eq. (2.19). For a diffuse-gray boundary with temperature T_w and emissivity ϵ_w, this is computed from Eq. (2.14).

Once the intensity distributions are known at all the grid-points, incident radiation

TH-1868_004301

G (Eq. (2.17)) and the net heat flux q_R are numerically computed from the following:

$$\begin{aligned} G &= \int_{\Phi=0}^{2\pi}\int_{\Theta=0}^{\pi} i(\Theta,\Phi)\sin\Theta\, d\Theta\, d\Phi \\ &\approx \sum_{k=1}^{M_\Phi}\sum_{l=1}^{M_\Theta} i(\Theta_k,\Phi_l)\sin\Theta_k\ \sin(\Delta\Theta)\ \Delta\Phi \end{aligned} \tag{2.20}$$

$$\begin{aligned} q_R &= \int_{\Phi=0}^{2\pi}\int_{\Theta=0}^{\pi} i(\Phi,\Theta)\sin\Theta\ \cos\Theta\, d\Theta\, d\Phi \\ &\approx \sum_{k=1}^{M_\Phi}\sum_{l=1}^{M_\Theta} i(\Theta_k,\Phi_l)\cos\Theta_k\sin\Theta_k\sin(\Delta\Theta)\Delta\Phi \end{aligned} \tag{2.21}$$

where M_Θ and M_Φ are the number of Θ and Φ directions considered over the complete span of Θ $(0 \le \Theta \le \pi)$ and Φ $(0 \le \phi \le 2\pi)$, respectively. In Eq. (2.14) for the boundary intensity, integration over the polar angle Θ is performed over $(0 \le \Theta \le \pi/2)$, therefore, in this case, the number of direction considered over Θ direction is $M_\Theta/2$. In the case of problems dealing with 1-D planar medium, radiation is azimuthally symmetric, i.e., $i(\Theta,\Phi) = i(\Theta)$. This azimuthally symmetric radiation brings lots of simplifications - intensities need to be traced only over the polar angle and hence integrations have to be performed over this angle only. Further, to calculate the source function at the middle of the path-leg, the bilinear interpolation is not required. The source function S in this case is just the average of its values at the upstream $(n+1)$ and the downstream n points.

With the divergence of radiative heat flux $\nabla \cdot q_R$ information known with the DTM, the energy equation (Eq. (2.1))is solved using any of the numerical solvers such as the finite difference method or the finite volume method.

In the first iteration, with the guess or the known values of boundary temperatures and with the guess value of the source function, $\nabla \cdot q_R$ is computed at all the internal grid-points. With the solution of the energy equation (along with continuity and momentum equations), a new temperature field is obtained with which again $\nabla \cdot q_R$ is computed. This procedure is repeated till the temperature values at all points have reached the convergence. These steps are explained with the flow chart shown in Fig. 2.5.

TH-1868_004301

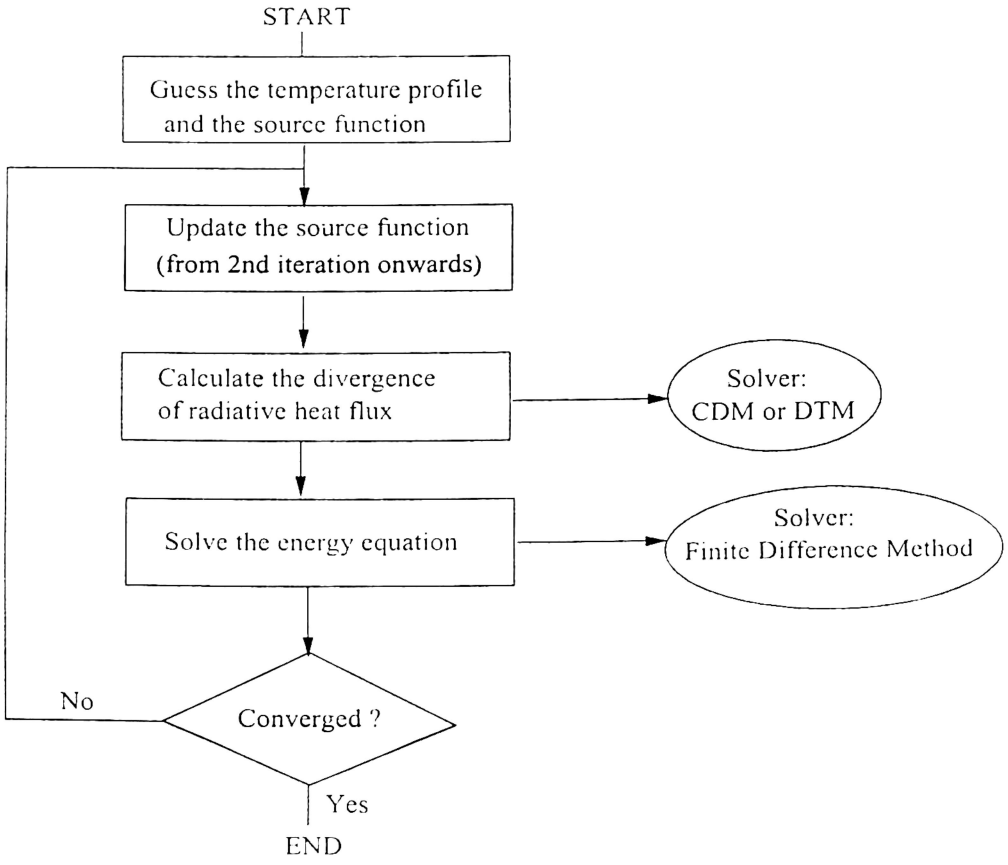


Figure 2.5: A flow chart showing the solution procedure

2.4 Collapsed Dimension Method

2.4.1 Introduction

The collapsed dimension method (CDM) is a relatively new method to compute radiative heat transfer in comparison to the other methods. Unlike other methods this method viewed radiation differently. This method transforms radiative information from a 3-D space to a 2-D plane. So, in case of a 2-D problem, radiative intensity has to be traced only in a 2-D plane unlike other ray tracing methods where the radiative intensity has to be traced in a 3-D plane. The formulation of this method is entirely different from rest of the methods.

TH-1868_004301

Effective intensity(EI) and the collapsing coefficient (CC) are two important parameters involved in the CDM. EI is defined in the 2-D plane and is a quantity analogous to the 3-D intensity for other methods like the DTM. CC is the parameter which enables translation of 3-D radiative quantities to a 2-D plane. In the subsequent sections, we will discuss the methodology involved in its formulations. The RTE and the divergence of radiative heat flux are also evaluated.

2.4.2 The Methodology

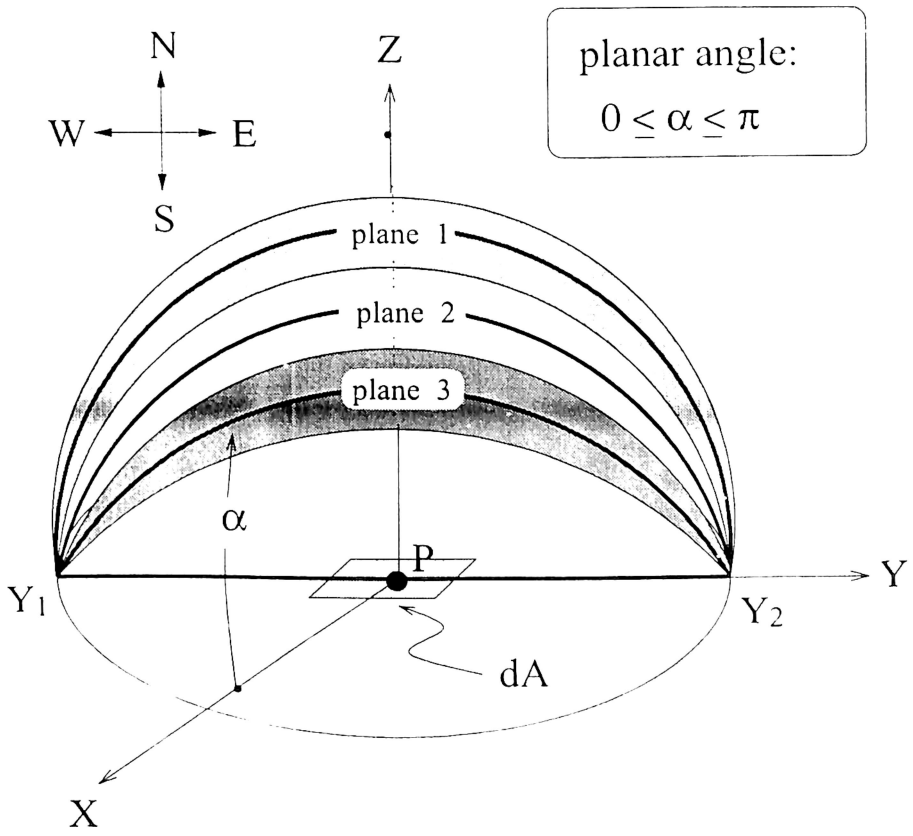


Figure 2.6: Discretization of hemisphere into longitudinal planes.

Consider Fig. 2.6 to define an EI in case of the CDM. As shown in this figure, south bound hemisphere is centered at point P of the elemental area dA. The base of the hemisphere coincide with the elemental area dA and lies on the $X-Y$ plane. The diameter Y_1 Y_2 of the hemisphere coincide with the Y axis. The Z axis is

TH-1868_004301

normal to the elemental area dA. The hemisphere is now divided into a number of longitudinal planes. Each plane has infinitesimal angular thickness depicted by the shaded regions around the plane and contains an infinite number of intensities $i(\Theta, \Phi)$. The bases of all such planes are coincident with Y_1 Y_2. These longitudinal planes are termed as discrete planes. In this figure, three such discrete planes are shown. Orientation of discrete plane is measured from the surface of the elemental area. The angle representing the position of the discrete plane from the elemental area is called the planar angle α.

In Fig. 2.6, south bound hemisphere has been discretized in such a way that the discrete planes are along Y_1 Y_2. The way in which the hemisphere has to be discretized is problem specific - it is mainly governed by the orientation of the solution plane. To make this point clear, let us consider a rectangular (2-D) control volume $ABCD$ in Fig. 2.7. This control volume is infinite in the Y-direction. Let us consider n, s, f and b as the central points on the north, south, front and the back faces of the control volume. These points are designated as control volume surface central points (CVSCPs). Radiative information are desired at these points. A plane which passes through these points is termed as the solution plane.

For determination of south bound heat flux through the north face of the control volume at the CVSCP n, we need to consider a hemisphere of south bound rays centered at CVSCP n (Fig. 2.6). In this figure, north face corresponds to elemental area dA and CVSCP n corresponds to point P. The hemisphere is discretized in such a way that the base of the discrete planes will coincide with the Y axis, in other words, will be normal to the solution plane.

A discrete plane with intensities and EI is shown in Fig. 2.8. The angular orientation of the EI is also shown in both the figures. In actual practice, a discrete plane contains infinite number of intensities $i(\Theta, \Phi)$, each focused at point n, as shown in Fig. 2.8(a). At this stage, in the CDM, it is assumed that in each discrete plane, it is possible to define an EI $I(\alpha)$ which stores the information of all the intensities $i(\Theta, \Phi)$, lying in the discrete plane and focused at the point of interest n and it produces the same effect as that by a conglomeration of intensities of that

TH-1868_004301

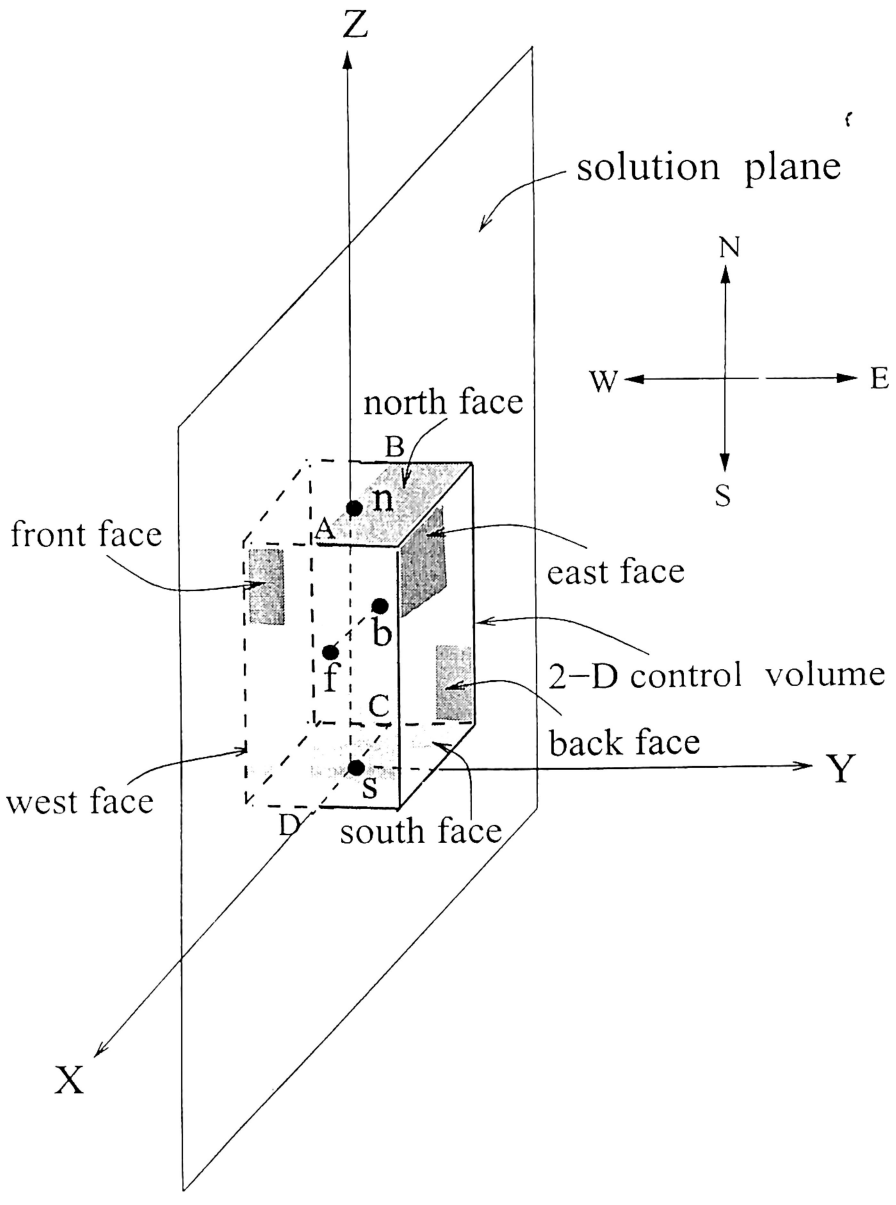


Figure 2.7: Solution plane and the 2-D control volume.

plane. The physical significance of this assumption is that it should be possible to translate the effect of a plane of intensities in terms of a single EI. Since we are finally interested in reducing the 3-D radiative problem to a 2-D solution plane, this kind of translation from a plane of intensities to a single EI will be useful only if this EI lies on the solution plane. This essentially means that EI must lie along the intersection of the discrete plane and solution plane. The angular location of EI

TH-1868_004301

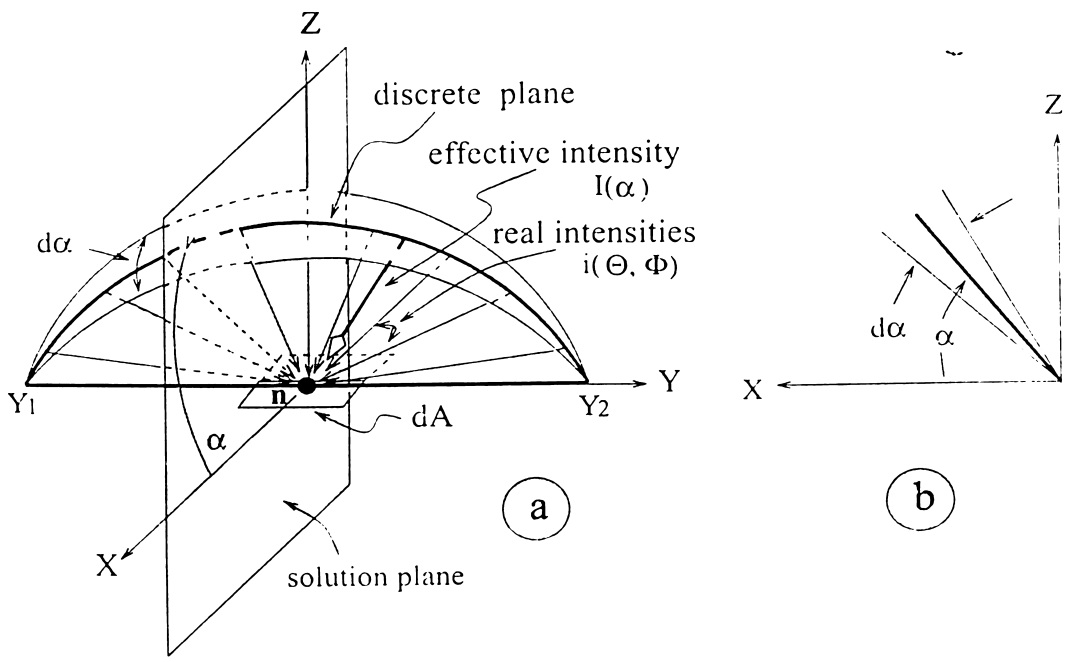


Figure 2.8: (a) Intensities $i(\Theta, \Phi)$ and EI $I(\alpha)$ in a representative discrete plane, (b) Discrete plane when viewed from Y axis towards $X - Z$ plane.

$I(\alpha)$ in a discrete plane is given by the angular orientation of line of intersection of the discrete plane and the solution plane.

The EIs can be defined only with a planar angle α in case of the CDM as the EIs lie only in a 2-D solution plane. Corresponding to a hemisphere of intensities $i(\Theta, \Phi)$ $(0 \leq \Theta \leq \pi/2)$ and $(0 \leq \Phi \leq 2\pi)$, in case of the DTM and other methods, in the CDM, there will be a semi circle of EIs with planar angle α in the range $0 \leq \alpha \leq \pi$.

In actuality, in a semi circle, there will be an infinite number of EIs corresponding to an infinite number of discrete planes of the hemisphere. But in actual analysis, we will be dealing with a finite number of EIs. Thus each EI is assumed to have its uniform influence over some angular span corresponding to the angular thickness of the discrete plane. For example, in Fig. 2.9, over a semi circle, seven representative EIs have been shown, and each intensity is shown acting over some angular span. Here, each EI corresponds to a discrete plane and the shaded angular sections represents the thickness of the respective discrete plane.

TH-1868_004301

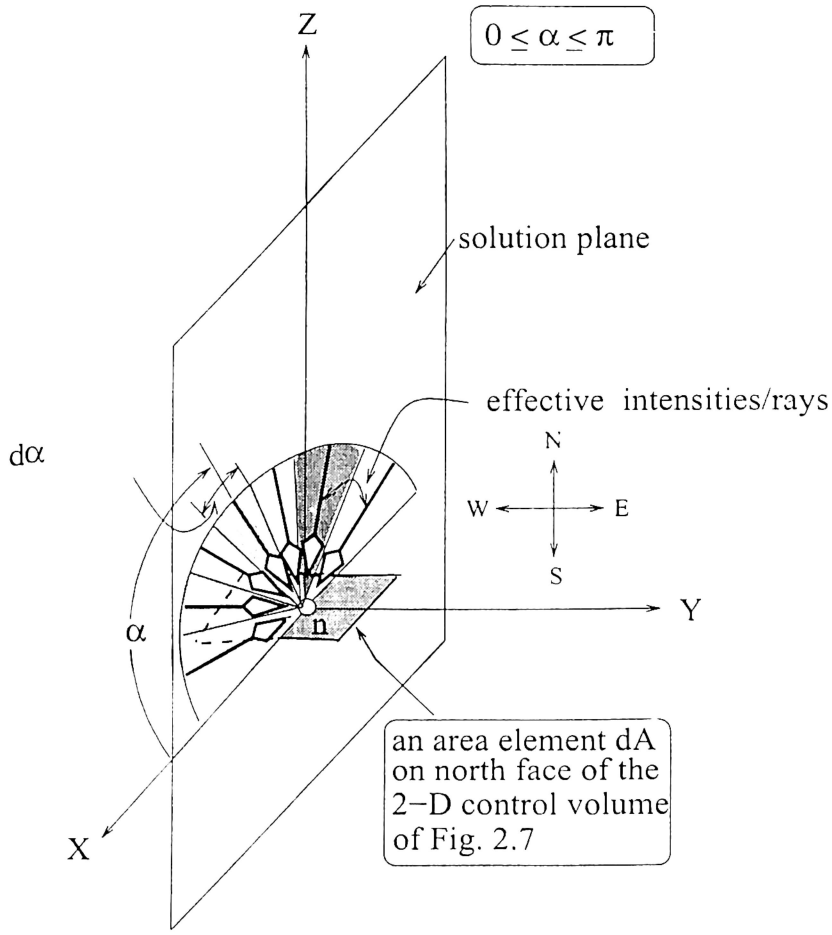


Figure 2.9: Some representative south bound EIs spanned over $0 \leq \alpha \leq \pi$

Hence, with this understanding, EI can be defined as the energy flow rate per unit area normal to the ray direction α per unit differential planar angle. Mathematically,

$$I(\alpha) = \frac{\delta Q}{dA_p \, d\alpha} = \frac{\delta Q}{dA \sin\alpha \, d\alpha} \tag{2.22}$$

Where δQ is the differential energy flow rate and dA_P is the projected area on a plane normal to the EI. Following above definition of the EI, the expression for south bound heat flux, in the CDM is given by

$$q_{S,P} = \int_{\alpha=0}^{\pi} I(\alpha) \sin\alpha \, d\alpha \tag{2.23}$$

and the effective incident radiation G' is given by,

$$G' = \int_{\alpha=0}^{2\pi} I(\alpha) \, d\alpha \tag{2.24}$$

TH-1868_004301

2.4.3 Collapsing Coefficient

In the CDM, apart from the effective intensity (EI), the other most important parameter controlling the method is the collapsing coefficient (CC). In fact, CC scales the radiative properties from a 3-D domain into a 2-D solution plane. In this section a brief description of CC is presented.

Determination of heat flux and temperature at any location strongly depends on the optical depth τ that the intensities encounter. These quantities are the integrated effects of intensities. To arrive at a specific location, intensities travel different geometric lengths. As a result, optical depth encountered by each intensity will be different. In the CDM, all the intensities $i(\Theta, \Phi)$ in a discrete plane are replaced by an equivalent EI $I(\alpha)$ which is contained in the discrete plane as well as in the solution plane. Hence, information about the optical depths of all the intensities are to be taken care by an equivalent optical depth to be encountered by the EI. This is achieved by CC.

The CCs for a given set of radiative parameters is found by comparing heat flux by the CDM with that of a reference method for 1-D planar medium. The reference method can be experimental or exact numerical method. Mishra [117] has taken exact method to be the reference method. Analytical expression of heat flux in the CDM contains CC (Γ) as an unknown variable (right hand side of Eq. (2.26)). Thus by equating the expressions of heat flux in the CDM and the reference method, for a given set of radiative parameters in a 1-D planar medium, CC is calculated as follows [117].

$$\Psi_{exact} = \Psi_{CDM} \tag{2.25}$$

or,

$$1 - 2\int_0^{\tau_l} \Phi(\tau')E_2(\tau')d\tau' + \left(\frac{a_1\omega}{2}\right)\Psi\int_0^{\tau_L} E_3(\tau')d\tau' = 1 - \sum_{m=1}^{N} b_m \int_0^{\frac{\tau_L\Gamma}{\sin\alpha}} \left(\Phi(\tau') - \left(\frac{a_1\omega}{\pi}\sin\alpha\right)\Psi\right)\exp\left(\frac{-\tau'\Gamma}{\sin\alpha}\right)d\left(\frac{\tau'\Gamma}{\sin\alpha}\right) \tag{2.26}$$

where Φ is the non-dimensional emissive power, Ψ is the non-dimensional heat flux and E_2 and E_3 are the exponential integrals of order 2 and 3 respectively. In Eq.

TH-1868_004301

(2.26), b_m is the integral angle factor, which is given by

$$\sum_{m=1}^{N} b_m = \int_{\alpha=0}^{\pi/2} \sin\alpha \, d\alpha \tag{2.27}$$

where

$$b_m = \left| \sin\left(\frac{(2m-1)\pi}{2(2N-1)}\right) - \sin\left(\frac{(2m-3)\pi}{2(2N-1)}\right) \right| \qquad m = 2, 3, \ldots\ldots N \tag{2.28}$$

In the above equations, N is the number of EIs over a quadrant of circle ($0 \leq \alpha \leq \pi/2$)

Since in Eq. (2.26), Φ and Ψ are known from the reference method, the only unknown is the CC (Γ). The Eq. (2.26) can be expressed as

$$f(\Gamma) = 0 \tag{2.29}$$

which can be solved by any root finding technique.

Following the above procedure, for both radiative equilibrium and non-radiative equilibrium, the CCs for 1-D planar absorbing, emitting and anisotropically medium can be found out [117]. The CCs found for 1-D planar geometry can equally be applied to any 2-D Cartesian Geometry. For other multidimensional geometries like cylindrical, L-shaped etc, the CCs found for the 1-D planar geometry can be applied by multiplying the CCs with a geometric factor [30].

In Appendix, CC expressions are presented for both radiative and non-radiative equilibrium situations. These expressions have been taken from [117].

2.4.4 Radiative Transfer Equation

The derivation of radiative transfer equation (RTE) for the CDM is similar to that of the DTM. Let us consider an effective intensity (EI) I (s_w, α) emitted from the enclosure boundary and travelling along a straight path from s to $s + ds$ at an angle

TH-1868_004301

α on a solution plane $X - Z$. Here s_w is the coordinate of the path at the wall. Different terms that contribute to the radiation as EI travels from s to $s + ds$ can be written in terms of EI as,

(i) Differential change in EI through ds:

$$\frac{\partial I(s,\alpha)}{\partial s}\, ds\, dA$$

(ii) Loss of radiant energy by absorption:

$$-(\kappa\, \eta)\, I(s,\alpha)\, ds\, dA$$

(iii) Loss of radiant energy by out-scattering:

$$-(\sigma_s\, \eta)\, I(s,\alpha)\, ds\, dA$$

(iv) Emission from the medium in α direction:

$$(\kappa\, \eta)\, I_b(s)\, ds\, dA$$

(v) In-scattering from all directions $\alpha^{'}$ to α:

$$\left(\frac{1}{2\pi}\right) \int_{\alpha'=2\pi} p(\alpha^{'} \rightarrow \alpha)\, I(s,\alpha^{'})\, d\alpha^{'}\, ds\, dA$$

In the above, in emission term (item iv), I_b is the blackbody effective intensity function. it is related to temperature as

$$I_b = \frac{\sigma\, T^4}{2} \tag{2.30}$$

The explanation of the above expressions (item i-v) are same as we discussed already in conjunction with the RTE of the DTM and hence not repeated here. Likewise in Eq. (2.5), here also the phase function must satisfy the conservation of scattered energy leading to the following equation.

$$\frac{1}{2\pi} \int_{\alpha'=2\pi} p(\alpha^{'} \rightarrow \alpha)\, d\alpha^{'} = 1 \tag{2.31}$$

TH-1868_004301

Considering the energy balance (item i-v), the following relationship is obtained.

$$\frac{dI(s,\alpha)}{ds} = (\kappa\,\Gamma)\; I_b(s) - (\beta\,\Gamma)\; I(s,\alpha) + \frac{(\sigma_s\,\Gamma)}{2\pi}\int_{\alpha'=2\pi} I(s,\alpha')\; p(\alpha' \rightarrow \alpha)\; d\alpha' \qquad (2.32)$$

The Eq. (2.32) can be expressed in terms of scattering albedo ω and effective optical thickness $\tilde{\tau}$

$$\frac{dI(\tilde{\tau},\alpha)}{d\tilde{\tau}} = -I(\tilde{\tau},\alpha) + (1-\omega)I_b(\tau) + \frac{\omega}{2\pi}\int_{\alpha'=2\pi} I(\tilde{\tau},\alpha')\; p(\alpha' \rightarrow \alpha)\; d\alpha' \qquad (2.33)$$

where $\tilde{\tau} = \tau\Gamma$

It should be noted in eq. (2.33) that the argument for I_b has been taken to be τ rather than $\tilde{\tau}$. This is for the reason that this argument is essentially indicative of the point in the solution plane at which I_b has to be computed. This argument has no other implication here.

The Eq. (2.33) is written in compact form as

$$\frac{dI(\tilde{\tau},\alpha)}{d\tilde{\tau}} + I(\tilde{\tau},\alpha) = S'(\tilde{\tau},\alpha) \qquad (2.34)$$

where the source function

$$S'(\tilde{\tau},\alpha) = (1-\omega)I_b(\tau) + \frac{\omega}{2\pi}\int_{\alpha'=2\pi} I(\tilde{\tau},\alpha')\; p(\alpha' \rightarrow \alpha)\; d\alpha' \qquad (2.35)$$

Equation (2.34) is the differential form of the RTE for the CDM. In integral form it can be expressed as

$$I(\tilde{\tau},\alpha) = I(0,\alpha)\exp(-\tilde{\tau}) + \int_0^{\tilde{\tau}} S'(\tilde{\tau}',\alpha)\; \exp\left\{-(\tilde{\tau} - \tilde{\tau}')\right\}\; d(\tilde{\tau}') \qquad (2.36)$$

2.4.5 Divergence of Radiative Heat Flux

In case of the DTM, the meaning for the divergence of the radiative flux $\nabla \cdot q_R$ has already been explained. The $\nabla \cdot q_R$ for the CDM can also be found in the same way as for the DTM and is shown below.

TH-1868_004301

To derive the relation defining $\nabla \cdot q_R$ for the case of the CDM, we consider the RTE (Eq. (2.32)) in the following form [42]

$$\frac{dI(s,\alpha)}{ds} = \vec{\alpha} \cdot \nabla I = (\kappa\,\Gamma)\, I_b(s) - (\beta\,\Gamma)\, I(s,\alpha) + \frac{(\sigma_s\,\Gamma)}{2\pi} \int_{\alpha'=2\pi} I(s,\alpha')\, p(\alpha' \rightarrow \alpha)\, d\alpha' \tag{2.37}$$

or,

$$\frac{dI}{ds} = \vec{\alpha} \cdot \nabla I = (\kappa\,\Gamma)\, I_b - (\beta\,\Gamma)\, I + \frac{(\sigma_s\,\Gamma)}{2\pi} \int_{\alpha'=2\pi} I(\alpha')\, p(\alpha' \rightarrow \alpha)\, d\alpha' \tag{2.38}$$

Operating both sides of the equation (2.38) by the operator $\int_{\alpha=2\pi}$, we obtain

$$\int_{2\pi} \vec{\alpha} \cdot \nabla I\, d\alpha = \int_{2\pi} (\kappa\Gamma)\, I_b\, d\alpha - \int_{2\pi} (\beta\Gamma)\, I(\alpha)\, d\alpha + \frac{(\sigma_s\Gamma)}{2\pi} \int_{2\pi} \left(\int_{\alpha'=2\pi} I(\alpha')\, p(\alpha' \rightarrow \alpha)\, d\alpha' \right) d\alpha \tag{2.39}$$

Rewriting the above equation in the form

$$\nabla \cdot \int_{2\pi} I\, \vec{\alpha}\, d\alpha = 2\pi(\kappa\Gamma) I_b - (\beta\Gamma) \int_{2\pi} I(\alpha)\, d\alpha + (\sigma_s\Gamma) \int_{\alpha'=2\pi} I(\alpha') \left(\frac{1}{2\pi} \int_{\alpha=2\pi} p(\alpha' \rightarrow \alpha)\, d\alpha \right) d\alpha' \tag{2.40}$$

Also, from equation (2.31)

$$\frac{1}{2\pi} \int_{\alpha=2\pi} p(\alpha' \rightarrow \alpha)\, d\alpha = 1$$

Therefore, equation (2.40) becomes

$$\nabla \cdot q_R = 2\pi(\kappa\Gamma) I_b - (\kappa\Gamma + \sigma_s\Gamma) \int_{2\pi} I(\alpha)\, d\alpha + (\sigma_s\Gamma) \int_{2\pi} I(\alpha')\, d\alpha' \tag{2.41}$$

Defining G', the effective incident radiation as $\int_{2\pi} I(\alpha)\, d\alpha$, above equation (2.41) can be written as

$$\nabla \cdot q_R = (\kappa\Gamma) \left[2\pi I_b - G' \right] = (\kappa\Gamma) \left[\pi\sigma T^4 - G' \right] \tag{2.42}$$

or, in terms of optical coordinate (similar to Eq. (2.18) in case of the DTM)

$$\nabla \cdot q_R = (1-\omega)\Gamma \left[\pi\sigma T^4 - G' \right] \tag{2.43}$$

TH-1868_004301

Equation (2.42) is the desired equation for conservation of radiative energy in the CDM. In this equation, the term $2\pi I_b \kappa \Gamma$ represents the radiation emitted, while $G' \kappa \Gamma$ is the radiation absorbed by the matter per unit time per unit volume. At this stage, it is worth noting the final form of the equations (2.15) and (2.42) representing conservation of radiative energy in the DTM and CDM, respectively are very similar.

2.4.6 Solution Methodology for the CDM

In the previous sections, we have discussed about the RTE and the divergence of radiative heat flux for the CDM. The solution procedure for the CDM is same as for the DTM since in both the methods intensities/rays have to be traced from the boundaries. Only difference between the two is that in case of the DTM rays have to be traced in a 3-D space whereas in case of the CDM, ray tracing is done only in the 2-D solution plane.

For the evaluation of the $\nabla \cdot q_R$, effective incident radiation G' has to be calculated. This is given by

$$G' = \int_{2\pi} I(\alpha)\, d\alpha \tag{2.44}$$

With similar arguments to those given for the DTM, in the CDM the recursive relation for finding the effective intensity I^* at any downstream point $(n+1)$ in the direction α in the solution plane can be found from the Eq. (2.36). If the source function is assumed to be constant over a small optical path between the points n and $n+1$, Eq. (2.36) can be expressed as

$$I_{n+1} = I_n \exp(-\tau\Gamma) + S'[1 - \exp(-\tau\Gamma)] \tag{2.45}$$

where the source function S' is given by

$$S'(\tau, \alpha) = (1-\omega)\frac{\sigma T^4}{2} + \frac{\omega}{2\pi}\int_{\alpha'=0}^{2\pi} I(\kappa, \alpha')p(\alpha \rightarrow \alpha')d\alpha' \tag{2.46}$$

It is to be noted that the expressions for the source function in the CDM (Eq. (2.46)) is different from that of the DTM (Eq. (2.12)). Also, the EI I exists only in the 2-D plane and hence the planar angle α varies from $0 \leq \alpha \leq 2\pi$. In the DTM, intensity

TH-1868_004301

i lies in the 3-D space and is identified with two angle, viz. the polar angle Θ and the azimuthal angle Φ (Fig. 2.1).

If anisotropy of the medium is approximated by linear anisotropic phase function ($p(\alpha' \rightarrow \alpha) = 1 + a_1 \sin\alpha \sin\alpha'$), the source function S' in terms of the effective incident radiation G' and the net radiative heat flux q_R is given by

$$S' = (1-\omega)\frac{\sigma T^4}{2} + \frac{\omega}{2\pi}\left(G' + a_1 \sin\alpha\, q_R\right) \tag{2.47}$$

where a_1 is the anisotropy factor. It lies in the range $-1 \leq a_1 \leq +1$. For $a_1 < 0$, medium is backward scattering and for $a_1 > 0$, it is forward scattering. For $a_1 = 0.0$, medium is isotropically scattering.

In the CDM, the net radiative heat flux q_R is given by

$$q_R = \frac{1}{2}\left[\int_{\alpha=0}^{\pi} I(\alpha)\sin\alpha\, d\alpha - \int_{\alpha=\pi}^{2\pi} I(\alpha)\sin\alpha\, d\alpha\right] \tag{2.48}$$

Like the DTM, in the CDM too, the intensities are always traced from the boundaries. If in Eq. (2.45), for the given direction α, if the upstream point n lies on the boundary, then $I_n = I_0$, and its values have to be found using the radiative boundary condition. For a diffuse-gray boundary with temperature T_w and emissivity ϵ_w, the boundary effective intensity in the CDM is given by

$$I_0 = \frac{\epsilon_w \sigma T_w^4}{2} + \frac{1-\epsilon_w}{2}\int_{\alpha=0}^{\pi} I \sin\alpha\, d\alpha \tag{2.49}$$

where the first and the second terms on the right-hand side represent the emitted and reflected components of the boundary effective intensity, respectively.

For the evaluation of G' and q_R, Eqs. (2.44) and (2.48) are numerically integrated as

$$G' = \int_0^{2\pi} I(\alpha)\, d\alpha \approx \sum_{n=1}^{M} I(\alpha_n)\, \Delta\alpha_n \tag{2.50}$$

$$q_R = \left[\int_0^{\pi} I(\alpha)\sin\alpha\, d\alpha - \int_{\pi}^{2\pi} I(\alpha)\sin\alpha\, d\alpha\right] \approx \left[\sum_{n=1}^{M/2} c_n\, I(\alpha_n) - \sum_{n=M/2}^{M} c_n\, I(\alpha_n)\right] \tag{2.51}$$

TH-1868_004301

where the weight factor is

$$c_n = \left|\cos\left(\alpha_n + \frac{\Delta\alpha_n}{2}\right) - \cos\left(\alpha_n - \frac{\Delta\alpha_n}{2}\right)\right| \tag{2.52}$$

In Eqs. (2.50) and (2.51), M is the number of effective intensities spanned over $0 \leq \alpha \leq 2\pi$, and in Eq. (2.52), $\Delta\alpha_n$ is the discrete angle in the 2-D plane over which the nth effective intensity is assumed to be isotropic. In all problems where the CDM has been used to find the radiative information, $\Delta\alpha_n$ is the same for all the effective intensities.

2.5 Summary

A general procedure to solve heat transfer problems involving radiation, conduction and/or convection was discussed. The overall energy equation requires information about the divergence of radiative heat flux $\nabla \cdot q_R$. In the present work, the DTM and the CDM have been used to compute this information. Therefore, the methodologies of the DTM and the CDM to compute the radiative information $\nabla \cdot q_R$ required for the energy equation were described. In the subsequent chapters, either the CDM or the DTM is used to solve combined radiation, conduction and/or convection mode problems.

TH-1868_004301

Chapter 3

1-D Steady State Conduction-Radiation with Flux Boundary

3.1 Introduction

Combined conduction and radiation heat transfer for steady [29,51,54,118,119] and unsteady [46, 61, 63, 66, 120, 121] cases has been the subject of interest for many researchers. Although most of the steady and unsteady state studies were associated with temperature boundary conditions [29, 55, 61, 63]; some of the papers discussed the problems with flux boundary conditions [20, 51, 58, 118–120]. Barker and Sutton [120] studied unsteady combined conduction and radiation problem for an isotropically scattering medium with externally heated semi-transparent boundaries. Mathews et al. [51] discussed the same problem with quasi-isotropic scattering. They used a two-flux model to solve the radiative part of the problem. Lin and Tsai [119] discussed the steady conduction-radiation problem for an isotropically scattering

TH-1868_004301

medium with constant temperature at one end and a constant net heat flux at the other end. Ho and Ozisik [58] also discussed the combined conduction-radiation problem for a two-layer planar medium subjected to flux boundary condition. Fernandes and Francis [118] and Sokman and Razzaque [20] have analyzed the combined conduction-radiation problem using the finite element method. They considered the problem for an isotropically scattering medium with constant temperature at one end and a constant total heat flux at the other end of the boundary.

In the previous works, the CDM [29, 31, 40–42, 46, 117, 122] was applied to many problems. It was found to provide satisfactory results for both pure radiation [31, 42,122] and conduction-radiation problems [29,46]. In earlier works on the conjugate mode problems, the CDM was applied to the problems in which the boundaries were subjected to the specified temperatures. It is obvious from the literature review that there are many situations in which the system boundaries are subjected to the specified flux. Therefore, in the subsequent chapters where the CDM is applied to more complex situations, the need has been felt to see how this method works for a new class of problems.

In this chapter, the CDM is used for the analysis of steady-state radiation and conduction heat transfer in an absorbing, emitting and anisotropically scattering 1-D planar medium. One boundary of the medium is assumed at specified temperature while the other is maintained at specified heat flux. To validate the accuracy of the method, first an inverse problem is solved in which, with the predicted wall temperature from the direct method, the unknown boundary heat flux is determined and temperature profiles in the direct and inverse methods are compared. Next, temperature, radiative heat flux and conductive heat flux information are found over the range of values for the boundary temperature, imposed heat flux, enclosure optical depth, conduction-radiation parameter, boundary emissivity and scattering albedo. For some sample cases, results are compared with those available in the literature.

TH-1868_004301

3.2 Formulation

Shown in Fig. 3.1 is a 1-D gray planar medium. Medium is absorbing, emitting and anisotropically scattering. Its thermo-physical and optical properties are constant. South boundary is subjected to a constant total heat flux, while the north boundary is maintained at a constant temperature. The south and the north boundaries of the medium are diffuse-gray with emissivities ϵ_S and ϵ_N, respectively.

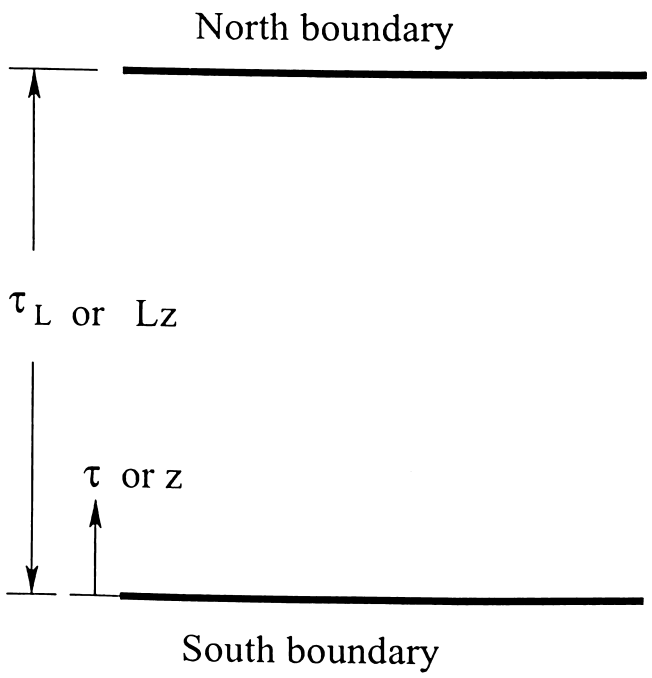


Figure 3.1: 1-D planar medium under consideration with physical/optical coordinates.

In the absence of convection and heat generation, 1-D steady state equation for conservation of total energy in z-direction is written as

$$k\frac{d^2T}{dz^2} = \frac{dq_R}{dz} \tag{3.1}$$

This equation is non-dimensionalized by the following parameters:

$$\theta = \frac{T}{T_{ref}}, \quad \tau = \beta z, \quad \Psi_R = \frac{q_R}{\sigma T_{ref}^4}$$

TH-1868_004301

where θ is the non-dimensional temperature, τ is the optical depth, Ψ_R is the non-dimensional radiative heat flux and T_{ref} is the reference temperature. The resulting non-dimensionalized equation is

$$\frac{d^2\theta}{d\tau^2} = \frac{1}{4N}\frac{d\Psi_R}{d\tau} \tag{3.2}$$

where N is the conduction-radiation parameter defined as

$$N = \frac{k\beta}{4\sigma T_{ref}^3}$$

It is to be noted here that the conduction-radiation parameter N describes the relative role of conduction and radiation heat transfer. If N is high, the heat transfer is mainly due to conduction and if lower, it signifies radiation dominated heat transfer. The limiting values $N = 0$ is the case with only radiation and $N = 10$ is the case with only conduction.

For the problem under consideration, boundary conditions in non-dimensional form are

$$\Psi_T = \Psi_R(0) - 4N\left(\frac{d\theta}{d\tau}\right)_{\tau=0} \quad \text{and} \quad \theta(\tau_L) = \theta_N \tag{3.3}$$

For the CDM, the divergence of radiative heat flux is given by Eq. (2.43) of chapter 2. The Eq. (2.43) for 1-D planar medium can be expressed as follows:

$$\frac{dq_R}{d\tau} = \Gamma(1-\omega)(\pi\sigma T^4 - G')$$

The above equation is non-dimensionalised to get the desired divergence of radiative heat flux in non-dimensional from as

$$\frac{d\left(\frac{q_R}{\sigma T_{ref}^4}\right)}{d\tau} = \Gamma(1-\omega)\left[\pi\frac{\sigma T^4}{\sigma T_{ref}^4} - \frac{\frac{G'}{\sigma T_{ref}^4/2}}{2}\right]$$

or,

$$\frac{d\Psi_R}{d\tau} = \Gamma(1-\omega)\left[\pi\theta^4 - \frac{G'^*}{2}\right] \tag{3.4}$$

where Γ is the collapsing coefficient, ω is the scattering albedo and G'^* is the non-dimensional effective incident radiant energy which in the CDM is given by

$$G'^* = \frac{G'}{\frac{\sigma T_{ref}^4}{2}} = \int_0^{2\pi} I^*(\alpha)\, d\alpha \tag{3.5}$$

TH-1868_004301

In the above equation, the effective intensity is non-dimensionalized as

$$I^* = \frac{I}{\frac{\sigma T_{ref}^4}{2}} \tag{3.6}$$

With justification given in Section 2.4.6, the recursive relation for calculating the non-dimensional effective intensity is given as

$$I^*_{n+1} = I^*_n \exp(-\tau\Gamma) + S'^* [1 - \exp(-\tau\Gamma)] \tag{3.7}$$

The non-dimensional form of source function at the middle of the point n and $n+1$ becomes

$$S'^* = (1-\omega)\theta^4 + \frac{\omega}{2\pi}\left(G'^* + 2a_1 \sin\alpha\ \Psi_R\right) \tag{3.8}$$

In the above equation, scattering is considered to be linearly anisotropic.

To solve energy Eq. (3.2), the $\nabla \cdot \Psi_R$ given by Eq. (3.4) is substituted in Eq. (3.2). This yields the desired governing integro-differential equation to be solved in the CDM.

$$\frac{d^2\theta}{d\tau^2} = \frac{1}{4N}\Gamma(1-\omega)\left[\pi\theta^4 - \frac{G'^*}{2}\right] \tag{3.9}$$

3.3 Calculations and Results

For getting distributions of temperature θ, radiative heat flux Ψ_R and conductive heat flux Ψ_C, the medium is divided into n control volumes constituting $(n+1)$ control surfaces including those at the boundaries. Since temperature is known only at one location (north boundary), for getting n unknown temperatures, n numbers of algebraic equations are required. Out of n equations, $(n-1)$ equations are found from the energy equation and the remaining one is developed from the flux boundary condition.

To solve Eq. (3.9), it is written in the finite difference form as

$$\frac{\theta_{n-1} - 2\theta_n + \theta_{n+1}}{\Delta\tau^2} = \frac{1}{4N}\Gamma(1-\omega)\left[\pi\theta_n^4 - \frac{G'^*_n}{2}\right] \tag{3.10}$$

TH-1868_004301

Initially, a linear temperature profile is guessed for the right hand side of Eq. (3.10). With this guess value of θ, incident radiation G'^* is calculated. For evaluation of G'^*, intensities are found from Eq. (3.7). The calculation of intensity starts from the boundary. The boundary intensity I_0^* for a diffuse-gray boundary having emissivity ϵ_w and temperature T_w is found from

$$I_0^* = \frac{\epsilon_w T_w^4}{T_{ref}^4} + \frac{1-\epsilon_w}{2} \int_{\alpha=0}^{\pi} I^{*-}(\alpha) \sin\alpha \, d\alpha \tag{3.11}$$

In Eq. (3.11), - suffix over I^* indicate that these are the effective intensities incident on the concerned boundary from where the bounding effective intensity $I^*(0)$ is being found. At any point on the concerned boundary, these effective intensities are spanned over a semi-circle, $0 \leq \alpha \leq \pi$.

With the right hand side of Eq. (3.10) known, left hand side is solved for θ_n using the Thomas algorithm. Under-relaxation is used in some of the cases. Depending upon the radiative parameters, for accuracy, control volumes considered have been in the range of 300-500. A maximum of 32 effective intensities have been found sufficient enough to predict correct temperature and heat flux distributions.

To establish the validity of the results generated in the present work, first the problem has been solved for temperature boundary conditions [29] which is referred here as an inverse method. In the inverse method, for given thermo-physical properties of the medium, with both the boundary temperatures (θ_S and θ_N) specified, total heat flux Ψ_T at one of the boundaries is predicted (for the chosen problem, $\Psi_T(\tau)$=constant at all τ, including the two boundaries). Then in the direct method (with flux boundary condition), keeping other conditions same, one of the boundaries is subjected to the predicted heat flux, and temperature at that boundary is calculated. Ultimately, temperature values in the two approaches have to be the same which is one validation of the present work. As a second validation, the results have been compared with those available in the literature. For example, for θ_N=0.5, ϵ (ϵ_N=ϵ_S)=1.0, N=0.1, τ_L=1.0 and ω=0.0, with θ_S=1.0, total heat flux Ψ_T is found to be 0.77785. Keeping other parameters unchanged, if the south boundary is subjected to Ψ_T = 0.77785, temperature at this boundary θ_S is found to be 1.0003. This thus establishes the validity of the results. In fact, in the two approaches,

TH-1868_004301

temperature should not only match at one boundary, rather it should match at all locations in the medium. This very fact has been proved through the results presented in Fig. 3.2. In this figure, lines represent temperature distributions found using the direct method and the markers represent the same obtained using the inverse method. These temperature results have been found to exactly match with the results presented in [29].

In Tables 3.1 and 3.2, the CDM results for θ and Ψ_R have been compared with the results reported by Fernandes and Francis [118] and Lin and Tsai [119]. In Table 3.1, with $\tau_L = 1$ and $\theta_N = 0.1$, for isotropic scattering with $\omega = 0.5$, θ values have been compared at locations $\tau/\tau_L = 0$ and 0.5. Enclosure boundaries have been assumed to be black. For three values of N, comparisons have been made for four different values of the imposed boundary flux Ψ_T. It is clear from this table that the CDM results for temperature compare very well with the results reported in the literature.

In Table 3.2, the CDM results for radiative heat flux $\Psi_R/4.0N$ are compared with that reported by Fernandes and Francis [118] and Lin and Tsai [119]. Here comparisons have been made at three locations, i.e, at the two boundaries and in the

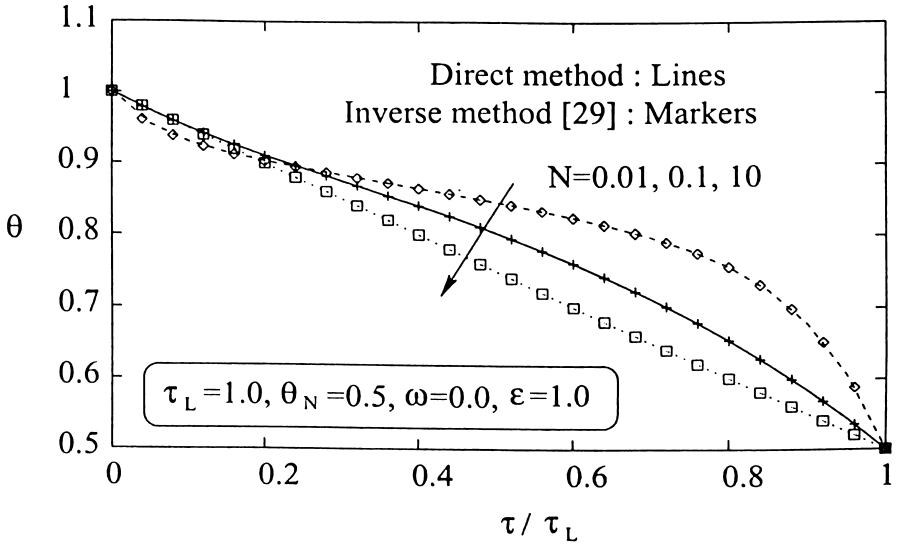


Figure 3.2: Variation of non-dimensional temperature θ with normalized optical depth τ/τ_L; comparison between the direct method and the inverse method.

TH-1868_004301

middle of the medium. For results presented in Table 3.2, values of ω, τ_L and θ_N are the same as that for the cases given in Table 3.1. However, in this case, both the boundaries are gray with $\epsilon_N = \epsilon_S = 0.5$. For all combinations of Ψ_T and N, the CDM results for $\Psi_R/4.0N$ are found to compare very well with the existing results.

Effects of various parameters like θ_N, Ψ_T, N, ϵ and ω on variations of temperature θ, conductive heat flux Ψ_C and radiative heat flux Ψ_R with normalized optical depth τ/τ_L are shown in Figs. 3.3 - 3.5. In all these figures, emissivity values of both the boundaries are taken same, i.e, $\epsilon_S = \epsilon_N = \epsilon$. Further, in all these figures, except the parameter whose effect is studied, the remaining five parameters remain unchanged. For example, in Fig. 3.3(a), effect of the north boundary temperature θ_N on variations of non-dimensional medium temperature θ has been studied, whereas in Fig. 3.3(b), effect of the imposed heat flux Ψ_T on θ has been studied. In both

Table 3.1: Comparison of temperature for isotropic scattering with $\omega = 0.5$ and $\tau_L = 1.0$, $\epsilon_N = \epsilon_S = 1.0$ and for $N = 0.5$, 0.1 and 0.05.

	Temperature θ at					
	$\tau/\tau_L = 0.0$			$\tau/\tau_L = 0.5$		
$N = 0.5$						
Ψ_T	Ref. [118]	Ref. [119]	Present	Ref. [118]	Ref. [119]	Present
2	0.961	0.961	0.961	0.546	0.546	0.546
4	1.425	1.425	1.426	0.835	0.835	0.835
6	1.706	1.707	1.708	1.043	1.044	1.044
8	1.909	1.910	1.911	1.211	1.212	1.213
$N = 0.1$						
0.4	0.786	0.786	0.786	0.475	0.475	0.475
0.8	1.059	1.060	1.060	0.677	0.677	0.677
1.2	1.226	1.227	1.228	0.821	0.822	0.822
1.6	1.350	1.351	1.351	0.936	0.937	0.937
$N = 0.05$						
0.2	0.701	0.701	0.701	0.439	0.439	0.439
0.4	0.919	0.919	0.920	0.610	0.611	0.611
0.6	1.054	1.055	1.055	0.732	0.733	0.733
0.8	1.155	1.157	1.156	0.828	0.830	0.829

TH-1868_004301

the figures, remaining parameters are the same.

It is seen from Figs. 3.3(a) and (b) that for the given values of radiative parameters, with decrease in the values of θ_N or Ψ_T, at any τ/τ_L, θ decreases. Fig. 3.3(a) shows the temperature distribution inside the medium for different θ_N. Since the flux is constant, a decrease in the value of θ_N decreases the temperature of the whole medium. A higher temperature of the north boundary ($\theta_N = 1.0$) produces higher radiative flux from that boundary which results in a flat temperature profile. On the other hand, a zero temperature of the north boundary, produces zero emission from that boundary which decreases the radiative flux of that boundary and results a relatively linear temperature profile .

Effects of optical thickness τ_L, conduction radiation-parameter N, boundary emissivity ϵ and scattering albedo ω on θ are shown in Figs. 3.3(c)-(f), respectively. It is seen from these figures that temperature at the north boundary is always the same. This is true, because the north boundary is at specified temperature and

Table 3.2: Comparison of radiative heat flux distribution for isotropic scattering with $\tau_L = 1.0$, $\theta_N = 0.1$, $\omega = 0.5$ and $\epsilon_N = \epsilon_S = 0.5$ for several values of N.

	Radiative heat flux $\Psi_R/4.0N$ at								
	$\tau/\tau_L = 0.0$			$\tau/\tau_L = 0.5$			$\tau/\tau_L = 1.0$		
$N = 0.5$									
Ψ_T	Ref [118]	Ref. [119]	Present	Ref. [118]	Ref. [119]	Present	Ref. [118]	Ref. [119]	Present
2	0.143	0.144	0.143	0.153	0.153	0.153	0.064	0.064	0.064
4	0.687	0.689	0.689	0.747	0.747	0.747	0.314	0.313	0.314
6	1.394	1.398	1.398	1.552	1.552	1.553	0.661	0.661	0.661
8	2.158	2.165	2.164	2.452	2.451	2.454	1.060	1.060	1.061
$N = 0.1$									
0.4	0.314	0.315	0.315	0.349	0.348	0.348	0.149	0.149	0.148
0.8	1.019	1.022	1.022	1.164	1.164	1.165	0.507	0.506	0.507
1.2	1.799	1.805	1.805	2.106	2.106	2.108	0.939	0.939	0.940
1.6	2.604	2.613	2.612	3.097	3.096	3.096	1.414	1.414	1.414
$N = 0.05$									
0.2	0.393	0.394	0.393	0.445	0.445	0.445	0.193	0.193	0.192
0.4	1.135	1.139	1.139	1.326	1.326	1.326	0.590	0.590	0.590
0.6	1.932	1.938	1.938	2.303	2.302	2.305	1.056	1.056	1.058
0.8	2.748	2.755	2.757	3.313	3.312	3.317	1.563	1.563	1.567

TH-1868_004301

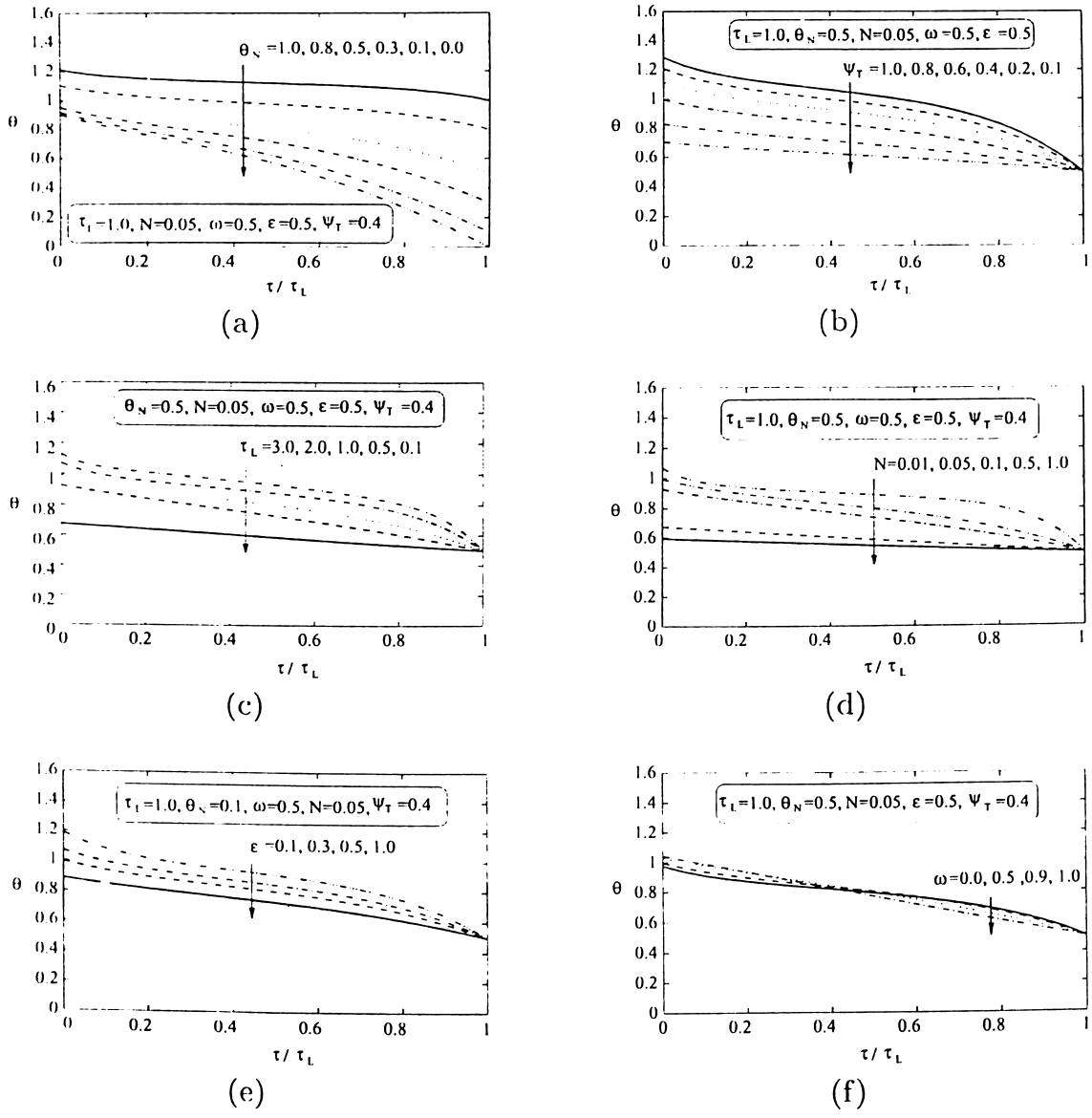


Figure 3.3: Variation of non-dimensional gas temperature θ with normalized optical depth τ/τ_L.

the boundary condition has to be satisfied. From Fig. 3.3(c), it is seen that with decrease in τ_L, θ decreases. It is important here to define the physical significance of the optical thickness τ. τ can be physically defined as the inverse of the mean free path of radiation. If the τ is high, then the mean free path of radiation decreases and the ra liative energy get absorbed or scattered in a very short distance. This decreases the radiative flux within the medium. On the other hand for a low optical

TH-1868_004301

thickness medium, more and more energy can be transported through the medium without getting absorbed or scattered by the medium. Hence for the same conditions, the heat flux in an optically thin medium is higher than a thick medium. In the present case, since the total heat flux is constant, the decrease in the optical thickness reduces the conductive heat flux (since radiative heat flux increases) which in tern gives a flat temperature profile in the medium. However, reverse trends are observed for the effects of N (Fig. 3.3(d)) and ϵ (Fig. 3.3(e)). In these figures, with increases in their values, θ values decrease. With increase in N values, medium becomes more conducting and temperature distribution becomes more linear. With increase in ϵ values, boundaries become more and more absorbing; radiative energy reflected back to the medium decreases which in turn decreases the medium temperature. It is seen from Fig. 3.3(f) that ω is not having much effect. For ω =1, θ profile is that for the case of a pure conduction problem. The reason for this type of trend at $\omega = 1$ is that in this situation, the medium is not capable of emitting and absorbing radiation and thus transforms radiant energy into thermal energy. This very fact is also mathematically established from Eq. (3.4). Here, for $\omega = 1$, $d\Psi_R/d\tau = 0$ and the energy equation becomes independent of radiation.

In Figs. 3.4 (a)-(d), effects on the variations of Ψ_R and Ψ_C are given for θ_N and Ψ_T, whereas the same are given for τ_L, N, ϵ and ω in Figs. 3.5 (a)-(h). It is seen from Figs. 3.4(a) and (b) that with increase in θ_N, Ψ_R increases, whereas Ψ_C decreases. This can be explained with the help of Fig. 3.3(a). It is seen from Fig. 3.3(a) that as θ_N decreases, the slope of θ profile increases. Hence the Ψ_C (Fig. 3.4(b)) increases with decrease in θ_N. Consequently, to keep total heat flux Ψ_T constant, the opposite trend is seen in case of Ψ_R (Fig. 3.4(a)). Again as in the case of θ variations, Ψ_R and Ψ_C are more influenced near the north boundary where the temperature θ_N is changed. In case with the effect of Ψ_T (Fig. 3.4(c) and (d)), with decrease in its value, both Ψ_R and Ψ_C are found to decrease. This is obvious because Ψ_T is the summation of Ψ_R and Ψ_C. Therefore, with decrease in Ψ_T, both Ψ_R and Ψ_C decrease. The corresponding change is more in the Ψ_R values. Ψ_R values are minimum at the two boundaries. Opposite is the case with Ψ_C values. This trend in Ψ_C is because of the fact that near the solid boundary, conduction is always dominant.

TH-1868_004301

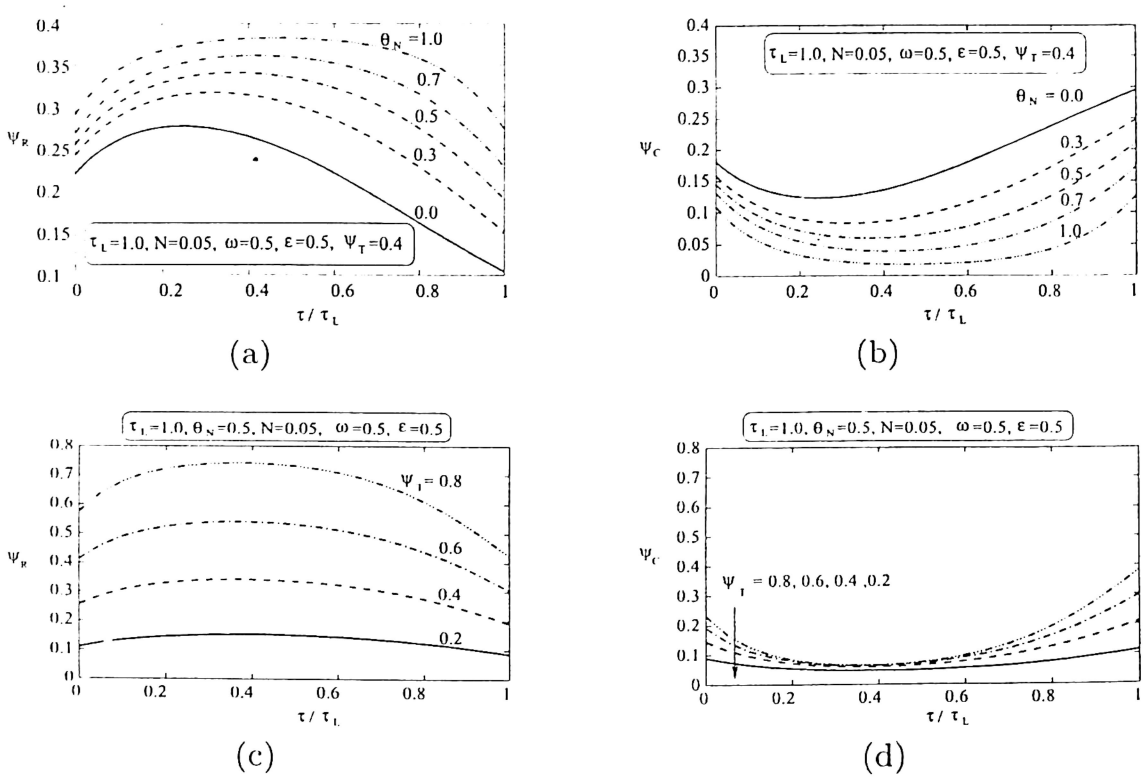


Figure 3.4: Variation of radiative heat flux Ψ_R, conductive heat flux Ψ_C with normalized optical depth τ/τ_L for various parameters.

Effects of τ_L on Ψ_R and Ψ_C are shown in Figs. 3.5(a) and (b). Here it is seen that with increase in τ_L, Ψ_R increases whereas Ψ_C decreases. With increase in τ_L, medium becomes more and more participating and thus radiative contribution to the total heat flux increases. As far as the boundary values of the two fluxes are concerned, trends similar to the previous cases are also observed here.

Effects of N on Ψ_R and Ψ_C have been studied in Figs. 3.5(c) and (d). Here, with increase in N, Ψ_R is found to decrease. Opposite is the case with Ψ_C. It increases with increase in N. With increase in N, radiative contribution to the total heat flux decreases. Hence, medium becomes more conducting. Variations of Ψ_R and Ψ_C with ϵ are shown in Figs. 3.5(e) and (f). The same is given for effects of ω in Figs. 3.5(g) and (h). Here, with decrease in ϵ, Ψ_R decreases and Ψ_C increases. For both Ψ_C and Ψ_R, effects are much more pronounced at the boundaries. In the central

TH-1868_004301

zone, not much effect is observed.

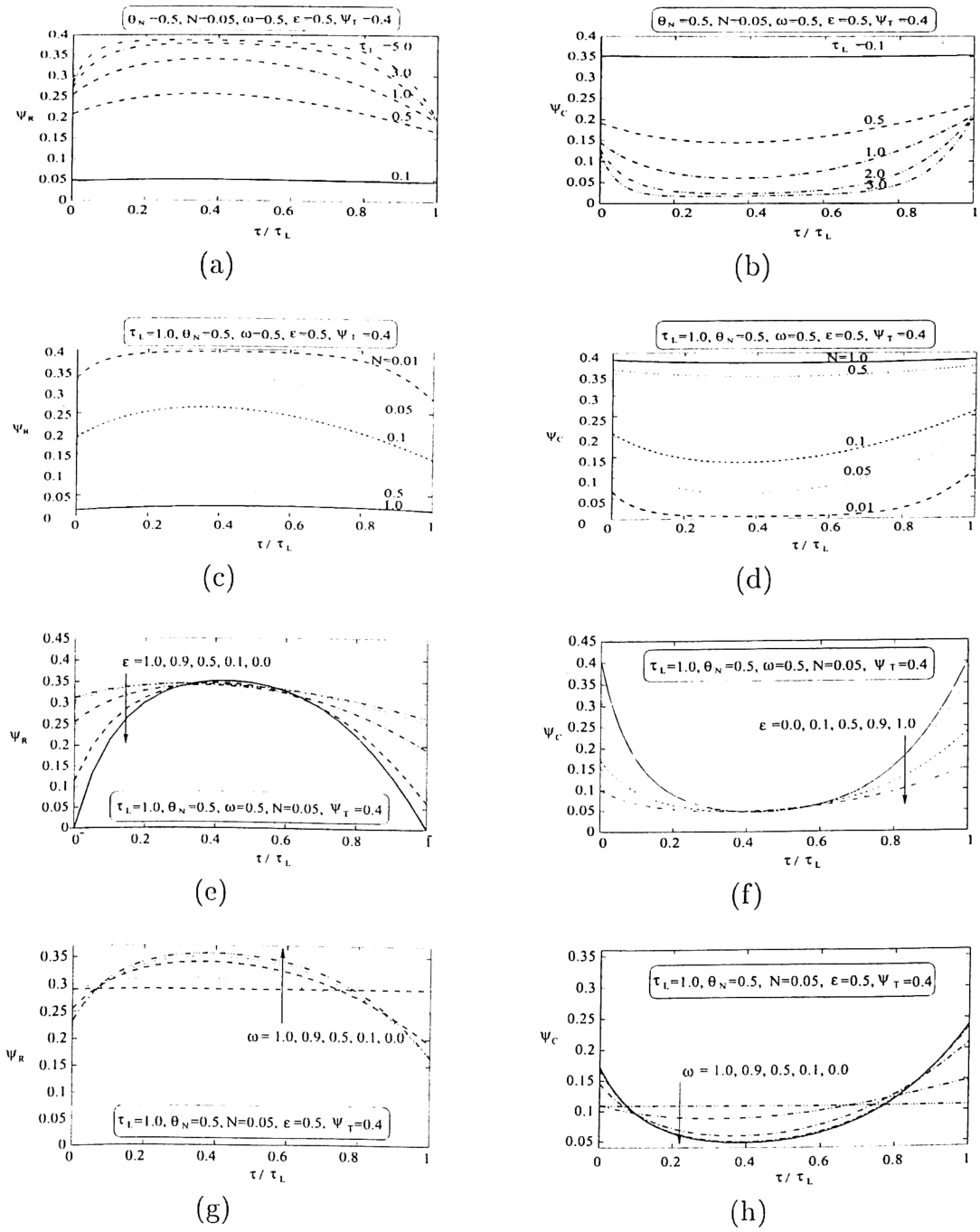


Figure 3.5: Variation of radiative heat flux Ψ_R, conductive heat flux Ψ_C with normalized optical depth τ/τ_L for various parameters.

TH-1868_004301

3.4 Conclusions

The problem of combined conduction and radiation heat transfer in a 1-D planar absorbing, emitting and isotropically scattering gray medium was investigated. Medium boundaries with specified temperature and heat flux were considered. The CDM was applied to get the radiative information required for the energy equation. Effects of enclosure optical thickness, conduction-radiation parameter, scattering albedo, boundary emissivity, temperature of the north boundary and the imposed heat flux were studied on the variations of medium temperature and conductive and radiative heat fluxes. Validity of the method was proved by solving a problem using the inverse method. Comparison of results obtained in the present work with those available in the literature showed a very good agreement.

TH-1868_004301

Chapter 4

1-D Transient Conduction-Radiation with Heat Generation

4.1 Introduction

Analysis of transient conduction and radiation heat transfer in a radiatively participating medium has got numerous engineering applications. Some important works in this area have been reported in [51,61,63,66,120,121,123 130]. A brief literature review on this subject is presented in the next paragraphs.

Tan and Lallemand [131] examined the transient temperature distribution in a glass plate subjected to various boundary conditions. The transient heating of an absorbing, emitting, and scattering material with different black plate boundary conditions was studied by Yuen and Khatami [132]. They used a semi-explicit finite-difference scheme to generate numerical solutions. The effect of anisotropy

TH-1868_004301

on transient conduction-radiation problem was studied by Tsai and Lin [125] and Siewert [128]. For solving the transient energy equation, Tsai and Lin [125] used the Crank-Nicholson scheme and the radiative part was solved by the nodal approximation technique. Tong et al. [123] analyzed transient radiation heat transfer through semi-isotropic scattering planar porous materials. They solved the radiative part using a two-flux model.

The transient cooling problem with isotropic scattering in a cylindrical geometry was analyzed by Baek et al. [127]. For solving the radiative part, they used discrete ordinate method and a finite difference scheme was used to solve the transient energy equation. Tsai and Nixon [124] considered a multilayered geometry without the effect of isotropic scattering. Hahn et al. [129] examined the transient heat transfer using a multi-flux model to solve the radiative part. They analyzed the transient state of heat transfer in a layer of ceramic powder during laser flash measurements of thermal diffusivity. Here also the effect of scattering was not included. Matthews et al. [51] discussed the steady and unsteady combined conduction-radiation heat transfer heated by a highly concentrated solar radiation. A two-flux model was used to solve the radiative part. Transient cooling of a semi transparent material was examined by Siegel [126]. A finite difference procedure was adopted to obtain a highly accurate temperature distribution across the layer. Yao and Chung [130] solved a similar type of problem using an implicit finite volume scheme. The integral equation for radiative heat flux was solved by a singularity subtraction technique and Gaussian quadrature. Recently, studies related to this subject have been reviewed in detail by Siegel [133].

As far as transient conduction and radiation problems are concerned, none of the previous works have discussed the effect of heat generation. In this chapter, the effect of heat generation on temperature and heat flux distributions are studied for transient conduction and radiation problem. The study is done for 1-D gray planar absorbing, emitting and isotropically scattering medium. The radiative part in the energy equation is solved using the collapsed dimension method (CDM). Enclosure boundaries are assumed at specified temperatures. Heat generation rate is considered uniform and constant throughout. Results are compared with the data

TH-1868_004301

reported in the literature. Excellent agreement has been found.

4.2 Formulation

Let us consider a 1-D planar absorbing, emitting and isotropically scattering gray medium (Fig. 3.1). Thermal conductivity of the medium is k and is assumed constant. Extinction coefficient β of the medium is also assumed constant. Initially the complete system is at uniform zero temperature and for times greater than zero, the south boundary is maintained at temperature T_S. Emissivities of the south and the north boundaries are ϵ_S and ϵ_N, respectively.

In the absence of convection, for 1-D geometry considered, unsteady state energy equation is written as

$$\rho C_p \frac{\partial T}{\partial t} = k\frac{\partial^2 T}{\partial z^2} - \frac{\partial q_R}{\partial z} + Q''' \tag{4.1}$$

where Q''' is the volumetric heat generation rate and t is the time.

With the south boundary temperature T_S as the reference temperature, Eq. (4.1) is non-dimensionalized with the following parameters.

$$\theta = \frac{T}{T_S},\ N = \frac{k\beta}{4\sigma T_S^3},\ \Psi_R = \frac{q_R}{\sigma T_S^4},\ Q'''^* = \frac{Q'''}{kT_S\beta^2},\ \xi = \frac{t}{\frac{\rho C_p}{k\beta^2}} = \frac{k\beta^2 t}{\rho C_p}$$

where Q'''^* is the non-dimensional volumetric heat generation rate and ξ is the non-dimensional time. The resulting non-dimensionalized equation is

$$\frac{\partial \theta}{\partial \xi} = \frac{\partial^2 \theta}{\partial \tau^2} - \frac{1}{4N}\frac{\partial \Psi_R}{\partial \tau} + Q'''^* \tag{4.2}$$

In Eq. (4.2), τ is the optical thickness (optical depth). It is measured from the south boundary of the enclosure. Corresponding to the finite distance between the south and the north boundaries, enclosure optical depth is τ_L.

In the present work, volumetric heat generation rate Q'''^* is considered constant and uniform throughout the optical depth τ. Its value for the present case is taken as

TH-1868_004301

unity. For the problem under consideration, boundary and initial conditions are the following:

$$\begin{aligned} \text{Boundary conditions:} \quad & \theta(0,\xi) = \theta_S = 1.0; \quad \theta(\tau_L,\xi) = \theta_N = 0.0 \\ \text{Initial condition:} \quad & \theta(\tau,0) = 0.0 \end{aligned} \tag{4.3}$$

For solving energy equation (Eq. (4.2)), information about divergence of radiative heat flux $\partial\Psi_R/\partial\tau$ is required.

In the CDM, divergence of radiative heat flux $\partial q_R/\partial\tau$ is given by (Eq. 2.43). In non-dimensional form it can be expressed as

$$\frac{\partial\Psi_R}{\partial\tau} = \Gamma(1-\omega)\left[\pi\theta^4 - \frac{G'^*}{2}\right] \tag{4.4}$$

The incident radiation, intensity and source function are non-dimensionalized with respect to the south boundary temperature T_S (Similar to the Eq. (3.5) and (3.6) where it is non-dimensionalized w.r.t T_{ref}).

To solve energy Eq. (4.2), divergence of radiative heat flux $\partial\Psi_R/\partial\tau$ given by Eq. (4.4) is substituted in Eq. (4.2). This yields the desired governing integro-differential equation

$$\frac{\partial\theta}{\partial\xi} = \frac{\partial^2\theta}{\partial\tau^2} - \frac{1}{4N}\Gamma(1-\omega)\left[\pi\theta^4 - \frac{G'^*}{2}\right] + Q'''^* \tag{4.5}$$

It should be noted that Eq. (4.5) is subjected to the boundary and initial conditions given by Eq. (4.3).

The transient energy equation given in Eq. (4.5) is solved using the Crank-Nicholson scheme. For n number of control volumes, it constitutes $n+1$ algebraic equations with $n+1$ unknowns. These equations are solved using Thomas algorithm. In the present work, for enclosure optical thickness $\tau_L > 1$, computations have been performed with 500 control volumes for achieving maximum accuracy. For $\tau_L < 1$, 100 control volumes have been found sufficient. All computations have been performed in double precision. Although the Crank-Nicholson scheme is unconditionally stable, for achieving good accuracy, computations have been performed with non-dimensional time step $\Delta\xi = 0.0001$.

TH-1868_004301

4.3 Results and Discussion

4.3.1 Transient Conduction-Radiation without Heat Generation

In Table 4.1, the CDM results for temperature are compared with the results reported by Lii and Ozisik [61], Barker and Sutton [120], Sutton [121] and Tsai and Lin [125]. Here comparisons have been made for transient conduction-radiation problem without heat generation. At time $\xi = 0.05$, values of non-dimensional gas temperature θ are given at three positions along normalized optical depth, viz. $\tau/\tau_L = 0.25$, 0.5 and 0.75. Results are presented for isotropic scattering with $\omega = 0.5$, conduction-radiation parameter $N = 0.1$ and enclosure optical thickness $\tau_L = 1.0$.

Table 4.1: Comparison of transient temperature θ at time $\xi = 0.05$ for $\tau_L = 1.0$, $\omega = 0.5$ and $N = 0.1$ and two sets of boundary reflectivities.

ϵ_S	ϵ_N	Investigators	Transient temperature θ at		
			$\tau/\tau_L = 0.25$	$\tau/\tau_L = 0.50$	$\tau/\tau_L = 0.75$
1.0	1.0	Lii and Ozisik [61]	0.4617	0.1474	0.0277
		Barker and Sutton [120]	0.4893	0.1775	0.0588
		Sutton [121]	0.4888	0.1778	0.0591
		Tsai and Lin [125]	0.4889	0.1773	0.0588
		CDM, 4 rays	0.4889	0.1777	0.0594
		CDM, 8 rays	0.4898	0.1772	0.0583
		CDM, 16 rays	0.4892	0.1768	0.0584
		CDM, 20 rays	0.4892	0.1768	0.0585
1.0	0.0	Lii and Ozisik [61]	0.4716	0.1630	0.0545
		Barker and Sutton [120]	0.5035	0.2003	0.0831
		Sutton [121]	0.5030	0.2005	0.0833
		Tsai and Lin [125]	0.5031	0.2001	0.0830
		CDM, 4 rays	0.5030	0.2001	0.0826
		CDM, 12 rays	0.5033	0.1993	0.0822
		CDM, 16 rays	0.5033	0.1994	0.0824
		CDM, 32 rays	0.5033	0.1995	0.0824

TH-1868_004301

Two different sets of boundary emissivity are considered and only diffuse reflection is taken into account. The CDM results have been presented for different number of rays. It is seen that the CDM results with only 4 rays are in good agreement with the existing results.

In Table 4.2, results for non-dimensional radiative heat flux Ψ_R from the present work are compared with the results reported by Lii and Ozisik [61], Barker and Sutton [120], Sutton [121], and Tsai and Lin [125]. At three locations viz. τ/τ_L = 0.0, 0.5 and 1.0, comparisons are done at non-dimensional time $\xi = 0.05$. Values of N, ω and τ_L are taken as 0.1, 0.5 and 1.0, respectively. Here also two different sets of boundary emissivity are considered. It is seen from this table that the CDM

Table 4.2: Comparison of transient net radiative heat flux distributions with isotropic scattering at time $\xi = 0.05$ for $\tau_L = 1.0$, $\theta_N = 1.0$, $\theta_S = 0.0$, $\omega = 0.5$ and $N = 0.1$ and two sets of boundary reflectivities.

ϵ_S	ϵ_N	Investigators	Net radiative heat flux $\frac{\Psi_R}{4.0N}$ at $\tau/\tau_L = 0.0$	$\tau/\tau_L = 0.5$	$\tau/\tau_L = 1.0$
1.0	1.0	Lii and Ozisik [61]	1.6436	1.2529	0.9746
		Barker and Sutton [120]	1.9300	1.3314	0.8335
		Sutton [121]	1.9304	1.3305	0.8332
		Tsai and Lin [125]	1.9328	1.3292	0.8321
		CDM, 4 rays	1.8932	1.2931	0.7816
		CDM, 8 rays	1.9059	1.1996	0.7992
		CDM, 12 rays	1.9149	1.3081	0.8131
		CDM, 20 rays	1.9212	1.3181	0.8188
		CDM, 32 rays	1.9238	1.3216	0.8202
1.0	0.0	Lii and Ozisik [61]	1.4000	0.9084	0.3411
		Barker and Sutton [120]	1.6261	0.8643	0.0000
		Sutton [121]	1.6279	0.8639	0.0000
		Tsai and Lin [125]	1.6308	0.8629	0.0001
		CDM, 4 rays	1.6211	0.8576	0.0000
		CDM, 8 rays	1.6229	0.8533	0.0000
		CDM, 12 rays	1.6236	0.8560	0.0000
		CDM, 24 rays	1.6276	0.8613	0.0000
		CDM, 32 rays	1.6286	0.8622	0.0000

TH-1868_004301

results for radiative heat flux compare very well with the results reported in the literature.

In Figs. 4.1(a)-(d), variations of non-dimensional gas temperature θ with normalized optical depth τ/τ_L are given. For $\tau_L = 1.0$, temperature distributions are given for three values of scattering albedo, i.e. $\omega = 0.0$, 0.5 and 1.0. For results presented in Figs. 4.1(a), 4.1(b), $\epsilon_S = \epsilon_N = \epsilon = 0.1$ and conduction-radiation parameter $N = 0.01$, whereas for results presented in Figs. 4.1(c), 4.1(d), boundaries are assumed black and conduction-radiation parameter N has been taken as 0.1. In Figs. 4.1(a) and 4.1(c), for the three values of ω, results are presented at ξ=0.001

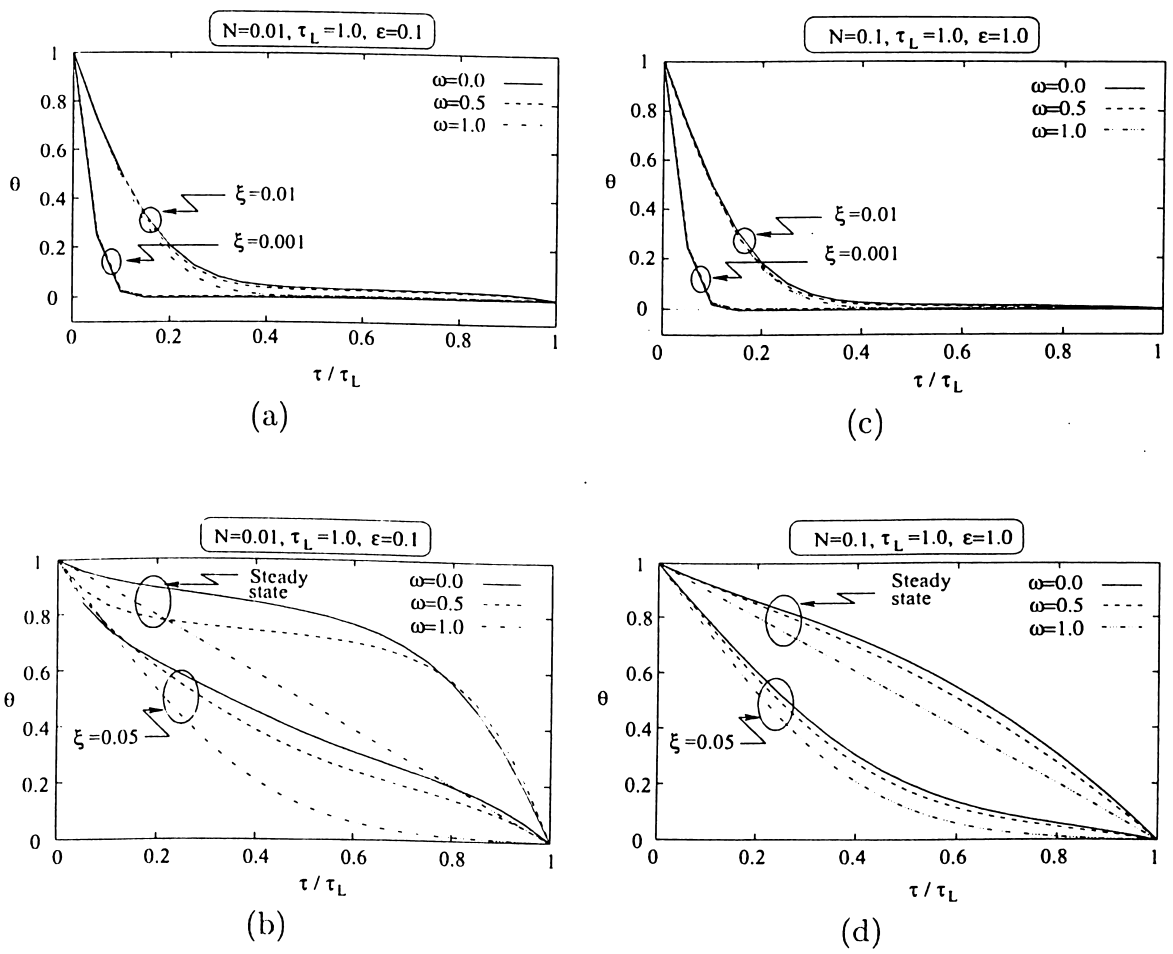


Figure 4.1: Variation of gas temperature θ with normalized optical depth τ/τ_L at different time ξ for N =0.01 and 0.1.

TH-1868_004301

and 0.01. In Fig. 4.1(b) and Fig. 4.1(d), the same are presented for ξ =0.05 and steady state condition. It is seen from these figures that in the early period of transience, ω is not having any effect on θ. This is because of the fact that in the early period, the medium temperature is low and hence the radiation effect is not prominent. As a result of which ω effect is very less. Further, in the early period, θ has a sharp variation near the hot (south) boundary. As the time increases, ω is seen to have prominent effect on θ values as the radiation domination increases. With increase in time, variation in θ is also seen to decrease near the hot (south) boundary.

Variations of conductive heat flux Ψ_C, radiative heat flux Ψ_R and total heat flux Ψ_T along normalized optical depth τ/τ_L at different time ξ are given in Fig. 4.2. For all the results presented in Fig. 4.2, values of conduction-radiation parameter N and enclosure optical depth τ_L are considered 0.1 and 1.0, respectively. Both the bounding boundaries are assumed black, $\epsilon_S = \epsilon_N = \epsilon = 1$. In Figs. 4.2(a) and 4.2(b), results are presented for absorbing-emitting situation, $\omega = 0$. Results are presented for absorbing, emitting and isotropically scattering situations, $\omega \neq 0$, in Figs. 4.2(c) and 4.2(d). Here ω=0.5. In Figs. 4.2(e) and 4.2(f), results are presented for 100% isotropically scattering situation, $\omega = 1$. In Figs. 4.2(a), 4.2(c) and 4.2(e), variations of heat fluxes are given at ξ=0.001 and 0.01. In Figs. 4.2(b), 4.2(d) and 4.2(f), the same are given at ξ=0.05 and steady state conditions. In these figures S. S. stands for steady state.

It is seen from Figs. 4.2(a), 4.2(c) and 4.2(e) that in the early period of transience, i.e. at $\xi = 0.001$, near the hot (south) boundary, there is a sharp variation in the conductive heat flux. This is because of the large temperature gradient found near the boundary as also seen from Fig. 4.1(a),(c). Near the hot (south) boundary, contributions to the total heat flux from radiation is very less. During this early period of transience, contribution is primarily from conduction. As τ/τ_L increases, relative contribution from conduction decreases. Further, it is observed from these figures that Ψ_R is higher at the hot (south) boundary and lower at the cold (north) boundary. It is also observed from these figures that with the passage of time, the gradient in Ψ_C and Ψ_T decrease slowly. At the steady state, in the absence of heat

TH-1868_004301

generation, total heat flux Ψ_T has to be constant (see energy equation (4.2)), and

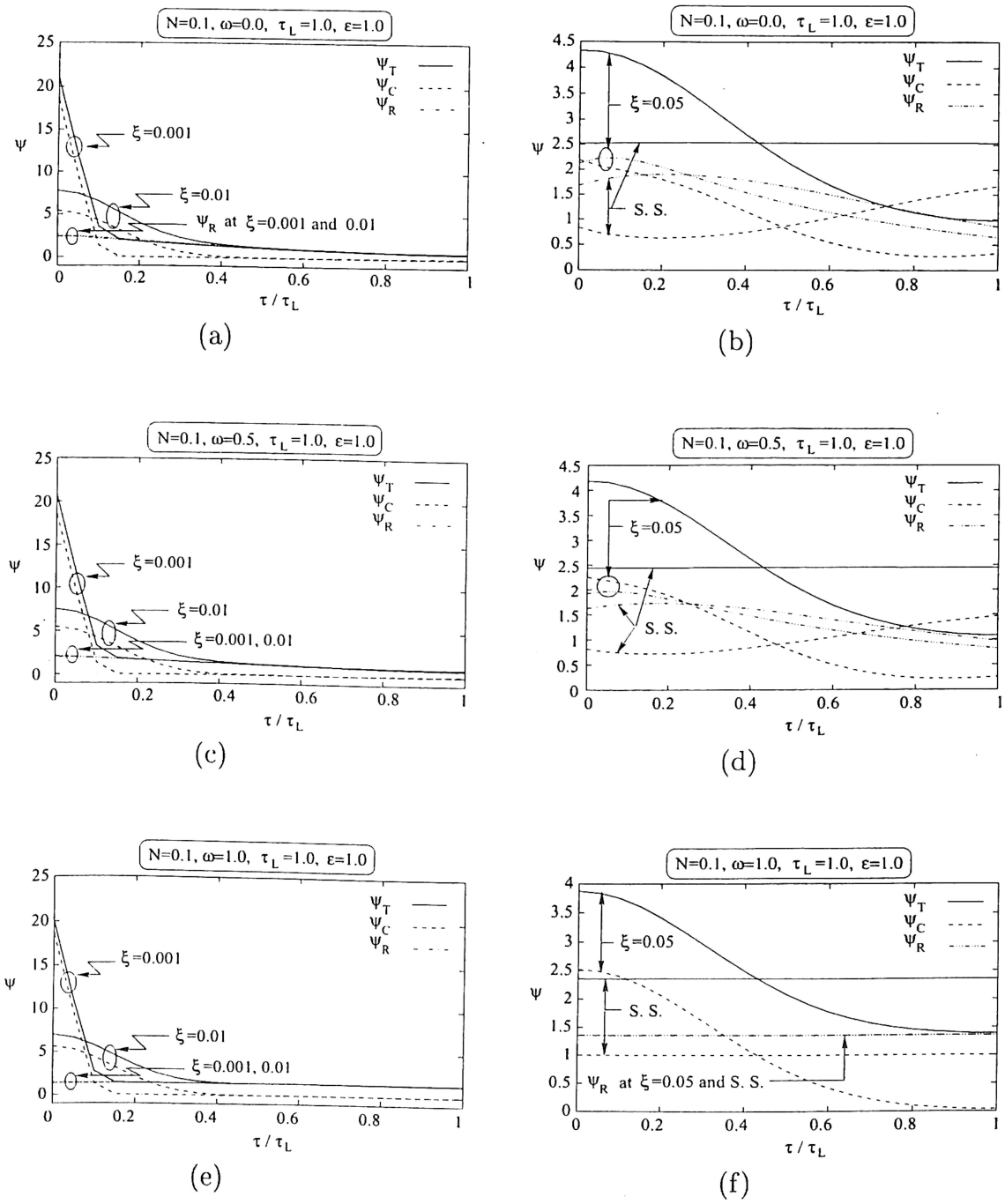


Figure 4.2: Variation of conductive heat flux Ψ_C, radiative heat flux Ψ_R and total heat flux Ψ_T with normalized optical depth τ/τ_L at different time ξ.

TH-1868_004301

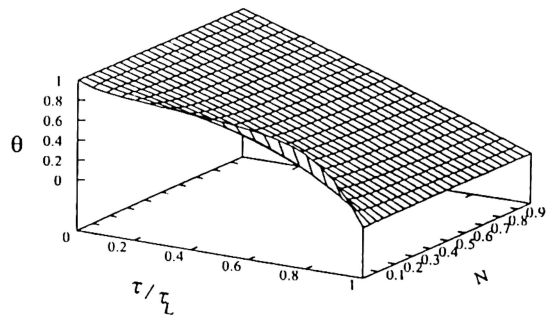
this very fact is being observed from Figs. 4.2(b), 4.2(d) and 4.2(f). Further in Fig. 4.3(f), apart from total heat flux, the conductive and the radiative heat flux is also constant. In this particular case, $\omega = 1$ and hence the radiation is decoupled (Eq. 4.4) from the energy equation. The Ψ_R becomes constant as seen from Eq. 4.4 which implies that Ψ_C is also constant (since $\Psi_T(= \Psi_R + \Psi_C)$ is constant for this situation).

So far we have presented results for the variations of θ, Ψ_C, Ψ_R and Ψ_T with normalized optical depth τ/τ_L for specific values of N, ω and τ_L. To see how θ and Ψ vary with τ/τ_L and over a range of values for ω, N and τ_L, some results are presented.

Figures 4.3(a)-(c) represent variations of temperature θ along τ/τ_L and one of the parameters like N, ω and τ_L. All these results are presented for black boundaries and steady state conditions. In Figs. 4.3(a)-(c), θ variations over entire optical depth τ/τ_L are respectively given for (a) conduction-radiation parameter N in the range [0.01, 1.0], (b) scattering albedo ω in the range [0.1, 1] and (c) enclosure optical thickness τ_L in the range [0.001, 5], respectively. For results presented in Fig. 4.3(a), the medium is considered absorbing-emitting, $\omega = 0$ and enclosure optical thickness τ_L has been taken as unity. In Fig. 4.3(b), results are presented for $N = 0.01$ and $\tau_L = 1$. In Fig. 4.3(c), N and ω values have been taken as 0.1 and 0.0, respectively.

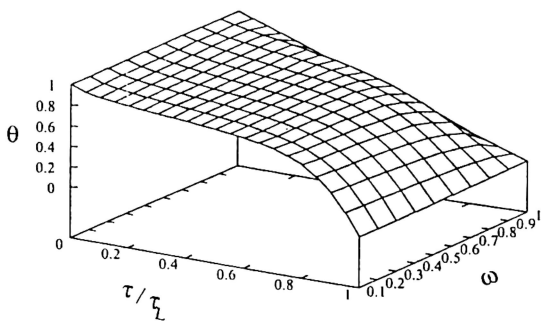
It is observed from Fig. 4.3(a) that as N increases, temperature profile becomes linear, indicating a conduction dominated situation. At higher values of N, this trend has been found true for all values of ω. However, here results have been shown only for $\omega = 0.0$. On the other hand, for $N = 0.01$, which is a highly radiation dominated situation, temperature profile deviates a lot from the linear one. It is seen from Fig. 4.3(b) that for given values of τ_L and N, for $\omega \neq 1$, θ profile is nonlinear. However, for $\omega = 1$, the θ profile is linear. For the chosen planar geometry, this profile is obtained in pure conduction heat transfer. The reason for this type of trend at $\omega = 1$ is that in this situation, medium is not capable of emitting and absorbing radiation and thus transforms radiant energy into thermal energy . This fact is also explained in chapter 3. In Fig. 4.3(c), variation of optical thickness(τ_L) is shown at different τ/τ_L. It is worthwhile to mention here that τ_L

TH-1868_004301



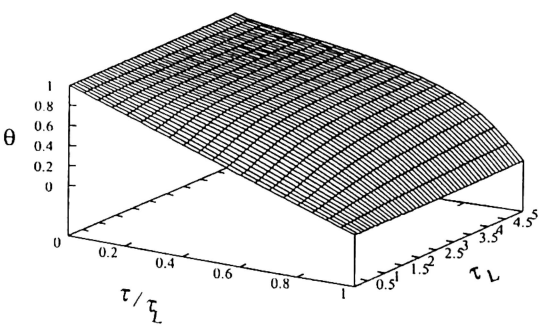
ω=0.0, τ_L=1.0, ε=1.0

(a)



N=0.01, τ_L=1.0, ε=1.0

(b)



N=0.1, ω=0.0, ε=1.0

(c)

Figure 4.3: Steady state temperature θ distributions with varying (a) τ/τ_L and N, (b) τ/τ_L and ω, and (c) τ/τ_L and τ_L; other radiative parameters fixed.

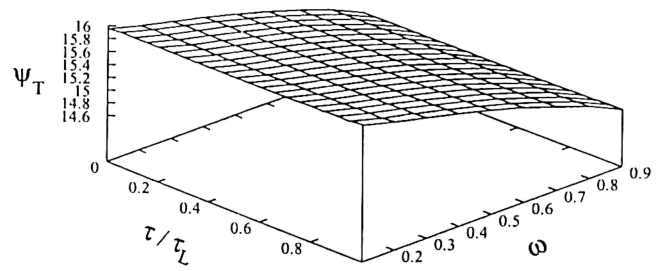
TH-1868_004301

is total optical depth of the medium and τ/τ_L is the normalized optical distance from the south boundary. it is seen that, for lower values of τ_L, temperature profile becomes linear. This is because at lower values of τ_L, medium participates less and thus influence of radiation is reduced. When $\tau_L = 0$, medium does not participate at all and it becomes a case of surface radiation. This trend has been observed irrespective of any values of N.

In Figs. 4.4-4.5, variations of Ψ_T, Ψ_C and Ψ_R are presented for different combinations of radiative parameters. For results presented in these figures, both boundaries have been assumed black. The steady state condition has been assumed in all these cases. In Figs. 4.4(a)-(c), variations along τ/τ_L and ω are respectively given for Ψ_T, Ψ_C and Ψ_R, respectively. Here $N = 0.01$ and $\tau_L = 1.0$. It is seen from Fig. 4.4(a) that Ψ_T decreases with increase in the values of ω, although for a particular ω, its value is constant along τ/τ_L. This is evident for the steady state situation without heat generation - total heat flux Ψ_T $(=\Psi_C+\Psi_R)$ is constant. It is also observed that Ψ_C values are high at the two boundaries (Fig. 4.4(b)) whereas Ψ_R is low at the two boundaries (Fig. 4.4(c)). The reason why Ψ_C is higher and Ψ_R is lower at the two boundaries (Fig. 4.4(b)-(c)) than in the medium adjacent to the boundaries is that the conduction forces the medium temperature in the vicinity of the boundaries to equal the boundary temperature. Further, the observed variations in Ψ_C and Ψ_R at the two boundaries with change in ω values can be explained very well with the help of Fig. 4.3(b). It is clear from Fig. 4.3(b) that with increase in ω, the temperature gradients at the two boundaries decrease and at $\omega = 1$, the gradient is the same throughout. It is a pure conduction-like situation. Hence, the variation of Ψ_C and Ψ_R is seen to be less near the boundaries as ω is increased.

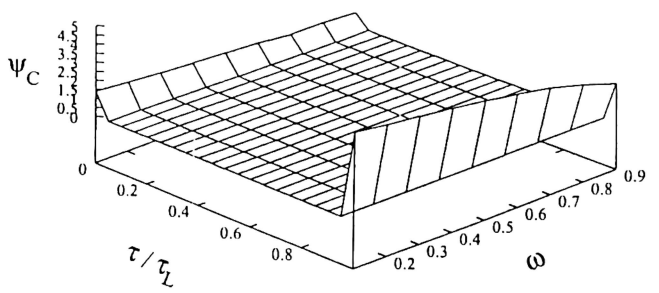
For $N = 0.1$ and $\omega = 0$, variations of Ψ_T, Ψ_C and Ψ_R with τ/τ_L and τ_L are given in Figs. 4.5(a)-(c). Here τ_L values are ranging from 0.1 to 5.0. It is seen from these figures that for lower optical thickness, Ψ_T and Ψ_R values are high. For low optical thickness, except at and near the boundaries, Ψ_C values are almost constant. Hence, from Figs. 4.4-4.5, it can be concluded that lower values of ω and τ_L produce more heat flux.

TH-1868_004301



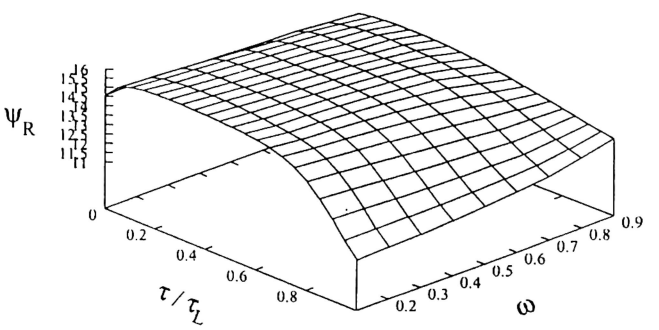
N=0.01, τ_L=1.0, ε=1.0

(a)



N=0.01, τ_L=1.0, ε=1.0

(b)

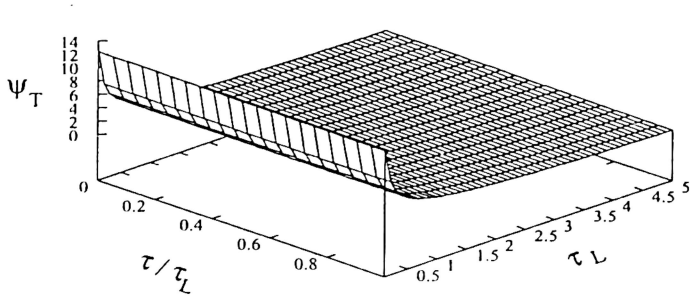


N=0.01, τ_L=1.0, ε=1.0

(c)

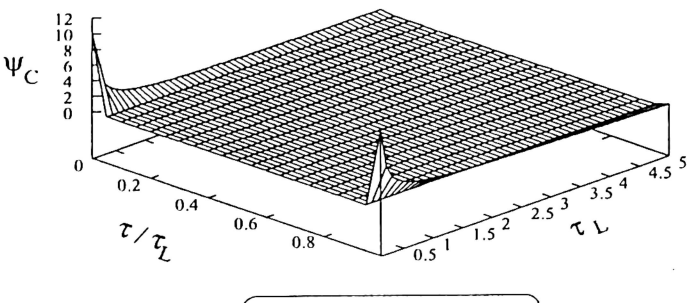
Figure 4.4: Steady state variations of (a) total heat flux Ψ_T, (b) conductive heat flux Ψ_C and (c) radiative heat flux Ψ_R with τ/τ_L and ω; $\tau_L = 1.0$ and $N = 0.01$.

TH-1868_004301



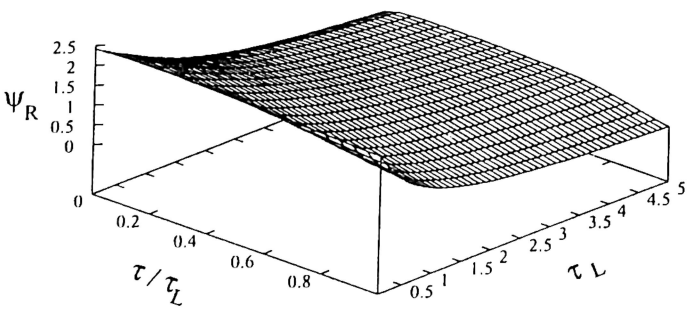
N=0.1, ω=0.0, ε=1.0

(a)



N=0.1, ω=0.0, ε=1.0

(b)



N=0.1, ω=0.0, ε=1.0

(c)

Figure 4.5: Steady state variations of (a) total heat flux Ψ_T, (b) conductive heat flux Ψ_C and (c) radiative heat flux Ψ_R with τ/τ_L and τ_L; $N = 0.1$ and $\omega = 0$.

TH-1868_004301

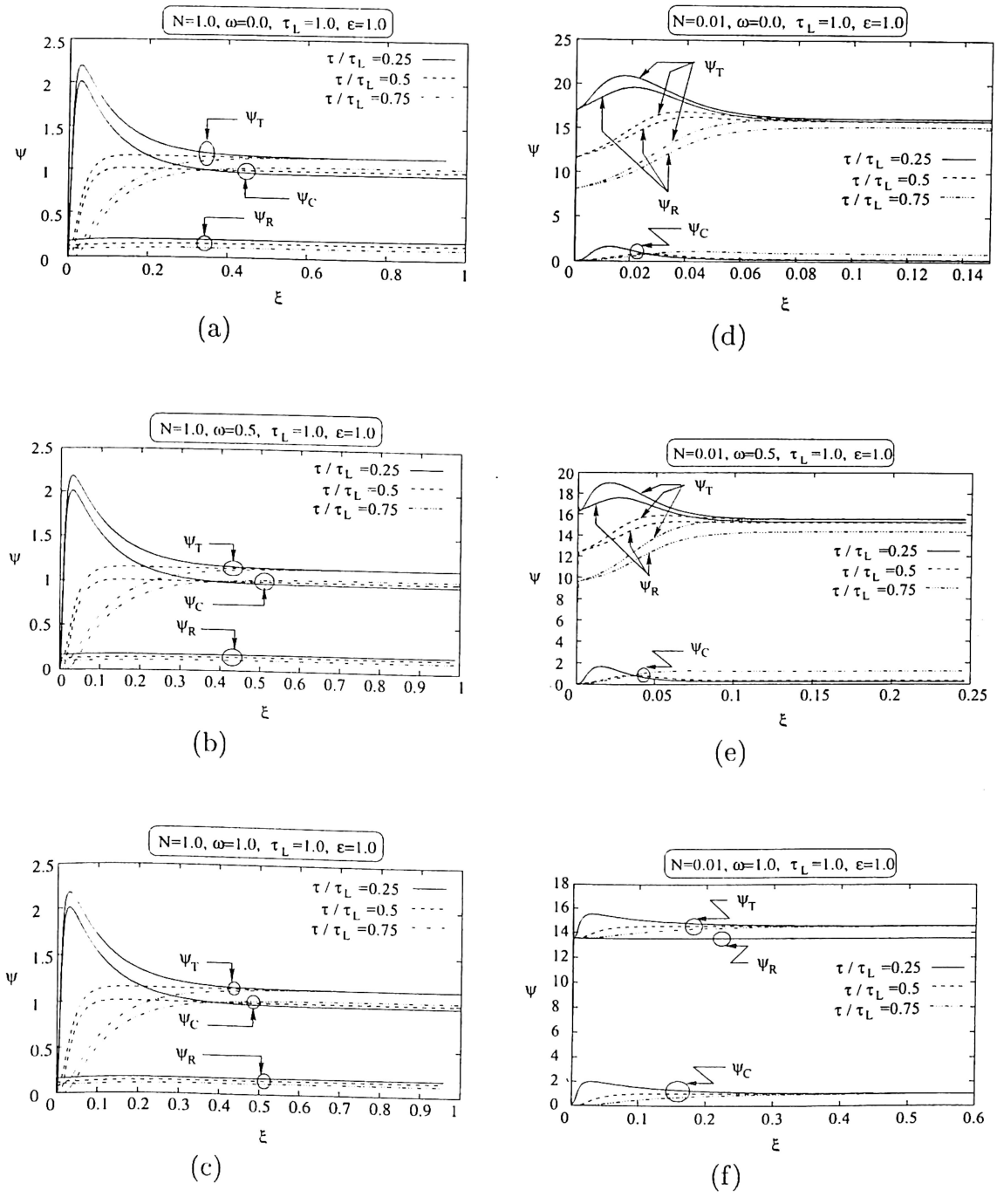
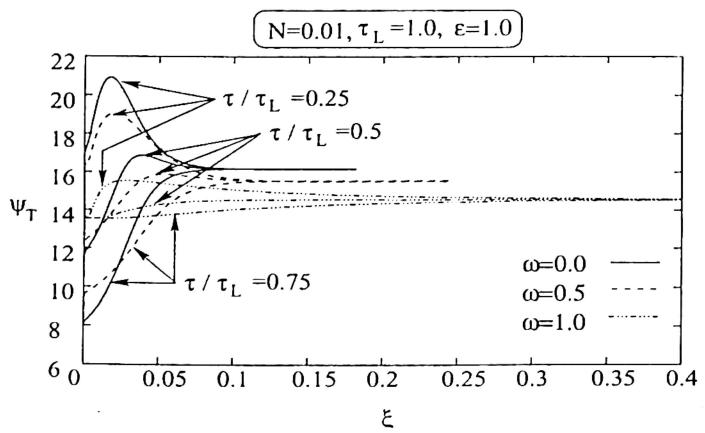


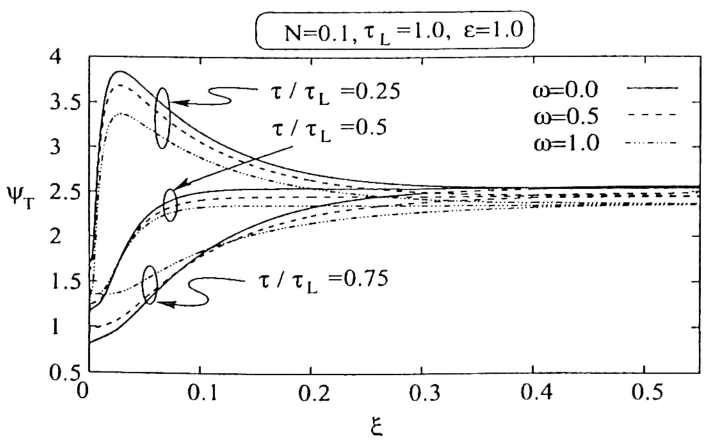
Figure 4.6: Variation of total heat flux Ψ_T, conductive heat flux Ψ_C and radiative heat flux Ψ_R at $\tau/\tau_L = 0.25$, 0.5 and 0.75 with non-dimensional time varying from unsteady to steady state for $N = 1.0$ and 0.01.

TH-1868_004301

In Figs. 4.6(a)-(f), variations of Ψ_T, Ψ_C and Ψ_R with time ξ are given at three different spatial locations, viz. τ/τ_L = 0.25, 0.5 and 0.75. Results in these figures are for three different values of ω (= 0.0, 0.5 and 1.0). Boundaries are assumed black. For all the cases, results are presented from the initial time to the steady state conditions. For results presented in Figs. 4.6(a)-(c), $N = 1$ and that for Figs. 4.6(d)-(f), $N = 0.01$. The enclosure optical thickness τ_L is unity for all the cases. For the conduction dominated situation ($N = 1$) it is seen that at all times, the major contribution to Ψ_T is mainly from Ψ_C. At all locations, magnitude of Ψ_R is



(a)



(b)

Figure 4.7: Effect of scattering on total heat flux Ψ_T at τ/τ_L = 0.25, 0.5 and 0.75 with ξ. (a) $N = 0.01$ and (b)$N = 0.1$

TH-1868_004301

less and is almost constant with time. However, in radiation dominated situation ($N = 0.01$), the major contribution to the total heat flux Ψ_T comes from radiation. It is observed further that trends for all three types of heat fluxes are the same for all ω. It is also seen that the Ψ_T values become same at all the locations as soon as it reaches the steady state. This is because, as mentioned earlier, Ψ_T is constant at the steady state when there is no heat generation.

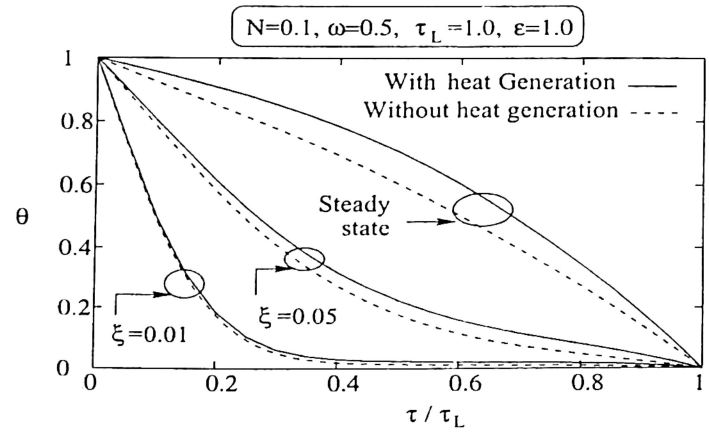
For $\tau_L = 1.0$ and values of $N = 0.01$ and 0.1, at three locations, Figs. 4.7(a)-(b) show the effect of ω on Ψ_T. One interesting point to be noted from Fig. 4.7(a) is that as the value of ω increases, time to reach the steady state also increases. For $\omega = 0$, the steady state is reached first, whereas for $\omega = 1$, it takes longer time to reach the steady state. The reason for this is that at lower values of ω, more radiative and combined radiative and conductive heat fluxes are transported from the hot region to the cold region than that at higher values of ω. This results in a faster balance in energy. In Fig. 4.7(b), this effect is not much, because here conduction contribution is more than the case with Fig. 4.7(a).

4.3.2 Transient Conduction-Radiation with Heat Generation

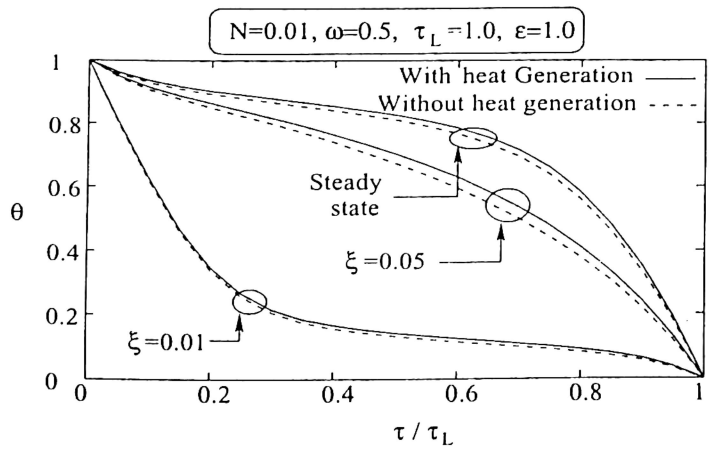
In the following sections, for various radiative parameters, effects of heat generation on temperature θ, conductive heat flux Ψ_C, radiative heat flux Ψ_R and total heat flux Ψ_T are examined. As in the earlier case, here too initially the entire system is at zero temperature and at time $\xi = 0$; the south boundary is subjected to uniform temperature T_S. Non-dimensional heat generation rate Q'''^* is taken as unity.

In Figs. 4.8(a) and 4.8(b), the effect of heat generation on temperature distributions has been shown. Here the boundaries are assumed black, the enclosure optical thickness $\tau_L = 1$ and the medium is considered absorbing, emitting and isotropically scattering with $\omega = 0.5$. For results presented in Fig. 4.8(a), $N = 0.1$ whereas in Fig. 4.8(b) results are presented for $N = 0.01$. It is seen from these figures that the effect of heat generation is not much in the early stage $\xi = 0.01$. As the time increases,

TH-1868_004301



(a)



(b)

Figure 4.8: Variation of temperature θ along optical depth τ/τ_L with and without heat generation at different time steps; (a) $N = 0.1$ (b) $N = 0.01$.

the difference in temperatures with and without heat generation increases. The above trend is because heat generation takes some time to influence the temperature profile. Therefore, in the early period of transience, difference in θ profiles with and without heat generation is less. However, at the boundary, temperatures are always the same for the two cases to satisfy the boundary conditions. Moreover, if the heat generation is intensified, it has been observed that difference in θ profiles at a given time ξ increases (results not shown). It is further observed that for lower value of N, i.e. at $N = 0.01$, the effect of Q'''^* on temperature distribution is less

TH-1868_004301

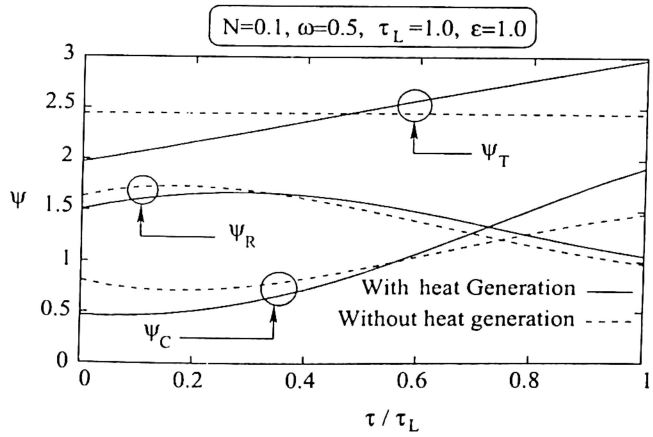


Figure 4.9: Variation of conductive heat flux Ψ_C, radiative heat flux Ψ_R and total heat flux Ψ_T with normalized optical depth τ/τ_L at steady state with and without heat generation.

because of radiation domination. This can be explained with Eq. (4.2). When N is high (conduction dominated), $\frac{1}{4N}\frac{\partial \Psi_R}{\partial \tau}$ is small and the temperature profile largely depends on Q'''^*. But for lower values of N (radiation dominated), $\frac{1}{4N}\frac{\partial \Psi_R}{\partial \tau}$ is high and the temperature profile does not depend much on Q'''^*.

Figure 4.9 shows the effect of heat generation Q'''^* on Ψ_C, Ψ_R and Ψ_T at the steady state. These results are presented for $N = 0.1$ and $\omega = 0.5$. It is seen from this figure that Q'''^* has less effect on Ψ_R than Ψ_C. With the introduction of Q'''^*, Ψ_C decreases near the hot (south) boundary and increases near the cold (north) boundary. This can be explained very well with the help of Fig. 4.8(a). From Fig. 4.8(a), it is seen that with the introduction of Q'''^*, the gradient of θ decreases near the hot (south) boundary and gradually it increases towards the cold (north) boundary. Since Ψ_C is proportional to the temperature gradient, the trend for Ψ_C distribution will closely depend on the θ distribution. It is further seen from Fig. 4.9 that Ψ_T for the case without Q'''^* is constant throughout the optical depth, whereas it is not constant for the case with heat generation ($Q'''^* \neq 0$). With $Q'''^* = 0.0$, $\nabla.\Psi_T = 0.0$; in the steady state, Ψ_T will be constant. With $Q'''^* \neq 0$, Ψ_T will have linear variations as shown in Fig. 4.9. For N =0.1, $\omega = 0.5$ and $\tau_L = 1.0$, variations of Ψ_C, Ψ_R and Ψ_T, respectively, with time ξ are given in Figs. 4.10(a)-(c). For all the results presented here, boundaries have been assumed black ($\epsilon_S = \epsilon_N = \epsilon = 1$). In this case, for the

TH-1868_004301

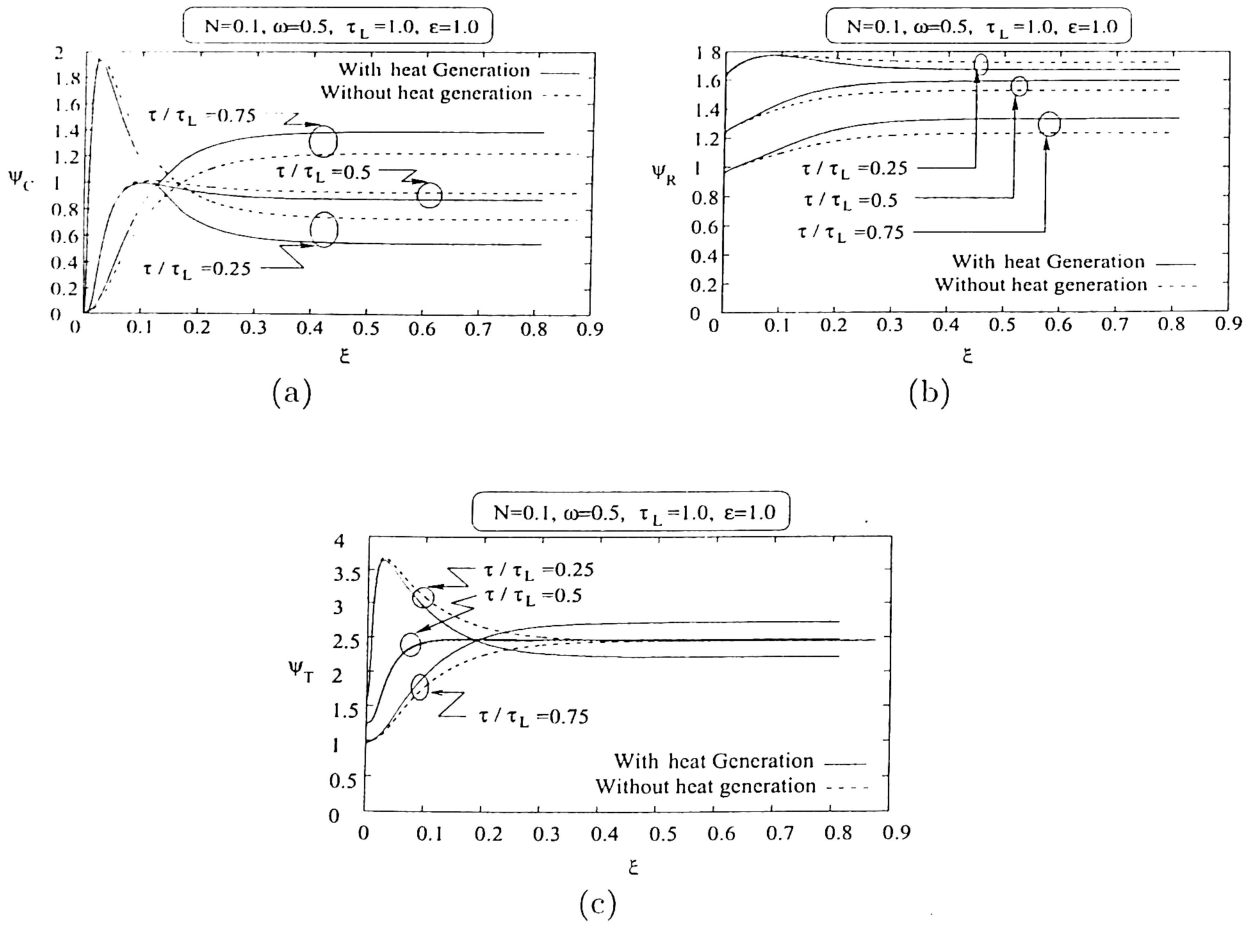


Figure 4.10: Variation of (a) conductive heat flux Ψ_C, (b) radiative heat flux Ψ_R and (c) total heat flux Ψ_T with non-dimensional time ξ.

purpose of comparison, results are also presented for the situation with and without heat generation. It is seen from Fig. 4.10(a) that as time ξ increases, difference between Ψ_C with and without heat generation increases and this difference is more near the two boundaries. The difference is less in the center ($\tau/\tau_L = 0.5$). Near the cold (north) boundary ($\tau/\tau_L = 0.75$), Ψ_C with heat generation is more. The reverse is the case near the hot (south) boundary. At the center too, Ψ_C is lower for the heat generation case. This trend already has been explained with reference to results presented in Fig. 4.9. With regard to the variation of Ψ_R with ξ, here too the heat generation has effect, but compared with Ψ_C it is less. The effect of heat generation on Ψ_T is shown in Fig. 4.10(c).

TH-1868_004301

4.4 Conclusions

Transient conduction-radiation problem with and without heat generation was solved. The radiative part was solved using the CDM. With the radiative term known, the Crank-Nicholson scheme was used to solve the energy equation. Analysis was done for a planar absorbing, emitting and isotropically scattering gray medium. Transient and steady state temperature and heat flux distributions were found for various radiative parameters. Heat generation was found to have effect on temperature and heat flux distributions. Comparison of results obtained in the present work with those available in the literature, showed a very good agreement.

TH-1868_004301

Chapter 5

Effect of Variable Thermal Conductivity on 1-D Conduction-Radiation

5.1 Introduction

In this chapter, transient conduction-radiation heat transfer with variable thermal conductivity is discussed. In general, in the analysis of combined conduction-radiation heat transfer, thermal conductivity is assumed to be constant and its variation with temperature is generally neglected. However, if there is a large temperature difference within a medium, the assumption of constant thermal conductivity is not appropriate. This variation in thermal conductivity becomes important in case of most non-metallic materials subjected to intermediate or large temperature difference [134].

Because of the increased complexities in solving the non-linear integro-differential

TH-1868_004301

energy equation involved with the variable thermal conductivity, not much literature is available. The two available works associated with the variable thermal conductivity include both planar geometry [60] and the one-dimensional cylindrical geometry [135]. Chu and Tseng [60] studied the effect of variable thermal conductivity in an absorbing, emitting and scattering planar medium. They used the differential discrete ordinate method for solving the radiative part. They found significant effects of temperature dependent variable thermal conductivity on both heat flux and temperature distributions. In cylindrical geometry, Krishnaprakas [135] analyzed the effect of variable thermal conductivity using the discrete ordinate method.

The two works reported in references [60, 135] are associated with the steady-state situation only. As far as transient conduction and radiation heat transfer is concerned, so far investigations have not been carried out to study the effects of temperature dependent thermal conductivity. In this chapter, the effects of variable thermal conductivity on transient conduction and radiation heat transfer in an absorbing, emitting and anisotropically scattering planar medium are studied. For the steady state case, for the planar geometry, some important investigations not covered in [60] are also presented.

When the temperature dependent variable thermal conductivity is introduced, the energy equation becomes a non-linear one, and this poses further complexity in solving the energy equation. In the present work, the effect of variable thermal conductivity on transient conduction and radiation heat transfer in a planar medium is investigated. Thermal conductivity of the medium is assumed to vary linearly with temperature, while the other thermo-physical properties and the optical properties are assumed constant. Radiative transfer equation is solved using the DTM and the non-linear energy equation is solved by an implicit scheme. Transient as well as steady state results are found for an absorbing, emitting and anisotropically scattering gray medium. Thermal conductivity has been found to have significant effects on both transient as well as steady state temperature and heat flux distributions. Some steady state results are compared with the results reported in the literature.

TH-1868_004301

5.2 Formulation

Consideration is given to a 1-D planar absorbing, emitting and anisotropically scattering gray medium (Fig. 3.1). Thermo-physical properties such as density ρ, specific heat C_p and the optical property, extinction coefficient β are assumed constant. Initially, the entire system is at some uniform temperature T, and at times greater than zero, the north and the south boundaries are maintained at different temperatures T_N and T_S, respectively. Thermal conductivity of the medium is assumed to vary linearly with temperature. Its variation is given by

$$k = k_o + \gamma'(T - T_S)$$

where k_o is the reference thermal conductivity and γ' is the coefficient of thermal conductivity variation. In the absence of convection, for planar geometry, the unsteady state energy equation is written as

$$\rho C_p \frac{\partial T}{\partial t} = \frac{\partial}{\partial z}\left(k\frac{\partial T}{\partial z}\right) - \frac{\partial q_R}{\partial z} \tag{5.1}$$

Introducing the variable thermal conductivity term, the non-dimensional form of the energy equation (Eq. (5.1)) becomes

$$\frac{\partial \theta}{\partial \xi} = \left(1 + \frac{\gamma(\theta - 1)}{N}\right)\frac{\partial^2 \theta}{\partial \tau^2} + \frac{\gamma}{N}\left(\frac{\partial \theta}{\partial \tau}\right)^2 - \frac{1}{4N}\frac{\partial \Psi_R}{\partial \tau} \tag{5.2}$$

With south boundary temperature T_S as the reference temperature, in Eq. (5.2), the non-dimensional values of temperature θ, conduction-radiation parameter N, radiative heat flux Ψ_R, and time ξ are defined as

$$\theta = \frac{T}{T_S},\ N = \frac{k_o\beta}{4\sigma T_S^3},\ \Psi_R = \frac{q_R}{\sigma T_S^4},\ \xi = \frac{t}{\frac{\rho C_p}{k_o\beta^2}} = \frac{k_o\beta^2 t}{\rho C_p}$$

In Eq. (5.2), γ is another non-dimensional variable thermal conductivity parameter defined as

$$\gamma = \frac{\gamma' T_S N}{k_o}$$

The initial temperature T of the medium is taken as half of the south boundary temperature, which is also equal to the temperature of the north boundary T_N.

TH-1868_004301

Accordingly, for the problem under consideration, boundary and initial conditions are the following:

Initial condition: $\theta(\tau, 0) = 0.5, \quad \text{for} \quad 0 \leq \tau \leq \tau_L$

Boundary conditions: $\theta(0, \xi) = \theta_S = 1.0; \quad \theta(\tau_L, \xi) = \theta_N = 0.5, \quad \text{for} \quad \xi > 0$

where in the above, $\tau = 0$ is indicative of the south boundary and $\tau = \tau_L$ is the optical depth at the north boundary.

Radiative Transfer Equations in the DTM

For solving energy equation (Eq. (5.2)), information about divergence of radiative heat flux $\partial\Psi_R/\partial\tau$ is required. In the DTM, this is found by non-dimensionalizing Eq. (2.18) as,

$$\frac{\partial \Psi_R}{\partial \tau} = 4(1-\omega)\left[\theta^4 - \frac{G^*}{4\pi}\right] \tag{5.3}$$

where G^* is the non-dimensional incident radiation and ω is the scattering albedo. If radiation is assumed azimuthally symmetric, which is always true for a planar geometry, G^* is given by

$$G^* = \frac{G}{\frac{\sigma T_S^4}{\pi}} = 2\pi \int_{\Theta=0}^{\pi} i^*(\Theta) \sin\Theta \, d\Theta \tag{5.4}$$

where i^* is the non-dimensional intensity $(=\frac{i}{\sigma T_S^4/\pi})$ and Θ is the polar angle.

With justifications given in the section (2.3), non-dimensional intensities are calculated as

$$i^*_{n+1} = i^*_n \exp(-\tau) + S^*[1 - \exp(-\tau)] \tag{5.5}$$

The non-dimensional source function appearing in the above equation can be simplified for a linear anisotropic phase function $(p(\Theta' \rightarrow \Theta) = 1 + a_1 \cos\Theta \cos\Theta')$ as

$$S^* = (1-\omega)\theta^4 + \frac{\omega}{4\pi}\left[G^* + a_1 \pi \cos\gamma \, \Psi_R\right] \tag{5.6}$$

In a ray tracing method like the DTM, to get the intensity information at any point in the enclosure, rays are always traced from the boundaries of the medium. For

TH-1868_004301

calculating the intensity at a downstream point next to the boundary ($n+1=1$), the information of intensity at the upstream point which is at the boundary ($n=0$) is required. For a diffuse gray boundary at temperature T_w and emissivity ϵ_w, in the DTM, the non-dimensional boundary intensity i_0^* for a planar medium is given by

$$i_0^* = \epsilon_w \frac{T_w^4}{T_S^4} + 2(1-\epsilon_w) \int_{\Theta=0}^{\pi/2} i^*(\Theta) \sin\Theta \cos\Theta \, d\Theta \tag{5.7}$$

For azimuthally symmetric radiation, non-dimensional net radiative heat flux Ψ_R appearing in Eq. (5.6) is given by

$$\Psi_R = 2 \int_{\Theta=0}^{\pi} i^*(\Theta) \sin\Theta \cos\Theta \, d\Theta \tag{5.8}$$

For numerical evaluation of Eqs. (5.4) and (5.8), spherical solid angle Ω is divided into a finite number of sub-solid angles $\Delta\Omega$, and in each sub-solid angle $\Delta\Omega$, intensity i^* is assumed isotropic. For azimuthally symmetric radiation, i.e., $i(\Theta,\phi) = i(\Theta)$, instead of spherical solid angle Ω, the spherical polar angle ($0 \le \Theta \le \pi$) is discretized into a finite number of discrete polar angles $\Delta\Theta$. In this situation, G^* and Ψ_R are respectively found from

$$G^* = 2\pi \sum_{j=1}^{M} i^*(\Theta_j) \sin\Theta_j \sin\Delta\Theta_j \tag{5.9}$$

$$\Psi_R = 2 \sum_{j=1}^{M} i^*(\Theta_j) \sin\Theta_j \cos\Theta_j \sin\Delta\Theta_j \tag{5.10}$$

where M is the total number of intensities/rays considered over $0 \le \Theta \le \pi$, and $\Delta\Theta_j$ is the angular span over which the jth intensity is assumed isotropic.

To solve the overall energy equation, the expression for $\frac{\partial \Psi_R}{\partial \tau}$ from Eq. (5.3) is substituted in Eq. (5.2), which results in the following equation to be solved.

$$\frac{\partial\theta}{\partial\xi} = \left(1 + \frac{\gamma(\theta-1)}{N}\right) \frac{\partial^2\theta}{\partial\tau^2} + \frac{\gamma}{N}\left(\frac{\partial\theta}{\partial\tau}\right)^2 - \frac{(1-\omega)}{N}\left[\theta^4 - \frac{G^*}{4\pi}\right] \tag{5.11}$$

Equation (5.11) is a highly non-linear equation. Apart from non-linearity in the radiative term, because of the variable thermal conductivity, the first and the second terms on the right hand side of Eq. (5.11) are also non-linear. To facilitate the

TH-1868_004301

solution of the nonlinear Eq. (5.11), time linearization technique is used, which results in the following equation.

$$\frac{\partial\theta}{\partial\xi} - \left[\left(1+\frac{\gamma(\theta-1)}{N}\right)_m\left(\frac{\partial^2\theta}{\partial\tau^2}\right)\right]_{m+1} + \frac{\gamma}{N}\left[\left(\frac{\partial\theta}{\partial\tau}\right)_m\left(\frac{\partial\theta}{\partial\tau}\right)\right]_{m+1} = -\frac{(1-\omega)}{N}\left[\theta^4 - \frac{G^*}{4\pi}\right]_m \quad (5.12)$$

In Eq. (5.12), suffixes m and $m+1$ indicate the time steps. In this equation, radiative term on the right hand side is evaluated at the mth time step. To solve Eq. (5.12) by an implicit scheme, θ values on the left hand side have to be evaluated at $(m+1)$th step. In time linearization technique, θ values in terms having suffix m on the left hand side, are the guess values taken from the mth step, which are then iterated to get the updated θ values at the $(m+1)$th step.

In solving Eq. (5.12), for grid and ray independent solutions, a maximum of 100 control volumes and 64 rays have been used. For the conduction dominated situation, fewer rays have been required. In the following paragraphs, all results are presented for grid and ray independent situations.

5.3 Results and Discussion

For an absorbing, emitting and anisotropically scattering planar medium, results are calculated and analyzed for both steady and transient situations. First, to validate the present work, steady state results are compared with the work of Chu and Tseng [60]. Next, for the steady state situation, with variable thermal conductivity, the effects of various parameters on heat flux and temperature are analyzed. Last, the transient situation is considered. In this case, at different instants, the effect of variable thermal conductivity on temperature and heat flux are addressed.

TH-1868_004301

5.3.1 Steady State Results

5.3.1.1 Results on Heat Flux

In the present conduction-radiation problem, at any location τ/τ_L in the medium, including the two boundaries, the total heat flux Ψ_T is the summation of the conductive heat flux Ψ_C and the radiative heat flux Ψ_R which is written as

$$\Psi_T = \Psi_C + \Psi_R = -4N\frac{d\theta}{d\tau} + \Psi_R \tag{5.13}$$

In the steady state situation, total heat flux Ψ_T will be constant at all τ/τ_L locations. When the north boundary temperature is half of the south boundary temperature ($\theta_N = 0.5$), it is shown in Table 5.1 that the values of radiative heat flux Ψ_R, conductive heat flux Ψ_C and total heat flux Ψ_T of the present work match with an accuracy of ± 0.0001 with that of the reference [60]. It is to be noted that for the comparison of the present work with that of reference [60], here the thermal conductivity variation has been taken as $k = k_0 + \gamma' T$. For the two values of γ, viz., 0.4 and -0.4, at five locations τ/τ_L in the medium, these comparisons have been made for extinction coefficient $\beta = 1$, conduction-radiation parameter $N = 0.5$ and boundary emissivities $\epsilon_S = \epsilon_N = 1$. Here, comparisons have been made for (a) absorbing-emitting medium $\omega = 0$, (b) absorbing, emitting and isotropically scattering medium with $\omega = 0.5$, and (c) isotropically scattering medium $\omega = 1$.

In Fig. 5.1(a), results are shown for the variation of Ψ_T with coefficient of thermal conductivity γ ranging from -0.5 to 0.5. Extinction coefficient β of the medium is 1.0, conduction-radiation parameter N is taken as 0.5, and both the boundaries are black. In this figure, Ψ_T variations with γ are given for scattering albedo $\omega = 1.0$, 0.5 and 0.0. It is seen from this figure that over the entire range of ω, Ψ_T decreases with the increase in γ values. This decrease is because of the fact that the reference thermal conductivity k_0 is taken at the south boundary where the temperature T_S is maximum ($\theta_S = 1$) and the second term of the right hand side of the equation $k = k_o + \gamma'(T - T_S)$ is always negative for $\gamma' > 0$ and positive for $\gamma' < 0$. The higher the value of γ, the lower the value of k, and hence for a given N, the Ψ_T will be lower.

TH-1868_004301

Table 5.1: Steady state heat flux results of present work with a difference of ± 0.0001 with that of reference [60]; Here $N = 0.5$, $\epsilon_S = \epsilon_N = 1$, $\tau_L = 1.0$, $\theta_N = 0.5$.

		ω					
		0		0.5		1.0	
γ	τ/τ_L	$\Psi_C/4.0$	$\Psi_R/4.0$	$\Psi_C/4.0$	$\Psi_R/4.0$	$\Psi_C/4.0$	$\Psi_R/4.0$
0.4	0.0	0.4061	0.1374	0.4001	0.1378	0.4000	0.1297
	0.25	0.3791	0.1644	0.3858	0.1520	0.4000	0.1297
	0.5	0.3876	0.1559	0.3924	0.1454	0.4000	0.1297
	0.75	0.4138	0.1297	0.4101	0.1277	0.4000	0.1297
	1.0	0.4480	0.0955	0.4317	0.1061	0.4000	0.1297
-0.4	0.0	0.0902	0.1502	0.0878	0.1481	0.1000	0.1297
	0.25	0.0739	0.1668	0.0809	0.1551	0.1000	0.1297
	0.5	0.0917	0.1490	0.0951	0.1409	0.1000	0.1297
	0.75	0.1203	0.1204	0.1157	0.1203	0.1000	0.1297
	1.0	0.1527	0.0880	0.1368	0.0993	0.1000	0.1297
0.4	$\Psi_T/4.0$	0.5435		0.5378		0.5297	
-0.4		0.2406		0.2360		0.2297	

For $\gamma = 0.01, -0.5$ and -1.0, variations of Ψ_T with N are given in Fig. 5.1(b). The range of N is chosen from highly radiation dominated situation ($N = 0.01$) to highly conduction dominated situation ($N = 10$). Emissivity of the south and the north boundaries are taken as 1.0 and 0.0, respectively, and extinction coefficient of the medium $\beta = 1$. It is seen from this figure that for any value of γ, with increase in N, Ψ_T values increase. Since increase of N increases the conductive heat flux Ψ_C (1st term of the left hand side of Eq. (5.13)), which in turn increases the total heat flux Ψ_T.

Figure 5.1(c) shows the variation of Ψ_T with β in the range [0.01, 5]. Here, for $N = 0.5$, $\omega = 0.5$, $\epsilon_S = 1$ and $\epsilon_N = 0.5$; for $\gamma = -0.5, 0.0$ and 0.5, the effects of anisotropy a_1 on variation of Ψ_T with β have been studied. It is seen from this figure that for a given a value of γ, Ψ_T decreases with increase in β. Increase in the extinction coefficient β increases the optical thickness ($\tau_L = \beta L$) of the medium and as a result Ψ_T decreases for the reason described in the 4th chapter. Further,

TH-1868_004301

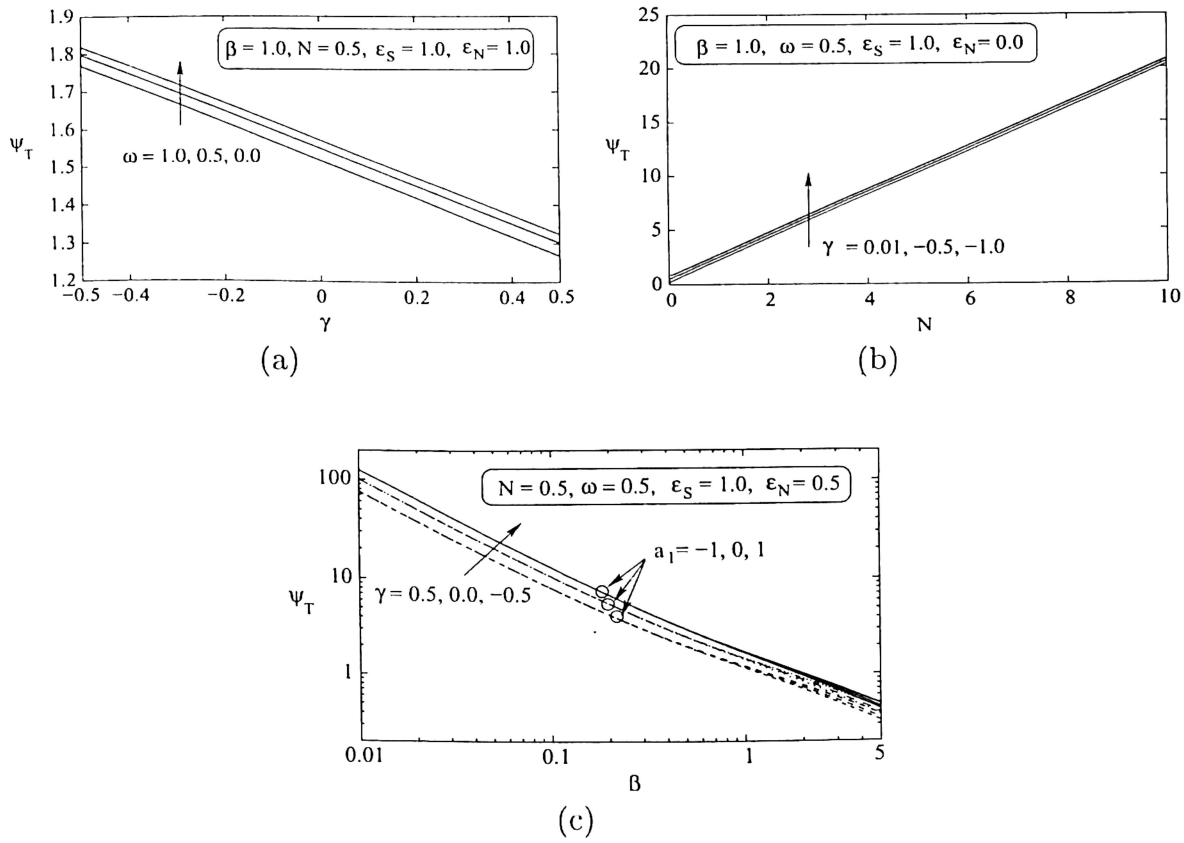
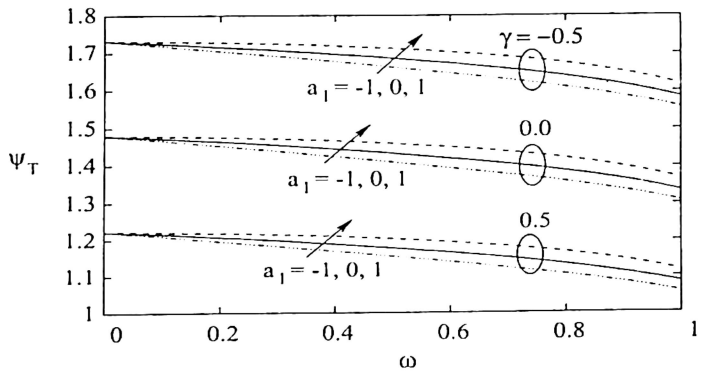


Figure 5.1: Steady state variation of total heat flux Ψ_T with (a) variable thermal conductivity parameter γ, (b) conduction-radiation parameter N and (c) extinction coefficient β.

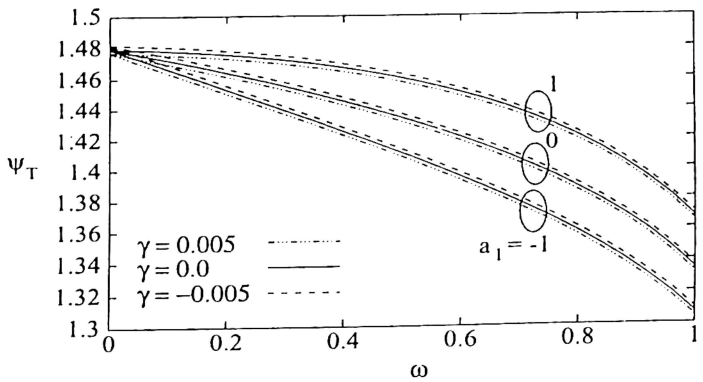
at low to medium values of β, for a given value of γ, anisotropy a_1 does not have any effect on Ψ_T. Its effect becomes distinct only at high β values.

The effect of scattering albedo ω on the total heat flux Ψ_T is shown in Figs. 5.2(a) and 5.2(b). In Fig. 5.2, results are presented for $\beta = 1$, $N = 0.5$, $\epsilon_S = \epsilon_N = 1.0$. In Fig. 5.2(a), γ values are taken as -0.5, 0.0 and 0.5, whereas the same are -0.005, 0.0 and 0.005 in Fig. 5.2(b). In these figures, the effects of anisotropy a_1 are also examined. In Fig. 5.2(a), for a given value of γ, the effects of a_1 for 100% forward scattering ($a_1 = +1$), isotropic scattering ($a_1 = 0$) and 100% backward scattering ($a_1 = -1$) are examined. In Fig. 5.2(b), the effects of three values of a_1 are examined

TH-1868_004301



(a)



(b)

Figure 5.2: Steady state variation of total heat flux Ψ_T with scattering albedo ω for different values of γ with anisotropic effect.

for $\gamma = 0.005, 0.0$ and -0.005.

It is seen from Figs. 5.2(a) and 5.2(b) that for a given value of γ, for all $a_1 = 1$, Ψ_T decreases with increase in ω. It is further observed that as ω approaches 0, for a given γ, Ψ_T values for all a_1 values approach the same value. This is true, as for $\omega = 0$, that the medium is absorbing-emitting, and hence anisotropy a_1 will not have any effect. It should be noted that for $a_1 = 0$, for any value of γ, trends for the variation of Ψ_T with ω given in Fig. 5.2 are consistent with the results given in Fig. 5.1(a), where it can be noticed that for a given γ value, Ψ_T decreases with

TH-1868_004301

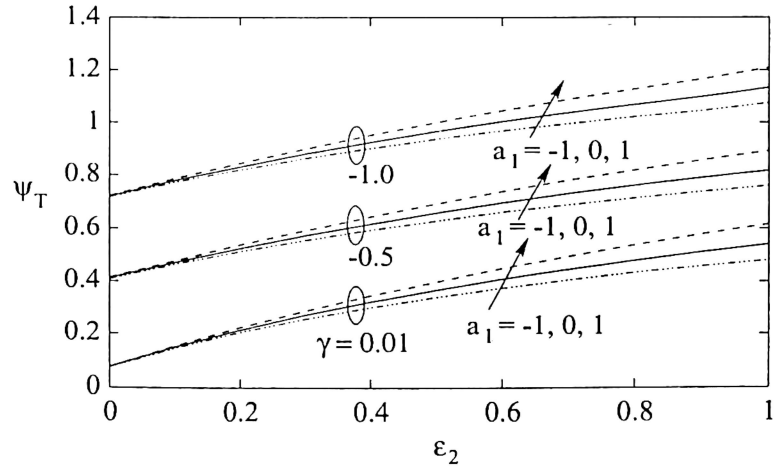


Figure 5.3: Steady state variation of total heat flux Ψ_T with north boundary emissivity ϵ_N for different γ with anisotropic effect.

increase in ω.

With south boundary as black ($\epsilon_S = 1$), for $\gamma = 0.01$, -0.5, and -1.0, Ψ_T variations with the north boundary emissivity ϵ_N are shown in Fig. 5.3. Here, again the effect of anisotropy a_1 is also shown. For results presented in this figure, values of β, ω and N are taken as 1.0, 0.9 and 0.01, respectively. It is seen that for a particular value of γ, total heat flux Ψ_T increases with increase in the value of ϵ_N and it is maximum for the black boundary ($\epsilon_N = 1.0$). Another interesting point to be observed is that the effect of anisotropy increases as ϵ_N increases, and when the north boundary is perfectly reflecting ($\epsilon_N = 0$), anisotropy does not have any effect.

5.3.1.2 Results on Temperature

In Figs. 5.4(a)-(c), for $\gamma = -1.0, -0.5, 0.0$ and 0.5, steady state temperature θ distributions with τ/τ_L in the medium are shown for $\beta = 0.1$, 1.0 and 10, respectively. These results are obtained for $\epsilon_S = 1.0$, $\epsilon_N = 0.5$, $\omega = 0.5$, $a_1 = 0.0$ and $N = 0.5$. It is seen from these figures that for all values of β, θ values all along τ/τ_L are less

TH-1868_004301

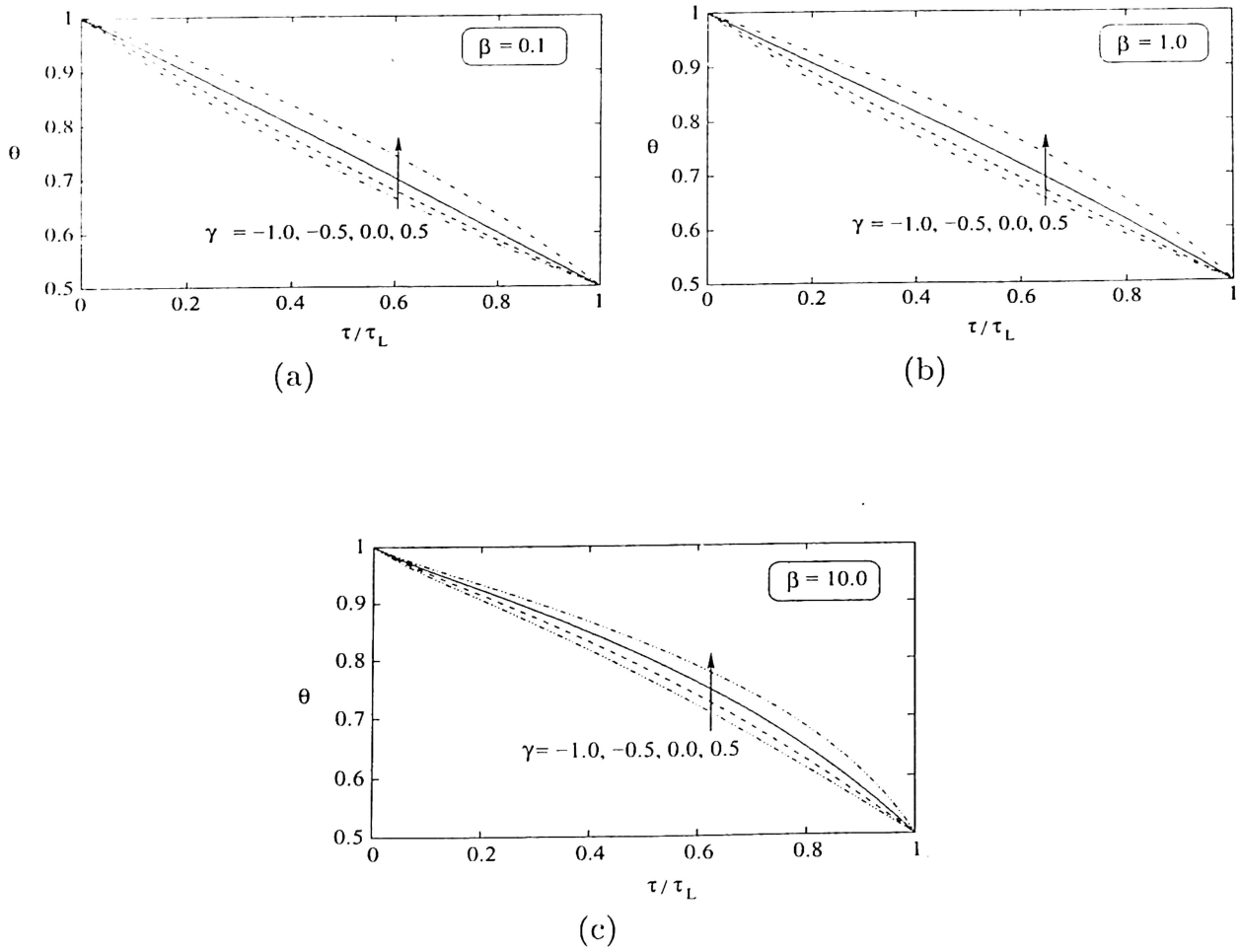


Figure 5.4: Effect of thermal conductivity parameter γ on steady state temperature θ variation with τ/τ_L for (a) $\beta = 0.1$, (b) $\beta = 1.0$ and (c) $\beta = 10.0$.

for lower values of γ. As the medium participates more ($\beta = 10$), the influences of both positive and negative values of γ decrease.

In Figs. 5.5(a) -(d), the effects of γ on temperature θ distributions along τ/τ_L are shown for conduction-radiation parameter $N = 1.0$, 0.5, 0.1 and 0.01, respectively. Here, results are presented for $\beta = 1.0$ and $\omega = 0.0$. Emissivities of the south and north boundaries are 1.0 and 0.5, respectively. It is seen from these figures that for lower values of N, i.e, in radiation dominated situations, the γ effect is more

TH-1868_004301

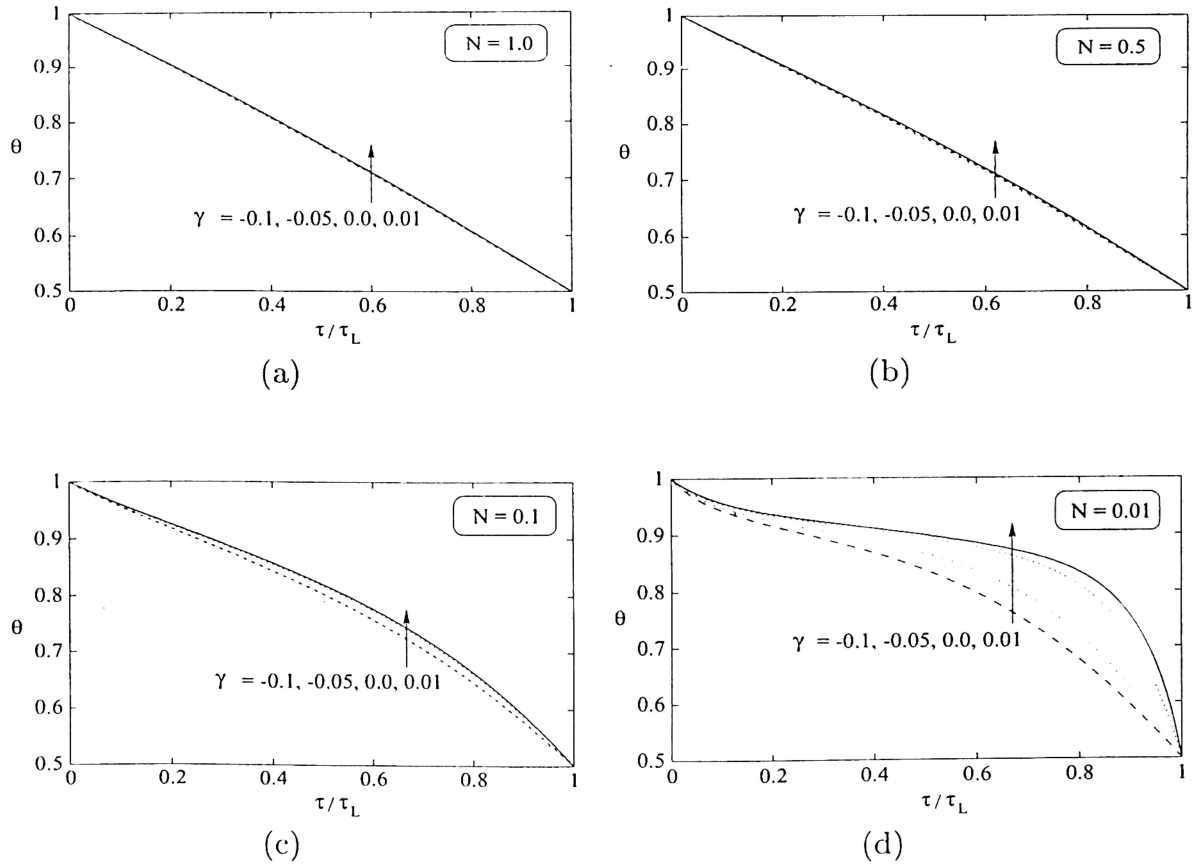


Figure 5.5: Effect of thermal conductivity parameter γ on steady state θ variation with τ/τ_L for conduction-radiation parameter (a) $N = 1.0$, (b) $N = 0.5$, (c) $N = 0.1$ and (d) $N = 0.01$.

pronounced. For conduction dominated cases (Fig. 5.5(a), 5.5(b)), θ profiles for all γ values are almost linear and hence, and in the medium, θ values are close to one another. But as radiation starts dominating, i.e., N is decreasing, influence of γ increases.

TH-1868_004301

5.3.2 Unsteady State Results

5.3.2.1 Results on Temperature

In Figs. 5.6-5.9, the effects of various parameters on temperature θ are given for the unsteady state situation. In Figs. 5.6(a)-(c), θ variations with τ/τ_L in the medium are given at non-dimensional time $\xi = 0.005, 0.01$ and 0.05, respectively. At each instant ξ, for $\gamma = -0.01, 0.0$ and 0.01, θ variations are given for $\beta = 1.0$, $\omega = 0.0$, $N = 0.01$, $\epsilon_S = 1.0$ and $\epsilon_N = 0.5$. It is observed from these figures that at an early

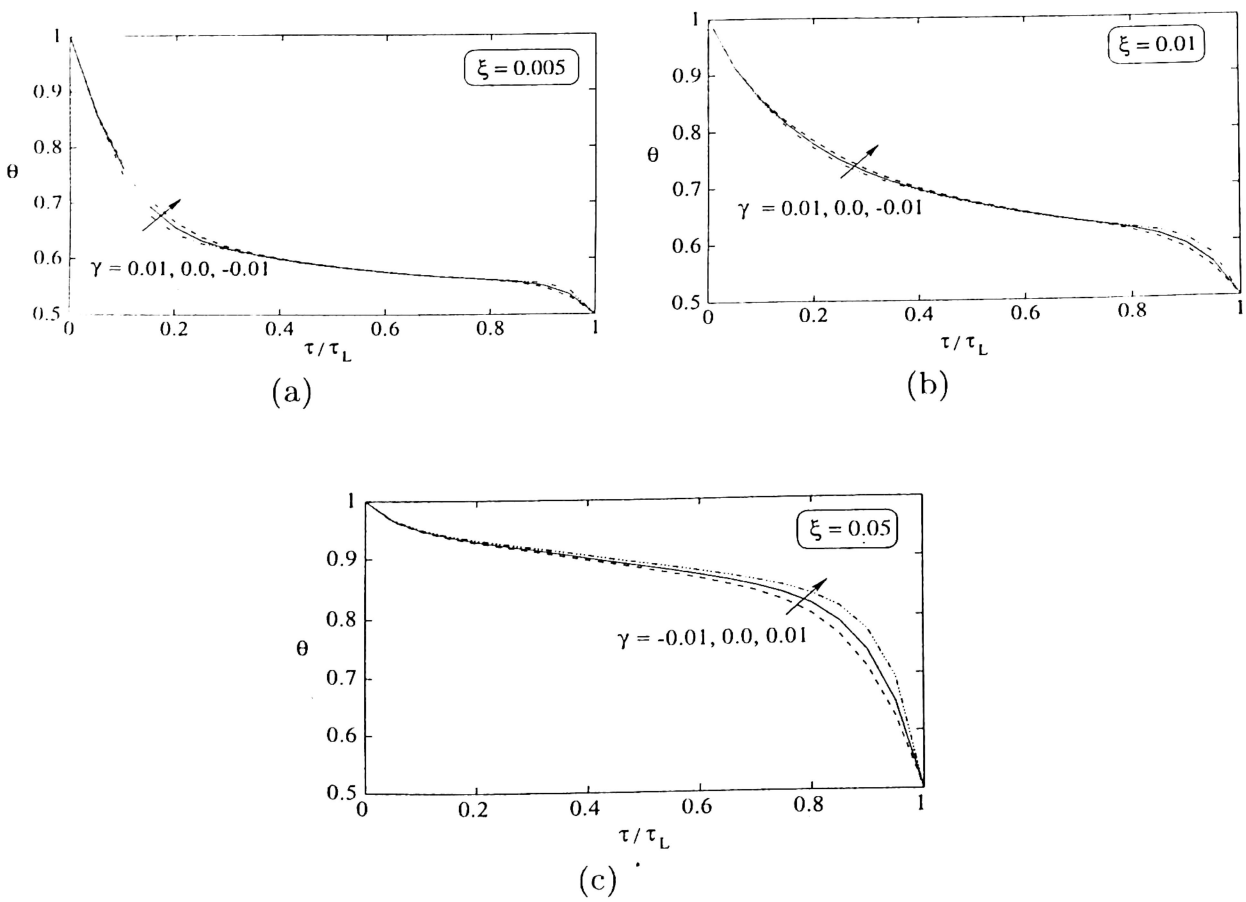


Figure 5.6: Effect of thermal conductivity parameter γ on temperature θ variation with τ/τ_L at time (a) $\xi = 0.005$, (b) $\xi = 0.01$, and (c) $\xi = 0.05$.

TH-1868_004301

period ($\xi = 0.005$ and 0.01) the influence of γ is less compared with the later stage ($\xi = 0.05$).

For a given value of ω, the effect of γ on θ variations with τ/τ_L at two instants, viz. $\xi = 0.1$ and steady state, are shown in Figs. 5.7(a)-(d). These results are presented for $\beta = 1$, $N = 0.5$, $\epsilon_S = 1.0$ and $\epsilon_N = 0.5$. In Fig. 5.7(a), θ distributions are given at time $\xi = 0.1$, whereas in Figs. 5.7(b)-(d), the same are given for the steady state situation.

In Fig. 5.7(a), for $\omega = 0, 0.5, 1.0$, θ distributions are given for $\gamma = 0.5$ and -1.0. It

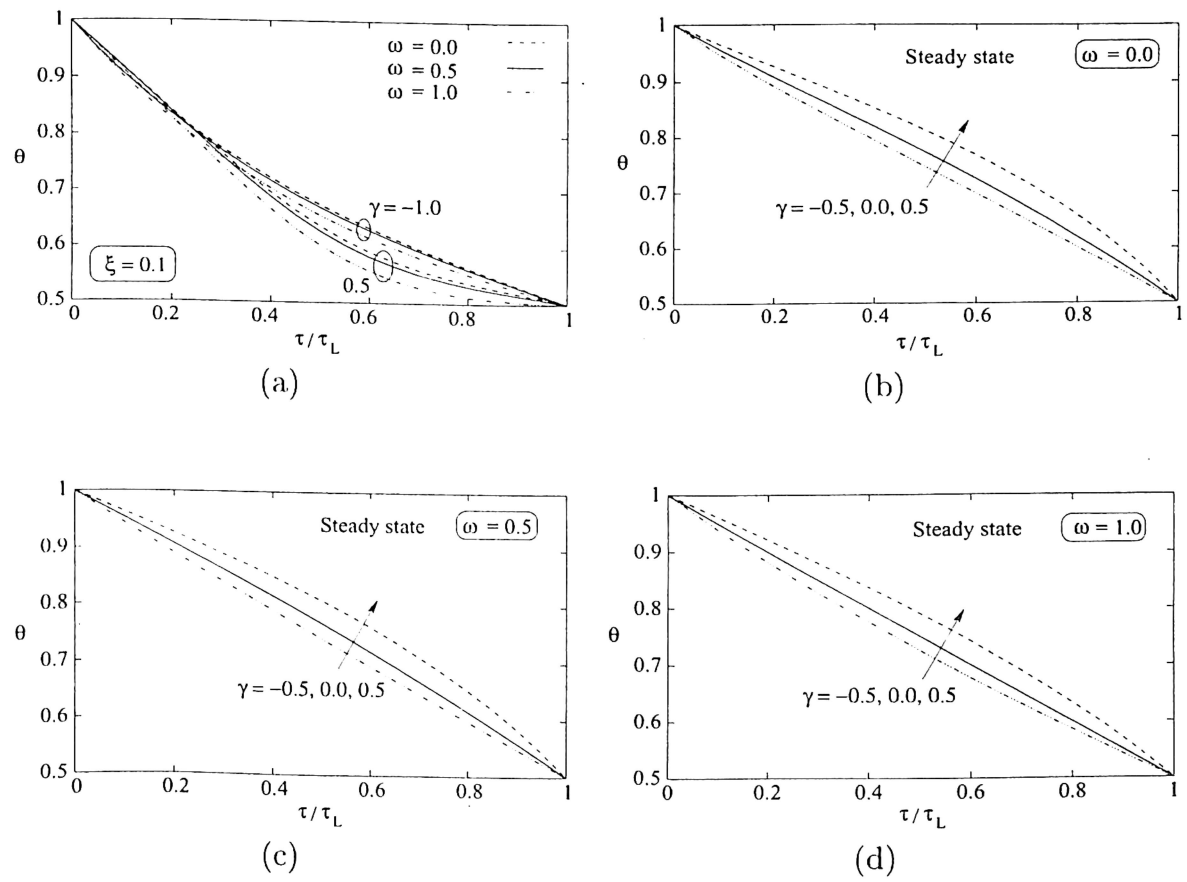
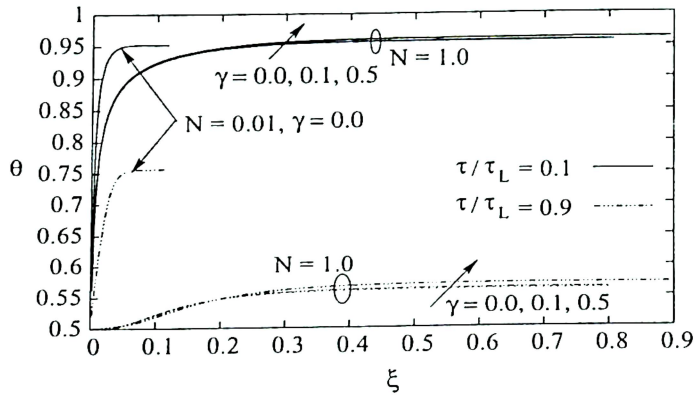


Figure 5.7: Effect of thermal conductivity parameter γ on temperature θ variations with τ/τ_L for different scattering albedo ω at (a) $\xi = 0.1$ and (b)-(d) steady state.

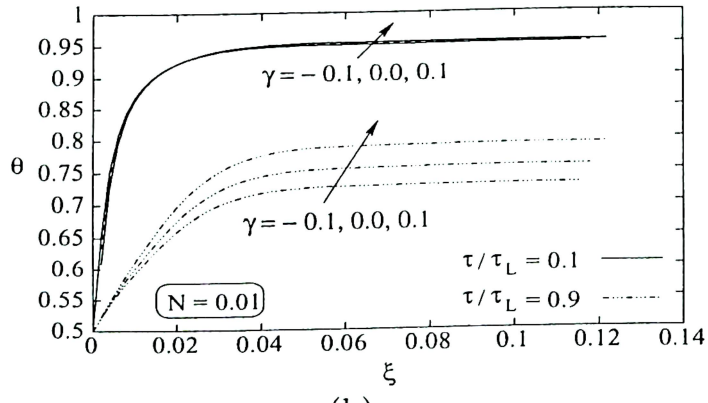
TH-1868_004301

is seen from this figure that at this instant, for a given value of ω, the effect of γ all along τ/τ_L is high. However, at the steady state, as seen from the Figs. 5.7(b-d), the effect of γ for all ω is almost the same.

For given values of β, ω, a_1 and N, for different values of γ to see how fast temperature θ reaches steady state at different locations in the medium, some results are presented in Figs. 5.8(a) and 5.8(b). Accordingly, in these figures, θ variations are



(a)



(b)

Figure 5.8: Effect of thermal conductivity parameter γ on temperature θ variation with time ξ at locations $\tau/\tau_L = 0.1$ and 0.9 for different values of conduction-radiation parameter N.

TH-1868_004301

620
TAL/C
P03

THESIS
Lakshminath Bezbaroa Central Library
Indian Institute of Technology Guwahati
ACC. No. TH.....1868.....
Date.....28/3/12.....

given with time ξ starting from the initial state to the steady state.

In Figs. 5.8(a) and 5.8(b), the variations of θ with time ξ are given at two locations, viz., $\tau/\tau_L = 0.1$ and 0.9. These two locations $\tau/\tau_L = 0.1$ and 0.9 are equidistant from the south and the north boundaries, respectively. In both figures, θ distributions are given for $\beta = 1.0$, $\omega = 0.0$, $\epsilon_S = 1.0$ and $\epsilon_N = 0.5$.

In Fig. 5.8(a), at the two locations, θ variations with time ξ are given for $N = 0.01$ and 1.0. In Fig. 5.8(b), the same are shown for $N = 0.01$. For a given value of N, the effects of γ are also shown. It is seen from Fig. 5.8(a) that for $N = 0.01$ and $\gamma = 0.0$, at both locations, temperature reaches steady state quickly as compared with $N = 1.0$. This trend can be explained in the following way. In this problem, compared with $N = 1.0$, the influence of radiation is more for $N = 0.01$. In this situation, in establishing the temperature field, radiation will have more influence than the conduction, although the resultant temperature field is the combined effect of both of the modes. Radiation being the faster mode of heat transfer, for $N = 0.01$, steady state is reached quickly.

It is seen from Fig. 5.8(b), that the influence of γ is more near the north boundary. This is because of the fact that the difference of $(T - T_S)$ increases near this region. As a result thermal conductivity of the medium varies more in this region.

5.3.2.2 Results on Heat Flux

In Figs. 5.9(a)-(c), variations of radiative heat flux Ψ_R, conductive heat flux Ψ_C and the total heat flux Ψ_T with time ξ are shown at a location close to the cold boundary, $\tau/\tau_L = 0.75$. These results are presented for $\beta = 1.0$, $N = 0.5$, $\epsilon_S = 1.0$ and $\epsilon_N = 0.5$. In these figures, for a given value of a_1, the effects of γ are also shown.

From these figures it is seen that Ψ_R is more influenced by the anisotropy a_1. For any value of γ, forward scattering increases the value of Ψ_R, whereas backward scattering decreases Ψ_R. It is observed from these figures that the time to reach the

TH-1868_004301

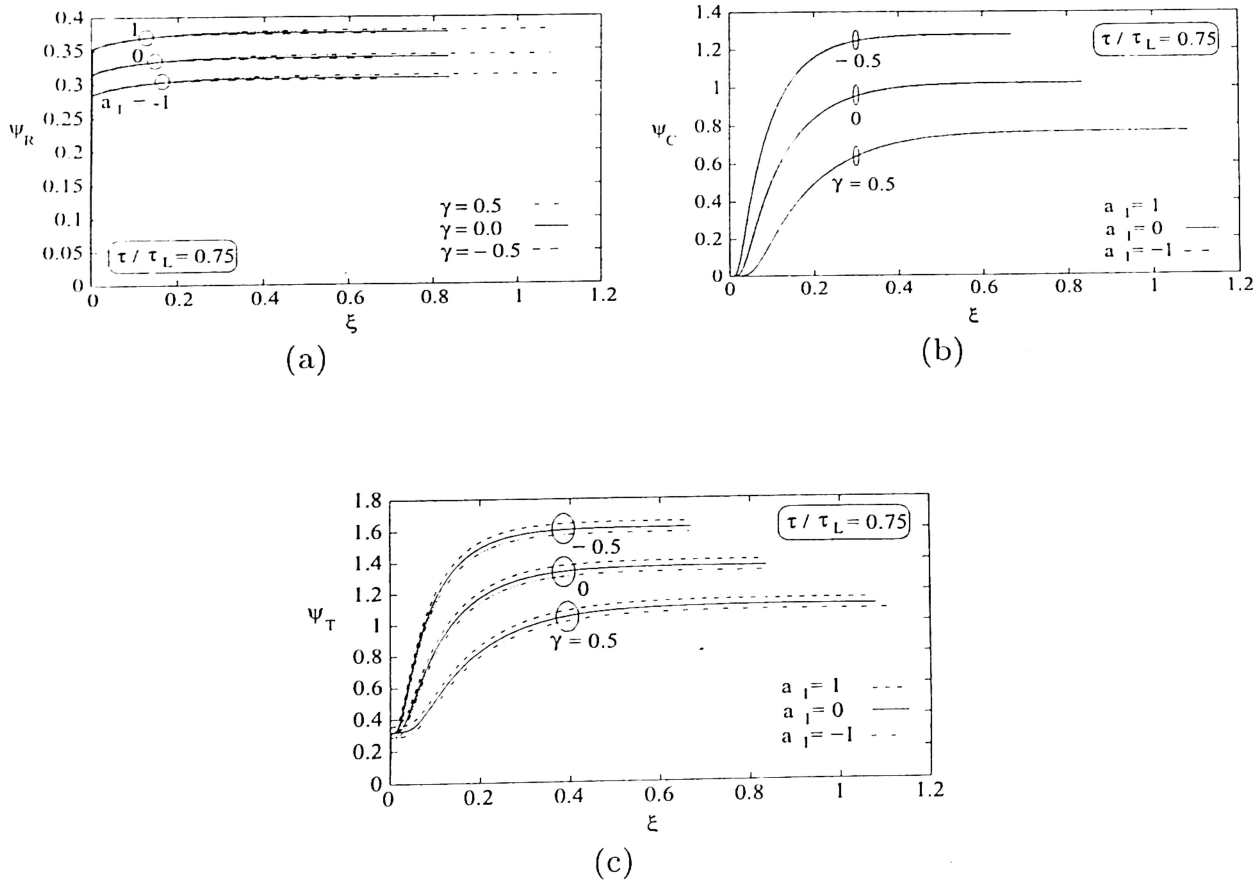


Figure 5.9: Effect of thermal conductivity parameter γ on variation of radiative heat flux Ψ_R, conductive heat flux Ψ_C and total heat flux Ψ_T at the location $\tau/\tau_L = 0.75$. with the effect of anisotropy.

steady state decreases with the decrease in the value of γ.

Although anisotropy is not seen to have any effect on Ψ_C, effect of γ on Ψ_C is more prominent. Here, for all values of γ, in the early period of transience, compared with Ψ_R values, there are more fluctuations in Ψ_C values. In the present conduction-radiation problem, Ψ_T is the summation of Ψ_R and Ψ_C. For results presented in Fig. 5.9, for the chosen values of parameters, Ψ_C values are more than Ψ_R. Therefore, on the total heat flux Ψ_T, the effect of γ is more than the effect of a_1.

TH-1868_004301

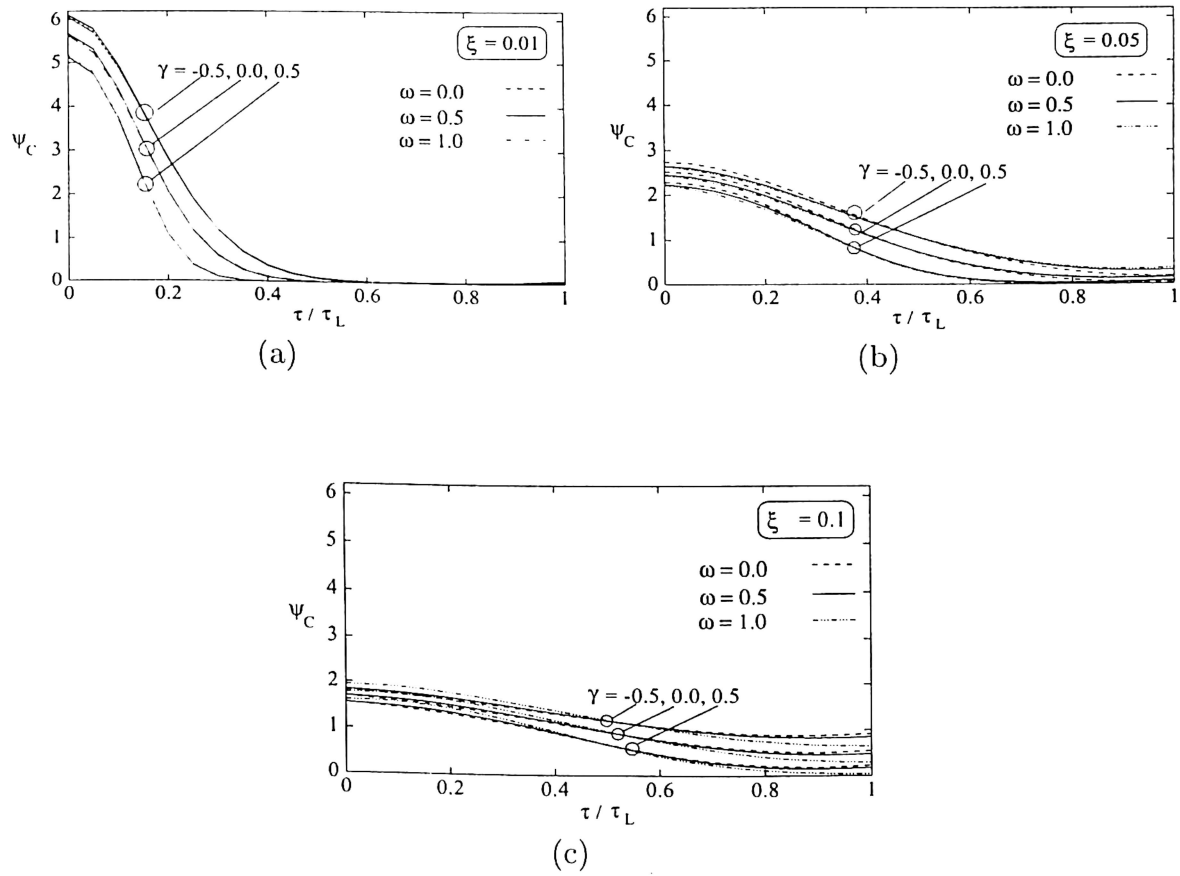


Figure 5.10: Effect of thermal conductivity parameter γ on conductive heat flux Ψ_C for different ω at time ξ (a) 0.01, (b) 0.05 and (c) 0.1.

In Figs. 5.10 and 5.11, for given values of ω, the effects of γ on Ψ_C and Ψ_R variations with τ/τ_L have been studied. In both the figures, these effects have been studied at three time levels, viz., $\xi = 0.01, 0.05$, and 0.1, respectively.

From Figs. 5.10(a)-(c), it is seen that at an early period, near the hot (south) boundary, Ψ_C values are high as compared with cold (north) boundary. This is due to sudden change in boundary condition at the south boundary from 0.5 to 1.0. But the north boundary is maintained at the same 0.5 temperature, so Ψ_C is almost zero near that boundary in the very early period. Further, the effect of scattering albedo ω is not prominent in the very early stage. In Figs. 5.11(a)-(c), Ψ_R variations have

TH-1868_004301

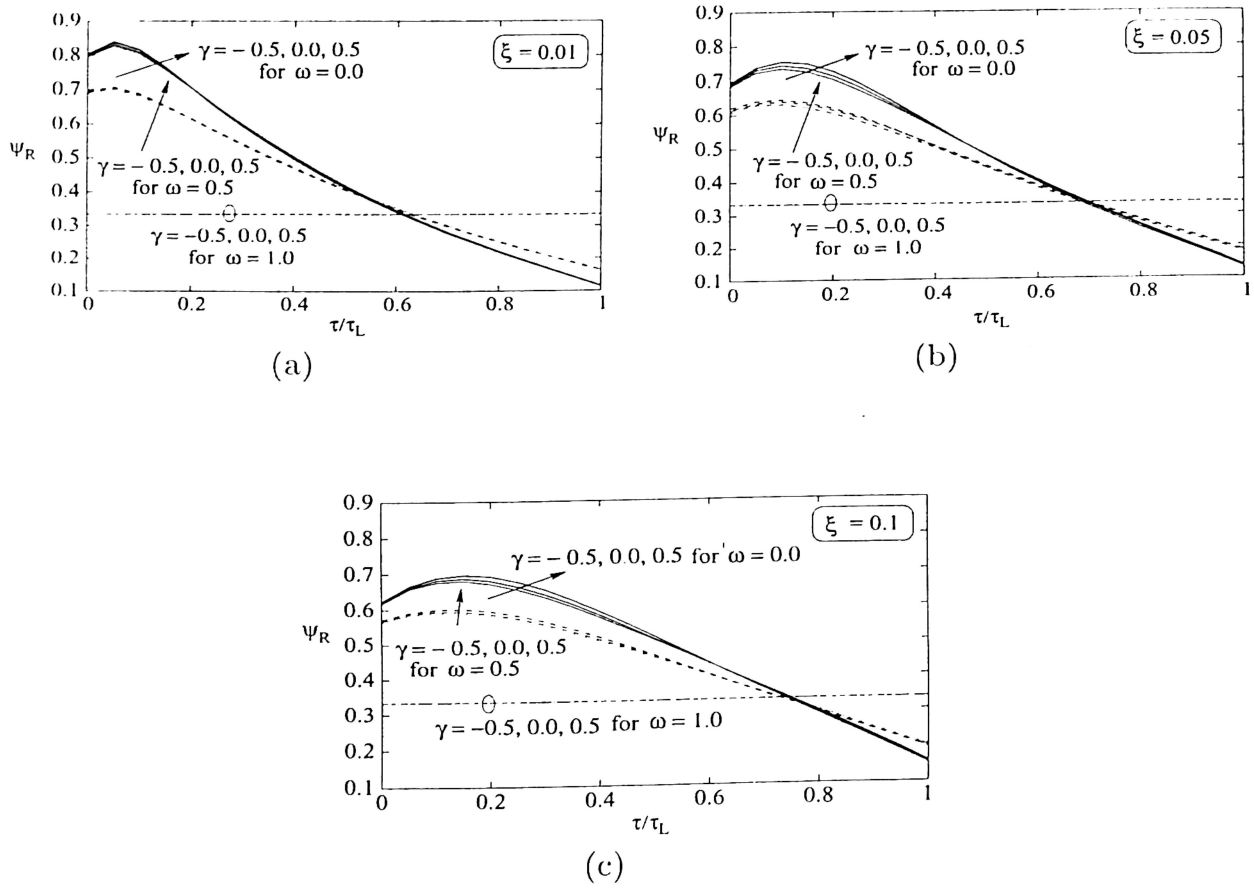


Figure 5.11: Effect of thermal conductivity parameter γ on radiative heat flux Ψ_R for different ω at time ξ (a) 0.01, (b) 0.05 and (c) 0.1.

been given. Here it is seen that at all times, compared with Ψ_C, all along τ/τ_L, Ψ_R values are much lower. It is observed from Figs. 5.11(a)-(c) that with increase in ω values, the effect of γ on Ψ_R decreases. For $\omega = 1$, at all time, Ψ_R value is the same all along τ/τ_L. This behavior is true, because for $\omega = 1$, divergence of radiative heat flux $\frac{\partial \Psi_R}{\partial \tau} = 0$ (see Eq. (5.3)), and hence for all γ, and at all time, Ψ_R will have constant value throughout the medium.

TH-1868_004301

5.4 Conclusions

Transient conduction-radiation problem with variable thermal conductivity was investigated for planar medium. Thermal conductivity was assumed to be vary linearly with temperature. The DTM was used to obtain the divergence of radiative heat flux information required for the energy equation. Using the time linearization technique, the non-linear energy equation was solved by an implicit scheme. For both transient and steady state situations, for the variable thermal conductivity, the effects of various parameters on temperature and heat flux distributions were studied. For the steady state situation, some sample results were compared with that available in the literature. The effects of variable thermal conductivity were found to be significant in some cases.

TH-1868_004301

Chapter 6

Conduction-Radiation Heat Transfer in Packed bed

6.1 Introduction

Heat transfer through packed bed has remained a subject of major interest in mechanical and chemical engineering. Most of the early studies with packed beds were related to low to moderate temperature ranges, thus requiring consideration of only the conduction and convection modes of heat transfer. However, in the recent past, the growing applications of the packed bed in energy conversion devices have necessitated the study of heat transfer in the packed bed [81, 83, 136, 137] at high temperatures. In such devices, therefore, consideration of radiation along with conduction and/or convection is essential.

Tien [83] and Kaviany and Singh [81] gave an overview of radiative heat transfer in packed beds. Drolen and Tien [138] predicted the radiative extinction characteristics of independent and dependent scattering in packed beds. Singh and

TH-1868_004301

Kaviany [139] simulated the radiative heat transfer through a packed bed of relatively large spherical particles by the Monte Carlo method and discussed the failure of independent theory. They showed that dependent properties of opaque spheres can be obtained from their independent properties by scaling the optical thickness without changing the albedo and phase function. Nasr et al. [140] measured the temperature-dependent effective thermal conductivity of packed bed of large particles and extracted the radiative conductivity from their experimental data. Kamiuto et al. [86] proposed a quasi-homogeneous model for packed-bed heat transfer at high temperatures. They studied combined conductive and radiative heat transfer within comparatively thin packed layers of cordierite bed and oxidized steel bed both theoretically and experimentally. They utilized a correlated-scattering theory for calculating the dependent properties of large particles from their independent properties. In addition, they also showed that results based on uncorrelated scattering theory always overestimate the total effective thermal conductivities of such beds. For the steady state situation, Wu and Chu [137] discussed the combined conductive and radiative heat transfer in a plane-parallel packed bed using Kamiuto's correlated scattering theory. They considered four different porosity distributions and studied their effects on total effective thermal conductivity and the radiative heat flux distributions. For solving the radiative part, they used P_3 approximation.

It is evident from the literature that for a packed bed, analysis of transient conduction combined with radiation has not been done. Further, it has been found that for dependent scattering, researchers have been using Kamiuto's correlated scattering theory [86] and Kaviany's scaling factor [81] independently, and no works has been reported for the comparative study of the two scattering theories. Also, even for the steady state situation, not enough investigations have been done on the predictions of total effective thermal conductivity, temperature and radiative, conductive and total heat flux distributions. The present work, thus aims at the transient analysis of combined conduction and radiation modes of heat transfer in a planar packed bed, comparing the two theories and studying the effects of various parameters on total effective thermal conductivity, temperature and heat flux distributions.

To solve the radiative part of the energy equation, in this work, the discrete trans-

TH-1868_004301

fer method (DTM) has been used. Energy equation has been solved using Euler's implicit finite difference scheme. For both steady and transient situations, the effects of effective thermal conductivity, bed depth to particle diameter ratio, scaled scattering albedo and conduction-radiation parameter are studied. For the purpose of validation, results are compared with the available results in the literature.

6.2 Formulation

Consideration is given to a planar packed bed bounded between two diffuse-gray surfaces (Fig. 3.1). The bed consists of large solid spheres. The packed spheres are opaque with diffuse-gray surfaces. The south and the north boundaries of the bed are at two different temperatures. For the variable porosity case, local porosity within the packed bed varies with distance from the boundary and is symmetric with respect to the mid plane of the packed bed.

Initially the entire system is at some temperature T_N and after some instant, the south boundary is maintained at a higher temperature T_S and the north boundary is maintained at T_N.

For the planar geometry under consideration, the energy equation for combined conduction and radiation is written as

$$\rho C_p \frac{\partial T}{\partial t} = \frac{\partial}{\partial z}\left(k_m \frac{\partial T}{\partial z}\right) - \frac{\partial q_R}{\partial z} \tag{6.1}$$

where k_m is the effective thermal conductivity of the packed bed. In dimensionless form, Eq. (6.1) is written as

$$\frac{\partial \theta}{\partial \xi} = \frac{\partial}{\partial \eta}\left[\lambda_m \frac{\partial \theta}{\partial \eta}\right] - \frac{1}{4N}\frac{\partial \Psi_R}{\partial \eta} \tag{6.2}$$

where η is the non-dimensional length, λ_m is the non-dimensional effective thermal conductivity. These dimensionless quantities are defined as

$$\theta = \frac{T}{T_S}, \xi = \frac{k_s t}{\rho C_p L^2}, \eta = \frac{z}{L}, \lambda_m = \frac{k_m}{k_s}, N = \frac{k_s}{4\sigma T_S^3 L}, \Psi_R = \frac{q_R}{\sigma T_S^4}$$

TH-1868_004301

Here, T_S is the temperature of the south (hot) boundary, L is the total geometric depth of the bed and k_s is the thermal conductivity of the dispersed phase of the packed bed.

For the problem under consideration, initial and the boundary conditions are given as

$$\begin{aligned} &\text{Initial condition:} \quad \theta(\eta, 0) = 0.5\ , \qquad \text{for } \ 0 \leq \eta \leq 1 \\ &\text{Boundary conditions:} \quad \theta(0, \xi) = \theta_S = 1.0\ , \\ &\qquad\qquad\qquad\qquad \theta(1, \xi) = \theta_N = 0.5\ ; \quad \text{for} \quad \xi > 0 \end{aligned}$$

6.2.1 Radiative Transfer Equations

The DTM has been used for finding the radiative calculations. The divergence of radiative heat flux, as found from Eq. (2.16), can be expressed for a planar medium as

$$\frac{\partial q_R}{\partial z} = \kappa \left[4\sigma T^4 - G\right]$$

In non-dimensional form the above equation can be expressed as

$$\frac{\partial \Psi_R}{\partial \eta} = (1-\omega)\beta(\eta) L \left[4\theta^4 - \frac{G^*}{\pi}\right] \tag{6.3}$$

where β is the scaled extinction coefficient, ω is the scaled scattering albedo and G^* is the dimensionless incident radiation. Here the extinction coefficient and the scattering albedo is called as scaled one as they are calculated based on different models of packed bed. It is important to mention here that in this present problem the gas is considered to be non-participating and the extinction and the scattering of the radiative intensity occurs because of the porous structures of the medium. The expressions for G^* and non-dimensional intensity i^* are same as in chapter (5).

For evaluation of intensity, source functions are required to be known. The dimensionless source function at any particular point in the ray direction Θ is found from

$$S^* = (1-\omega)\theta^4 + \frac{\omega}{2}\int_{\Theta=0}^{\pi} i^*\ p(\Theta', \Phi' \rightarrow \Theta, \Phi) \sin\Theta\ d\Theta \tag{6.4}$$

TH-1868_004301

where $p(\Theta', \Phi' \rightarrow \Theta, \Phi)$ is the approximating phase function. Since the packed bed is made of diffuse, opaque and gray spheres, phase function considered for this problem is a different one. This is given by

$$p(\Theta', \Phi' \rightarrow \Theta, \Phi) = \int_0^{2\pi} p(\psi) \frac{d\Phi}{2\pi}$$

where

$$p(\psi) = (8/3\pi)(\sin\psi - \psi\cos\psi)$$

and the scattering angle ψ is given by

$$\psi = \cos^{-1}[\cos\Theta\cos\Theta' + \sin\Theta\sin\Theta'\cos(\Phi - \Phi')]$$

In the above equation, Θ and Φ are the outgoing polar and azimuthal angles and Θ' and Φ' are the incoming polar and azimuthal angles. This phase function is similar to backward scattering as the more and more radiative energy scattered in a backward direction as it fall in this type of opaque, diffuse and gray spheres.

6.2.2 Porosity Distribution Function

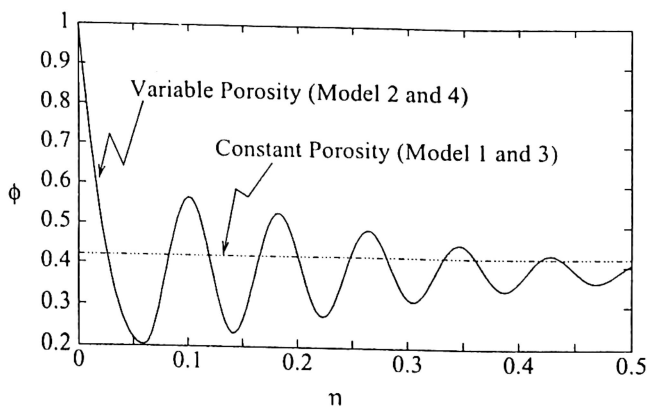


Figure 6.1: Porosity distribution along the thickness for the four models ($L/D_p = 10$)

For solving Eq. (6.2), values of the effective thermal conductivity and the optical thickness of the packed bed are required. These two parameters are functions of the porosity. Thus, porosity of the packed bed has to be known beforehand. In the present work, as shown in Fig. 6.1, two cases of constant porosity and two cases of variable porosity are considered. These are the following:

TH-1868_004301

Model 1: Constant porosity $\phi = \phi_\infty = 0.39$

Model 2: Variable porosity

for $0.0 \leq \zeta \leq 0.6$,

$$\phi(\zeta) = 1 - 3.10036\zeta + 3.70243\zeta^2 - 1.24612\zeta^3,$$

for $0.6 \leq \zeta \leq 0.5\zeta_0$,

$$\phi(\zeta) = -0.1865 \exp(-0.22{\zeta_1}^{1.5}) \cos(7.66\zeta_1) + 0.39,$$

where $\zeta = z/D_p$, $\zeta_0 = L/D_p$ and $\zeta_1 = \zeta - 0.6$. Here D_p is the mean diameter of the packed bed.

Model 3: Constant porosity $\phi = \phi_\infty = 0.39$.

Model 4: Variable porosity with the same distribution of porosity as in Model 2.

It should be noted that the porosity models 1 and 2 use Kamiuto's correlated scattering theory [86](see Eq. (6.6)) and model 3 and 4 use scaling factors derived by Kaviany [139] (see Eq. (6.8)). Porosity model 1 has been used in [137], whereas models 2 and 3 have been used in [86, 87, 137] and [139], respectively. It is to be further noted that the porosity model 2 is based on Ridgway-Tarbuck's [141] experimental data.

6.2.3 Effective Thermal Conductivity

Since the medium consists of two different phases viz. the material of the packed bed and the fluid surrounding it, for calculating the effective thermal conductivity both have to be considered. The following expression from references [86, 137] is used for calculating the effective thermal conductivity.

$$\lambda_m(\eta) = (k_a/k_s)\left[(\kappa - 1)\kappa^{\frac{1}{3}}\phi[((\sqrt{A} - 1)/2)^{\frac{1}{3}} - ((\sqrt{A} + 1)/2)^{\frac{1}{3}}] + \kappa\right] \qquad (6.5)$$

where $A = 1 + 4/27\phi^3(\kappa - 1)^3/\kappa^2$, and $\kappa = k_s/k_a$. Here k_s and k_a are thermal conductivities of the dispersed and continuous phases of a packed bed, respectively.

TH-1868_004301

6.2.4 Radiative Properties

The calculation of radiative properties in a porous medium is a very difficult task. In case of a packed bed, fortunately because of its somewhat regular structures, radiative properties can be calculated based on some theories as discussed below. In all these analyses, the medium is considered to be homogeneous.

According to the correlated-scattering theory of Kamiuto [86], the scaled radiative properties for a packed bed can be described as

$$\begin{aligned} \tau(\eta) = \beta(\eta)L &= \frac{\pi {D_p}^2 n_p L(2\gamma_2 - 1)}{4} \\ &= 1.5(L/D_p)(1-\phi)(2\gamma_2 - 1) \end{aligned} \tag{6.6}$$

and

$$\omega = \rho_s \tag{6.7}$$

where $\gamma_2 = 1 + 1.5(1-\phi) - (3/4)(1-\phi)^2$, τ is the scaled optical thickness, β is the scaled extinction coefficient, ρ_s is the hemispherical reflectivity of a packing sphere, and n_p is the number density of packed spheres.

According to Kaviany's theory [81], the scaled radiative properties for a packed bed can be described as

$$\tau(\eta) = \beta(\eta)L = 1.5(1-\phi)\frac{S_r L}{D_p} \tag{6.8}$$

The values of scaling factor S_r is given as

$$S_r = 1 + 1.84(1-\phi) - 3.15(1-\phi)^2 + 7.20(1-\phi)^3, \qquad \text{for} \quad \phi > 0.3$$

6.2.5 Heat Flux

The dimensionless total heat flux across a packed bed is calculated from

$$\Psi_T = 4N\left(-\lambda_m \frac{d\theta}{d\eta}\right) + \Psi_R = -K_{\text{eff}}(\eta)\frac{d\theta}{d\eta} \tag{6.9}$$

TH-1868_004301

where K_{eff} represents the total effective thermal conductivity and the dimensionless radiative heat flux Ψ_R is given by

$$\Psi_R = 2\int_0^{\pi} I^*(\Theta)\sin\Theta\cos\Theta\, d\Theta \tag{6.10}$$

Another parameter, mean total effective thermal conductivity of a packed bed between the two boundaries, is calculated from

$$\overline{K}_{\text{eff}} = \int_0^1 K_{\text{eff}}\, d\eta \tag{6.11}$$

6.2.6 Numerical Methods

The energy equation (Eq. (6.2)) is solved by Euler's backward time-implicit finite difference scheme. The radiation term is evaluated at known time levels using the DTM. The resulting set of equations for temperature forms a tridiagonal matrix which is solved by the Thomas algorithm. For finite difference calculations, the solution domain is divided into 300 control volumes. Sixty four rays and 300 control volumes have been found to give correct information for the radiative part, and the same number of control volumes have also been used for the finite difference part. Steady state conditions have been found when the temperature difference between the two adjacent time levels at each control volume points does not exceed the value 0.00001, i.e.

$$|\theta^{(\xi)} - \theta^{(\xi+1)}| < 0.00001$$

6.3 Results and Discussion

Steady State Results

To show the accuracy of the present work, in Fig. 6.2, temperature results from the present work are compared with the experimental results of Kamiuto et al. [86].

TH-1868_004301

These comparisons are for $\kappa = 781.7$, conduction-radiation parameter $N = 2.95$, scaled scattering albedo $\omega = 0.35$ and $L/D_p = 9.82$. It is seen that the results from models 2 and 4, which represent the variable porosity case, compare very well with the experimental results. The results found from models 1 and 3 lead to slight under prediction.

In Figs. 6.3(a)-(e), the effects of κ on effective thermal conductivity λ_m, total effective thermal conductivity K_{eff}, radiative heat flux Ψ_R, conductive heat flux Ψ_C and total heat flux Ψ_T are shown, respectively. In Fig. 6.3(a), variation of effective thermal conductivity λ_m along the bed depth η is shown. For models 1 and 2, for $N = 0.1$, $\omega = 0.5$ and $L/D_p = 20$, these variations are shown for three different values of $\kappa(= 10, 100, 1000)$.

Since λ_m is a function of κ and ϕ, and models 1 and 3 are the constant porosity cases (ϕ=constant), the λ_m values for the two models are the same. It is seen from Fig. 6.3(a) that for model 2, variation of λ_m near the two boundaries is significant, and this fluctuation dampens towards the centerline as distance from the boundaries

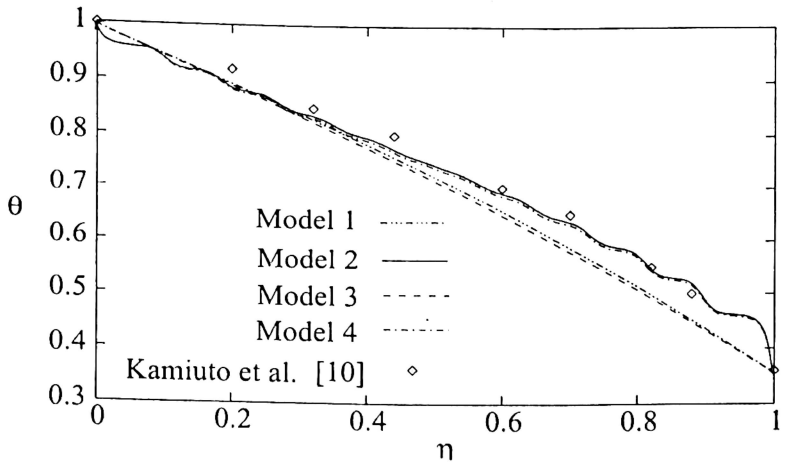


Figure 6.2: Comparison of dimensionless temperature θ with experimental results from reference [86]

TH-1868_004301

increases. In the central portion, where the bed is homogeneous, λ_m is constant and equal to its value for the model 1. Further it is seen that with increase of κ,

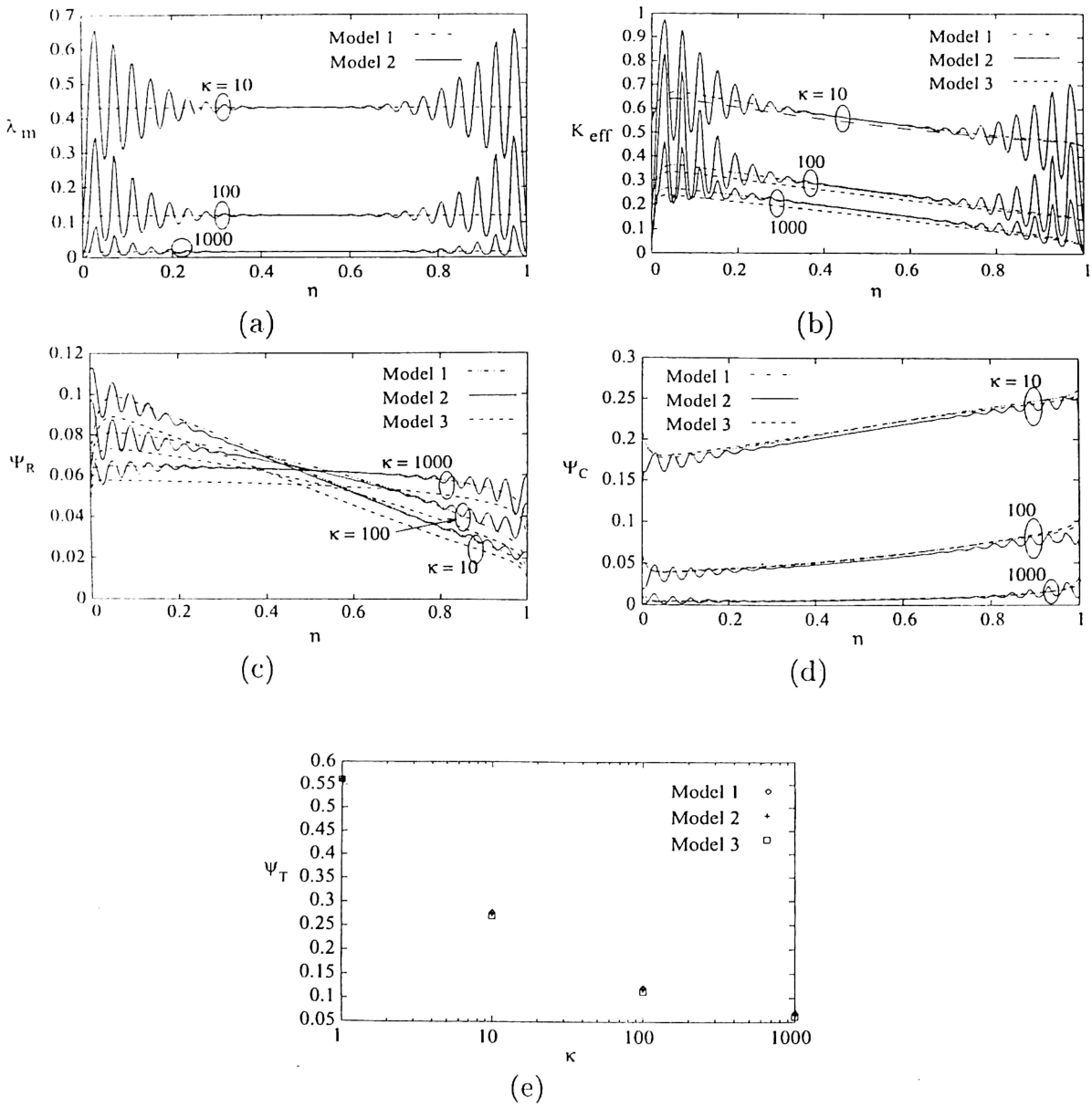


Figure 6.3: Effects of κ on variations of (a) effective thermal conductivity λ_m, (b) total effective thermal conductivity K_{eff}, (c) radiative heat flux Ψ_R, (d) conductive heat flux Ψ_C and (e) total heat flux Ψ_T with η when $\omega = 0.5$, $N = 0.1$ and $L/D_p = 20$.

TH-1868_004301

These comparisons are for $\kappa = 781.7$, conduction-radiation parameter $N = 2.95$, scaled scattering albedo $\omega = 0.35$ and $L/D_p = 9.82$. It is seen that the results from models 2 and 4, which represent the variable porosity case, compare very well with the experimental results. The results found from models 1 and 3 lead to slight under prediction.

In Figs. 6.3(a)-(e), the effects of κ on effective thermal conductivity λ_m, total effective thermal conductivity K_{eff}, radiative heat flux Ψ_R, conductive heat flux Ψ_C and total heat flux Ψ_T are shown, respectively. In Fig. 6.3(a), variation of effective thermal conductivity λ_m along the bed depth η is shown. For models 1 and 2, for $N = 0.1$, $\omega = 0.5$ and $L/D_p = 20$, these variations are shown for three different values of $\kappa(= 10, 100, 1000)$.

Since λ_m is a function of κ and ϕ, and models 1 and 3 are the constant porosity cases (ϕ=constant), the λ_m values for the two models are the same. It is seen from Fig. 6.3(a) that for model 2, variation of λ_m near the two boundaries is significant, and this fluctuation dampens towards the centerline as distance from the boundaries

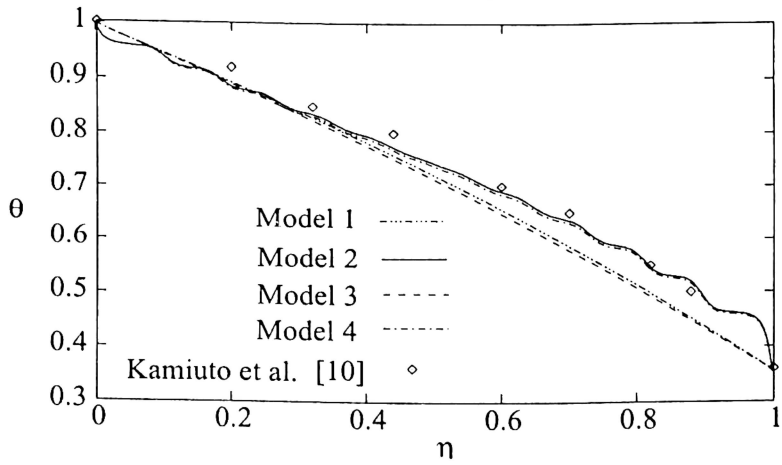


Figure 6.2: Comparison of dimensionless temperature θ with experimental results from reference [86]

TH-1868_004301

increases. In the central portion, where the bed is homogeneous, λ_m is constant and equal to its value for the model 1. Further it is seen that with increase of κ,

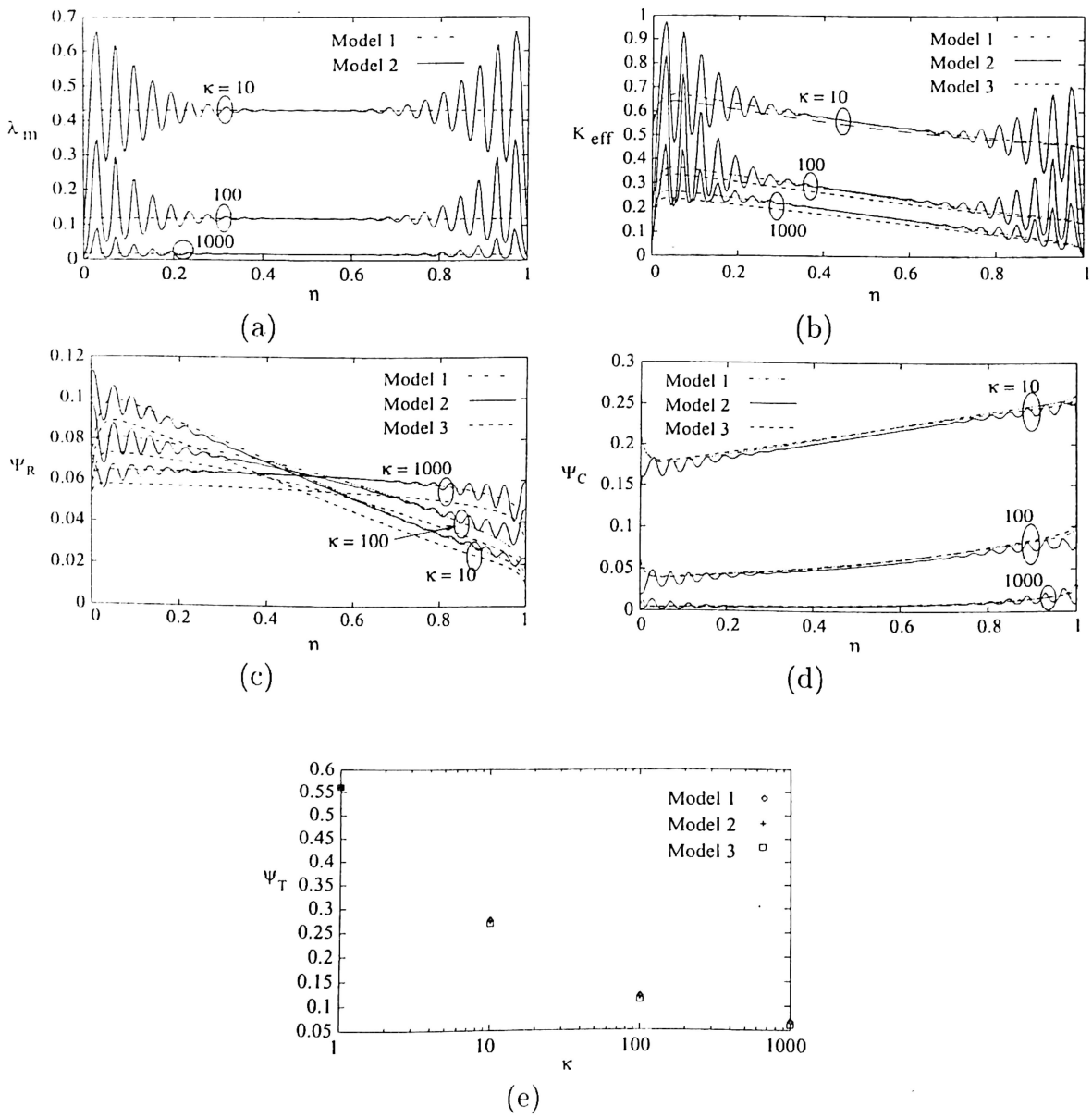


Figure 6.3: Effects of κ on variations of (a) effective thermal conductivity λ_m, (b) total effective thermal conductivity K_{eff}, (c) radiative heat flux Ψ_R, (d) conductive heat flux Ψ_C and (e) total heat flux Ψ_T with η when $\omega = 0.5$, $N = 0.1$ and $L/D_p = 20$.

TH-1868_004301

fluctuations in λ_m decrease near the boundaries and at any location η, higher the value of κ, lower is the value of λ_m.

Figure 6.3(b) shows the effect of κ on total effective thermal conductivity K_{eff}. It is seen that the values of K_{eff} decrease with increase in κ. κ is the ratio of the thermal conductivity of the dispersed phase to that of the continuous phase. If the thermal conductivity of the continuous phase is fixed, increase in κ could be treated as increase in the thermal conductivity of the dispersed phase. Therefore, increase

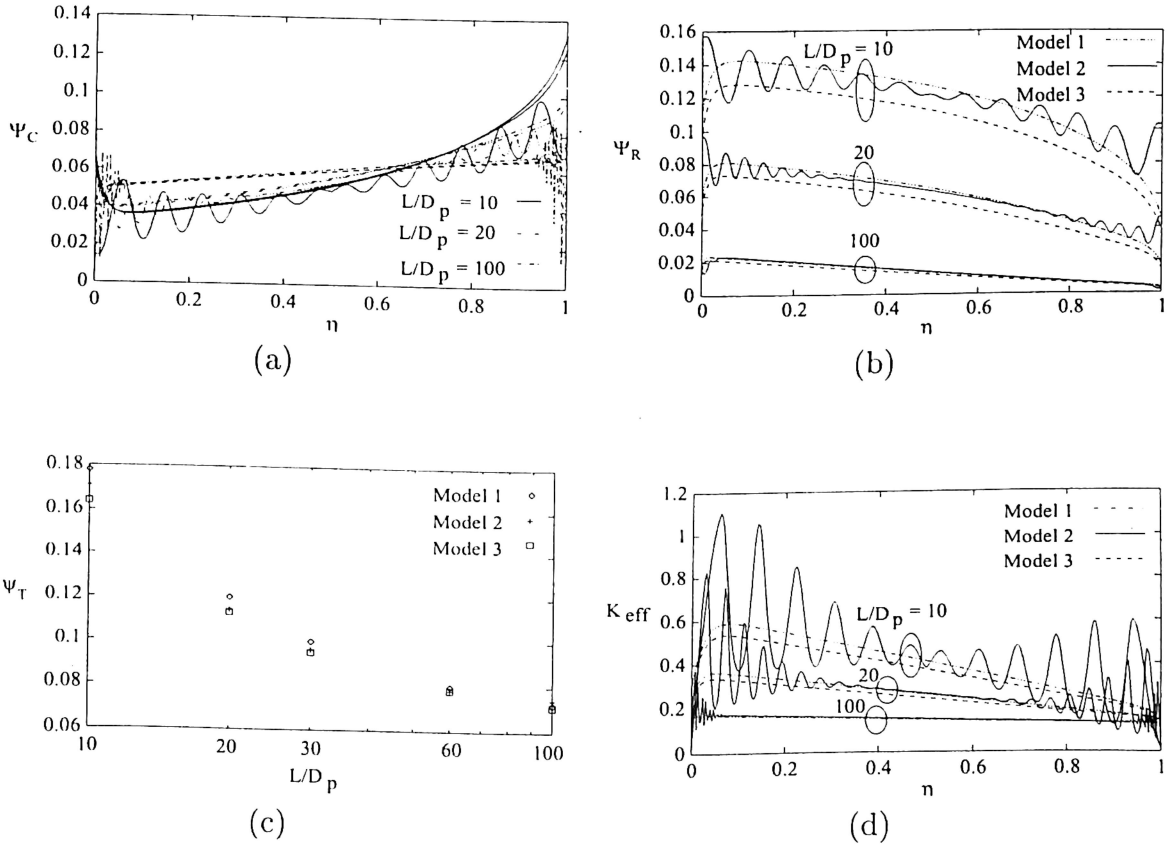


Figure 6.4: Effects of L/D_p ratio on variations of (a) conductive heat flux Ψ_C, (b) radiative heat flux Ψ_R, (c) total heat flux Ψ_T and (d) total effective thermal conductivity K_{eff} with η when $\omega = 0.5$, $N = 0.1$ and $\kappa = 100$.

TH-1868_004301

in κ leads to a decrease in λ_m as well as decrease in K_{eff}.

Effects of κ on radiative heat flux Ψ_R and the conductive heat flux Ψ_C are shown in Figs. 6.3(c), 6.3(d), respectively. For all values of κ, Ψ_R is more near the hot boundary ($\eta = 0$) than near the cold boundary ($\eta = 1$). However, the opposite is the case for variations of Ψ_C. Further, it is observed from these figures that the effect of κ is more prominent on Ψ_C than on Ψ_R. Increase of κ can also be treated as the decrease in the thermal conductivity of the continuous phase, which in turn lowers Ψ_C. Decrease in the value of Ψ_C with the increase in κ finally decreases the total heat flux Ψ_T (Fig. 6.3(e)). Results for all the models are almost closed to each

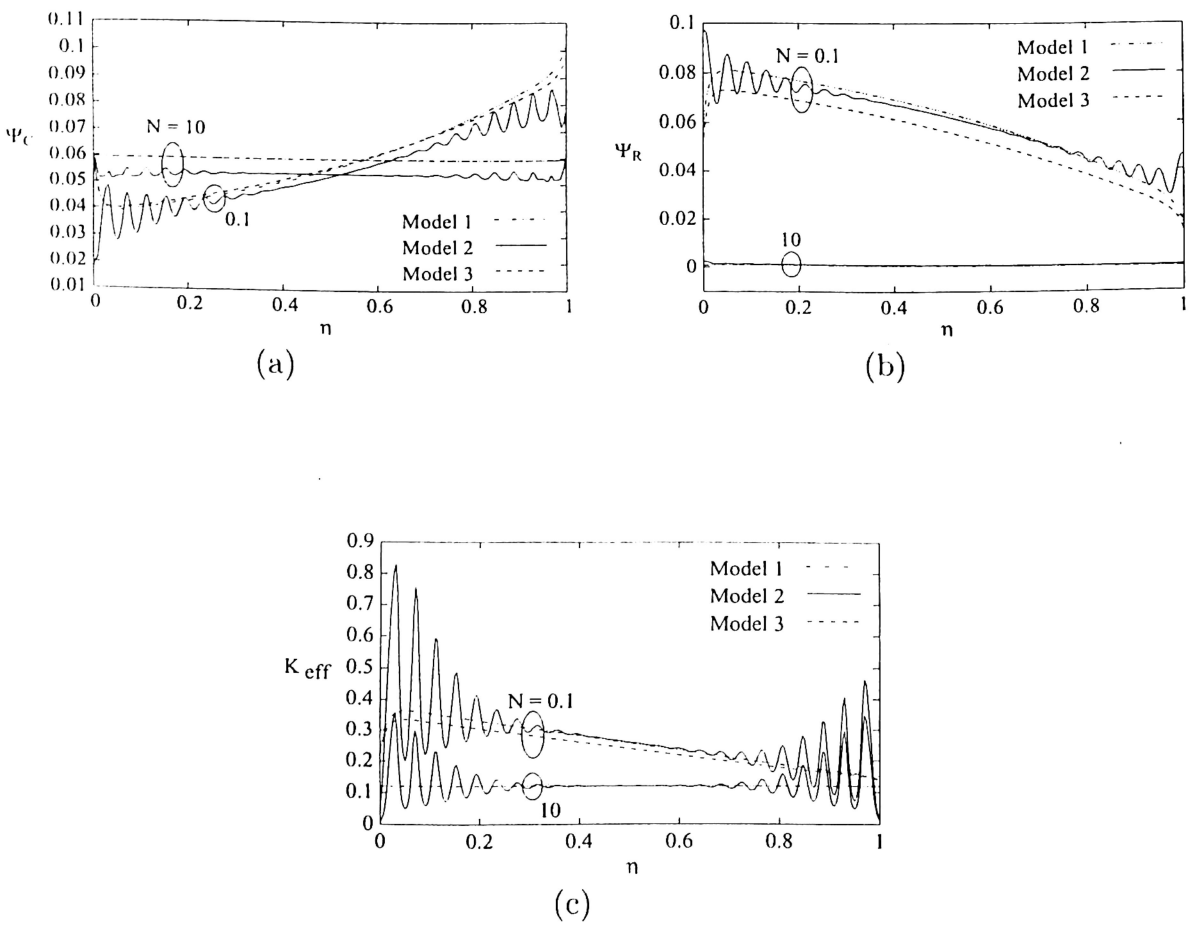


Figure 6.5: Effects of conduction-radiation parameter N on variations of (a) conductive heat flux Ψ_C, (b) radiative heat flux Ψ_R, and (c) total effective thermal conductivity K_{eff} with η when $\omega = 0.5$, $L/D_p = 20$. and $\kappa = 100$.

TH-1868_004301

other.

The edge effects on conductive heat flux Ψ_C, radiative heat flux Ψ_R, total heat flux Ψ_T and total effective thermal conductivity K_{eff} are shown in Figs. 6.4(a)-(d) for $\kappa = 100$, $\omega = 0.5$ and $N = 0.1$. The lower value of L/D_p means presence of large spheres (D_p is large) whereas its higher value signifies presence of small spheres. So, it can be thought physically that presence of large spheres can cause more extinction of radiative energy, hence increases the optical thickness. That can also be explained with the Eq. (6.6) and (6.8). The values for the ratio of the bed thickness to particle diameter L/D_p are taken as 10, 20 and 100. In Figs. 6.4(a) and 6.4(b), the effects

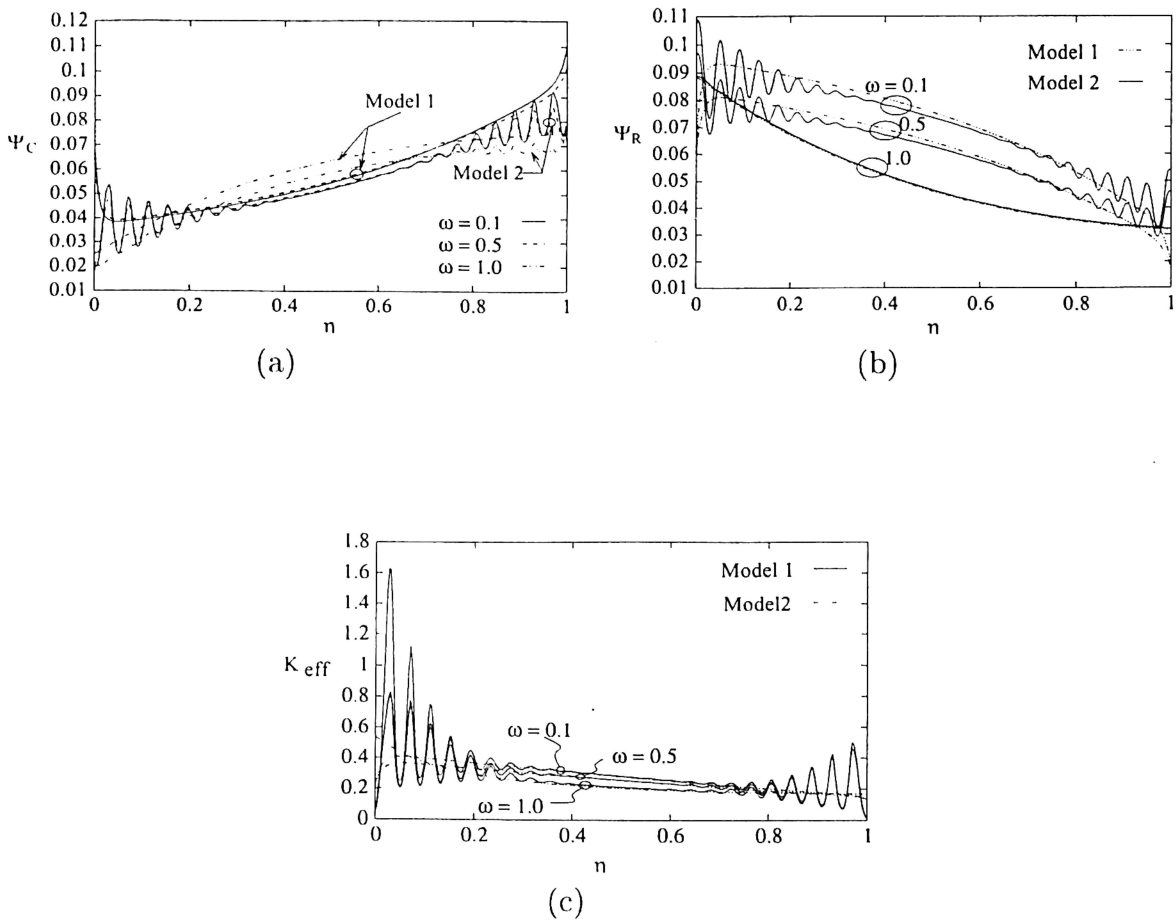


Figure 6.6: Effects of scaled scattering albedo ω on variations of (a) conductive heat flux Ψ_C, (b) radiative heat flux Ψ_R, and (c) total effective thermal conductivity K_{eff} with η when $N = 0.1$, $L/D_p = 20$ and $\kappa = 100$.

TH-1868_004301

of L/D_p ratio on Ψ_C and Ψ_R are shown, respectively. It is seen that the effect of L/D_p is greater on Ψ_R. For smaller values of L/D_p ratio, Ψ_R has a high value. This is because, as given by Eq. (6.6) and (6.8), an increase in L/D_p means increase in the optical thickness, which results in increased absorption from the medium, which in turn causes reduced radiation effects.

Since for different values of L/D_p, the values Ψ_C do not change much, the decrease in Ψ_T values with L/D_p (Fig. 6.4(c)) is primarily due to decrease in Ψ_R with L/D_p.

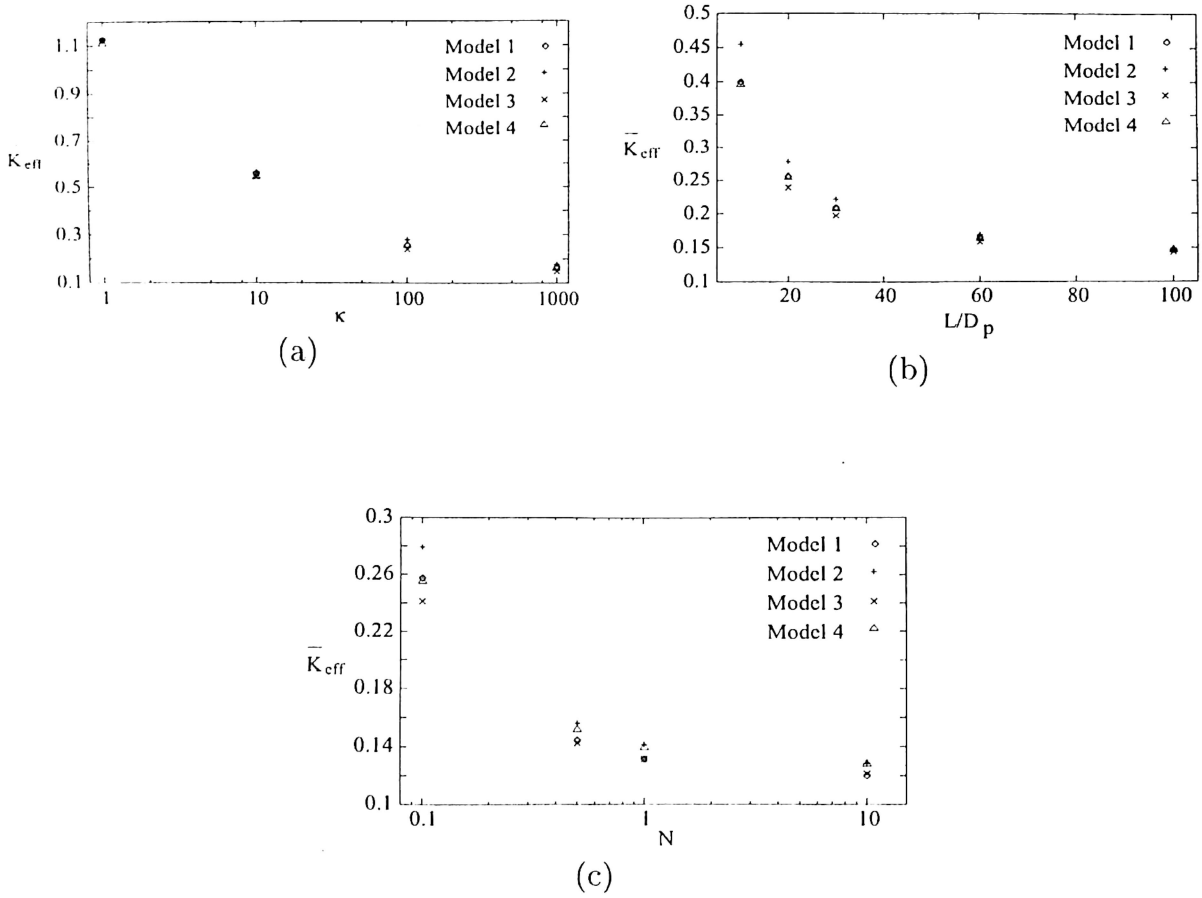


Figure 6.7: (a) Mean total effective thermal conductivity for different models with variation of κ when $\omega = 0.5$, $N = 0.1$ and $L/D_p = 20$ (b) Mean total effective thermal conductivity for different models with variation of L/D_p ratio when $\omega = 0.5$, $N = 0.1$ and $\kappa = 100$ (c) Mean total effective thermal conductivity for different models with variation of N when $\omega = 0.5$, $\kappa = 100$ and $L/D_p = 20$.

TH-1868_004301

Because of the increase in Ψ_T for lower L/D_p ratio, the total effective thermal conductivity K_{eff} also increases for lower values (Fig. 6.4(d)) of L/D_p.

For the three porosity models, results are different for the lower values of L/D_p. Further, for model 2, the amplitudes of oscillations are more for lower values of L/D_p. For a given value of L/D_p, oscillations dampen towards the mid-plane.

Figures 6.5(a)-(c) illustrate the effects of conduction-radiation parameter N on Ψ_C, Ψ_R and K_{eff}, respectively. For $\kappa = 100$, $\omega = 0.5$ and $L/D_p = 20$, these results are presented for a lower ($N = 0.1$) and a higher ($N = 10$) values of N.

Conduction-radiation parameter N represents relative contributions of conduction and radiation. For lower values of N, problem is radiation dominated. Therefore, as seen from Fig. 6.5(b), radiative heat flux Ψ_R is greater for $N = 0.1$. However, as seen from Fig. 6.5(a), for $N = 0.1$, Ψ_C is less near the south (hot) boundary and is more near the north (cold) boundary. However, this difference between the values at the two boundaries decreases with the higher values of N. For $N = 10$, this is also observed for Ψ_R.

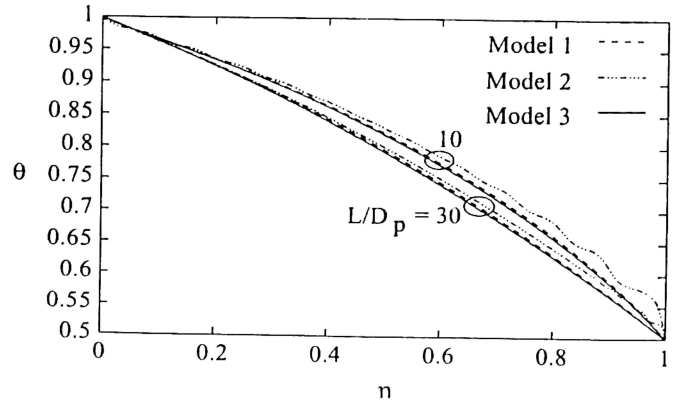
Since the effective thermal conductivity λ_m is constant (as κ is constant), for $N = 0.1$ and 10, there is not much difference in the average values of Ψ_C. However, same is not the case for Ψ_R.

It is seen from Fig. 6.5(c) that K_{eff} is greater for lower values of N. This trend is because of the fact that for lower values of N, Ψ_R is greater, and hence the total heat flux is also greater.

Effects of the scaled scattering albedo ω on Ψ_C, Ψ_R and k_{eff} are shown in Figs. 6.6(a)-(c). For $\kappa = 100$, $N = 0.1$ and $L/D_p = 20$, these results are presented for $\omega = 0.1, 0.5$ and 1. It is seen from these figures that for model 2, for lower values of ω, amplitudes of oscillations are greater. However, when $\omega = 1$, i.e., when the bed is fully reflecting, these fluctuations are dampened. Further, in the central region, ω has more effect on Ψ_R.

TH-1868_004301

Figures 6.7(a)-(c) show the variations of the mean total effective thermal conductivity $\overline{K}_{\text{eff}}$ with κ, L/D_p ratio and N, respectively for four models. $\overline{K}_{\text{eff}}$ is the average of total effective thermal conductivity over the whole depth (from $\eta = 0$ to 1). Like total heat flux, its values (Fig. 6.4(e) and Fig. 6.5(c)) decrease with increase in κ and L/D_p ratio, respectively. As seen from Fig. 6.7(a), for the variations in κ, in the entire range, values from the four models are close to each other. However, as seen from Fig. 6.7(b), model 2 yields higher values than the three other models for the lower L/D_p ratio. The value of $\overline{K}_{\text{eff}}$ with different conduction-radiation parameter



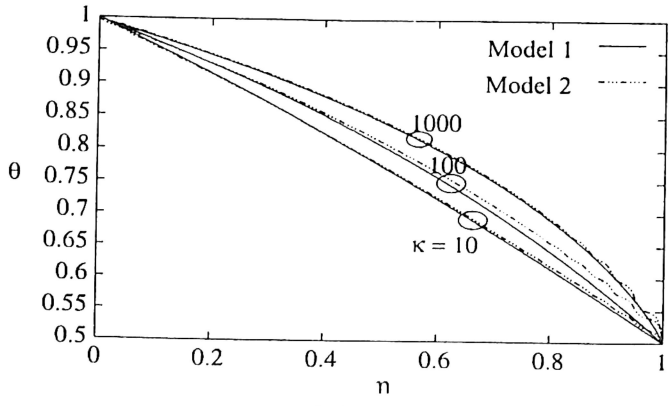


Figure 6.8: Variations of temperature θ with geometric depth η for different models with the effects of (a) L/D_p ratio when $\omega = 0.5$, $N = 0.1$ and $\kappa = 100$ and (b) κ when $\omega = 0.5$, $N = 0.1$ and $L/D_p = 20$.

TH-1868_004301

N is shown in the Fig. 6.7(c). It is seen that for radiation dominated situation (small N), the four models differ from each other.

For the three models, in Figs. 6.8(a) and 6.8(b), the effects of L/D_p ratio and κ on steady state temperature distribution θ along the bed depth η are shown respectively. For $L/D_p = 10$ and 30, in Fig. 6.8(a), θ variation with η are given for $\omega = 0.5$, $N = 0.1$ and $\kappa = 100$. It is seen from Fig. 6.8(a) that for higher values of L/D_p ratio, θ profiles tend to become linear. Since at higher values of L/D_p ratio, radiation effect decreases (Fig. 6.4(b)), the temperature profile almost become a pure conduction temperature profile.

For the effects of κ on θ variations (Fig. 6.8(b)), results are shown for $\omega = 0.5$, $N = 0.1$ and $L/D_p = 20$. It is seen here that for lower values of κ, temperature profiles tend to become linear. This is because, for the lower values of κ, conduction effect is greater (Fig. 6.3(d)) and thus the profile tends to become linear.

Transient Results

Transient results for temperature and conduction, radiation and total heat fluxes are given in this section. Temperature variations at two different locations, viz. $\eta = 0.25$ and 0.75 are chosen. Location $\eta = 0.25$ is close to the south (hot) boundary and the location $\eta = 0.75$ is near the north (cold) boundary.

In Fig. 6.9(a), the effect of κ on dimensionless temperature θ is shown. It is seen that at both locations, in the transient state, temperature is higher for lower values of κ, and as it reaches the steady state, opposite trends are observed. For higher values of κ, time to reach steady state is greater.

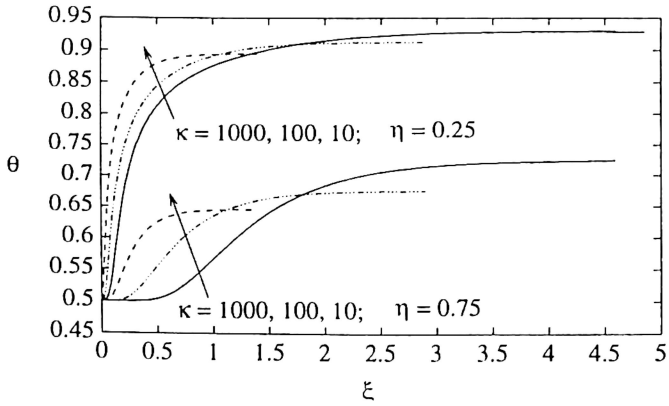
Effect of L/D_p ratio on transient temperature θ is shown in Fig. 6.9(b). It is seen that at both locations, at all instants, θ is greater for the lower values of L/D_p. Further, it is observed that for the lower values of L/D_p, steady state is reached quickly. This trend is for the reason that when L/D_p ratio is less, radiation effect becomes more, and as a result, steady state is reached quickly. The above results

TH-1868_004301

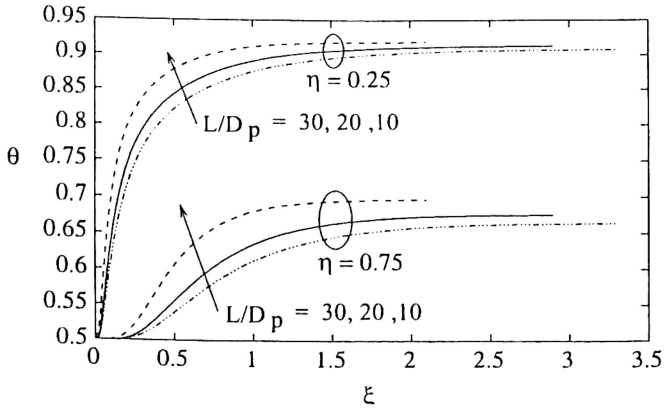
have been plotted only for the model 1.

Variations of total heat flux Ψ_T with non-dimensional time ξ for different situations are shown in Fig 6.10. For these results, porosity models 1 and 2 are considered. Three different locations, viz. $\eta = 0.25$, 0.5 and 0.75 are chosen for calculating the fluxes.

In Fig. 6.10(a), effect of κ on Ψ_T is examined. The values of ω, N and L/D_p are



(a)



(b)

Figure 6.9: Effects of (a) κ when $\omega = 0.5$, $N = 0.1$ and $L/D_p = 20$ and (b) L/D_p ratio when $\omega = 0.5$, $N = 0.1$ and $\kappa = 100$ on transient temperature θ distributions at locations $\eta = 0.25$ and 0.75.

TH-1868_004301

taken as 0.5, 0.1 and 20 respectively. Like the temperature plots, here it is seen that with increase of κ, time to reach steady state is delayed. It is also seen that with decrease of κ, Ψ_T increases.

In Fig. 6.10(b), the effect of L/D_p ratio on Ψ_T is observed. The values of ω, N and κ are taken as 0.5, 0.1 and 100, respectively. For the lower values of L/D_p, Ψ_T is always greater, and steady state is also reached quickly. In Fig. 6.10(c), the effect of conduction-radiation parameter N on Ψ_T is shown for $\omega = 0.5$, $\kappa = 100$ and $L/D_p = 20$. Here it is seen that for lower values of N, steady state is reached quickly.

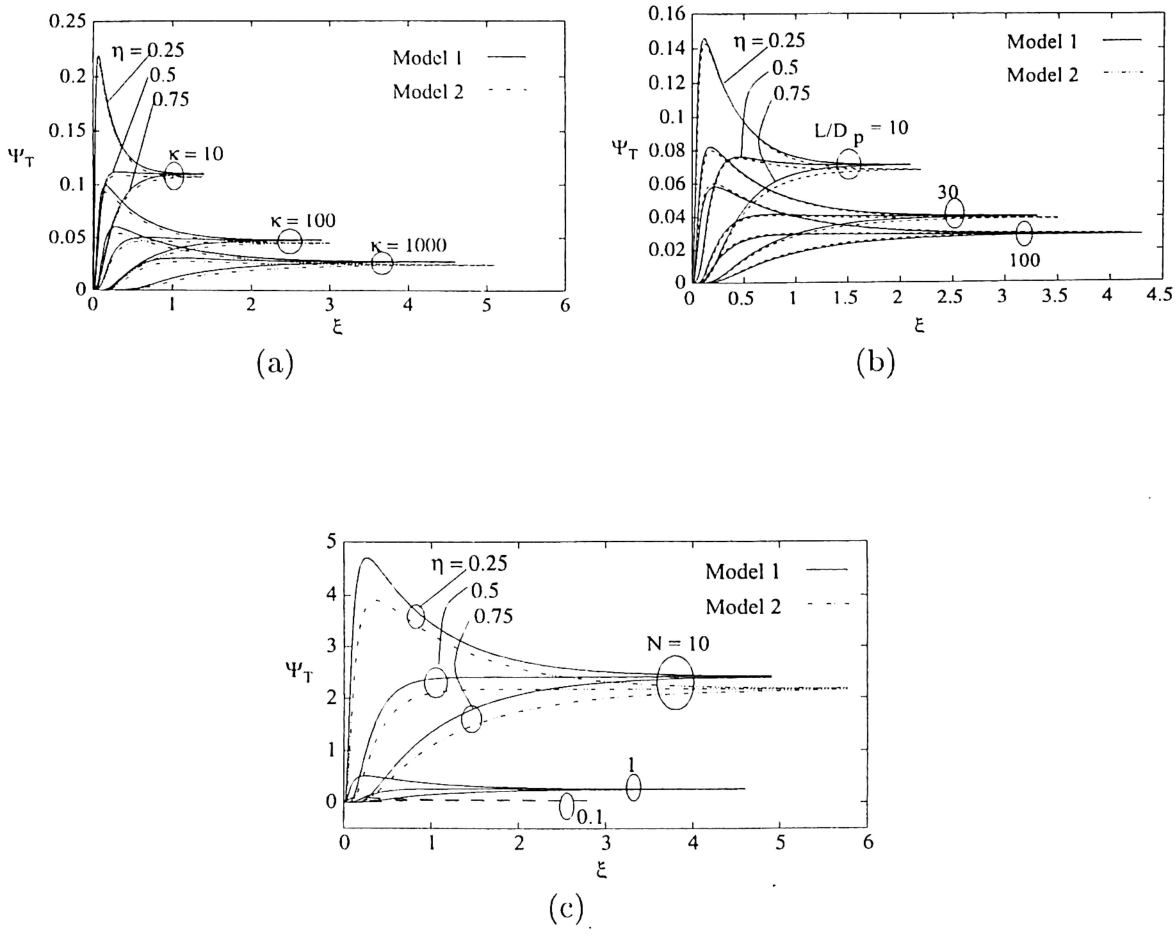


Figure 6.10: Effects of (a) κ when $\omega = 0.5$, $N = 0.1$ and $L/D_p = 20$, (b) L/D_p ratio when $\omega = 0.5$, $N = 0.1$ and $\kappa = 100$ and (c) N when $\omega = 0.5$, $L/D_p = 20$ and $\kappa = 100$ on transient total heat flux Ψ_T distributions at locations $\eta = 0.25$, 0.5 and 0.75.

TH-1868_004301

This is because, smaller values of N represent a radiation dominated situation, and when radiation is dominant, steady state is attained quickly.

It is seen from the above figures that for all three parameters, viz. κ, L/D_p, and N, for a given set of values, at all three locations, as the steady state is approached, the total heat flux Ψ_T converges to the same value. This is true, because in the steady state, the divergence of the total heat flux ($\frac{d\Psi_T}{d\eta}$) equals zero. Further it is observed that, in the transient state, at location $\eta = 0.25$, Ψ_T is very high and then slowly decreases as it reaches the steady state, and close to the cold boundary ($\eta = 0.75$),

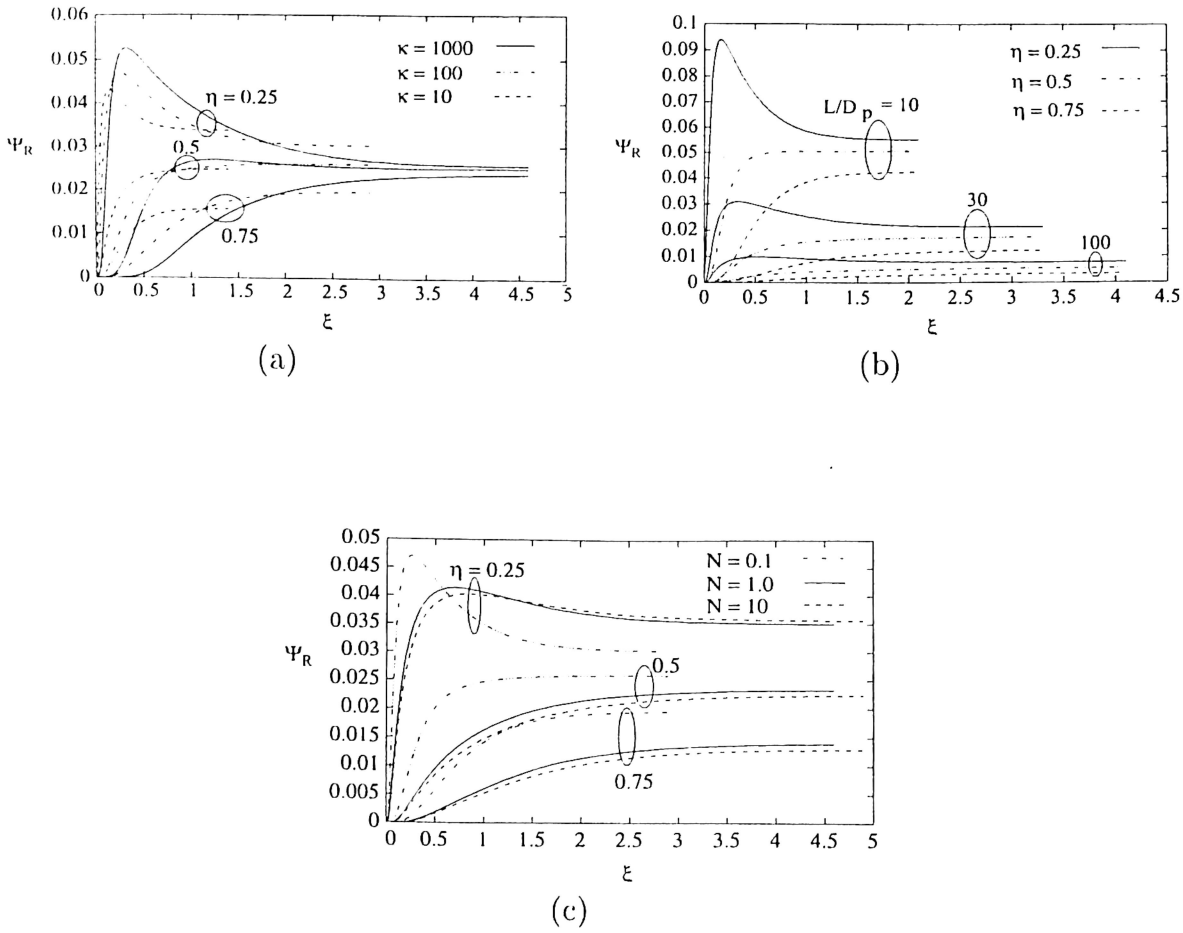
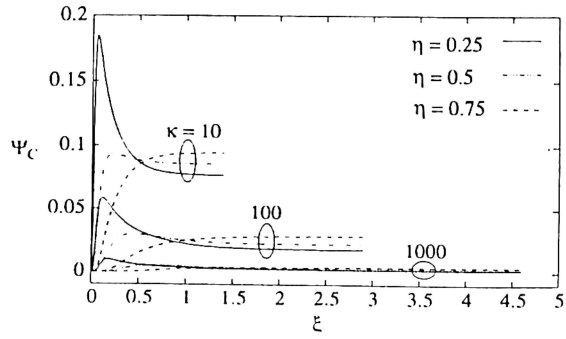


Figure 6.11: Effects of (a) κ when $\omega = 0.5$, $N = 0.1$ and $L/D_p = 20$, (b) L/D_p ratio when $\omega = 0.5$, $N = 0.1$ and $\kappa = 100$ and (c) N when $\omega = 0.5$, $L/D_p = 20$ and $\kappa = 100$ on transient radiative heat flux Ψ_R distributions at locations $\eta = 0.25$, 0.5 and 0.75.

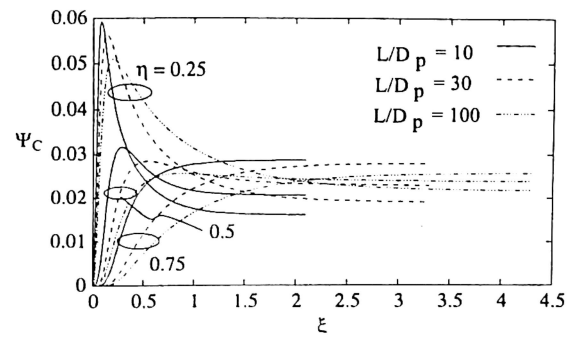
TH-1868_004301

Ψ_T continuously increases as long as it reaches steady state. At all the locations, at all times, results from models 1 and 2 are very close to each other with the effects of κ and L/D_p. However, as seen from Fig. 6.10(c), for the conduction dominated situation ($N = 10$), at all times, Ψ_T from model 1 is always higher than that from model 2.

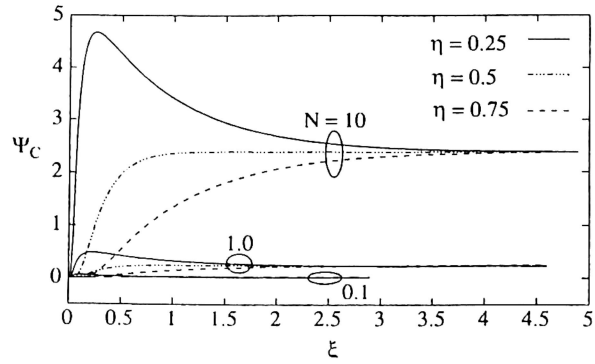
For parameters same as that for the results presented in Figs. 6.10(a)-(c), temporal variations of Ψ_R and Ψ_C are shown in Figs. 6.11 and 6.12, respectively. Here, these variations are given for the porosity model 1.



(a)



(b)



(c)

Figure 6.12: Effects of (a) κ when $\omega = 0.5$, $N = 0.1$ and $L/D_p = 20$, (b) L/D_p ratio when $\omega = 0.5$, $N = 0.1$ and $\kappa = 100$ and (c) N when $\omega = 0.5$, $L/D_p = 20$ and $\kappa = 100$ on transient conductive heat flux Ψ_C distributions at locations $\eta = 0.25$, 0.5 and 0.75.

TH-1868_004301

Comparison of Figs. 6.11(a) and 6.12(a) shows that for a given value of κ, the major contribution to Ψ_T comes from conduction. However, the reverse is the trend for a given value of the L/D_p ratio. With regard to the effect of N, as expected, for higher values of N, maximum contribution is from conduction.

6.4 Conclusions

Combined conduction and radiation heat transfer in a planar packed bed was investigated for steady as well as transient situations. Both constant and variable porosity distributions were assumed. The DTM was used for solving the radiative part of the energy equation. For the dependent scattering, comparative study of both Kamiuto's correlated scattering theory and Kaviany's scaling factors was made. Models 2 and 4 of variable porosity were found to compare well with the experimental results for the temperature distribution. With the increase of κ and L/D_p, mean effective thermal conductivity and the total heat flux were found to decrease. For all values of κ, for the three porosity models, the values of total heat flux were found almost close to one other. However, for the lower values of L/D_p, total heat flux from model 1 was found more than that from models 2 and 3. Similar trends were also observed for the mean total effective thermal conductivity. Time to reach steady state was found to increase with the increase of κ, L/D_p and N.

TH-1868_004301

Chapter 7

Radiation-Convection Heat Transfer in a Porous Channel

7.1 Introduction

Porous media have played an important role in improving the performance of many thermal systems. In recent years, in high-temperature applications, a great deal of attention has been focused on the usage of porous media [102, 105, 108, 110, 142–146]. Apart from many other applications, porous media have been utilized for the enhancement of heat transfer in coolant passages [101,147] and in thermal insulation systems [102,143], in which consideration of radiation along with conduction and/or convection is required.

There have been various studies of the analysis of the combined radiation and convection modes of heat transfer [96, 100, 148–150]. In all these analyses, the medium considered is a general fluid continuum. In some investigations [108, 110, 142, 143], combined conduction, convection and radiation heat transfer problems in porous

TH-1868_004301

media have been analyzed with known uniform velocity across the medium. When the porosity and permeability of the porous medium are relatively high, boundary and inertia effects come into play, and in this situation, the assumption of uniform velocity across the medium is not valid [103]. In this case, the velocity distribution near the wall is non-uniform and hence it affects the heat transfer to or from the wall [103]. This aspect of non-uniform velocity distribution near the wall has been accounted by Kaviany [103]. He obtained the solution for the velocity distribution which is applicable to flow with or without a porous medium. The solution for the velocity distribution over the complete range, including the limiting case of flow with or without a porous medium, was developed by Kaviany [103] by introducing a parameter called the porous medium shape parameter (PMSP), $\gamma = (W^2\phi/K)^{1/2}$, where W is the channel width, ϕ is the porosity and K is the permeability. When the PMSP $\gamma \to 0$, a fully developed velocity profile for Poiseuille flow is obtained. When the PMSP $\gamma \to \infty$, the slug-flow condition is achieved and, in this case, the velocity distribution is uniform. Kaviany found the Nusselt number Nu and the temperature distributions over a wide range of values of the PMSP γ. He showed that Nu for fully developed fields varies from 7.54 for $\gamma \to 0$ to 9.87 for $\gamma \to \infty$. The PMSP γ has also been found to have a significant effect on the temperature distribution. Kaviany did not consider the effect of radiation.

Chawla and Chan [96] carried out an analysis for the combined radiation and convection in thermally developing Poiseuille flow. They showed that in the presence of radiation, unlike the case of pure convection, there is no fully developed thermal field. Nu varies in the flow direction, and the radiation contribution to the total heat flux, Nu and temperature increases along the flow direction. Further, radiative parameters such as the extinction coefficient, the scattering albedo and the boundary emissivity have significant effects on heat flux, Nu and temperature. The work of Chawla and Chan [96] can be viewed as a study of convection-radiation heat transfer for the limiting case of the PMSP $\gamma \to 0$. Kaviany's work [103] can be seen as the limiting case of the convection-radiation problem with a general porous medium in which the radiation effect is negligible.

After the work of Chawla and Chan [96] and Kaviany [103], many studies have been

TH-1868_004301

performed for different geometries [100, 149, 151, 152]. However, none of the previous studies took into account the effect of convection and radiation for a general medium with PMSP γ, and therefore, results for the variations of the Nusselt number Nu, heat flux and temperature are not available for various values of the PMSP γ. The present work was aimed at extending the work of Chawla and Chan [96] by incorporating a general medium with PMSP γ, and that of Kaviany [103] by considering the effect of radiation. The present work thus bears significance in providing more accurate predictions especially in the area of porous medium combustion where the analysis is done either by considering fluid and solid phases as a single continuum [146] or separate continua [102, 105, 108, 110, 142–145]. In all these studies [102, 105, 108, 110, 142–146], analysis was performed for the slug-flow condition.

In the present work, the effect of radiation on flow through a porous medium bounded between two isothermal parallel plates is investigated. For parameters such as extinction coefficient, scattering albedo, conduction-radiation parameter, wall emissivity, etc., Nu, temperature and heat flux values at different axial locations are found for various values of the PMSP γ, including the two limits $\gamma \to 0$, and ∞. For $\gamma \to 0$, results from the present work are validated against the results of Chawla and Chan [96]. When the extinction coefficient $\beta \to 0$, the radiation effect is absent, and in this case, the present problem is the same as that of Kaviany [103]. For this case, results from the present work are found to match those of Kaviany [103]. For the purpose of comparison, results are presented in both tabular and graphical forms. The discrete transfer method (DTM) [24] is used to solve the radiative part of the energy equation, and an implicit finite difference scheme is used to solve the energy equation.

7.2 Formulation

Consider a porous medium with uniform porosity ϕ and permeability K bounded between two gray isothermal parallel plates as shown in Fig. 7.1. An absorbing,

TH-1868_004301

emitting and scattering porous medium is embedded in a fluid with a fully developed velocity field. The fluid and the solid matrix are in local thermal equilibrium and the two phases are considered as a continuum. The density ρ, specific heat C_P and dynamic viscosity μ of the fluid are uniform and constant. The thermal conductivity k and extinction coefficient β of the fluid-solid continuum are also assumed to be uniform and constant.

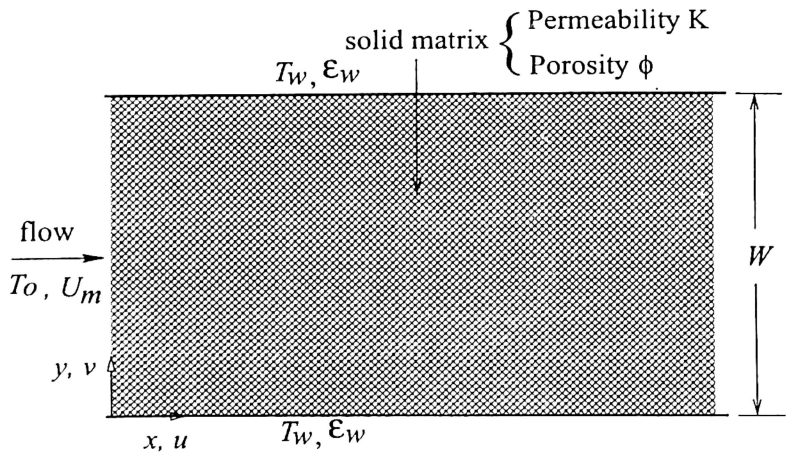


Figure 7.1: Schematic diagram of the problem under consideration.

By incorporating the effect of radiation, for a planar geometry, the steady-state energy equation for the fluid-solid continuum [103] is modified to

$$\rho C_p\left(u\frac{\partial T}{\partial x}+v\frac{\partial T}{\partial y}\right)=k\left(\frac{\partial^2 T}{\partial x^2}+\frac{\partial^2 T}{\partial y^2}\right)-\left(\frac{\partial q_R}{\partial x}+\frac{\partial q_R}{\partial y}\right) \tag{7.1}$$

where u and v are velocities parallel and perpendicular to the flow, respectively. In Eq. (7.1), the left-hand side is the contribution of the fluid convection, and the first and the second terms on the right-hand side represent contributions of conduction and radiation, respectively by the fluid-solid continuum. Neglecting the conductive and the radiative heat fluxes in the axial direction, for a fully developed velocity field, in non-dimensional form, Eq. (7.1) is written as

$$u^*\frac{\partial\theta}{\partial\eta_x}=\left(\frac{2}{Pe}\right)\frac{\partial^2\theta}{\partial\eta_y^2}-\left(\frac{\beta W}{2NPe}\right)\frac{\partial\Psi_R}{\partial\eta_y} \tag{7.2}$$

TH-1868_004301

where $\eta_x = x/W$ and $\eta_y = y/W$ are the non-dimensional lengths in the x and y directions, respectively, β is the extinction coefficient and W is the physical thickness of the porous medium (Fig. 7.1). In Eq. (7.2), non-dimensional values of axial velocity u^*, temperature θ, Peclet number Pe, conduction-radiation parameter N, and radiative heat flux Ψ_R are defined as

$$u^* = \frac{u}{U_m},\ \theta = \frac{T}{T_{ref}},\ Pe = RePr = \left(\frac{\rho U_m D_h}{\mu}\right)\left(\frac{\mu C_p}{k}\right),\ N = \frac{k\beta}{4\sigma T_{ref}^3},\ \Psi_R = \frac{q_R}{\sigma T_{ref}^4}$$

where U_m is the mean x-direction velocity, T_{ref} is some reference temperature and D_h $(= 2W)$ is the hydraulic diameter.

At the entrance to the porous medium (Fig. 7.1), the fluid has uniform velocity U_m and temperature T_0. The temperatures of both the plates T_w are the same. For the problem under consideration, the boundary conditions in non-dimensional form are

$$\begin{aligned} \text{Entrance } (\eta_x = 0.0): &\quad v^* = 0.0, u^* = 1.0,\ \theta = \theta_0 = \tfrac{T_0}{T_{ref}} \\ \text{Solid boundaries } (\eta_y = 0.0, 1.0): &\quad v^* = 0.0, u^* = 0.0,\ \theta = \theta_w = \tfrac{T_w}{T_{ref}} \end{aligned} \tag{7.3}$$

In flows though a porous medium with relatively high porosity ϕ and permeability K, boundary and inertia effects are important, and the velocity field develops in a short distance from the entrance at a distance of the order of KU_m/ν, in contrast to a developing velocity field where no rigid matrix is present [103]. For the boundary conditions as given in Eq. (7.3), for flow through a porous medium with PMSP γ, the fully developed velocity profile u^* obtained by Kaviany [103] is

$$u^* = \frac{1 - e^{-2\gamma} - (1 - e^{-\gamma})\left(e^{\gamma(\eta_y - 1)} + e^{-\eta_y \gamma}\right)}{1 - e^{-2\gamma} - 2(1 - e^{-\gamma})^2 \gamma^{-1}} \tag{7.4}$$

It should be noted that the PMSP $\gamma = (W^2\phi/K)^{1/2}$ is the ratio of the two natural length scales, viz., the pore-particle dimension $(K/\phi)^{1/2}$ and the channel width W. When $\gamma \to 0$, the permeability $K \to \infty$, meaning that obstructions are absent from the flow field. This is the situation with fully-developed Poiseuille flow. When $\gamma \to \infty$, $K \to 0$. This is the case of a slug flow. In this situation, the boundary and the inertia effects are negligible, and the velocity profile across the porous medium is uniform. The velocity u^* profile given by Eq. (7.4) is applicable to all values of

TH-1868_004301

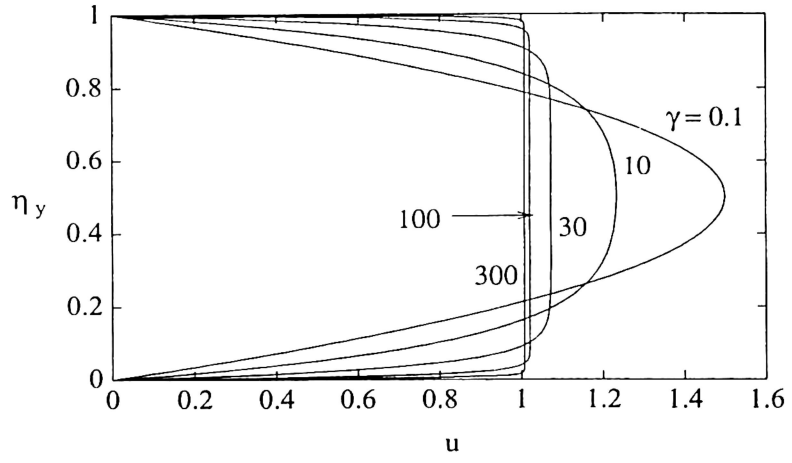


Figure 7.2: The fully-developed velocity distribution for several values of the porous media shape parameter.

γ. In Fig. 7.2, velocity profiles for different values of γ are plotted as given by Eq. (7.4).

With the velocity distribution u^* known from Eq. (7.4), for the solution of the energy equation Eq. (7.2), information about the divergence of radiative heat $\frac{\partial \Psi_R}{\partial \eta_y}$ is required. Eq. (2.16) can be non-dimensionalised as described before to get the following expression.

$$\frac{\partial \Psi_R}{\partial \eta_y} = 4\beta W(1-\omega)\left[\theta^4 - \frac{G^*}{4\pi}\right] \tag{7.5}$$

The incident radiation, intensity and source function are non-dimensionalized with respect to the reference temperature T_{ref} (Similarly as in section 5.2 where it is non-dimensionalized w.r.t T_S).

To solve energy Eq. (7.2), the divergence of radiative heat flux given by Eq. (7.5) is substituted in Eq. (7.2), which yields the desired governing integro-differential equation to be solved:

$$u^* \frac{\partial \theta}{\partial \eta_x} = \left(\frac{2}{Pe}\right)\frac{\partial^2 \theta}{\partial \eta_y^2} - \left(\frac{2(\beta W)^2(1-\omega)}{NPe}\right)\left(\theta^4 - \frac{G^*}{4\pi}\right) \tag{7.6}$$

With the radiative component known, Eq. (7.6) is solved using the implicit finite

TH-1868_004301

difference scheme in which η_x is the marching direction. For the grid independent situation, depending on the extinction coefficient β, the requirement for the control volumes has been found to be between 200 to 500. Depending on the conduction-radiation parameter N, the length increment in the axial direction has been taken between 1×10^{-6} and 1×10^{-4}. For all cases, a maximum of 64 rays has been found sufficient for the ray independent situation.

The Nusselt number Nu at the boundary is computed from

$$Nu = \frac{2}{\theta_w - \theta_m}\left(- \frac{\partial \theta}{\partial \eta_y} + \frac{\beta D_h}{4N}\Psi_R \right)_{\eta_y = 0.0} = Nu_C + Nu_R \tag{7.7}$$

where $\theta_m (= \frac{\int_0^1 u^* \theta d\eta_y}{\int_0^1 u^* d\eta_y})$ is the bulk mean temperature of the fluid. The total Nusselt number Nu can be split as the summation of the convection Nusselt number Nu_C and the radiation Nusselt number Nu_R.

Table 7.1: Effect of the PMSP γ on Nu_C, Nu_R, Nu, Ψ_C and Ψ_R at various axial locations η_x corresponding to $\beta = 0.2, N = 0.01, \epsilon = 0.5$ and $\omega = 0.5$. Numbers in brackets are values from [96].

η_x	γ	Nu_C	Nu_R	Nu	Ψ_C	Ψ_R
5×10^{-5}	0.1	18.2650	1.4373	19.7023	1.7624	0.1387
		(18.2631)	(1.4357)	(19.6988)	(1.7621)	(0.1385)
	10	22.0936	1.4603	23.5539	2.1152	0.1398
	100	32.6706	1.5166	34.1872	3.0478	0.1415
	300	34.9135	1.5301	35.9135	3.1822	0.1416
1×10^{-3}	0.1	8.0035	1.7027	9.7062	0.5880	0.1251
		(7.9930)	(1.7010)	(9.6940)	(0.5868)	(0.1249)
	10	9.1020	1.8058	10.9078	0.6376	0.1265
	100	10.8249	2.0147	12.8396	0.6845	0.1274
	300	10.9447	2.0428	12.9875	0.6820	0.1273
1×10^{-2}	0.1	7.4369	4.2898	11.7261	0.0507	0.0292
		(7.4661	(4.2452)	(11.7113)	(0.0509)	(0.0289)
	10	8.3656	4.7297	13.0953	0.0408	0.0231
	100	9.6861	5.4027	15.0888	0.0270	0.0151
	300	9.5178	5.3230	14.8407	0.0257	0.0144

TH-1868_004301

Table 7.2: Effect of the PMSP γ on Nu_C, Nu_R, Nu, Ψ_C and Ψ_R at various axial locations η_x corresponding to $\beta = 0.2, N = 0.1, \epsilon = 0.5$ and $\omega = 0.65$. Numbers in brackets are values from [96].

η_x	γ	Nu_C	Nu_R	Nu	Ψ_C	Ψ_R
5×10^{-5}	0.1	18.3555	0.1096	18.4651	17.7387	0.1059
		(18.3507)	(0.1094)	(18.4600)	(17.7330)	(0.1057)
	10	22.1614	0.1114	22.2728	21.2507	0.1068
	100	32.6992	0.1156	32.8148	30.5568	0.1080
	300	34.4083	0.1166	34.5250	31.8991	0.1081
1×10^{-3}	0.1	8.1762	0.1271	8.3032	6.2001	0.0964
		(8.1765)	(0.1267)	(8.3032)	(6.1998)	(0.0961)
	10	9.2270	0.1343	9.3614	6.6866	0.0973
	100	10.8915	0.1492	11.0406	7.1546	0.0980
	300	11.0108	0.1512	11.1620	7.1320	0.0979
1×10^{-2}	0.1	7.5355	0.2974	7.8330	0.9928	0.0392
		(7.5272)	(0.2947)	(7.8219)	(0.9914)	(0.0388)
	10	8.3506	0.3302	8.6807	0.8651	0.0342
	100	9.6204	0.3848	10.0052	0.6652	0.0266
	300	9.6356	0.3866	10.0222	0.6462	0.0259

7.3 Results and Discussion

Results for variations of the Nusselt number, temperature and heat flux are presented for both the hot-plate and the cold-plate condition. For the hot-plate condition, results for the Nusselt number and heat flux are presented in tabular form and, for the limiting case of Poiseuille flow, these are compared with the results available in the literature. All Nusselt number and heat flux values are calculated for the wall-porous medium interfaces.

It should be noted that in the absence of radiation, for the both hot and cold plate condition, the asymptotic value of the Nusselt number Nu is independent of the Peclet number Pe [103]. In the presence of radiation, the minimum Nu for the hot-plate condition or the asymptotic value of Nu for the cold-plate condition are independent of the Peclet number Pe. However, for low Pe the position of

TH-1868_004301

Table 7.3: Effect of the PMSP γ on Nu_C, Nu_R, Nu, Ψ_C and Ψ_R at various axial locations η_x corresponding to $\beta = 0.2, N = 0.5, \epsilon = 0.5$ and $\omega = 0.35$. Numbers in brackets are values from [96].

η_x	γ	Nu_C	Nu_R	Nu	Ψ_C	Ψ_R
5×10^{-5}	0.1	18.3612	0.0345	18.3957	88.7290	0.1665
		(18.3560)	(0.0344)	(18.3905)	(88.699)	(0.1664)
	10	22.1659	0.0350	22.2010	106.2850	0.1679
	100	32.7014	0.0364	32.7378	152.8085	0.1699
	300	34.4103	0.0367	34.4470	159.5200	0.1700
1×10^{-3}	0.1	8.1885	0.0399	8.2283	31.1024	0.1514
		(8.1883)	(0.0398)	(8.2281)	(31.0990)	(0.1513)
	10	9.2370	0.0421	9.2791	33.5330	(0.1529)
	100	10.8986	0.0468	10.9454	35.8738	0.1539
	300	11.0181	0.0474	11.0655	35.7615	0.1538
1×10^{-2}	0.1	7.5503	0.0923	7.6426	5.1385	0.0628
		(7.5392)	(0.0920)	(7.6312)	(5.1290)	(0.0626)
	10	8.3609	0.1024	8.4632	4.4954	0.0550
	100	9.6256	0.1192	9.7448	3.4815	0.0431
	300	9.6448	0.1197	9.7646	3.3843	0.0420

the minimum or the asymptotic values shift towards the entrance. When comparing results from the present work, values of Pe are taken according to the literature [96]. For other cases, Pe has been specified in the text.

Hot-plate condition

For plate temperatures higher than that of the fluid, some numerical results are presented in tabular form. For different values of the PMSP γ, these results are presented for various values of the extinction coefficient β, the scattering albedo ω, the conduction-radiation parameter N and the emissivity of the plates ϵ. The emissivities ϵ of both plates are the same. PMSP $\gamma \to 0$ represents the Poiseuille flow condition. For this limiting case, the results of the present work are validated against those of Chawla and Chan [96]. In the present study, this lower limiting

TH-1868_004301

Table 7.4: Effect of the PMSP γ on Nu_C, Nu_R, Nu, Ψ_C and Ψ_R at various axial locations η_x corresponding to $\beta = 2.0, N = 0.01, \epsilon = 0.5$ and $\omega = 0.65$. Numbers in brackets are values from [96].

η_x	γ	Nu_C	Nu_R	Nu	Ψ_C	Ψ_R
5×10^{-4}	0.1	38.0285	38.3328	76.3613	0.3758	0.3788
		(38.1617)	(38.2953)	(76.4570)	(0.3784)	(0.3771)
	10	47.7491	38.6457	86.3947	0.4709	0.3811
	100	84.3904	39.3199	123.7103	0.8264	0.3850
	300	100.5869	39.5239	140.1109	0.9817	0.3857
1.7×10^{-2}	0.1	12.1285	43.1489	55.2774	0.0949	0.3374
		(12.3321)	(43.0596)	(55.3917)	(0.0964)	(0.3367)
	10	14.6493	45.3705	60.0198	0.1120	0.3468
	100	20.1548	49.5306	69.6854	0.1451	0.3566
	300	20.6410	50.1743	70.8153	0.1467	0.3567
7.5×10^{-2}	0.1	14.9881	78.4209	93.4089	0.0419	0.2192
		(15.8528)	(77.9556)	(93.8084)	(0.0442)	(0.2175)
	10	17.6969	89.4096	107.1065	0.0427	0.2158
	100	22.4731	106.8565	129.3296	0.0413	0.1964
	300	22.9721	108.8939	131.8660	0.0404	0.1917

value of γ is 0.1, and for this case, results from the present work have been found to match those of Chawla and Chan [96].

In Tables 7.1-7.9, values of the convection Nusselt number Nu_C, the radiation Nusselt number Nu_R, the total Nusselt number Nu, the conductive heat flux Ψ_C and the radiative heat flux Ψ_R are given for $\gamma = 0.1$, 10, 100 and 300. In all these tables, numbers in the bracket are taken from [96]. All results are given for gray plates with emissivity $\epsilon = 0.5$. The Peclet number Pe corresponding to $\beta = 0.2$, 2.0, 10.0 are 0.08, 8 and 200, respectively.

It should be noted that the locations η_x in the axial direction and the values of β, ω, N and ϵ have been chosen as above to compare the results from the present work for $\gamma \to 0.0$ (which is 0.1 in this study) with those from [96]. For various values of the radiative parameters, after comparing the results for the limiting value of the PMSP γ, for the purpose of comparison with the future work, tabulated results have

TH-1868_004301

Table 7.5: Effect of the PMSP γ on Nu_C, Nu_R, Nu, Ψ_C and Ψ_R at various axial locations η_x corresponding to $\beta = 2.0, N = 0.1, \epsilon = 0.5$ and $\omega = 0.65$. Numbers in brackets are values from [96].

η_x	γ	Nu_C	Nu_R	Nu	Ψ_C	Ψ_R
5×10^{-4}	0.1	38.9269	3.8212	42.7481	3.8627	0.3792
		(38.9057)	(3.8174)	(42.7232)	(3.8604)	(0.3788)
	10	48.4780	3.8503	52.3283	4.8016	0.3814
	100	84.7300	3.9153	88.6454	8.3333	0.3851
	300	100.5869	3.9354	104.7597	9.8833	0.3858
1.7×10^{-2}	0.1	12.4103	3.8731	16.2835	1.1300	0.3527
		(12.4267)	(3.8661)	(16.2928)	(1.1315)	(0.3520)
	10	14.7206	3.9955	18.7160	1.3181	0.3578
	100	19.6965	4.2643	23.9608	1.6820	0.3642
	300	20.1436	4.3113	24.4550	1.6526	0.3636
7.5×10^{-2}	0.1	8.5077	4.3560	12.8637	0.6337	0.3245
		(8.5302)	(4.3456)	(12.8758)	(0.6353)	(0.3237)
	10	9.7774	4.6207	14.3981	0.6977	0.3297
	100	11.8253	5.1447	16.9700	0.7671	0.3337
	300	11.9618	5.2149	17.1767	0.7649	0.3334
5×10^{-1}	0.1	9.1921	9.6248	18.8170	0.1347	0.1411
		(9.3705)	(9.4918)	(18.8623)	(0.1370)	(0.1387)
	10	10.4825	10.7989	21.2814	0.1196	0.1232
	100	12.4876	12.7332	25.2208	0.0910	0.0928
	300	12.5015	12.8150	25.3165	0.0876	0.0898

been provided for different values of γ.

It can be seen from Tables 7.1-7.9 that for $\gamma \to 0.0$, the results from the present work compare very well with those from [96] for Poiseuille flow.

Comparison of the results from Tables 7.1-7.9 shows that at a particular location η_x, the Nusselt number increases with decrease in the conduction-radiation parameter N. This means that when the effect of radiation increases, heat transfer is greater and as a result the Nusselt number increases. From these tables, it is also seen that with increase in the extinction coefficient β , the Nusselt number increases. Therefore, the maximum value of the Nusselt number can be found when β is high

TH-1868_004301

Table 7.6: Effect of the PMSP γ on Nu_C, Nu_R, Nu, Ψ_C and Ψ_R at various axial locations η_x corresponding to $\beta = 2.0, N = 0.5, \epsilon = 0.5$ and $\omega = 0.65$. Numbers in brackets are values from [96].

η_x	γ	Nu_C	Nu_R	Nu	Ψ_C	Ψ_R
5×10^{-4}	0.1	39.0108	0.7640	39.7749	19.3623	0.3792
		(38.9758)	(0.7633)	(39.7391)	(19.3440)	(0.3788)
	10	48.5449	0.7698	49.3147	24.0503	0.3814
	100	84.7604	0.7828	85.5431	41.6974	0.3851
	300	100.8453	0.7868	101.6321	49.4459	0.3858
1.7×10^{-2}	0.1	12.5557	0.7676	13.3233	5.7882	0.3539
		(12.5587)	(0.7662)	(13.3249)	(5.7893)	(0.3532)
	10	14.8170	0.7907	15.6077	6.7201	0.3586
	100	19.7197	0.8424	20.5621	8.5375	0.3647
	300	20.1639	0.8515	21.0154	8.6398	0.3649
7.5×10^{-2}	0.1	8.5888	0.8357	9.4245	3.3923	0.3301
		(8.5942)	(0.8337)	(9.4280)	(3.3942)	(0.3293)
	10	9.7817	0.8810	10.6626	3.7150	0.3346
	100	11.7250	0.9731	12.6981	4.0763	0.3383
	300	11.8564	0.9857	12.8421	4.0668	0.3381
5×10^{-1}	0.1	7.7343	1.4958	9.2300	1.1881	0.2298
		(7.7450)	(1.4868)	(9.2318)	(1.1893)	(0.2283)
	10	8.6370	1.6700	10.3017	1.1435	0.2211
	100	10.0718	1.9871	12.0588	1.0214	0.2015
	300	10.1630	2.0171	12.1801	1.0033	0.1991

and N is low (Table 7.9). Further, it is seen that the value of the Nusselt number is very high near the entrance and it continues to decrease, reaches a minimum value, and then increases again. This behavior can be explained well by Fig. 7.3(a) and (b). In Fig. 7.3(a), the effect of β on variation of the Nusselt number along the axial length η_x is shown, and in Fig. 7.3(b) the same is shown for the effect of N. The value of N in Fig. 7.3(a) is 0.1 and the value of β in Fig. 7.3(b) is 1.0. Both plates are black ($\epsilon = 1$) and an absorbing-emitting situation ($\omega = 0.0$) is considered in both cases. The Peclet number Pe in both cases is 20. The plots in these figures clearly explain the trends described above. The phenomena may be explained as follows: Downstream from the inlet the convective heat flux decreases more rapidly than the temperature difference, $\theta_w - \theta_m$ (Eq. 7.7), causing a steady decrease in the

TH-1868_004301

Table 7.7: Effect of the PMSP γ on Nu_C, Nu_R, Nu, Ψ_C and Ψ_R at various axial locations η_x corresponding to $\beta = 10.0, N = 0.01, \epsilon = 0.5$ and $\omega = 0.65$. Numbers in brackets are values from [96].

η_x	γ	Nu_C	Nu_R	Nu	Ψ_C	Ψ_R
1.25×10^{-2}	0.1	40.0834	191.4109	231.4943	0.0777	0.3708
		(40.0439)	(191.0990)	(231.1430)	(0.0776)	(0.3702)
	10	47.2705	200.2732	247.5437	0.0914	0.3871
	100	79.5535	214.4573	294.0109	0.1525	0.4110
	300	93.2099	217.3074	310.5173	0.1779	0.4147
0.25	0.1	31.0859	188.3844	219.4703	0.0367	0.2227
		(33.5402)	(185.9680)	(219.5080)	(0.0396)	(0.2195)
	10	34.8296	207.8403	242.6699	0.0391	0.2334
	100	40.7965	238.7365	279.5330	0.0415	0.2429
	300	41.4571	242.0937	283.5508	0.0415	0.2425
0.8375	0.1	36.6441	479.6952	516.3393	0.0053	0.0696
		(76.0301)	(439.1020)	(515.1320)	(0.0109)	(0.0627)
	10	54.5008	517.2532	570.0750	0.0030	0.0576
	100	43.4243	611.1619	654.5862	0.0038	0.0376
	300	41.5927	621.1797	662.7094	0.0036	0.0361

convective contribution to the Nusselt number; the fractional radiative heat flux, on the other hand, increases monotonically with axial distance x, leading to the observed behavior.

Another important finding from Tables 7.1-7.9 and Fig. 7.3(a) and (b) is that the value of the Nusselt number increases with increase in PMSP γ. For particular β and N, this trend is the same for all γ values. The Nusselt number reaches a maximum as the situation approaches the slug-flow condition ($\gamma \to \infty$). It also indicates that with the insertion of a solid porous matrix, the heat transfer increases and with the consideration of radiation, more and more heat is transferred. In Fig. 7.3(a) and (b), the result for $\beta = 0$ indicates the absence of radiation. The value of the Nusselt number is found to be a minimum in this case. Also, it is seen that the results for $N = 10$ almost coincide with those for $\beta = 0$. This is because, for higher values of N, the effect of radiation is lower. For $N = 10$, the effect of radiation is negligible, and situation becomes pure convection-like.

TH-1868_004301

Table 7.8: Effect of the PMSP γ on Nu_C, Nu_R, Nu, Ψ_C and Ψ_R at various axial locations η_x corresponding to $\beta = 10.0, N = 0.1, \epsilon = 0.5$ and $\omega = 0.65$. Numbers in brackets are values from [96].

η_x	γ	Nu_C	Nu_R	Nu	Ψ_C	Ψ_R
1.25×10^{-2}	0.1	38.2455	19.7157	57.9613	0.7544	0.3905
		(38.2081)	(19.6944)	(57.9024)	(0.7568)	(0.3901)
	10	47.8008	20.1942	67.9950	0.9419	0.3992
	100	83.0224	21.1173	104.1396	1.6257	0.4143
	300	97.1288	21.3529	118.4817	1.8941	0.4172
0.25	0.1	14.7375	17.0947	31.8322	0.2649	0.3099
		(14.8006)	(17.0401)	(31.8407)	(0.2683)	(0.3089)
	10	17.4104	18.3143	35.7247	0.3087	0.3274
	100	23.9488	20.4925	44.4413	0.4083	0.3517
	300	24.6617	20.7712	45.4383	0.4161	0.3527
0.8375	0.1	11.8354	16.4123	28.2477	0.1791	0.2505
		(11.9335)	(16.3170)	(28.2505)	(0.1821)	0.2490
	10	13.4328	17.9809	31.4137	0.1965	0.2653
	100	16.3539	20.6106	36.9645	0.2210	0.2809
	300	16.5953	20.8843	37.4796	0.2210	0.2806
2.5	0.1	13.3499	20.1011	33.4510	0.1232	0.1865
		(13.5552)	(19.8900)	(33.4452)	(0.1257)	(0.1844)
	10	15.0317	22.4745	37.5063	0.1267	0.1905
	100	17.9534	26.6272	44.5806	0.1268	0.1891
	300	18.2783	27.1124	45.3906	0.1262	0.1883

It can be seen from Fig. 7.3 that when the radiation effect is negligible ($\beta = 0$ in Fig. 7.3(a) and $N = 10$ in Fig. 7.3(b)), the Nusselt number reaches an asymptotic value. This is possible when the temperature profile reaches a fully developed state. In the absence of radiation, it can be interpreted from these figures that this fully developed temperature profile is achieved for all values of γ. However, with radiation a fully developed temperature profile is not obtained and, therefore, an asymptotic value of the Nusselt number is not achieved for any value of γ. This behavior is consistent with the findings of previous work [96, 100] for Poiseuille flow ($\gamma \to 0$).

As mentioned above,the trend of the developing temperature profile can be clearly understood from Fig. 7.4(a) and (b) where at four axial locations η_x, similarity

TH-1868_004301

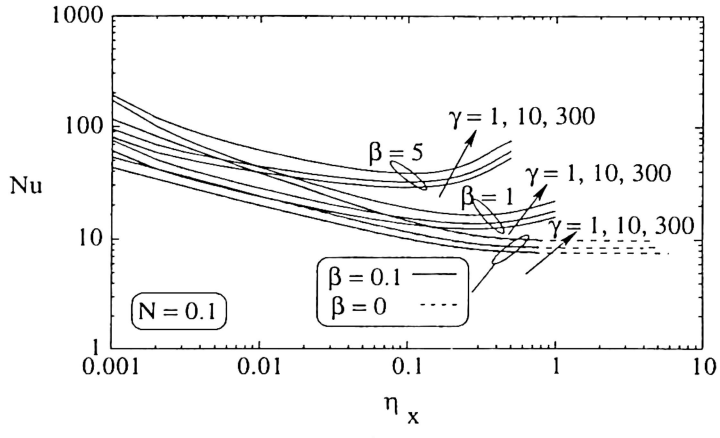
Table 7.9: Effect of the PMSP γ on Nu_C, Nu_R, Nu, Ψ_C and Ψ_R at various axial locations η_x corresponding to $\beta = 10.0, N = 0.5, \epsilon = 0.5$ and $\omega = 0.65$. Numbers in brackets are values from [96].

η_x	γ	Nu_C	Nu_R	Nu	Ψ_C	Ψ_R
1.25×10^{-2}	0.1	38.8602	3.9545	42.8147	3.8528	0.3924
		(38.8142)	(3.9496)	(42.7639)	(3.8513)	(0.3919)
	10	48.3675	4.0420	52.4095	4.7871	0.4003
	100	83.4446	4.2178	87.6624	8.1987	0.4146
	300	97.5544	4.2640	101.8184	9.5435	0.4175
0.25	0.1	14.5551	3.5020	18.0571	1.3641	0.3288
		(14.5670)	(3.4932)	(18.0602)	1.3677	(0.3280)
	10	17.3984	3.6896	21.0879	1.6110	0.3422
	100	24.2549	4.0504	28.3053	2.1640	0.3619
	300	25.0294	4.1032	29.1326	2.2103	0.3628
0.8375	0.1	10.3223	3.3320	13.6543	0.8843	0.2861
		(10.3334)	(3.3186)	(13.6520)	(0.8872)	(0.2849)
	10	11.9906	3.5732	15.5637	1.0011	0.2990
	100	15.1114	4.0052	19.1166	1.1817	0.3138
	300	15.3448	4.0568	19.4016	1.1846	0.3138
2.5	0.1	8.4760	3.3994	11.8754	0.5908	0.2375
		(8.4963)	(3.3797)	(11.8761)	(0.5935)	(0.2361)
	10	9.5688	3.7045	13.2733	0.6332	0.2457
	100	11.3123	4.2286	15.5410	0.6704	0.2512
	300	11.4532	4.2873	15.7404	0.6680	0.2506

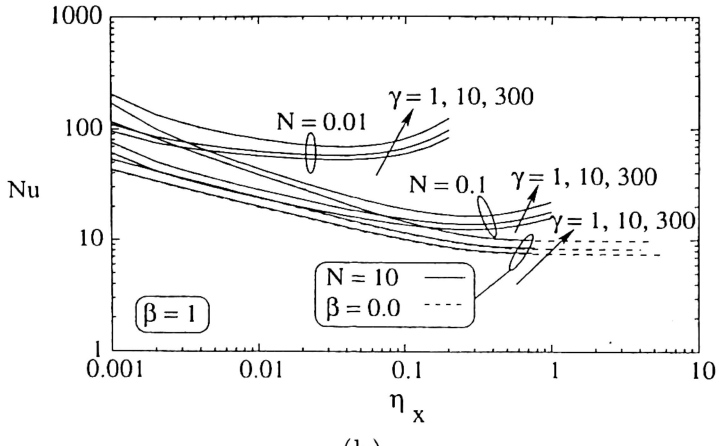
temperature profiles $((\theta_w - \theta)/(\theta_w - \theta_m))$ are drawn from the centerline ($\eta_y = 0.5$) to the plate ($\eta_y = 1$). Figure 7.4(a) represents the situation of Poiseuille flow ($\gamma = 0.1$), whereas Fig. 7.4(b) is a case of flow through a porous medium with PMSP $\gamma = 10$. These two figures clearly indicate that irrespective of the value of PMSP γ, in the presence of radiation, a fully developed temperature profile does not occur.

The increase in the Nusselt number with PMSP γ is shown in Fig. 7.5. For the results shown in Fig. 7.5(a), the radiation effect is absent. The Nusselt number values represented by the plot in Fig. 7.5(a) are the asymptotic values found from the fully developed temperature fields. This plot has been provided to show the

TH-1868_004301



(a)

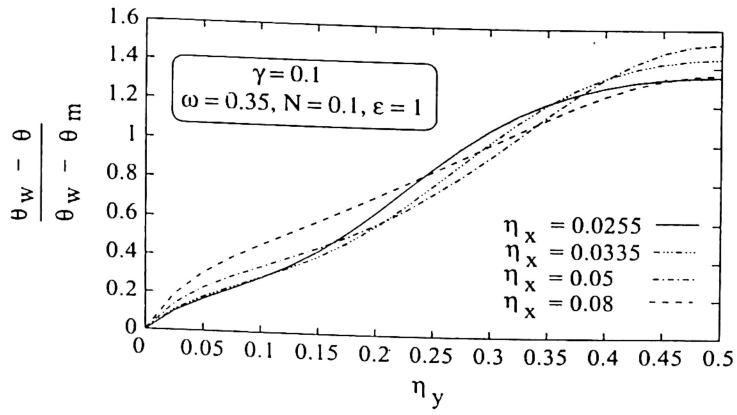


(b)

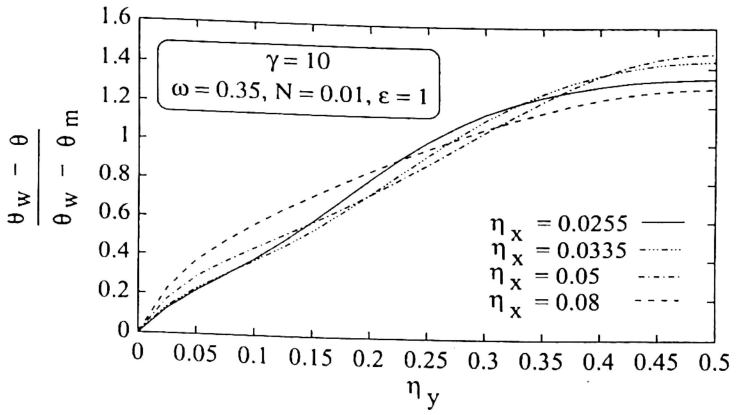
Figure 7.3: Variation of the total Nusselt number Nu along the axial length η_x for various values of PMSP γ: (a) effect of the extinction coefficient β; (b) effect of the conduction-radiation parameter N. Results for Nu without radiation effect ($\beta = 0$) are also shown.

correctness of the results from the present work. The minimum value of the Nusselt number (7.54) corresponds to $\gamma = 0.1$ (Poiseuille flow) and the maximum value of 9.87 is found at $\gamma = 1000$ (slug flow). These values are identical with those found by Kaviany [103]. Since with radiation there is no asymptotic value of the Nusselt number, in Fig. 7.5(b) and (c) Nu variations with γ are shown at two different axial

TH-1868_004301



(a)



(b)

Figure 7.4: Similarity temperature profile $\frac{\theta_w-\theta}{\theta_w-\theta_m}$ at different axial locations, (a) $\gamma = 0.1$ and (b) $\gamma = 10$, corresponding to $\beta = 2$, ω =0.35, $N = 0.01$, $\epsilon = 1$ and $Pe = 8$

locations, η_x= 0.0001 and 0.001. In both the figures, at different η_x, the trend for the variation of Nu with γ is similar to that without radiation (Fig. 7.5(a)). With increase in PMSP γ, the Nusselt number changes, and at different η_x, the trends are similar.

The effects of the PMSP γ on the convection Nusselt number Nu_C, the radiation Nusselt number Nu_R, the total Nusselt number Nu and the bulk mean temperature

TH-1868_004301

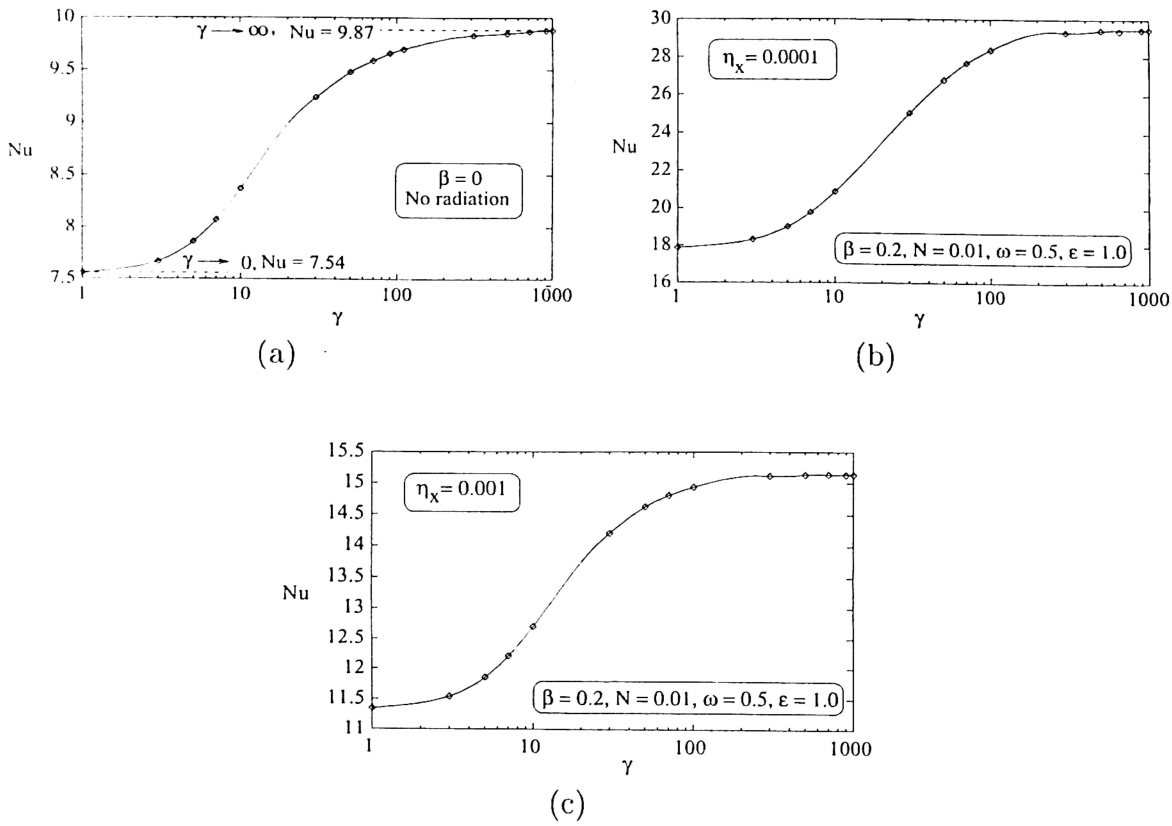


Figure 7.5: Variation of the total Nusselt number Nu with PMSP γ, (a) without radiation ($\beta = 0.0$), (b) with radiation at axial location $\eta_x = 0.0001$ and (c) with radiation at axial location $\eta_x = 0.001$; $Pe = 0.08$ in both the figures

θ_m are shown in Fig. 7.6(a) - (c). The variations of Nu_C and Nu_R in Fig. 7.6(a) explain the trends of the variation of Nu in Fig. 7.6(b). It can be seen from Fig. 7.6(a) that radiation effect increases as the distance from the entrance ($\eta_x = 0.0$) increases. Nu_R increases very sharply in the later part of the axial length, and, as a result, the total Nusselt number Nu increases again after it has reached a minimum value. With increase in γ, the values of Nu_C, Nu_R and Nu increase. The effect of γ on Nu_C is maximum at the entrance and it decreases as the distance from the entrance increases. In Fig. 7.5(c), the effect of γ on the bulk mean temperature θ_m is shown. It can be seen that θ_m increases with η_x and also that with increase in γ, θ_m increases.

TH-1868_004301

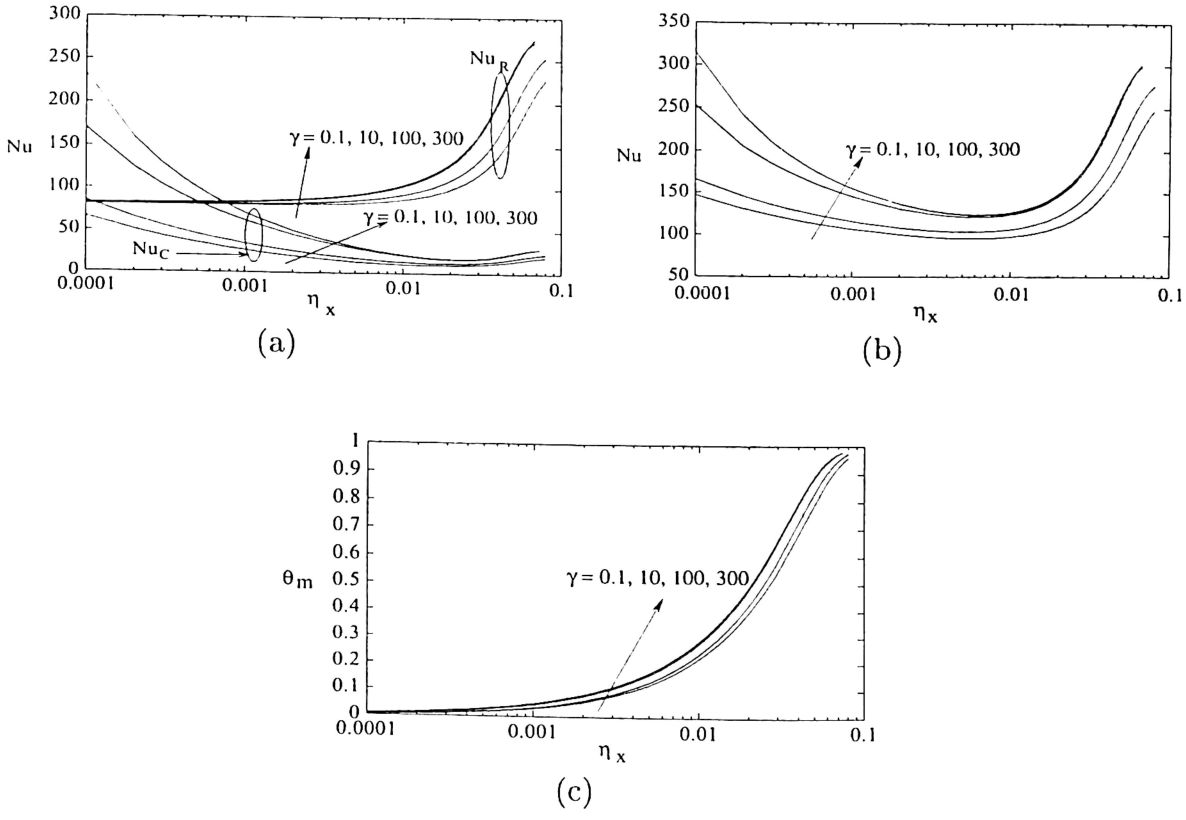


Figure 7.6: Effect of PMSP γ on variations of (a) convection Nusselt number Nu_C and radiation Nusselt number Nu_R, (b) total Nusselt number Nu and (c) bulk-mean temperature θ_m along the axial distance η_x; $\beta = 2.0, \omega = 0.35, \epsilon_w = 1.0, N = 0.01$ and $Pe = 8.0$.

The effect of the PMSP γ on temperature θ distributions along the channel width at different axial locations η_x are plotted in Fig. 7.7. In Fig. 7.7(a) - (d), the η_x values are 0.005, 0.0335, 0.05 and 0.8, respectively. To demonstrate the effect of radiation, the results without radiation ($\beta = 0.0$) are considered. In Fig. 7.7(d), θ profiles are presented at two η_x locations, viz. $\eta_x = 0.08$ and 1.

It can be seen from Fig. 7.7(a) - (d) that with radiation ($\beta = 2.0$), at a given axial location η_x, the fluid temperature is closer to the plate temperature than in the case without radiation ($\beta = 0.0$). In Fig. 7.7 (d), ($\beta = 2.0$ and $\eta_x = 0.08$), the fluid temperature is closer to the plate temperature than that for $\beta = 0.0$ at the axial location $\eta_x = 0.08$ and 1.0. This clearly shows the high rate of heat

TH-1868_004301

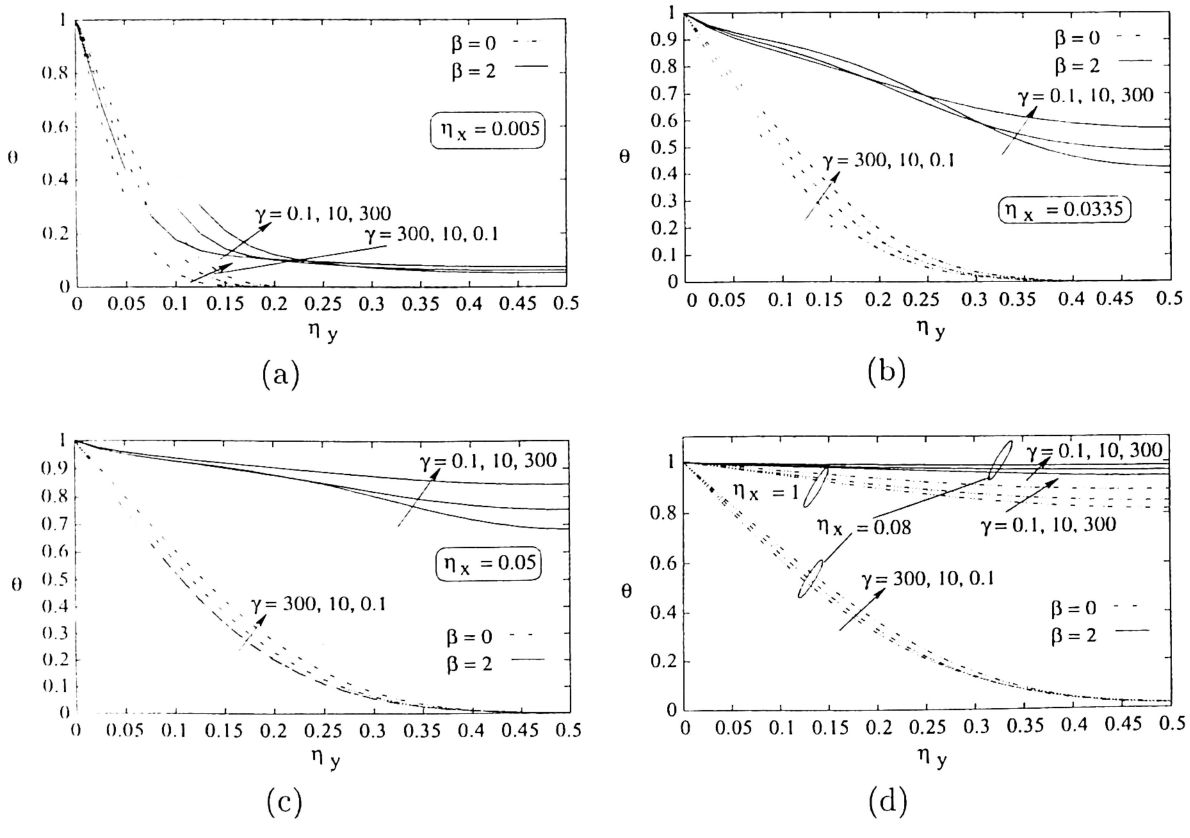


Figure 7.7: Effect of PMSP γ on variation of temperature θ normal to the flow direction at axial locations (a) $\eta_x = 0.005$, (b) $\eta_x = 0.0335$, (c) $\eta_x = 0.05$ and (d) $\eta_x = 0.08$ and 1.0; $\omega = 0.35, N = 0.01$, $\epsilon = 1$ and $Pe = 8.0$. Results without radiation effect ($\beta = 0$) are also shown.

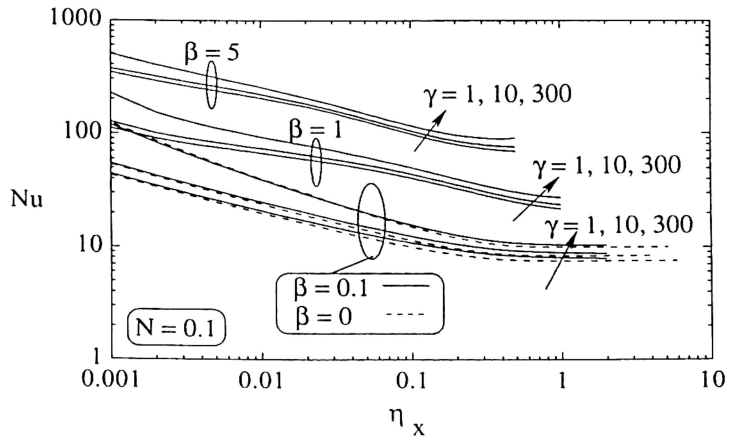
transfer due to radiation. For $\beta = 0.0$ (without radiation), (Fig. 7.7(a) - (c)), the temperature decreases with increase in γ close to the entrance, but far from the entrance ($\eta_x = 1.0$), the opposite trend is observed (Fig. 7.7(d)). However, in the presence of radiation ($\beta = 2.0$), the temperature always increases with increase in γ at all axial locations.

Cold-plate condition

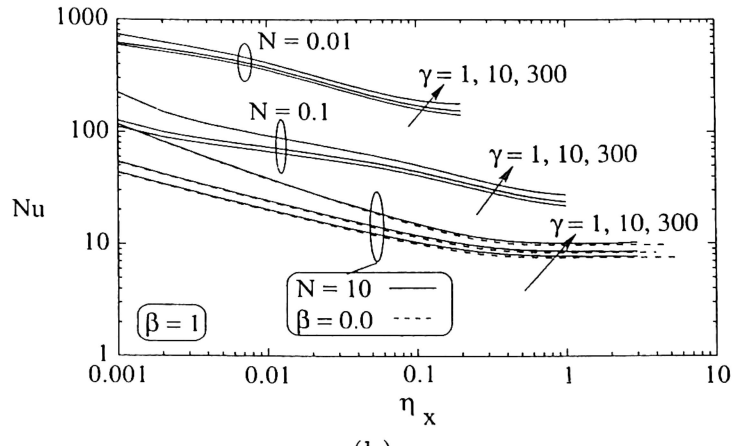
In Figs. 7.8 and 7.9, results for plate temperatures lower than the fluid temperature are provided.

TH-1868_004301

For various values of PMSP γ, the effects of β and N on the total Nusselt number Nu are shown in Fig. 7.8(a) and (b), respectively. For $\omega = 0.0$, $\epsilon = 1.0$, and $Pe = 20$, in Fig. 7.8(a), results are shown for $N = 0.1$, and in Fig. 7.8(b) results are given for $\beta = 1$. Unlike the cases with heating (Fig. 7.3(a)-(b)), in the present case of cooling, the Nusselt number reaches an asymptotic value. This trend for all values of the PMSP γ is consistent with the earlier work of Azad and Modest [153] for the cold condition of gas-particulate tube flow ($\gamma \rightarrow 0.0$). Like before, Nu is higher for



(a)



(b)

Figure 7.8: Variation of the total Nusselt number Nu along the axial length η_x for various values of PMSP γ: (a) effect of the extinction coefficient β and (b) effect of the conduction-radiation parameter N. Results for Nu without radiation effect ($\beta = 0$) are also shown.

TH-1868_004301

higher values of γ, and when $\beta \to 0.0$ (Fig. 7.8(a)) or N becomes high (Fig. 7.8(b)), the effect of radiation becomes negligible, and Nu for these cases approach the Nu values obtained without radiation. Furthermore, the Nusselt number is found to be higher for lower values of N and higher values of β.

Results for the effects of γ on variations of Nu_C, Nu_R, Nu and the bulk-mean temperature θ_m are given in Fig. 7.9(a)-(c). Unlike the heating case (Fig. 7.6), the radiation effect is found to be maximum at the entrance and decreases downstream. Accordingly, Nu_R decreases along the axial length and reaches an asymptotic value. With increase in γ, both the Nusselt number and θ_m increase. However, θ_m decreases along the axial length η_x.

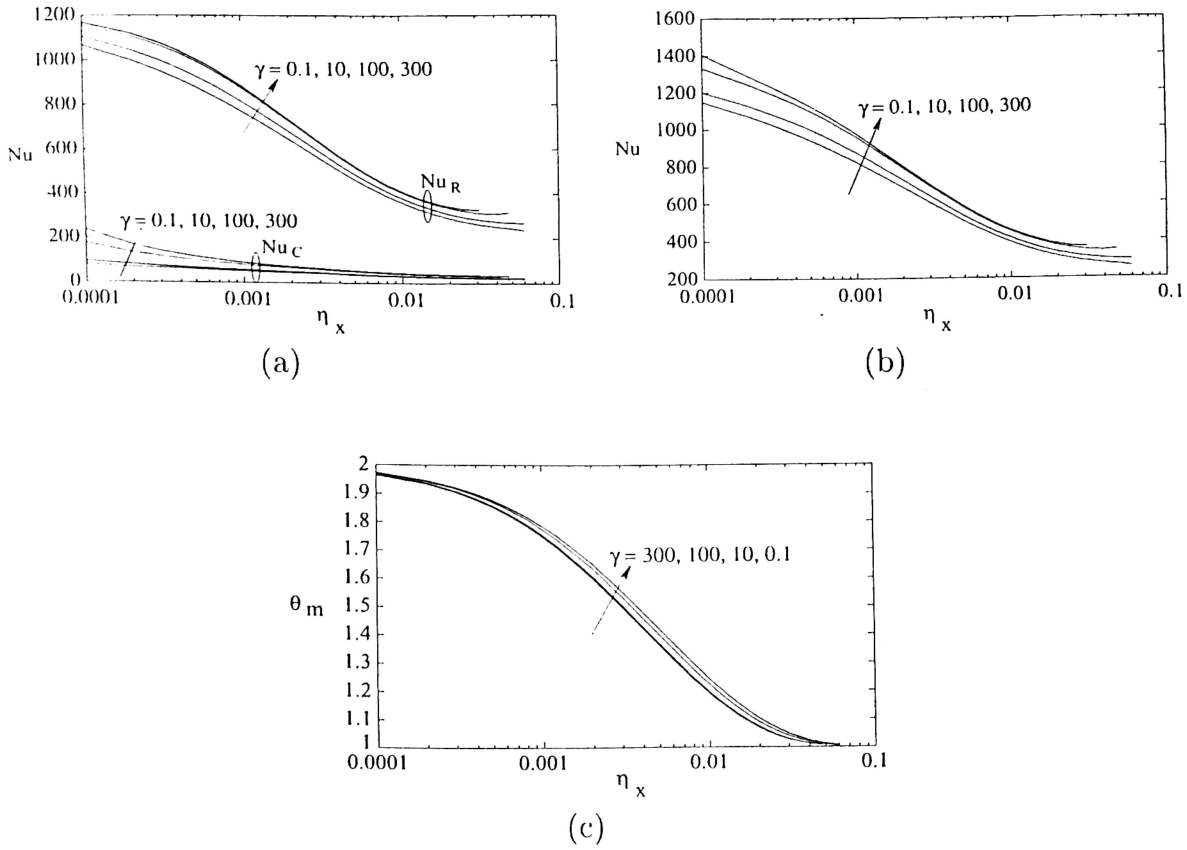


Figure 7.9: Effects of PMSP γ on variations of (a) convection Nusselt number Nu_C and radiation Nusselt number Nu_R, (b) total Nusselt number Nu and (c) bulk-mean temperature θ_m along the axial distance η_x; $\beta = 2.0, \omega = 0.35, \epsilon_w = 1.0, N = 0.01$ and $Pe = 8.0$.

TH-1868_004301

7.4 Conclusions

With the insertion of a porous solid matrix, heat transfer is significantly enhanced. Both the radiation Nusselt number and the convection Nusselt number increase with increase in PMSP γ. The behavior of the total Nusselt number for all values of PMSP γ is found to be the same as that for the combined radiative and convective heat transfer in Poiseuille flow ($\gamma \rightarrow 0.0$). For the hot-plate condition, the Nusselt number decreases along the axial length, reaches a minimum value and then increases again. For the cold-plate condition, the total Nusselt number decreases along the axial length and reaches an asymptotic value. For the hot-plate condition, the effect of γ on the radiation Nusselt number is smaller near the entrance, but it increases along the axial length. The opposite is the case with the convection Nusselt number. For the cold-plate condition, the effect of γ decreases gradually in the streamwise direction. In the presence of radiation, a fully developed temperature field is not obtained. In the limiting cases of $\gamma \rightarrow 0.0$ and $\beta = 0.0$, the results from the present work were found to match those available in the literature.

TH-1868_004301

Chapter 8

2-D Conduction-Radiation Heat Transfer

8.1 Introduction

Efficiency improvements in most industrial thermal processes are achieved by increased process temperatures. The optimum design of such processes is leading to temperature loads near the existing material limits. In recent years, high-temperature-resistant materials, made not only of ceramics but also of special alloys, have become available to realize high-temperature furnaces, gas turbine combustion chambers and blades, heat exchangers, porous volumetric solar receivers, surface and porous IR-radiant burners, etc. [106]. Experimental and numerical investigations are necessary in order to perform an optimum design and to elucidate the advantages of the temperature increase of such improved processes utilizing advanced high-temperature materials. Numerical computations of flow with heat and mass transfer in such high-temperature appliances require a through consideration of radiative heat transfer. Numerical computations of radiation based on conventional methods such as

TH-1868_004301

the zonal method, the Monte Carlo method (MCM), etc., coupled with the finite volume solvers of the conservation equations prove to be laborious and very time consuming. For this reason, numerous investigations [18, 114, 154] are currently being carried out worldwide to assess computationally efficient methods. The work presented in this chapter deals with the evaluation of such methods and shows that the collapsed dimension method (CDM) provides advantages that should be utilized in treating radiative transport problems with or without heat conduction.

Numerical simulations of the high-temperature appliances mentioned above require multi-dimensional analysis. Treatment of radiative transport in the multi-dimensional geometry is difficult mainly because of the three extra independent variables namely the polar angle, the azimuthal angle and the wavelength. Since there is no way out to get rid of the physical dimensions of the geometry and the wavelength of radiation, all numerical models, except the zonal method and the MCM, deal with different types of discretization schemes to make radiation less and less dependent on angular dimensions. The various methods differ primarily in the angular discretization schemes and the use of either the differential form or the integral form of the radiative transfer equation.

The main objective behind the development of any method for the solution of radiative transport problems, apart from its versatility for various geometries, complex medium conditions, etc., is that the method should be computationally efficient.

The DTM is a ray tracing method. It employs discretization of the entire spherical solid angle (4π) into a finite number of sub-solid angles. In each sub-solid angle, it assumes radiation to be isotropic. In planar geometry, and in multi-dimensional geometry with an absorbing-emitting medium, it is computationally not very expensive. However, in multi-dimensional geometry with an absorbing, emitting and scattering medium, it requires a large number of rays, and thus becomes computationally expensive. Further, this computational time becomes a great concern especially when one applies this method to combined radiation, conduction and/or convection mode problems, where large numbers of iterations are required for the converged solution. Hence the use of an alternative method having the potential to

TH-1868_004301

provide accurate results with better economy is very desirable.

In terms of problem formulation, accuracy of results and computational efforts, the CDM is a promising method [29, 30, 46, 117, 155]. Unlike other methods, in this method radiative information from 3-D space is collapsed to a 2-D plane in terms of the effective intensity and the collapsing coefficient. Since in the CDM radiation is viewed in the 2-D plane, all 2-D angular integrations over the polar angle and the azimuthal angle in other methods such as the DTM are replaced with 1-D integrations over the planar angle. This collapsing of angular dimension brings many simplifications and makes this method computationally very efficient.

Although the accuracy aspect of the CDM has been well established in earlier studies, with reference to a competitive method such as the DTM or any other methods, its economy aspect has so far not been investigated. This chapter deals with the performance evaluation of the CDM and the DTM in terms of computational time and their abilities to provide accurate results in solving radiation and/or conduction mode problems in a 2-D rectangular enclosure containing an absorbing, emitting and scattering medium.

In this work, both the CDM and DTM are used first to solve two benchmark radiative transport problems in a 2-D rectangular enclosure in which only radiative information is required. The first benchmark problem belongs to radiative equilibrium, while the other belongs to non-radiative equilibrium. For these two problems, for a range of parameters such as the extinction coefficient, the scattering albedo and the aspect ratio, the CDM and the DTM results are compared and CPU times are discussed. Next, transient conduction and radiation heat transfer in a 2-D gray enclosure is considered. This is relatively a complex problem, as for the chosen 2-D rectangular geometry, very few studies [76, 80] are available, and they deal with steady-state situations. For the transient case, some results for a black enclosure have been presented in [65]. In all these studies [65, 76, 80], the applicability of different methods for multi-dimensional conduction-radiation problems was tested. The objective behind choosing the third problem, therefore, is also to check the applicability of the CDM and the DTM for this problem, and thereby to see how

TH-1868_004301

the results from the two methods match at different time levels, and compared with the DTM, how much less time the CDM takes. This comparison is made for various values of aspect ratio, conduction-radiation parameter, scattering albedo, extinction coefficient and hot boundary emissivity. Further, as part of the validation of the combined mode results from the two methods, for some cases, the results are compared with those available in the literature [29, 65, 76].

8.2 Formulation

The 2-D rectangular geometry under consideration is shown in Fig. 8.1. All four boundaries are diffuse and gray, and the contained homogeneous medium is absorbing, emitting and scattering. Thermophysical properties such as density ρ, specific heat C_p, thermal conductivity k and the optical property, extinction coefficient β, are assumed to be constant. For the three types of problems considered in this work, specifications are as follows:

Problem 1. The south boundary of the 2-D enclosure is at some finite temperature T_S

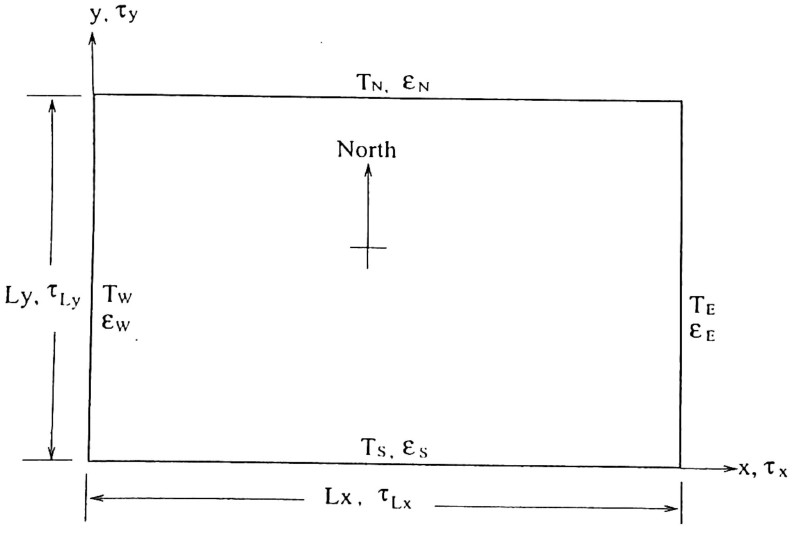


Figure 8.1: Geometry and the coordinates of the problems under consideration.

TH-1868_004301

and is thus the radiation source. The other three boundaries are cold (at zero temperature). The temperature of the medium is unknown. This case is the representative of a 2-D benchmark radiative equilibrium problem. In this type of problems, energy is exchanged only by radiation and hence equilibrium is achieved only through radiation.

Problem 2. All four boundaries of the enclosure are cold and the temperature of the medium is uniform and constant. The absorbing, emitting and scattering medium is thus the known radiation source. This case is the representative 2-D benchmark problem for the validation of any method for solving only the radiative part of a non-radiative equilibrium problem. This can be taken as a problem where conduction and/or convection are present, but the problem is solved only for radiation to see the radiation characteristics. This can be done only when the temperature of the medium is known. In the benchmark problems temperature of the medium is assumed to be uniform to get rid of this problem.

Problem 3. Initially at time $t = 0$, the entire system is at some finite temperature T_O. For time $t > 0$, the south boundary is brought to temperature $T_S = 2T_O$. The temperature of the stationary conducting-radiating participating medium is unknown. This is a combined mode problem. It belongs to the class of non-radiative equilibrium problems in which both conduction and radiation modes have to be solved together. This type of problems are the most practical problems.

Of the three problems chosen above, problem 3 is the general one. Hence the formulation is given for that case. Problems 1 and 2 are special cases of problem 3.

In the absence of convection and heat generation, for a 2-D rectangular geometry, the equation for conservation of total energy is

$$\rho C_p \frac{\partial T}{\partial t} = \frac{\partial}{\partial x}\left(k\frac{\partial T}{\partial x}\right) + \frac{\partial}{\partial y}\left(k\frac{\partial T}{\partial y}\right) - \nabla \cdot q_R \tag{8.1}$$

TH-1868_004301

For constant thermal conductivity k, in non-dimensional form, Eq. (8.1) is written as

$$\frac{\partial\theta}{\partial\xi} = \frac{\partial^2\theta}{\partial\tau_x^2} + \frac{\partial^2\theta}{\partial\tau_y^2} - \frac{1}{4N}\nabla\cdot\Psi_R \tag{8.2}$$

where $\tau_x = \beta x$ and $\tau_y = \beta y$ are the optical coordinates in the x and y coordinate directions (Fig. 8.1), respectively. It should be noted that in Eq. (8.1), $\nabla = (\frac{\partial}{\partial x} + \frac{\partial}{\partial y})$ and in Eq. (8.2), $\nabla = (\frac{\partial}{\partial\tau_x} + \frac{\partial}{\partial\tau_y})$. With T_{ref} as the reference temperature, in Eq. (8.2), in non-dimensional form, the temperature θ, the conduction-radiation parameter N, the radiative heat flux Ψ_R and the time ξ are defined as

$$\theta = \frac{T}{T_{ref}},\ N = \frac{k\beta}{4\sigma T_{ref}^3},\ \Psi_R = \frac{q_R}{\sigma T_{ref}^4},\ \xi = \frac{t}{\frac{\rho C_p}{k\beta^2}} = \frac{k\beta^2 t}{\rho C_p}$$

For problem 3, the initial and boundary conditions are as follows:

$$\begin{aligned}
\text{Initial condition:}\quad & \theta(\tau_x,\tau_y,0) = 0.5 \\
\text{Boundary conditions:}\quad & \theta(0,\tau_y,\xi) = 0.5 \\
& \theta(\tau_{L_x},\tau_y,\xi) = 0.5 \\
& \theta(\tau_x,0,\xi) = 1.0 \\
& \theta(\tau_x,\tau_{L_y},\xi) = 0.5
\end{aligned} \tag{8.3}$$

Divergence of the radiative heat flux $\nabla\cdot\Psi_R$ for Eq. (8.2) is calculated by both the CDM and the DTM.

In the CDM, divergence of radiative heat flux $\nabla\cdot\Psi_R$ is given by (Eq. 3.4),

$$\nabla\cdot\Psi_R = \Gamma(1-\omega)\left(\pi\theta^4 - \frac{G'^*}{2}\right) \tag{8.4}$$

To solve the energy equation (Eq. (8.2)), $\nabla\cdot\Psi_R$ given by Eq. (8.4) is substituted in Eq. (8.2). This yields the desired governing integro-differential equation to be solved in the CDM:

$$\frac{\partial\theta}{\partial\xi} = \frac{\partial^2\theta}{\partial\tau_x^2} + \frac{\partial^2\theta}{\partial\tau_y^2} - \frac{1}{4N}\Gamma(1-\omega)\left(\pi\theta^4 - \frac{G'^*}{2}\right) \tag{8.5}$$

TH-1868_004301

For problem 1, which is representative of the radiative equilibrium case, $\nabla \cdot \Psi_R = 0$, meaning that only the radiation mode is present. In this case, the temperature θ of the medium is calculated from

$$\theta = \left(\frac{G'^*}{2\pi}\right)^{1/4} \tag{8.6}$$

For problem 2, $\nabla \cdot \Psi_R \neq 0$. Here the temperature θ of the medium is known and the radiative calculations can be done explicitly.

In case of the DTM, the divergence of the radiative heat flux $\nabla \cdot \Psi_R$ appearing in Eq. (8.2) is given by (Eq. 5.3)

$$\nabla \cdot \Psi_R = 4(1-\omega)\left(\theta^4 - \frac{G^*}{4\pi}\right) \tag{8.7}$$

To solve energy Eq. (8.2), the divergence of radiative heat flux given by Eq. (8.7) is substituted in Eq. (8.2), which yields the desired governing integro-differential equation to be solved in the DTM.

$$\frac{\partial \theta}{\partial \xi} = \frac{\partial^2 \theta}{\partial \tau_x^2} + \frac{\partial^2 \theta}{\partial \tau_y^2} - \frac{1-\omega}{N}\left(\theta^4 - \frac{G^*}{4\pi}\right) \tag{8.8}$$

For solving problem 1 using the DTM, the unknown temperature θ of the medium is obtained from

$$\theta = \left(\frac{G^*}{4\pi}\right)^{1/4} \tag{8.9}$$

8.3 Results and discussion

Here the CDM and DTM results for the three types of problems are presented. All results from the two methods are for grid and ray independent situations. Although numbers of rays required in the two methods are different, for a particular situation the grid size in the two methods was kept the same.

TH-1868_004301

For problems 1 and 2, for aspect ratio $L_x/L_y = r = 1$, the CDM and the DTM results were compared against the MCM results generated by the authors. For problem 3, results from the two methods were validated against each other. The computational times required in the CDM and the DTM are presented for various conditions.

In problem 1, the CDM and the DTM results for heat flux variations along the hot (south) boundary and the centerline ($x/L_x = 0.5$) emissive power distributions were compared for different values of the extinction coefficient β and aspect ratio r. In problem 2, results from the two methods were compared for the effects of β, scattering albedo ω and r. For the combined mode problem (problem 3), first the CDM and the DTM results for the steady-state temperature θ obtained from the 2-D rectangular geometry codes for $r = 10.0$ were validated by comparison with the 1-D CDM results [29]. For $r = 1.0$, for some cases, steady-state results from the two methods were compared with the numerical data presented in the literature [65, 76]. Next, to assess the performance of the two methods for the transient situation, the CDM and the DTM results at different instants ξ were compared against each other over a wide range of values of conduction-radiation parameter N, extinction coefficient β, scattering albedo ω, hot boundary emissivity ϵ_S and r. Transient problems in both methods were solved with the time step $\Delta\xi = 0.001$, and steady-state conditions were assumed to have been achieved when the temperature difference between the two consecutive time levels at each grid point did not exceed 0.00001. It should be noted that in all cases where the effects of aspect ratio r were studied, L_y was always kept at unity. All computations were performed on a SUN Ultra-60 workstation (2× CPU UltraSPARC 360 MHz, RAM 1280 MB at 120 MHz).

In all results presented below, the temperature of the south boundary T_S is the reference temperature T_{ref} for problems 1 and 3. The medium temperature T_g is the T_{ref} for problem 2.

TH-1868_004301

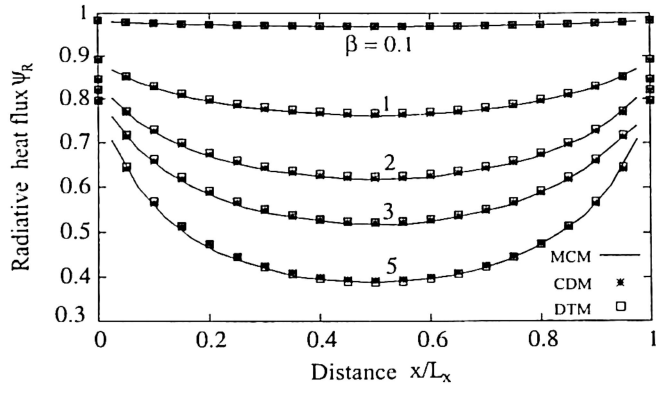
8.3.1 Problem 1: Radiative equilibrium - Boundary emission case

In Figs. 8.2 and 8.3, the CDM and the DTM results are compared for non-dimensional heat flux Ψ_R and emissive power $(T/T_S)^4$ distributions. For these results, all boundaries are black and the medium is absorbing, emitting and isotropically scattering. The south boundary is hot, whereas the other three boundaries are cold. For grid and ray independent situations, in the CDM, the results presented in Figs. 8.2 and 8.3 required 20×20 control volumes and 64 rays. However, in the DTM, for extinction coefficients $\beta = 0.1$, 1.0 and 2.0, 12×24 rays were used, and for $\beta = 3.0$ and 5.0, 24×48 rays were used.

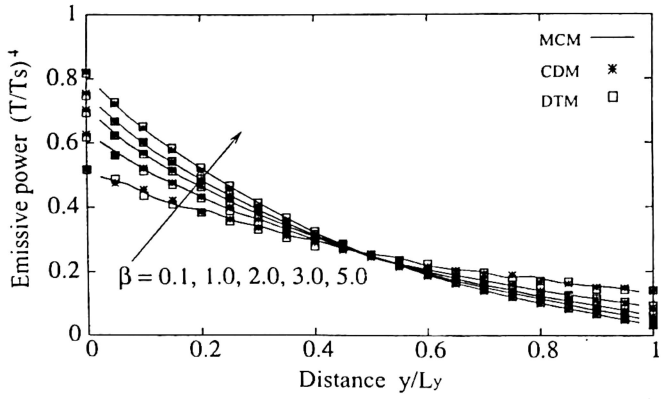
In Fig. 8.2(a), the CDM and the DTM results for the variations of Ψ_R along the hot (south) boundary are compared for various values of the extinction coefficient β. In Fig. 8.2(b), comparisons of emissive power $(T/T_S)^4$ variations at $x/L_x = 0.5$ along y/L_y are made. It can be seen that both the CDM and DTM results compare well with the MCM results. For the level of accuracy shown in Fig. 8.2, for $\beta = 0.1$, 1.0, 2.0, 3.0 and 5.0, CPU times in the CDM were 9.65, 24.23, 39.74, 61.36 and 109.28 s, respectively, and the corresponding CPU times for the DTM were 31.21, 138.83, 229.95, 1399.78 and 2501.48 s, respectively. Thus, from above results it is seen that for the same level of accuracy, the CDM is much more faster than the DTM.

In Fig. 8.3(a)-(b), for $\beta = 1.0$, the CDM and DTM results for Ψ_R and $(T/T_S)^4$ are compared against each other for $r = 0.1$, 1.0, 3.0 and 5.0. For all values of the aspect ratio r, the CDM results compare very well with the DTM results. In this case, for r=0.1, 1.0, 2.0, and 5.0, the CPU times in the CDM were 9.56, 24.23, 28.92, and 29.76 s, respectively, and the corresponding CPU times in the DTM were 55.49, 138.83, 162.17, and 181.51 s, respectively.

TH-1868_004301



(a)



(b)

Figure 8.2: Comparison of the CDM and the DTM results with the MCM results for the effects of extinction coefficient β on (a) heat flux Ψ_R along the hot (south) boundary and (b) the centerline emissive power $(T/T_S)^4$.

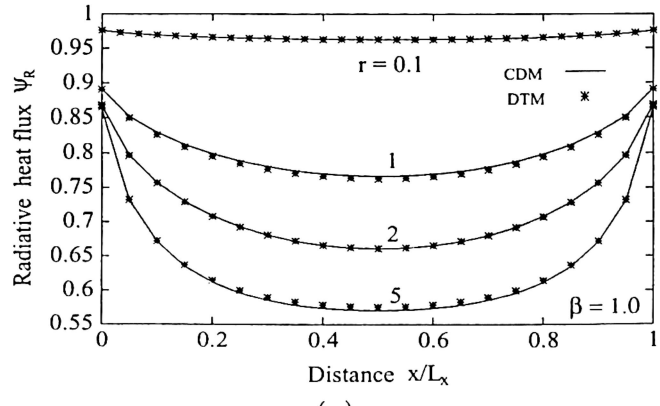
8.3.2 Problem 2: Non-radiative equilibrium - Isothermal medium emission case

In this case, all four boundaries are black and cold. The absorbing, emitting and isotropically scattering medium is at constant temperature. In Fig. 8.4(a)-(c), variations of non-dimensional radiative heat flux Ψ_R along the south boundary are compared. In this case, in the CDM 64 rays were used, while in the DTM, 12×24 rays were used for $\beta = 0.1$ and 1.0 and 24×48 rays were used for $\beta = 3.0$ and 5.0.

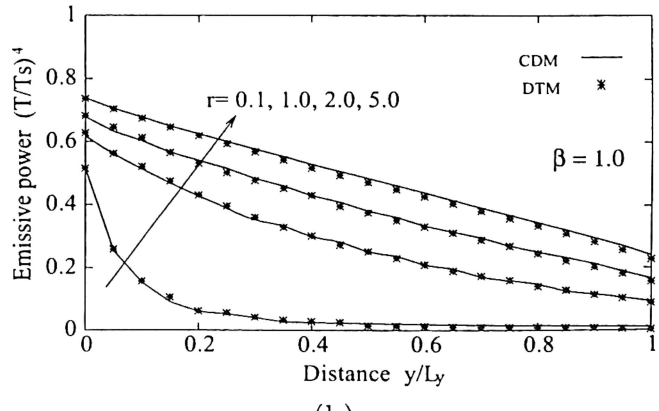
TH-1868_004301

For $r = 1.0$, in Fig. 8.4(a) and (b), the CDM and the DTM results for different values of β and ω are compared with the MCM results. Both the CDM and DTM are found to give a very good comparison.

In Fig. 8.4(c), for $\beta = 1.0$ and $\omega = 0.0$, results from the two methods are compared for $r = 0.1$, 1.0, 2.0 and 5.0. The CDM results are found to compare very well with the DTM results. For the results presented in Fig. 8.4(b), for $\omega = 0.5$ and 0.9, CPU times in the CDM are 1.64 and 2.58 s, respectively. The corresponding CPU times



(a)



(b)

Figure 8.3: Comparison of the CDM and the DTM results for the effects of aspect ratio r on (a) heat flux Ψ_R along the hot (south) boundary and (b) the centerline emissive power $(T/T_S)^4$.

TH-1868_004301

in the DTM are 13.57 and 21.91 s. In problem 2, for $\omega = 0.0$, no iterations are required. The CPU times in both the methods are negligible.

It is to be noted that the situations which require iterations, for different sets of parameters, even though the ratio of the number of rays in the CDM and the DTM are the same, the ratio of the CPU times in the two methods are different. This is for the reason that the number of iterations required for the converged solutions are different for different sets of parameters and CPU times per iteration in the two methods are also different. However, for a given set of parameters, the number of

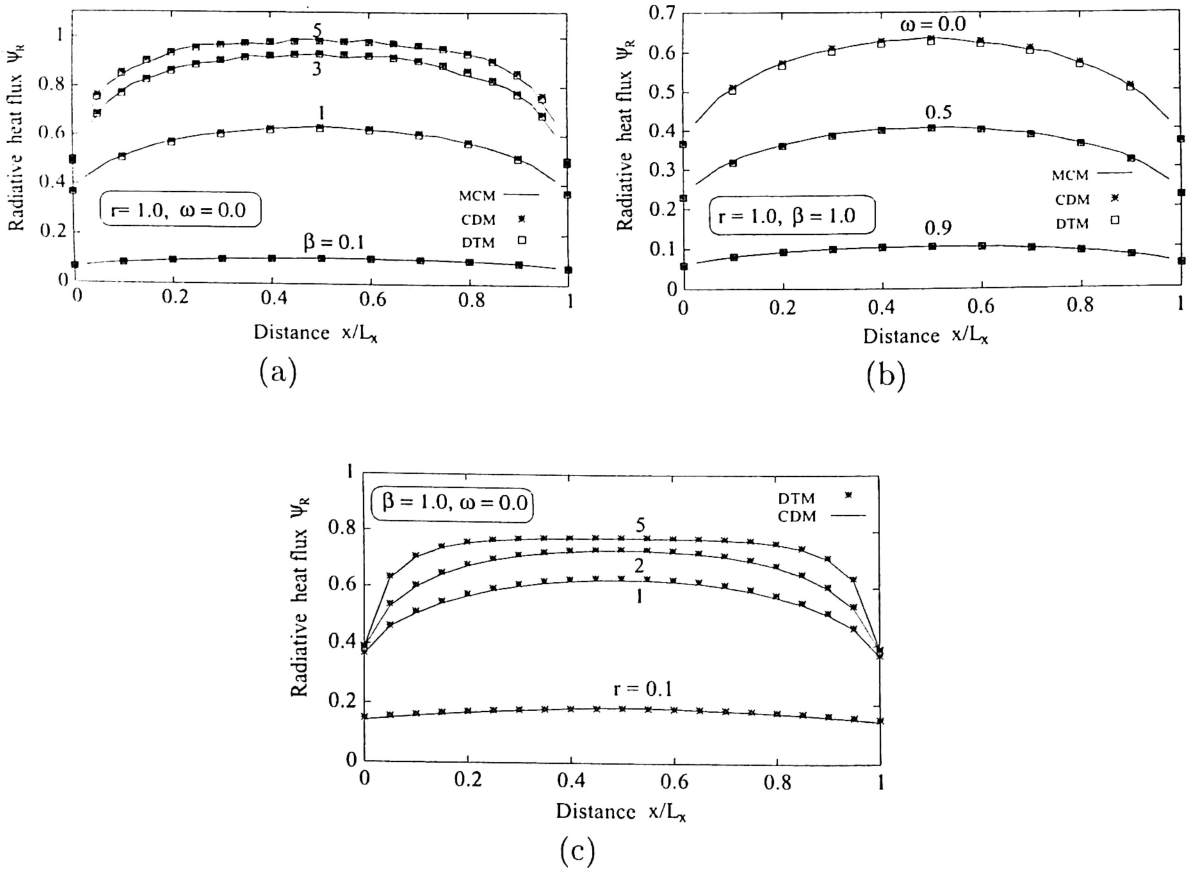


Figure 8.4: Comparison of the CDM and the DTM results for heat flux Ψ_R variations along the south boundary for the effects of (a) extinction coefficient β, (b) scattering albedo ω and (c) aspect ratio r.

TH-1868_004301

iterations in the two methods have been found the same.

8.3.3 Problem 3: Combined mode - Transient conduction and radiation

Having validated the CDM and the DTM against the MCM, and also against each other for problems 1 and 2 above, before proceeding to the complex situation, it

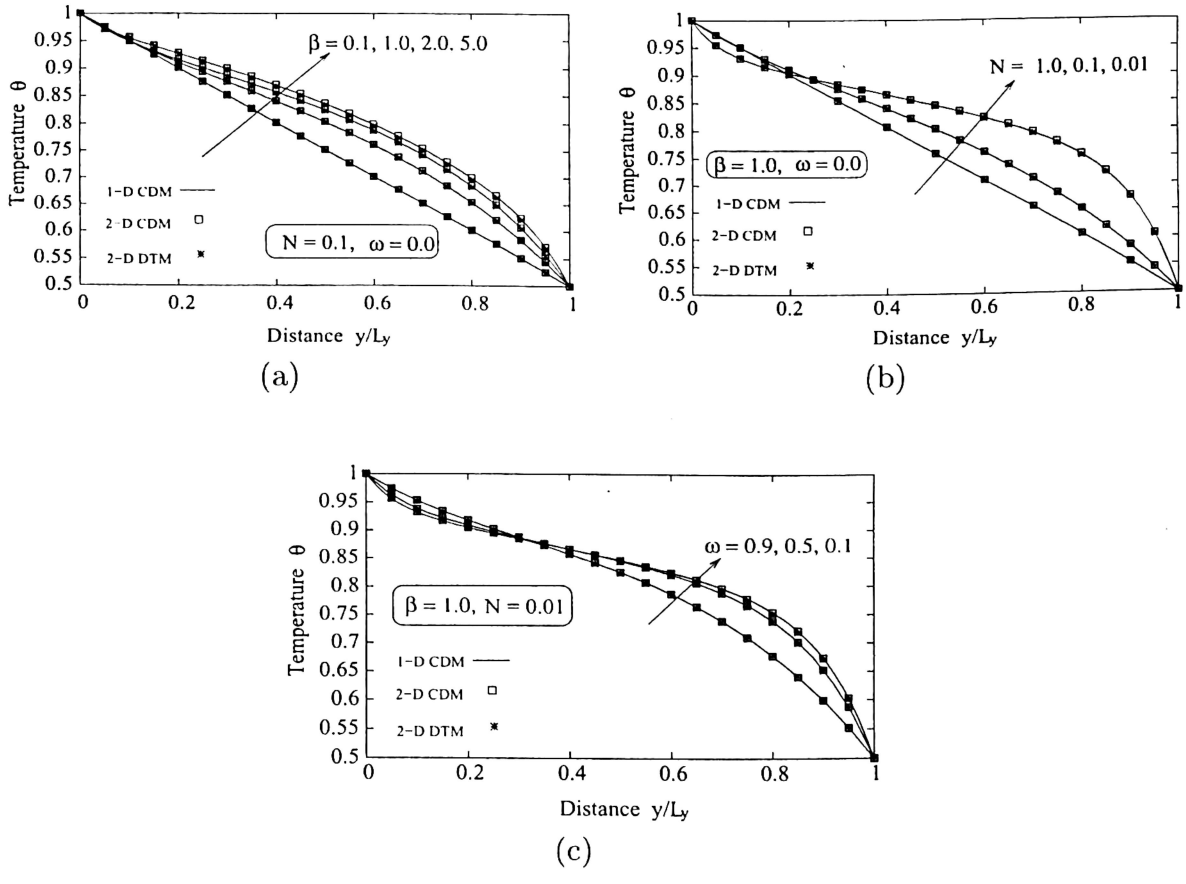


Figure 8.5: Comparison of the 2-D CDM and the 2-D DTM results for the steady-state centerline temperature θ distribution for aspect ratio $r = 10$ with 1-D CDM results [29] for the effects of (a) extinction coefficient β, (b) conduction-radiation parameter N and (c) scattering albedo ω.

TH-1868_004301

is important to check that for higher aspect ratios, such as $r = 10.0$, results from the two methods for the 2-D rectangular enclosure problem compare satisfactorily with the 1-D planar medium results [29]. Next, as part of the further validation studies, for a square enclosure ($r = 1.0$), for three different values of the conduction-radiation parameter N and the extinction coefficient β, the CDM and the DTM steady-state temperature θ results are compared with the numerical data provided in the literature [76, 80]. It should be noted that for grid and ray independent situations, for all results presented in the following paragraphs, in both the methods runs were taken for 20×20 control volumes, and in the CDM 64 rays and in the DTM 24×48 rays were used.

In Fig. 8.5(a)-(c), for $r = 10.0$, at $x/L_x = 0.5$, the variations in the temperature θ of the medium along y/L_y are given. When r is large ($L_x = 10, L_y = 1$), the effects of the east and west boundaries are insignificant and the centerline temperature in this case approaches that for the temperature distribution for the 1-D planar medium having same boundary conditions at the south and north boundaries [29]. This fact is demonstrated in Fig. 8.5(a)-(c). For all results presented in Fig. 8.5, the boundaries are black. It should be noted that in these figures, the 2-D CDM and the 2-D DTM results are the steady-state results for the transient problem.

For scattering albedo $\omega = 0.0$ and the conduction-radiation parameter $N = 0.1$, in Fig. 8.5(a), θ results from the 2-D CDM and the 2-D DTM codes for extinction coefficient $\beta = 0.1, 1.0, 2.0$ and 5.0, are compared against the 1-D CDM results. In Fig. 8.5(b), for $\beta = 1.0$ and $\omega = 0.0$, these comparisons are made for $N = 1.0, 0.1$ and 0.01. For $\beta = 1.0$ and $N = 0.01$, in Fig. 8.5(c), comparisons are made for $\omega = 0.1, 0.5$ and 0.9. It can be seen that in all cases, when the effects of the side boundaries are negligible, the 2-D CDM and the 2-D DTM results obtained by solving the transient problems match perfectly with the 1-D planar medium results.

In Table 8.1, for three different values of β (0.1, 1.0 and 5.0) and N (0.01, 0.1 and 1.0), the CDM and DTM temperature results for 20×20 control volumes are compared with those of Yuen and Takara [76] and Wu and Ou [65], which are for 10×10 and 20×20 control volumes, respectively. For the black square enclosure

TH-1868_004301

($r = 1.0$) for all these results, the medium is absorbing-emitting ($\omega = 0.0$). It can be seen from Table 8.1 that the results from the CDM and the DTM are in very good agreement with each other and also with those in the literature obtained using two different methods.

After having proved the correctness of the 2-D CDM and the 2-D DTM codes above, the temperature θ distributions at various instants ξ obtained from the CDM and the DTM are compared and remarks about the CPU times of the two methods are made in the subsequent paragraphs.

Table 8.1: Comparison of the steady-state centerline ($x/L_x = 0.5$) temperature θ results from the CDM and the DTM at various locations along y/L_y with results in Refs. [76] and [65] for different values of the extinction coefficient β and conduction-radiation parameter N; $r = 1.0$, ω=0.0, all boundaries are black.

β	N	Method	Centerline θ at different y/L_y				
			1.0	0.7	0.5	0.3	0.0
0.1	0.1	Ref. [76]	0.500	0.561	0.626	0.733	1.000
		Ref. [65]	0.500	0.563	0.630	0.733	1.000
		DTM	0.500	0.561	0.626	0.734	1.000
		CDM	0.500	0.561	0.626	0.734	1.000
1.0	1.0	Ref. [76]	0.500	0.564	0.630	0.737	1.000
		Ref. [65]	0.500	0.560	0.630	0.733	1.000
		DTM	0.500	0.564	0.630	0.737	1.000
		CDM	0.500	0.564	0.630	0.737	1.000
1.0	0.1	Ref. [76]	0.500	0.589	0.661	0.763	1.000
		Ref. [65]	0.500	0.590	0.663	0.760	1.000
		DTM	0.500	0.594	0.663	0.760	1.000
		CDM	0.500	0.594	0.663	0.759	1.000
1.0	0.01	Ref. [76]	0.500	0.653	0.726	0.807	1.000
		Ref. [65]	0.500	0.663	0.725	0.791	1.000
		DTM	0.500	0.665	0.725	0.790	1.000
		CDM	0.500	0.666	0.725	0.789	1.000
5.0	0.1	Ref. [76]	0.500	0.585	0.689	0.834	1.000
		Ref. [65]	0.500	0.626	0.707	0.802	1.000
		DTM	0.500	0.628	0.708	0.802	1.000
		CDM	0.500	0.626	0.706	0.802	1.000

TH-1868_004301

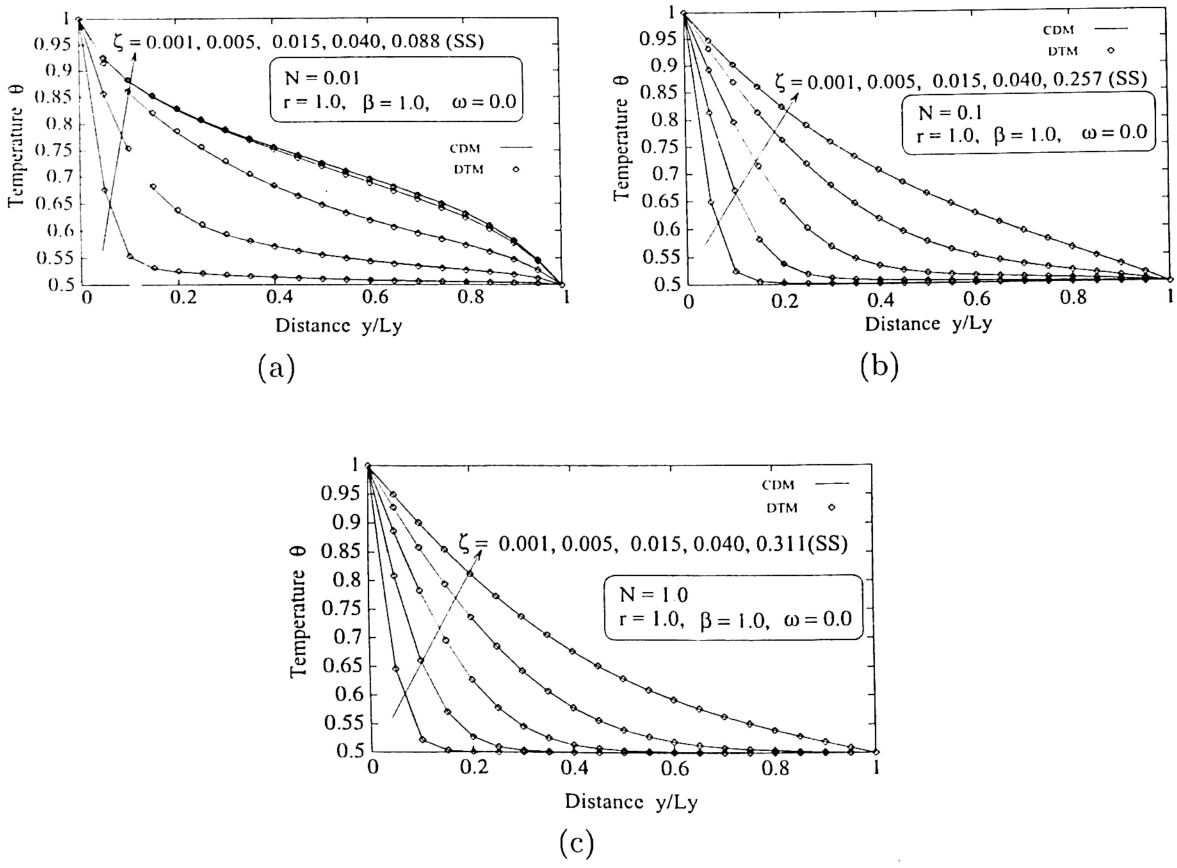


Figure 8.6: Comparison of the CDM and the DTM results for the centerline temperature θ distribution at time $\xi = 0.001$, 0.005, 0.015, 0.04 and steady state (SS) for conduction-radiation parameter $N =$ (a) 0.01, (b) 0.1 and (c) 1.0.

In Fig. 8.6 (a)-(c), θ results from the CDM and DTM are compared for $N = 0.01$, 0.1 and 1.0 respectively. All these results are for $r = 1.0$, $\beta = 1.0$ and $\omega = 0.0$. The θ results are compared at time $\xi = 0.001$, 0.005, 0.015, 0.040 and steady-state. For all values of N, at all times ξ, the CDM results compare very well with the DTM results. For $N = 0.01$, 0.1 and 1.0, CPU times in the CDM were 144.69, 402.37 and 488.18 s, respectively. The corresponding CPU times in the DTM were 3398.39, 10139.58 and 10492.26 s. The CDM is thus more than 20 times faster than the DTM.

TH-1868_004301

From Fig. 8.6(a)-(c), it is observed that in the early stage ($\xi = 0.001$), N does not have much effect on the θ distribution. However, as time passes, the effect increases. For the radiation-dominated situation ($N = 0.01$, Fig. 8.6(a)), owing to an increased contribution from radiation, at any instant ξ, the temperature in the medium is high. Further, since radiation is an instantaneous process, when its dominance is greater (for lower values of N), the steady-state is reached quickly. As can be seen from Fig. 8.6(a)-(c), the non-dimensional steady-state times ξ for $N = 0.01$, 0.1 and 1.0 are 0.088, 0.257 and 0.311 respectively.

In Fig. 8.7(a)-(c), comparisons of the CDM and the DTM results are made for the effects of the extinction coefficient β. For these results, the values of r, ω and N are 1.0, 0.1 and 0.0 respectively. For all cases, the CDM and the DTM results are found to match very well. For $\beta = 0.1$, 1.0 and 5.0, CPU times in the CDM were 77.12, 402.37 and 442.30 s, respectively. For the DTM, the corresponding CPU times were 1710.11, 10139.58 and 10702.83 s. The CDM is more than 22 times faster than the DTM.

From Fig. 8.7(a)-(c), it is seen that as the medium becomes optically thick, i.e., as β increases, the steady-state is delayed, and the steady-state temperature in the medium increases. However, at any time ξ, the transient temperatures in the medium are lower for higher values of β. With all other parameters fixed, with an increase in β, the increased absorption and scattering in the medium does not allow the radiation from the boundaries to penetrate deep into the medium. As a result of which steady state is delayed.

In Fig. 8.8(a)-(c), comparisons of the CDM and DTM results are made for the effects of scattering albedo ω. For all these results, θ distributions are presented for $r = 1.0$, $\beta = 1.0$ and $N = 0.01$. It can be seen that as ω increases, the steady-state time increases. This trend is due to the fact that with increase in ω, the medium absorbs and emits less energy and approaches a conduction-like situation. For example, for $\omega = 1.0$, $\nabla \cdot \Psi_R = 0.0$, the radiation term does not appear in the energy equation. For all the results presented in Fig. 8.8, the results from the CDM and the DTM match each other very well. In this case, the CDM is about 22 times faster than the

TH-1868_004301

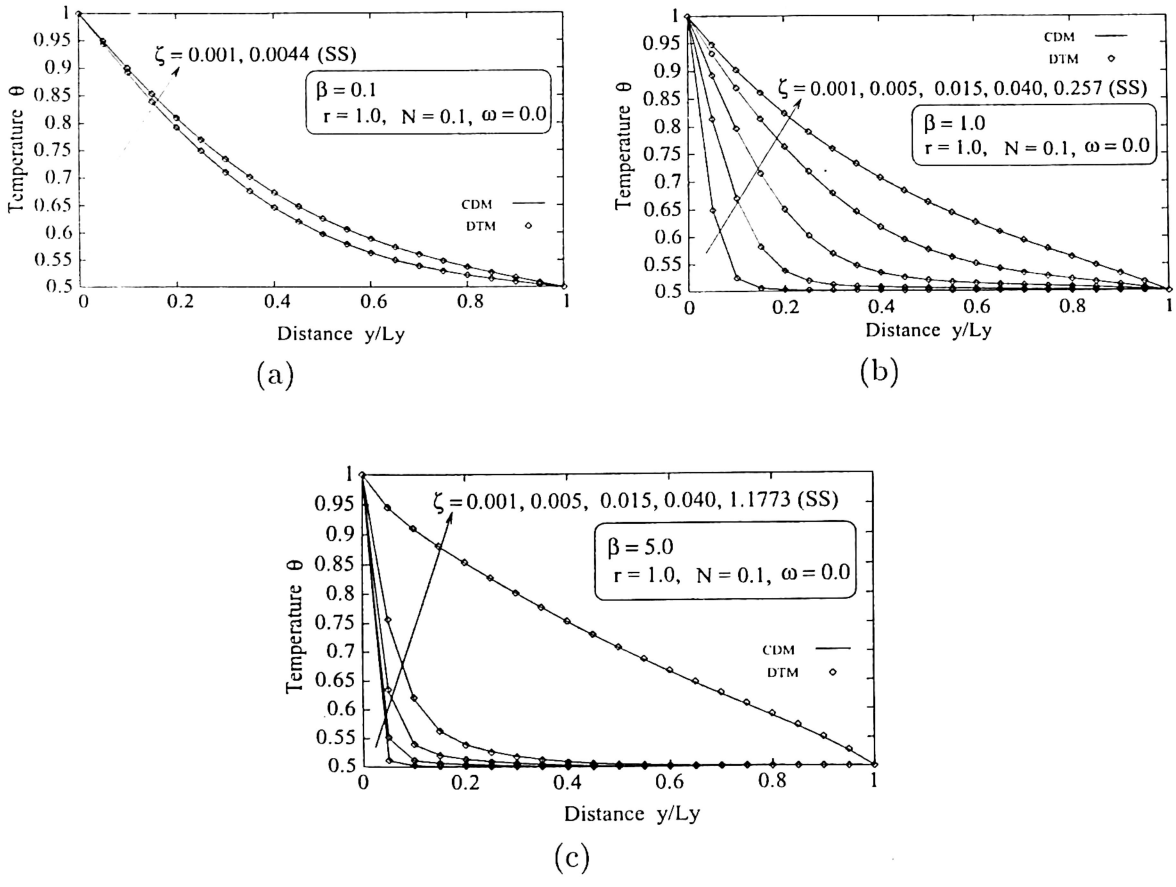


Figure 8.7: Comparison of the CDM and the DTM results for the centerline temperature θ distribution at time ξ = 0.001, 0.005, 0.015, 0.04 and steady state (SS) for extinction coefficient β = (a) 0.1, (b) 1.0 and (c) 5.0.

DTM.

Comparisons of the CDM and DTM results for the effects of hot (south) boundary emissivity ϵ_S on θ distributions at different instants ξ are shown in Fig. 8.9(a)-(c). For these results, the values of β, N, ω and r are 1.0, 0.01, 0.0 and 1.0 respectively. In Fig. 8.9(a)-(c), the hot (south) boundary emissivity ϵ_S = 1.0, 0.5 and 0.1, respectively. However, for all these results, the other three boundaries, viz north, east and the west, are black. As in all previous cases, in this this case also, it is seen that at all times, the CDM and the DTM results compare with each other very well. The

TH-1868_004301

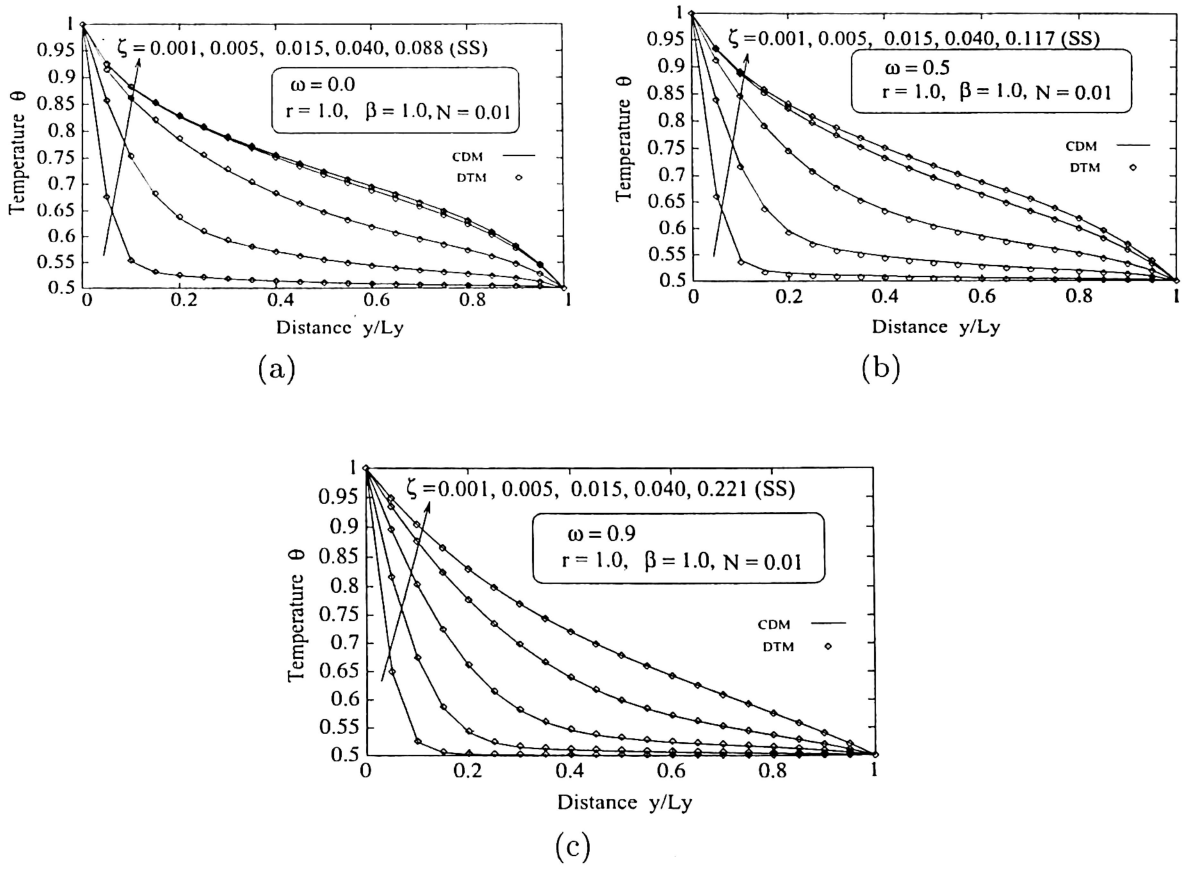


Figure 8.8: Comparison of the CDM and the DTM results for the centerline temperature θ distribution at time $\xi = 0.001, 0.005, 0.015, 0.04$ and steady state (SS) for scattering albedo $\omega =$ (a) 0.0, (b) 0.5 and (c) 0.9.

CDM is about 20 times faster than the DTM.

It can be seen from Fig. 8.9(a)-(c) that when the south boundary is reflecting more ($\epsilon_S = 0.1$), the steady state is attained late and at any instant ξ, the temperature of the medium is lower. Further, for lower values of ϵ_S, the temperature gradients near the hot boundary are higher. As the hot boundary becomes more reflecting, radiation emanating from the hot boundary becomes weak, as a result of which sharp gradients are observed near the hot boundary, the temperature at any instant in the medium is lower and, since the radiative contribution decreases, the steady

TH-1868_004301

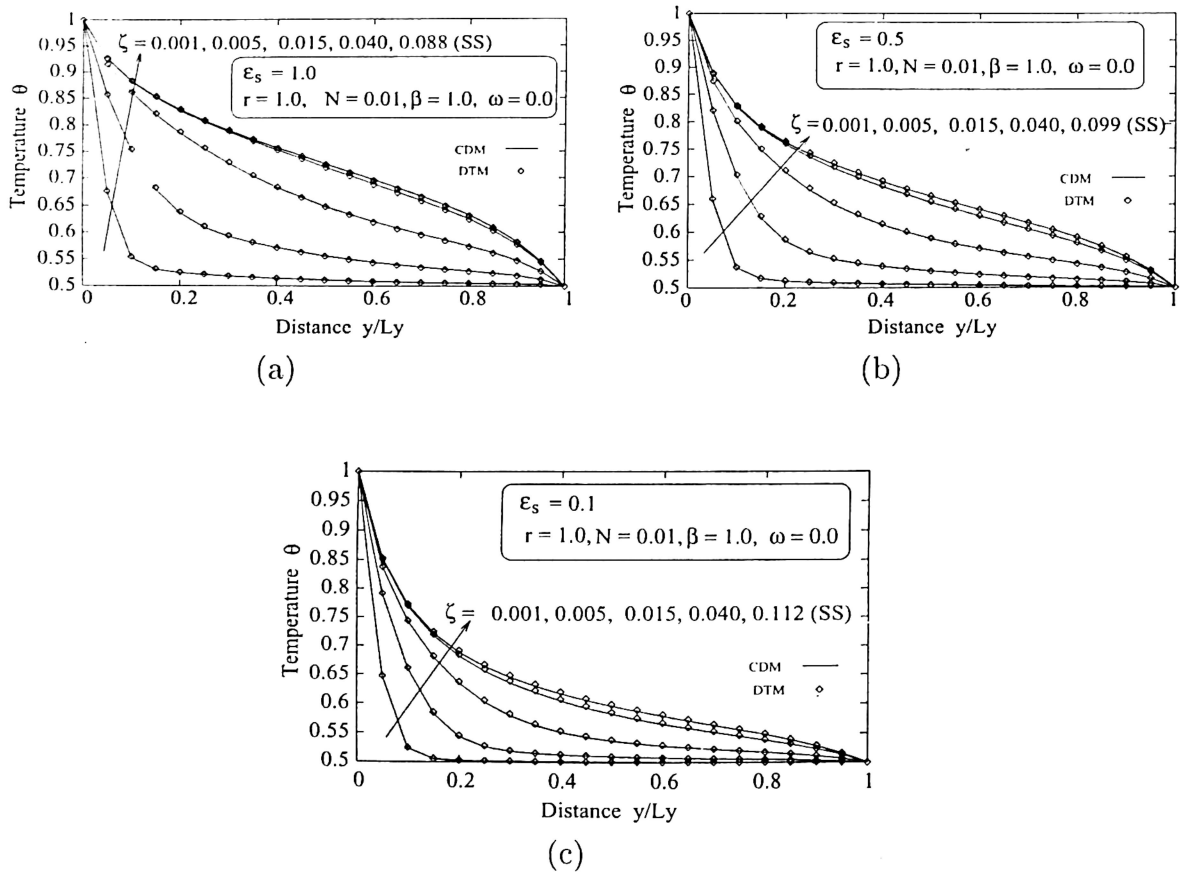


Figure 8.9: Comparison of the CDM and the DTM results for the centerline temperature θ distribution at time ξ = 0.001, 0.005, 0.015, 0.04 and steady state (SS) for the hot (south) boundary emissivity ϵ_S = (a) 1.0, (b) 0.5 and (c) 0.1.

state is reached late.

8.4 Conclusions

The performance of the CDM and the DTM in terms of the computational time and their abilit es to provide accurate results was evaluated for three types of problems. For the boundary emission and the isothermal medium emission cases, the CDM

TH-1868_004301

and DTM results for aspect ratio $r = 1$ were compared with the MCM results. For $r \neq 1$, results from the two methods were compared against each other. For the combined mode problem, for the steady state, for the effects of the extinction coefficient β, the conduction-radiation parameter N, and the scattering albedo ω, the 2-D CDM and the 2-D DTM codes for $r = 10.0$ were found to give the same results as given by the CDM code for the 1-D planar medium [29]. For the black square enclosure ($r = 1$), for various values of N and β, the CDM and DTM steady-state results were found to give an excellent comparison with the results available in the literature [65, 76]. In this way once the 2-D CDM and the 2-D DTM codes had been validated for the boundary emission, the isothermal medium emission and some steady-state benchmark results for the combined mode problems, transient temperature distributions were found and compared for various parameters such as N, β, ω and ϵ_S. For all the parameters considered, the CDM results were found to give an excellent comparison with the DTM results. Further, for all cases, the CDM was found much more economical than the DTM.

TH-1868_004301

Chapter 9

Effect of Variable Thermal Conductivity on 2-D Conduction-Radiation Interaction

9.1 Introduction

For better performance, especially in the design of porous burners and volumetric porous solar receivers, various types of ceramic and foam structures are used [3, 106]. Thermal analysis of such ceramic and foam structures involve consideration of radiation along with conduction and/or convection. In the porous burners because of combustion and in the volumetric porous solar receivers because of an intense solar radiation on the receiving surface, temperature and its gradient in the medium are generally very high. In these applications, in some of the cases, very high temperature in some region has been found to create hot spots causing the failure of the the porous structure [3]. For the varying temperatures in the medium, the thermal conductivity of the medium also undergo sharp variations. Therefore, in

TH-1868_004301

such cases of multi-dimensional geometries, for the correct numerical analysis, the assumption of the constant thermal conductivity does not hold valid. Consideration of the effects of the temperature dependent thermal conductivity in such analysis, thus becomes important.

In chapter 5, the effect of variable thermal conductivity on one-dimensional conduction-radiation heat transfer was discussed. The same work is extended here for two-dimensional rectangular enclosure. As far as combined conduction and radiation heat transfer in a 2-D rectangular enclosure is concerned, so far investigations have not been carried out to study the effects of temperature dependent thermal conductivity. The present work was thus aimed at the study of the effects of temperature dependent thermal conductivity on transient conduction and radiation heat transfer in a 2-D rectangular enclosure containing an absorbing, emitting and scattering medium.

With temperature dependent thermal conductivity, the energy equation becomes a non-linear one and for a 2-D geometry, in the presence of radiation, it poses further complexity in the solution. In the present work, to get rid of the non-linearity, first the time linearization is done, and then the energy equation is solved using the alternating direction implicit (ADI) scheme. The collapsed dimension method (CDM) [29,46,155] is used to obtain the radiative information required for the energy equation.

9.2 Formulation

A 2-D rectangular geometry is considered here (Fig. 8.1). All four walls are diffuse and gray, and the contained homogeneous medium is absorbing, emitting and scattering. Thermophysical properties such as the density ρ, the specific heat C_p, and the optical property, the extinction coefficient β, are assumed to be constant.

Initially at time $t = 0$, the entire system is at some finite temperature T_O. For

TH-1868_004301

time $t > 0$, the bottom (South) wall is brought to temperature $T_S = 2T_O$. The thermal conductivity of the medium is assumed to vary linearly with temperature. Its variation with temperature is given by

$$k = k_0 + \gamma'(T - T_S) \tag{9.1}$$

where k_0 is the reference thermal conductivity and γ' is the coefficient of thermal conductivity variation. In the absence of convection and heat generation, for a 2-D rectangular geometry, the equation for conservation of total energy is

$$\rho C_p \frac{\partial T}{\partial t} = \frac{\partial}{\partial x}\left(k\frac{\partial T}{\partial x}\right) + \frac{\partial}{\partial y}\left(k\frac{\partial T}{\partial y}\right) - \nabla \cdot q_R \tag{9.2}$$

After substituting for k from Eq. (9.1) in Eq. (9.2), the resulting equation in non-dimensional form is

$$\frac{\partial \theta}{\partial \xi} = \left(1 + \frac{\gamma(\theta - 1)}{N}\right)\left(\frac{\partial^2 \theta}{\partial \tau_x^2} + \frac{\partial^2 \theta}{\partial \tau_y^2}\right) + \frac{\gamma}{N}\left[\left(\frac{\partial \theta}{\partial \tau_x}\right)^2 + \left(\frac{\partial \theta}{\partial \tau_y}\right)^2\right] - \frac{1}{4N}\nabla \cdot \Psi_R \tag{9.3}$$

where $\tau_x = \beta x$ and $\tau_y = \beta y$ are the optical coordinates in the x and y coordinate directions (Fig. 8.1), respectively. It should be noted that in Eq. (9.2), $\nabla = (\frac{\partial}{\partial x} + \frac{\partial}{\partial y})$ and in Eq. (9.3), $\nabla = (\frac{\partial}{\partial \tau_x} + \frac{\partial}{\partial \tau_y})$. The above equations are non-dimensionalized taking bottom wall temperature T_S as the reference temperature. The non-dimensional quantities are defined exactly same way as in Chapter 5 and so are not repeated here.

The initial and the boundary conditions for the problem under consideration are the following:

$$\begin{aligned} \text{Initial condition:} \quad & \theta(\tau_x, \tau_y, 0) = 0.5 \\ \text{Boundary conditions:} \quad & \theta(0, \tau_y, \xi) = 0.5 \\ & \theta(\tau_{L_x}, \tau_y, \xi) = 0.5 \\ & \theta(\tau_x, 0, \xi) = 1.0 \\ & \theta(\tau_x, \tau_{L_y}, \xi) = 0.5 \end{aligned} \tag{9.4}$$

Substituting the value of $\nabla \cdot \Psi_R$ (Eq. 3.4) for the CDM, the equation to be solved is

TH-1868_004301

$$\frac{\partial\theta}{\partial\xi} = \left(1+\frac{\gamma(\theta-1)}{N}\right)\left(\frac{\partial^2\theta}{\partial\tau_x^2}+\frac{\partial^2\theta}{\partial\tau_y^2}\right)+\frac{\gamma}{N}\left[\left(\frac{\partial\theta}{\partial\tau_x}\right)^2+\left(\frac{\partial\theta}{\partial\tau_y}\right)^2\right] - \frac{\Gamma(1-\omega)}{4N}\left(\pi\theta^4-\frac{G'^*}{2}\right) \tag{9.5}$$

Equation (9.5) is a highly non-linear equation. Apart from the non-linearity because of the radiative term, because of the temperature dependent thermal conductivity, other terms on the right-hand side of Eq. (9.5) are also non-linear. To facilitate the solution of the non-linear equation, the time linearization technique is employed, which results in the following equation.

$$\begin{aligned}\frac{\partial\theta}{\partial\xi} &- \left(1+\frac{\gamma(\theta-1)}{N}\right)_m\left(\frac{\partial^2\theta}{\partial\tau_x^2}+\frac{\partial^2\theta}{\partial\tau_y^2}\right)_{m+1} \\ &- \frac{\gamma}{N}\left[\left(\frac{\partial\theta}{\partial\tau_x}\right)_m\left(\frac{\partial\theta}{\partial\tau_x}\right)_{m+1}+\left(\frac{\partial\theta}{\partial\tau_y}\right)_m\left(\frac{\partial\theta}{\partial\tau_y}\right)_{m+1}\right] \\ &= \left[\frac{\Gamma(1-\omega)}{4N}\left(\pi\theta^4-\frac{G'^*}{2}\right)\right]_m\end{aligned} \tag{9.6}$$

In Eq. (9.6), suffixes m and $m+1$ indicate the time steps. For solving θ at the $(m+1)$th step, all terms at mth step are known from the previous step. With terms causing non-linearity, including the radiative term on the right-hand side known at the mth step, θ values at the $(m+1)$th step are evaluated using the ADI scheme. When the calculation starts for the first time, terms at mth level are computed from the initial values.

In solving Eq. (9.6), for grid and ray independent solutions, 20×20 control volumes and 64 rays were used. The transient problem were solved with the time step $\Delta\xi = 0.0001$, and steady-state conditions were assumed to have been achieved when the temperature difference between two consecutive time levels at each grid point did not exceed 0.00001. The collapsing coefficient Γ values (see the appendix) for any β and ω were calculated from the expressions given in [117]. In the following paragraphs, all results are presented for grid and ray independent situations.

TH-1868_004301

9.3 Results and Discussion

Results for the effects of the coefficient of thermal conductivity variation γ on temperature and heat flux distributions are presented for both steady state and transient situations. For black walls and scattering albedo $\omega = 0.5$, these results are presented for different values of the aspect ratio r, the conduction-radiation parameter N and the extinction coefficient β. To validate the results for the 2-D rectangular geometry code, for a sample case of high aspect ratio ($r = L_x/L_y = 10$), results are compared with those for the 1-D planar medium case [26]. It should be noted that the cases in which the aspect ratio r was varied, L_y was always kept at unity. In all the cases where the effect of γ has been studied, the positive value of γ means that the thermal conductivity increases with increase of temperature whereas its negative value signifies that the thermal conductivity decreases with increase in temperature. The zero value indicates the case of constant thermal conductivity.

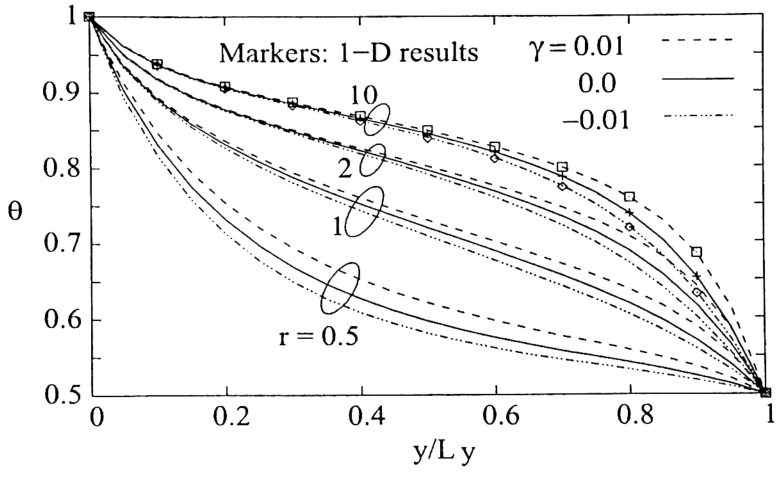


Figure 9.1: Effect of γ on centerline temperature θ for different values of the aspect ratio r; $\beta = 1$, $N = 0.01$ and $\omega = 0.5$.

TH-1868_004301

Steady state results

In Fig. 9.1, effect of γ on centerline ($x/L_x = 0.5$) temperature θ profile is shown. For γ = - 0.01, 0.0 and 0.01, these θ profiles are shown for aspect ratio r = 0.5, 1, 2, and 10. These results are presented for conduction-radiation parameter N = 0.01 and extinction coefficient β = 1.

It can be seen from Fig. 9.1 that for a given value of N and β, the effect of γ is greater for the lower values of r. With increase in r, the effect increases towards the top (cold) wall. Further, for the same amount of change in γ, effect is greater for

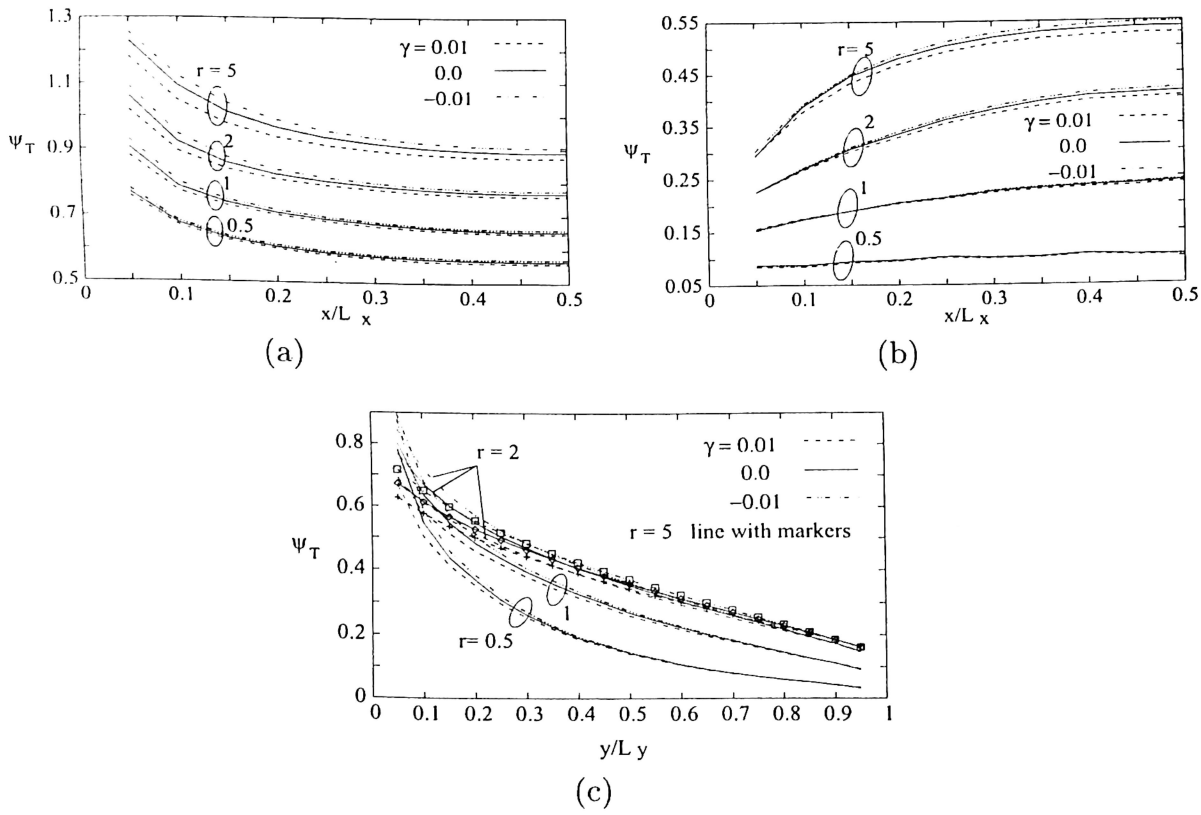


Figure 9.2: Effect of γ on total heat flux Ψ_T at (a) the bottom (hot) wall, (b) the top wall and (c) the side wall(s) for different values of the aspect ratio r; β = 1, N = 0.01 and ω = 0.5.

TH-1868_004301

the positive value of γ. At all y/L_y locations, θ is higher for the higher values of γ. For $r = 10$, for the three values of γ, the 2-D rectangular geometry results are found to perfectly match with those for the 1-D planar medium results obtained using the discrete transfer method [26].

Figure 9.2(a)-(c) shows the effect of γ on variations of total heat flux Ψ_T at the bottom (hot), the top and the side walls, respectively. For $N = 0.01$ and $\beta = 1$, here these effects are shown for $r = 0.5$, 1, 2 and 5. It can be seen from this figure that the effect of γ on Ψ_T is greater for higher values of r. For a given r, at the bottom (hot) wall (Fig. 9.2(a)), effect is less in the center and it increases towards the side walls. For the top wall (Fig. 9.2(b)), the effect is greater in the center

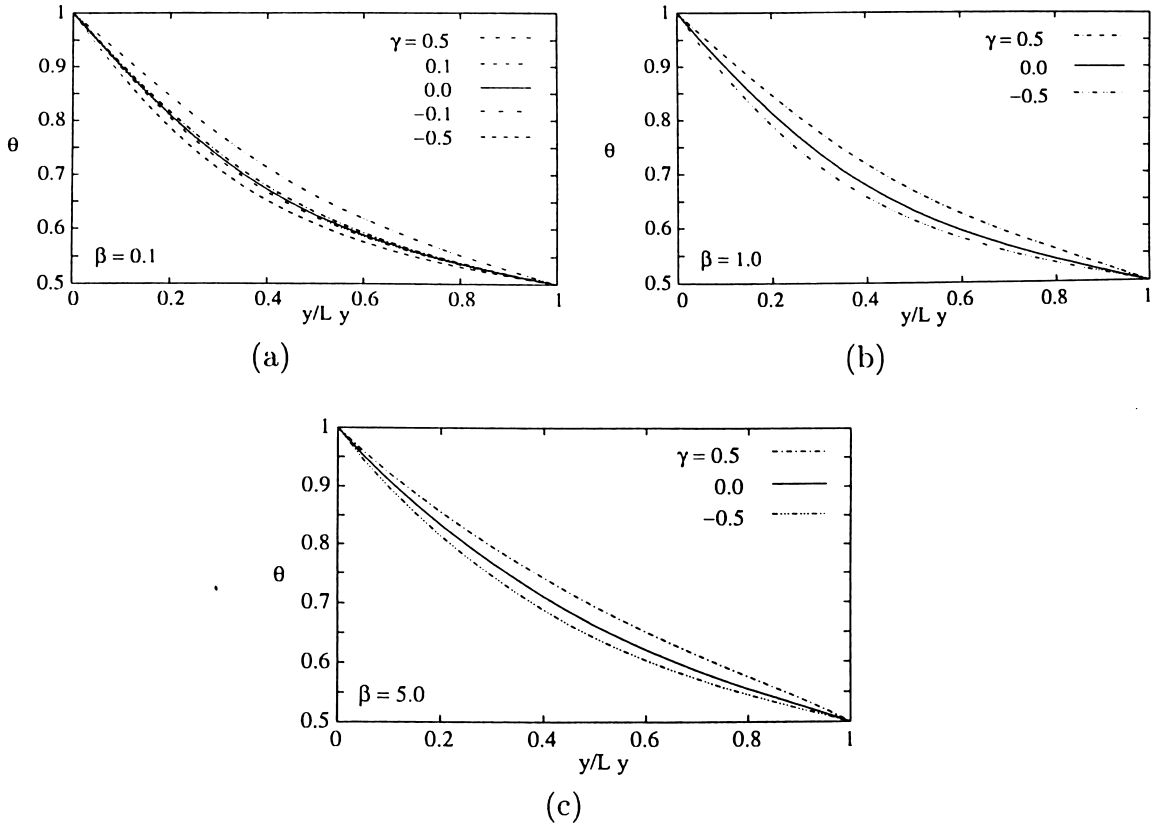


Figure 9.3: Effect of γ on centerline temperature θ profile for the extinction coefficient β = (a) 0.1, (b) 1.0 and (c) 5.0; $r = 1$, $N = 0.5$ and $\omega = 0.5$.

TH-1868_004301

whereas for the side wall(s) (Fig. 9.2(c)), effect is greater towards the bottom (hot) wall.

In Fig. 9.3(a)-(c), effect of γ on the centerline θ profiles is shown for the extinction coefficient $\beta = 0.1$, 1 and 5, respectively. For these results, $r = 1$, $N = 0.5$ and $\omega = 0.5$. From this figure it is seen that for different values of β, effect of γ on θ remains almost the same. For different values of β, for the effect of γ, similar trends are observed for other combinations of r, N and ω.

For the cases considered in Fig. 9.3, the total heat flux Ψ_T results at the bottom (hot) wall are presented in Fig. 9.4. Unlike the effect on θ variations, for different

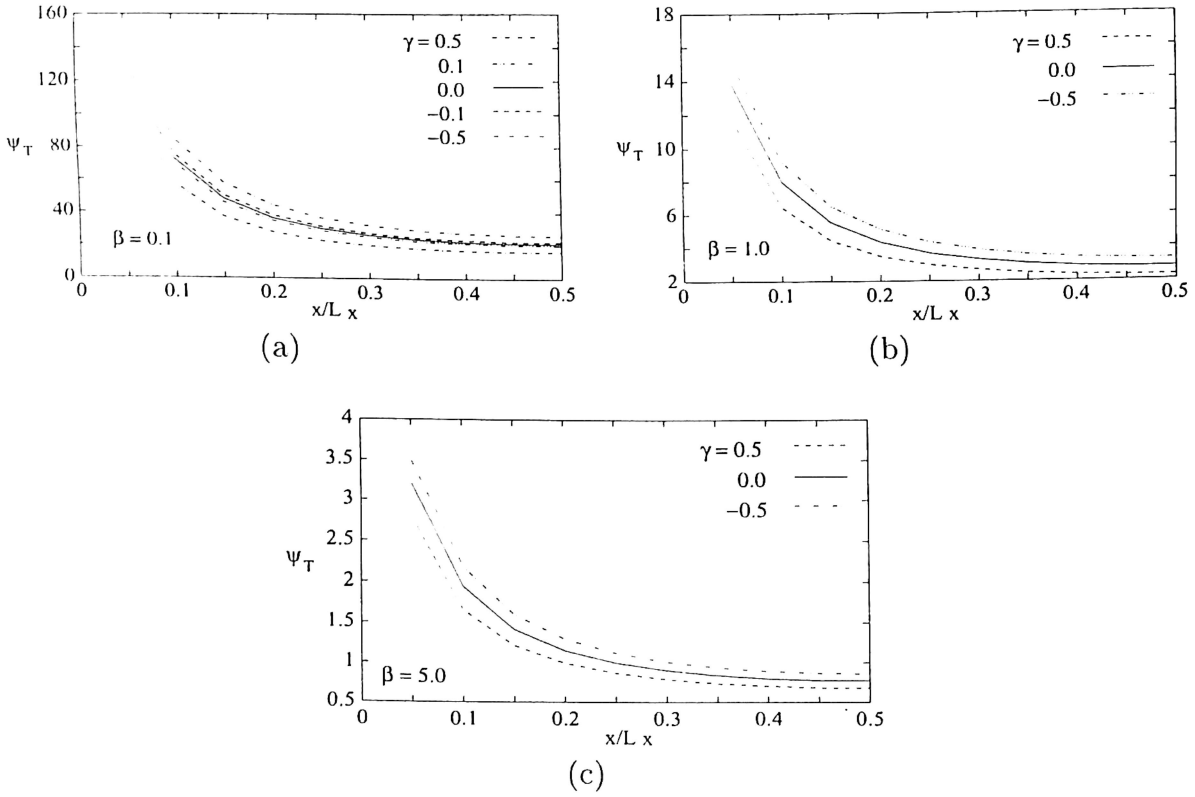


Figure 9.4: Effect of γ on total heat flux Ψ_T at the bottom (hot) wall for the extinction coefficient β = (a) 0.1, (b) 1.0 and (c) 5.0; $r = 1$, $N = 0.5$ and $\omega = 0.5$.

TH-1868_004301

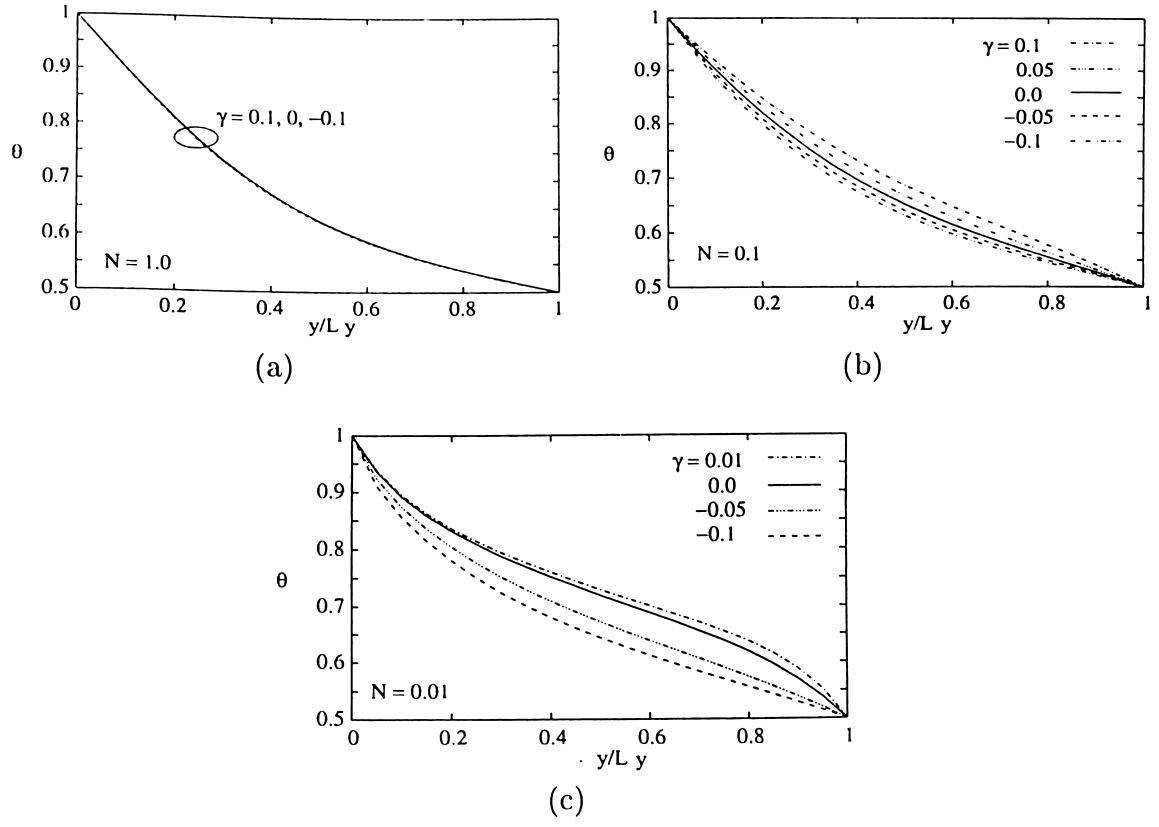


Figure 9.5: Effect of γ on centerline temperature θ profile for the conduction-radiation parameter N = (a) 1, (b) 0.1 and (c) 0.01; $r = 1$, $\beta = 1$ and $\omega = 0.5$.

values of β, in this case, effect of γ is greater. The effect is greater for the lower values of β.

In Fig. 9.5(a)-(c), effect of γ on centerline θ profile is shown for conduction-radiation parameter N =1, 0.1, and 0.01, respectively. For results presented in this figure, r =1, $\beta = 1$ and $\omega = 0.5$. It is seen from this figure that in the radiation dominated situation (lower values of N), γ effect is greater.

For parameters considered in Fig. 9.5, the total heat flux Ψ_T variations at the bottom wall are given in the Fig. 9.6(a)-(c). In this case also, γ is seen to have significant effect for the lower values of N.

TH-1868_004301

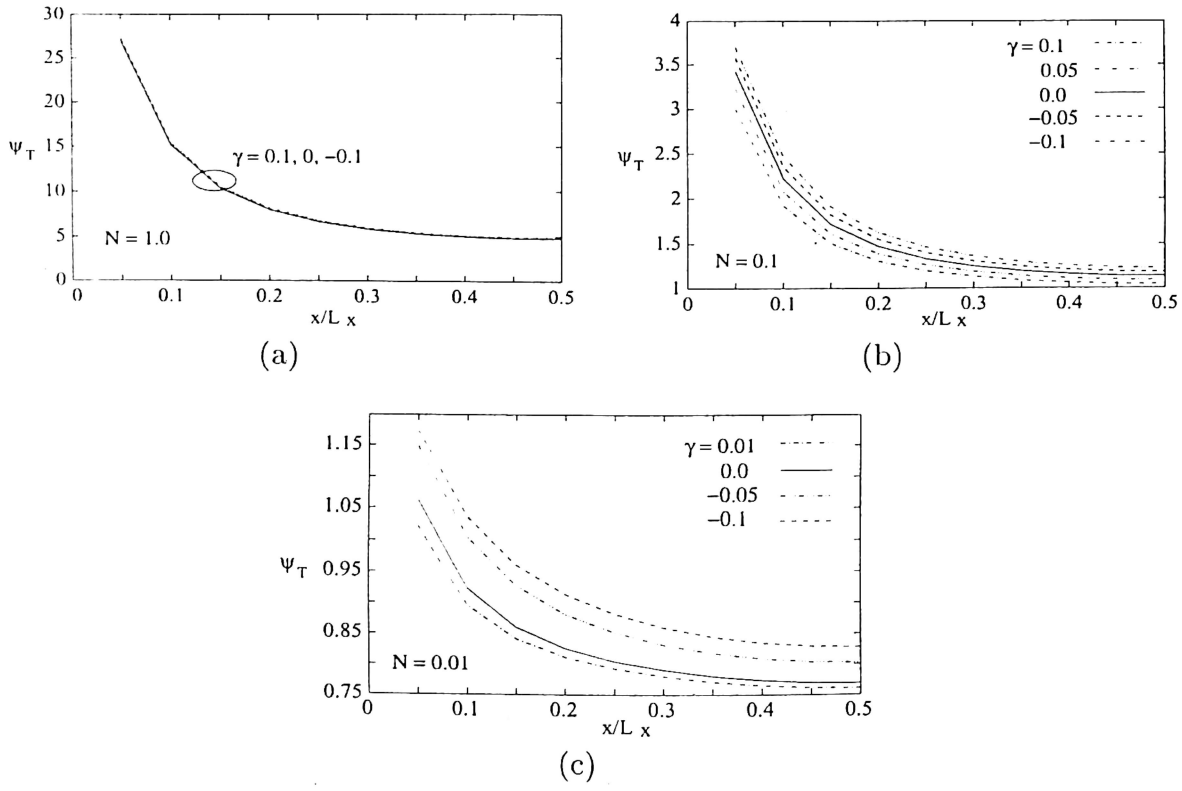


Figure 9.6: Effect of γ on total heat flux Ψ_T at the bottom (hot) wall for the conduction-radiation parameter N = (a) 1, (b) 0.1 and (c) 0.01; $r = 1$, $\beta = 1$ and $\omega = 0.5$.

The trends for the variations of Ψ_T results as shown in Fig. 9.6 can be better understood from Fig. 9.7. For N values ranging from 0.005 to 1.0, in this figure, percentage change in Ψ_T corresponding to $\gamma = 0.01$ and - 0.01 are plotted at the bottom (hot) wall. The percentage change has been calculated as

$$\frac{\Psi_T(\gamma = 0.01) - \Psi_T(\gamma = -0.01)}{\frac{(\Psi_T(\gamma=0.01)+\Psi_T(\gamma=-0.01))}{2.0}}) \times 100$$

With change in N, this figure clearly indicates the effect of γ on Ψ_T. The percentage change in Ψ_T is higher for the radiation dominated situation (lower values of N). For these results $r = 1$, $\beta = 1$ and $\omega = 0.5$.

TH-1868_004301

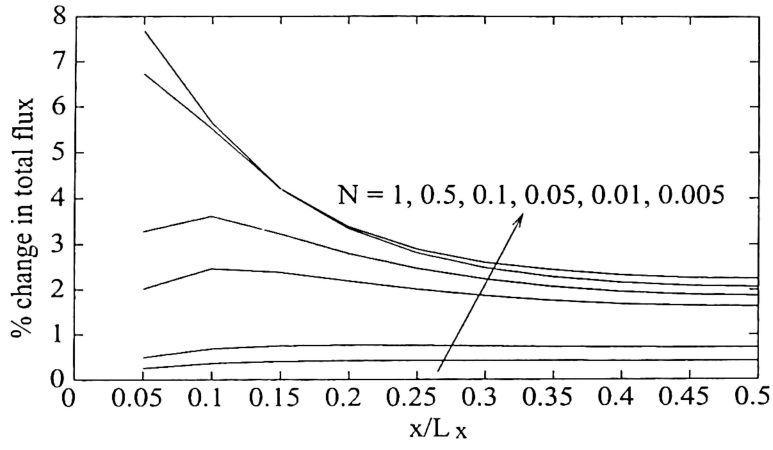


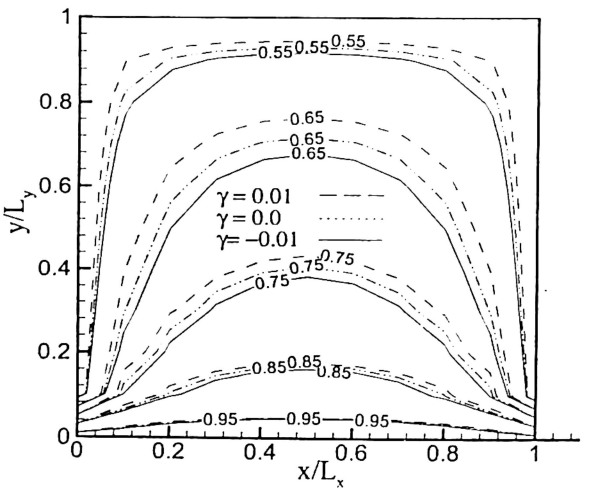
Figure 9.7: Percentage change in total heat flux Ψ_T due to the effect of γ for different values of the conduction-radiation parameter N; $r = 1$, $\beta = 1$ and $\omega = 0.5$.

To have an idea about the effect of γ on temperature distribution in the enclosure, for $N = 0.01$ and 0.1, isotherms are given in Fig. 9.8(a) and (b), respectively. For these results $r = 1$, $\beta = 1$ and $\omega = 0.5$. For a particular γ, the temperature difference between two contours is 0.1, and the minimum and the maximum values of the contours are 0.55 and 0.95, respectively. It can be seen from this figure that for the radiation dominated situations (N=0.01), temperature distribution is more uniform in the enclosure. For a given value of N, temperature becomes more uniform for the higher values of γ.

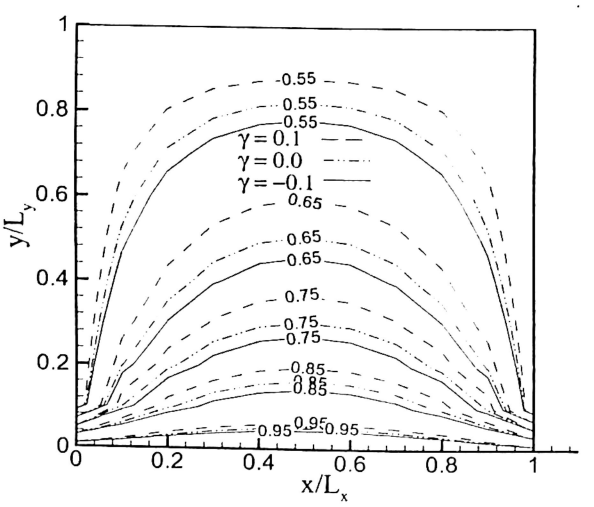
Transient results

In Figs. 9.9 and 9.10, the effects of γ on temperature θ are given for the transient situation. In Fig. 9.9(a)-(c) effect of γ on transient θ distributions are shown for N= 0.01, 0.1, and 1.0, respectively. For these results, $r = 1$, β =1 and $\omega = 0.5$. θ distributions have been plotted at non-dimensional time $\xi = 0.001$, 0.005, 0.015, 0.04 and the steady state. It is seen from this figure that the effect of γ increases as θ reaches steady state value. At all times ξ, in radiation dominated situation, effect

TH-1868_004301



(a)



(b)

Figure 9.8: Isotherms showing the effect of γ for N = (a) 0.01 and (b) 0.1; $r = 1$, $\beta = 1$ and $\omega = 0.5$.

of γ is found greater.

TH-1868_004301

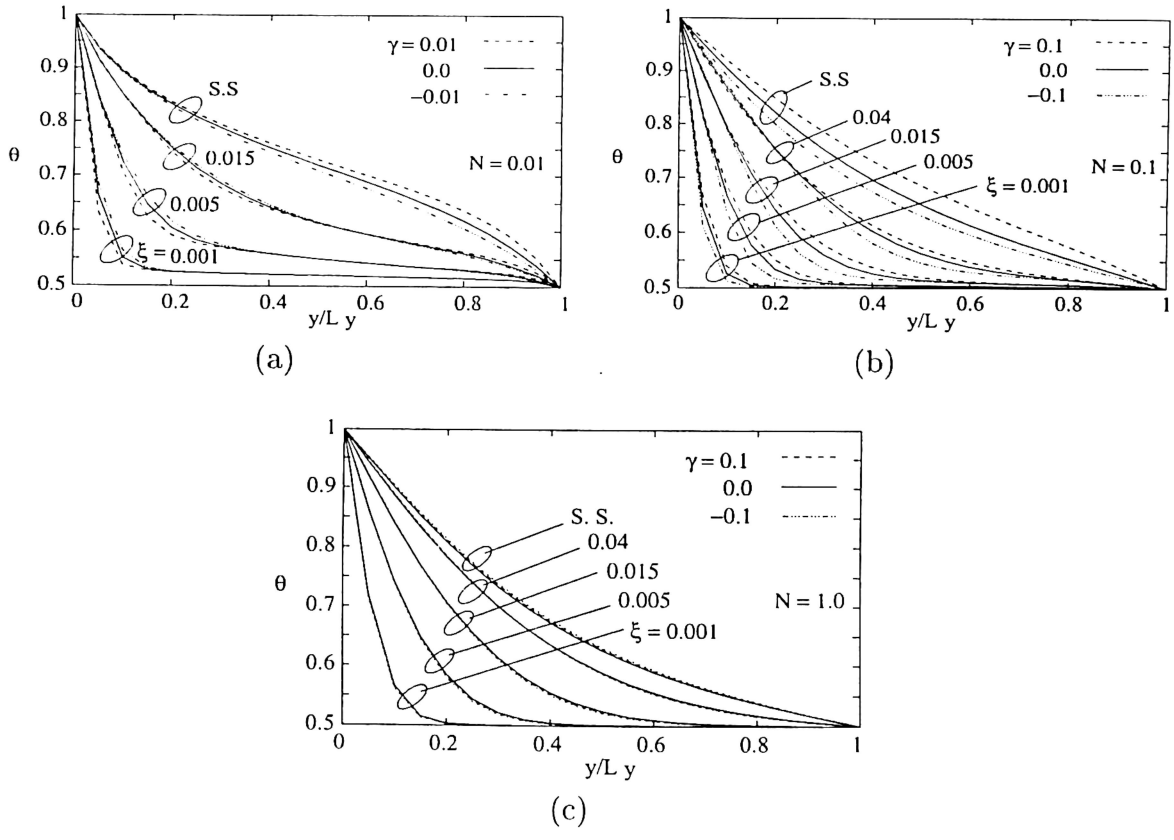


Figure 9.9: Effect of γ on transient temperature θ along the centerline for the conduction-radiation parameter N = (a) 0.01, (b) 0.1 and (c) 1; $r = 1$, $\beta = 1$ and $\omega = 0.5$.

In Fig. 9.10(a)-(c), variations of θ with non-dimensional time ξ are given at two locations, viz., $y/L_y = 0.25$ and 0.75 along the centerline ($x/L_x = 0.5$). These two locations are equidistant from the bottom and the top walls. For $r = 1$, $\beta = 1$ and $\omega = 0.5$, in Fig. 9.10(a)-(c), θ distributions are given for $N = 0.01$, 0.1 and 1, respectively. It is seen from the plots that compared with the case of constant thermal conductivity ($\gamma = 0.0$), the time to reach the steady state increases with positive value of γ and it decreases with the negative value of γ.

TH-1868_004301

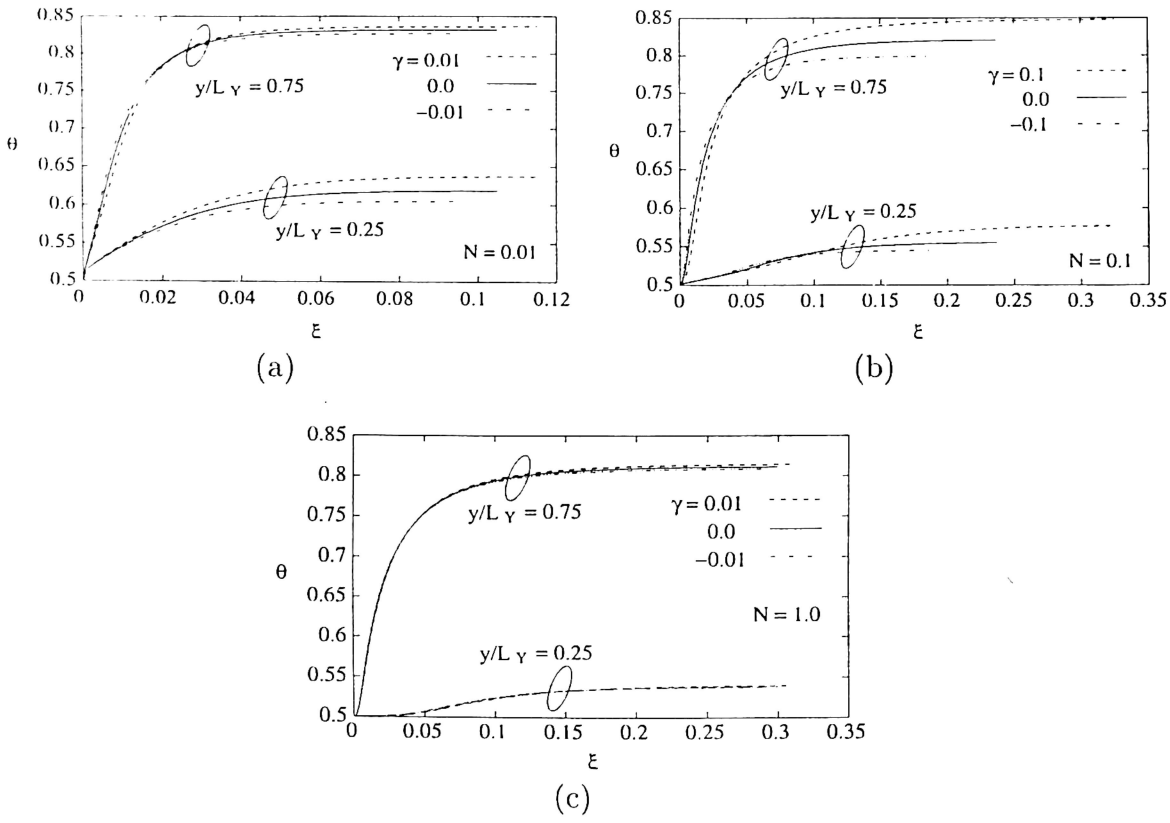


Figure 9.10: Effect of γ on transient temperature at locations $y/L_y = 0.25$ and 0.75 along the centerline ($x/L_x = 0.5$) for the conduction-radiation parameter N = (a) 0.01, (b) 0.1 and (c) 1; $r = 1$, $\beta = 1$ and $\omega = 0.5$.

9.4 Conclusions

Steady state and transient conduction and radiation heat transfer problems with variable thermal conductivity were investigated for a 2-D black rectangular enclosure containing an absorbing, emitting and scattering medium. Thermal conductivity was assumed to vary linearly with temperature. The CDM was used to solve the radiative part of the energy equation. After doing time linearization, the energy equation was solved using the ADI scheme. For scattering albedo $\omega = 0.5$, steady state temperature and heat flux results for the effects of variable thermal conductivity were obtained for different values of the aspect ratio r, the extinction coefficient

TH-1868_004301

β and the conduction-radiation parameter N. For different values of N, transient temperature results for effect of the variable thermal conductivity were also presented for different values of N. For the aspect ratio r and the conduction-radiation parameter N, the variable thermal conductivity was found to have significant effect on temperature and heat flux distributions. For different values of β, the variable thermal conductivity was found to have almost the same effect on the centerline temperature variation. However, for the hot wall heat flux, the effect was found greater for the lower values of β.

TH-1868_004301

Chapter 10

Heat Transfer Characteristics of a Porous Radiant Burner

10.1 Introduction

In the last decade, devices based on porous medium combustion have emerged as a potential alternative to devices based on free flame combustion. This shift has been directed by the needs of industry to develop high-performance burners while complying with the increasingly stringent emissions regulations. Burners and radiant heaters based on porous medium combustion have distinctive advantages over those based on free flame combustion. Devices based on porous medium combustion are characterized by high power density, very low emissions of pollutants such as NOx and CO, high flame speeds, extended lean flammability limits, homogeneous temperature level, large power modulation range and compact size. Because of these desirable features, porous medium combustion finds applications in diverse fields such as paper drying, paper finishing, powder and paint curing, baking, textile drying, polymer thermal processing, glass manufacturing, household heating systems,

TH-1868_004301

etc. [105, 156].

Owing to the simplicity of the analysis, a numerous studies on porous medium combustion have been devoted to 1-D planar or cylindrical porous burners [9, 109, 110, 157–159]. In these, the analysis were done by assuming the solid matrix and the gas phase to be in non-local thermal equilibrium. Further, for 1-D porous burners, combustion was simulated by an artificial heat generation zone within the porous medium [110] or by a one-step global mechanism [109] or by multi-step detailed chemical kinetics [158–160]. Heat transfer by radiation was incorporated by considering the solid matrix to be absorbing, emitting and/or scattering [109, 110, 159, 160].

As far as numerical analysis of 2-D rectangular porous burners is concerned, not much work has been directed towards the characterization of these burners. For a 2-D rectangular burner, Hackert et al. [161] analyzed two simple geometries. One geometry considered was a honeycomb porous medium consisting of parallel non-connecting passages, and the other was with walls parallel but broken such that there was no continuous solid path. They simulated combustion by a single-step global reaction mechanism and used the Monte Carlo method to account for the surface radiative exchange. However, they did not consider the porous medium to be absorbing, emitting and scattering, and therefore the effect of radiative parameters such as the extinction coefficient and the scattering albedo on the performance of the burner could not be studied. Brenner et al. [146] carried out a numerical and experimental investigation of a 2-D rectangular porous radiant burner. In their study, the porous matrix was made of SiC. They considered detailed chemical kinetics to simulate the combustion and solved the continuity, momentum and energy equations. However, in their analysis, they considered the solid and the gas phase to be in local thermal equilibrium and in the energy equation, radiation was accounted by the experimentally determined effective conductivity.

In porous medium combustion, radiation is the dominant mode of heat transfer [9, 110, 157, 159, 160, 162–164] and the performance of the burners is greatly influenced by the radiative parameters. From the literature review it was found that for a 2-D

TH-1868_004301

rectangular porous burner, so far investigations have not been carried out to study the influence of radiative parameters such as the extinction coefficient, the scattering albedo, the emissivity, etc. Therefore, the present work is mainly aimed at the heat transfer analysis of a 2-D rectangular porous burner in which the influence of various parameters on temperature and heat flux distributions is studied. To study the influence of various parameters, analysis are made for both steady-state and transient situations. Since locally the solid and the gas temperatures could be different, non-local thermal equilibrium is considered between the two phases and, therefore, separate energy equations are solved for the two phases. Combustion is modeled as a spatially dependent heat generation zone. Flow is considered to be constant and therefore only energy equations are solved. The radiative part of the solid-phase energy equation is computed using the collapsed dimension method (CDM). The alternating direction implicit scheme is used to solve the gas-phase and the solid-phase energy equations.

10.2 Formulation

The problem under consideration is shown schematically in Fig. 10.1. An inert porous medium of length L_x and thickness L_y is placed in between two parallel adiabatic plates. The dimensions of both the adiabatic plates and the porous medium in the direction normal to the plane of the paper (z direction, not shown) are very large compared with the other two dimensions. Hence, the effect of this third spatial dimension is neglected. The gaseous fuel-air mixture enters the porous medium from the left with uniform velocity u. In the porous medium, the slug-flow condition is assumed. Adiabatic plates extend to a length $-x_i$ upstream and to a length $(x_e - L_x)$ downstream of the porous medium. The uniform heat generation zone of dimensions $\Delta x \times L_y$, representing combustion, is situated in the porous region and its location can be variable. The porous solid matrix is assumed to be gray, and to emit, absorb and scatter radiation isotropically. Gaseous radiation is neglected compared with the solid radiation. Since locally the solid and the gas temperatures may be different, non-local thermal equilibrium between the solid and the gas is

TH-1868_004301

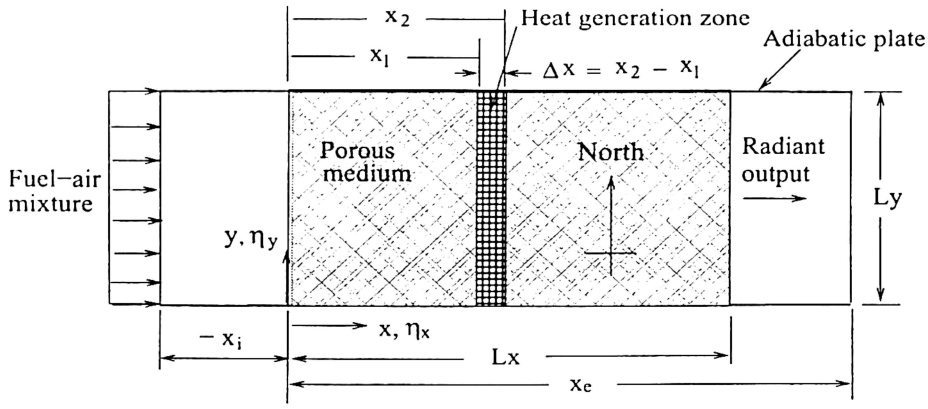


Figure 10.1: Schematic diagram of the problem under consideration.

accounted by considering separate energy equations for the two phases. The two equations are coupled through a convective heat transfer term that accounts for the inter-phase heat exchange. All properties of the solid and the gas phases are assumed to be uniform and constant.

Initially both the phases are at the ambient temperature T_i, and for times greater than zero, combustion modeled as a uniform heat generation zone is introduced in the medium.

The energy equations for the gas and the solid phases are written respectively as follows:

$$\phi\rho_g c_g\left(\frac{\partial T_g}{\partial t}+u\frac{\partial T_g}{\partial x}\right)+(1-\phi)Ah(T_g-T_s)=\phi Q'''\delta(x)+\phi k_g\left(\frac{\partial^2 T_g}{\partial x^2}+\frac{\partial^2 T_g}{\partial y^2}\right) \quad (10.1)$$

$$(1-\phi)\rho_s c_s\frac{\partial T_s}{\partial t}=(1-\phi)Ah(T_g-T_s)+(1-\phi)k_s\left(\frac{\partial^2 T_s}{\partial x^2}+\frac{\partial^2 T_s}{\partial y^2}\right)-\nabla\cdot q_R \quad (10.2)$$

where ϕ, ρ, c, k, h and A are porosity, density, specific heat, thermal conductivity, heat transfer coefficient and specific surface area, respectively. The term $Q'''\delta(x)$ is the unit heat generation and $\delta(x)$ is the delta function defined as unity for $x_1 \leq x \leq x_2$ and zero elsewhere. In Eq. (10.2), q_R is the radiative heat flux.

TH-1868_004301

In non-dimensional form, Eqs. (10.1) and (10.2) are written as follows:

$$\phi P_3 \frac{\partial \theta_g}{\partial \xi} + \phi P_1 \frac{\partial \theta_g}{\partial \eta_x} + (1-\phi) P_2 (\theta_g - \theta_s) = \phi \delta(\eta_x) + \phi P_3 \left(\frac{\partial^2 \theta_g}{\partial \eta_x^2} + \frac{\partial^2 \theta_g}{\partial \eta_y^2} \right) \quad (10.3)$$

$$(1-\phi) P_5 \frac{\partial \theta_s}{\partial \xi} = (1-\phi) \frac{P_4}{P_3} \left(\frac{\partial^2 \theta_s}{\partial \eta_x^2} + \frac{\partial^2 \theta_s}{\partial \eta_y^2} \right) + (1-\phi) \frac{P_2}{P_3} (\theta_g - \theta_s) - \frac{1}{P_3} \nabla \cdot \Psi_R \quad (10.4)$$

where $\eta_x = x/L_x$ and $\eta_y = y/L_x$ are the non-dimensional lengths in the x and y directions, respectively. It should be noted that in Eq. (10.2) $\nabla = (\frac{\partial}{\partial x} + \frac{\partial}{\partial y})$ and in Eq. (10.4) $\nabla = (\frac{\partial}{\partial \eta_x} + \frac{\partial}{\partial \eta_y})$.

Equation (10.3) is applied to the entire domain shown in Fig. 10.1, that is, $-\eta_{x_i} \leq \eta_x \leq \eta_{x_e}$. Accordingly, ϕ is defined such that ϕ =1 for $\eta_x < 0$, $0 \leq \phi \leq 1$ for $0 \leq \eta_x \leq 1$ and ϕ =1 for $\eta_x > 1$. The computational domain for Eq. (10.3) has been extended beyond the porous region on either side to model accurately flames close to the edges of the porous region.

In Eqs. (10.3) and (10.4), non-dimensional values of temperature θ, time ξ, radiative heat flux Ψ_R and parameters P_1 to P_5 are defined as

$$\theta = \frac{T - T_i}{T_i}, \quad \xi = \frac{t}{\rho_g c_g L_x^2 / k_g}, \quad \Psi_R = \frac{q_R}{Q''' L_x}$$

$$P_1 = \frac{\rho_g u c_g T_i}{L_x}, \quad P_2 = \frac{hAT_i}{Q'''}, \quad P_3 = \frac{k_g T_i}{Q''' L_x^2}, \quad P_4 = \frac{k_s T_i}{Q''' L_x^2}, \quad P_5 = \frac{\rho_s c_s}{\rho_g c_g}$$

In the above, parameters $P_1 - P_4$ give the measure of flow enthalpy, convective energy coupling between gas and solid, gas conduction and solid conduction, respectively.

The initial conditions for both the gas-phase and solid-phase energy equations are

$$\theta_g = 0, \quad \theta_s = 0 \quad (10.5)$$

At the inlet ($\eta_x = -\eta_{x_i}$), gas is at the ambient temperature T_i, and at the exhaust section ($\eta_x = \eta_{x_e}$), a vanishing gradient condition is assumed to prevail [156]. The south ($\eta_y = 0$) and north ($\eta_y = \eta_{L_y}$) boundaries are insulated. With these, the

TH-1868_004301

boundary conditions for the gas-phase energy equation (Eq. (10.3)) are the following:

$$\begin{aligned} \theta_g &= 0 \quad \text{at} \quad \eta_x = -\eta_{x_i} \\ \frac{\partial \theta_g}{\partial \eta_x} &= 0 \quad \text{at} \quad \eta_x = \eta_{x_e} \\ \frac{\partial \theta_g}{\partial \eta_y} &= 0 \quad \text{at} \quad \eta_y = 0 \\ \frac{\partial \theta_g}{\partial \eta_y} &= 0 \quad \text{at} \quad \eta_y = \eta_{Ly} \end{aligned} \tag{10.6}$$

For the solid phase, in the gas flow direction, at locations $\eta_x = 0$ and $\eta_x = 1$, heat transfer between the gas and the solid is by conduction, convection and radiation. On the other hand, like the gas phase, the south ($\eta_y = 0$) and the north ($\eta_y = \eta_{Ly}$) boundaries of the porous medium are insulated. So , the boundary conditions for the solid-phase energy equation (Eq. (10.4)) are the following:

$$\begin{aligned} -\frac{\partial \theta_s}{\partial \eta_x} + \frac{P_7}{1-\phi}(\theta_s^4 - \theta_i^4) &= P_6(\theta_g - \theta_s) \quad \text{at} \quad \eta_x = 0 \\ \frac{\partial \theta_s}{\partial \eta_x} + \frac{P_7}{1-\phi}(\theta_s^4 - \theta_e^4) &= P_6(\theta_g - \theta_s) \quad \text{at} \quad \eta_x = 1 \\ \frac{\partial \theta_s}{\partial \eta_y} &= 0 \quad \text{at} \quad \eta_y = 0 \\ \frac{\partial \theta_s}{\partial \eta_y} &= 0 \quad \text{at} \quad \eta_y = \eta_{Ly} \end{aligned} \tag{10.7}$$

where θ_e is the outlet ambient temperature and $P_6 = hL_x/k_s$ is the Biot number and $P_7 = \epsilon k_s/(\sigma T_i^3 L_x)$ is the conduction-radiation parameter at the boundaries $\eta_x = 0$ and $\eta_x = 1$. In the definition of the parameter P_7, σ is Stefan-Boltzmann constant and ϵ is the emissivity of the respective boundaries at $\eta_x = 0$ and $\eta_x = 1$.

With the initial and the boundary conditions known, Eqs. (10.3) and (10.4) are solved simultaneously. For the solution of these equations, Eq. (10.4) requires information about the divergence of the radiative heat flux $\nabla \cdot \Psi_R$. With the definition of temperature given as above in the CDM, non-dimensional form of divergence of heat flux $\nabla \cdot \Psi_R$ becomes

$$\nabla \cdot \Psi_R = (1-\omega)(\Gamma \beta L_x)\left[\pi G'^*_i (1+\theta)^4 - G'^*\right] \tag{10.8}$$

TH-1868_004301

where ω is the scattering albedo, Γ is the collapsing coefficient, β is the extinction coefficient, $G_i'^*$ is the non-dimensional emissive power at the inlet ($\eta_x = -\eta_{x_i}$) defined as $G_i'^* = \frac{\sigma T_i^4}{Q''' L_x}$ and G'^* is the incident radiation. In the CDM, G'^* is given by

$$G'^* = \frac{G'}{Q''' L_x} = \int_0^{2\pi} I^*(\alpha)\, d\alpha \tag{10.9}$$

where $I^* = \frac{I}{Q''' L_x}$ is the non-dimensional effective intensity and α is the planar angle, the angle of the effective intensity measured from the control surface.

In Eq. (10.9), the effective intensity I^* at any optical depth τ in direction α in the solution plane is found from the recursive use of the following equation:

$$I^*_{n+1} = I^*_n \exp(-\tau\Gamma) + S'^*[1 - \exp(-\tau\Gamma)] \tag{10.10}$$

where in the direction of interest α, S^* is the constant value of the source function between the downstream point $(n+1)$ and the upstream point n over which the optical path-leg is τ. For isotropic scattering, the source function S'^* is given by

$$S'^* = (1-\omega)\frac{G_i'^*}{2}(1+\theta)^4 + \frac{\omega}{2\pi} G'^* \tag{10.11}$$

The solid boundary at $\eta_x = 0$ is assumed to be diffuse gray. At $\eta_x = 1$, it is exposed to the black ($\epsilon = 1$) environment at $T_i = 298$ K. The north and the south boundaries are diffuse gray. Therefore, for the problem under consideration, the radiative conditions at the four boundaries are the following:

$$\begin{aligned}
I^*(0, \eta_y) &= \epsilon\frac{G_i'^*}{2} + \frac{(1-\epsilon)}{2}\int_{\alpha=0}^{\pi} I^* \sin\alpha\, d\alpha \\
I^*(1, \eta_y) &= \frac{G_e'^*}{2} \\
I^*(\eta_x, 0) &= \epsilon\frac{G_i'^*}{2}(1+\theta_s)^4 + \frac{(1-\epsilon)}{2}\int_{\alpha=0}^{\pi} I^* \sin\alpha\, d\alpha \\
I^*(\eta_x, \eta_{L_y}) &= \epsilon\frac{G_i'^*}{2}(1+\theta_s)^4 + \frac{(1-\epsilon)}{2}\int_{\alpha=0}^{\pi} I^* \sin\alpha\, d\alpha
\end{aligned} \tag{10.12}$$

where $G_e'^* = \frac{\sigma T_e^4}{Q''' L_x}$. It should be noted that for the left and the right boundaries, the emitted components are constant as they are exposed to the ambient, whereas

TH-1868_004301

for the the south and the north boundaries, since temperature varies along η_x, they also vary with η_x. The reflected components are not constant for either of the three boundaries which are considered to be diffuse gray ($\epsilon \neq 1$).

The energy equations (Eqs. (10.3) and (10.4)) are simultaneously solved using the alternating direction implicit scheme. For the grid-independent situation, 140 × 20 control volumes are used in the x and y directions, respectively. The high-temperature gradient in the x direction is the reason for considering a relatively large number of control volumes in this direction. For all the cases, a maximum of 64 effective intensities are found to be sufficient. In solving the transient problem, depending on the parameters, the time steps $\Delta\zeta = 10^{-5}$ and 10^{-6} are found to be necessary. The steady-state conditions are assumed to have been achieved when the temperature difference between the two consecutive time levels does not not exceed 10^{-6}. In the following paragraphs, all results are presented for grid- and ray-independent situations.

Since the radiative calculations are time consuming, test runs were performed to see if updating of the radiative information could be avoided for every iteration. For the chosen time steps, it was found that the radiative information could be updated at every five iterations. This resulted in a considerable reduction in the CPU times.

10.3 Results and Discussion

In the 2-D rectangular porous radiant burner considered in the present study, the south and north boundaries are insulated. For this configuration, if the radiation effect is neglected, the problem turns out to be a 1-D case, and in this instance solutions are required only in the flow direction. However, in the presence of radiation, as long as L_x and L_y are comparable to each other, the problem no longer remains a 1-D case.

It should be noted that in all cases where the effects of the aspect ratio $r = L_x/L_y$

TH-1868_004301

were studied, L_x was always kept constant. In the present work, the thickness of the porous medium L_x, the width of the heat generation zone Δx and G_i^* (appearing in Eqs . (10.8) and (10.12)) were 10 cm, 1 cm and 2.98×10^{-5}, respectively. Since the ambient temperatures at $\eta_x = -\eta_{x_e}$ and $\eta_x = 1$ are the same, the value of G_e^* (Eq. (10.12)) was taken as equal to G_i^*. The heat generation zone started at $0.5L_x$ from $\eta_x = 0$. The porosity ϕ of the solid matrix was taken to be 0.95 and the values of different parameters P_1 - P_7 were calculated on the basis of reference values given in [110]. Of these seven parameters, the effects of variations in the convective energy coupling between gas and solid, P_2 on temperature and heat flux distributions were studied. The effects of variation in P_2 were studied along with the effects of the aspect ratio r, the extinction coefficient β, the scattering albedo ω and the boundary emissivity ϵ. The values of the dimensionless parameters which are kept same for all the results presented in the following paragraphs are $P_1 = 0.01$, $P_3 = 0.00025$, $P_4 = 0.02$, $P_5 = 300$, $P_6 = 5$ and $P_7 = 66.6$. The left boundary was assumed to be black in all the cases.

In Fig. 10.2(a)-(d), the effects of the aspect ratios r on the steady-state centerline ($\eta_y = 0.5$) solid temperature θ_s and the gas temperature θ_g are shown. For an absorbing-emitting medium ($\omega = 0.0$) and $\epsilon_N = \epsilon_S = 1.0$, for $P_2 = 1$ and 500 and $\beta = 10$ and 0.0, results are presented for four different combinations of P_2 and β. It should be noted that $\beta = 0.0$ indicates the absence of radiation from the solid matrix (see Eq. (10.8)) and the parameter P_2 shows the heat transfer coupling between the two phases. When the heat transfer coefficient is low, coupling is weak and the P_2 value is smaller.

For an extinction coefficient $\beta = 10$, in Fig. 10.2(a) and (b), θ distributions are shown for $P_2 = 1$ and 500, respectively. For $\beta = 0.0$, θ distributions are shown for $P_2 = 1$ and 500 in Fig. 10.2(c) and (d), respectively.

It can be seen from Fig. 10.2(a) and (c) that when the convective coupling between the two phases is weak ($P_2 = 1$), for all r, θ_s and θ_g are different. When the coupling is strong ($P_2 = 500$), for a given r, θ_s and θ_g are the same (Fig. 10.2(b)). In the absence of radiation ($\beta = 0$), the aspect ratio r has no effect on θ. In

TH-1868_004301

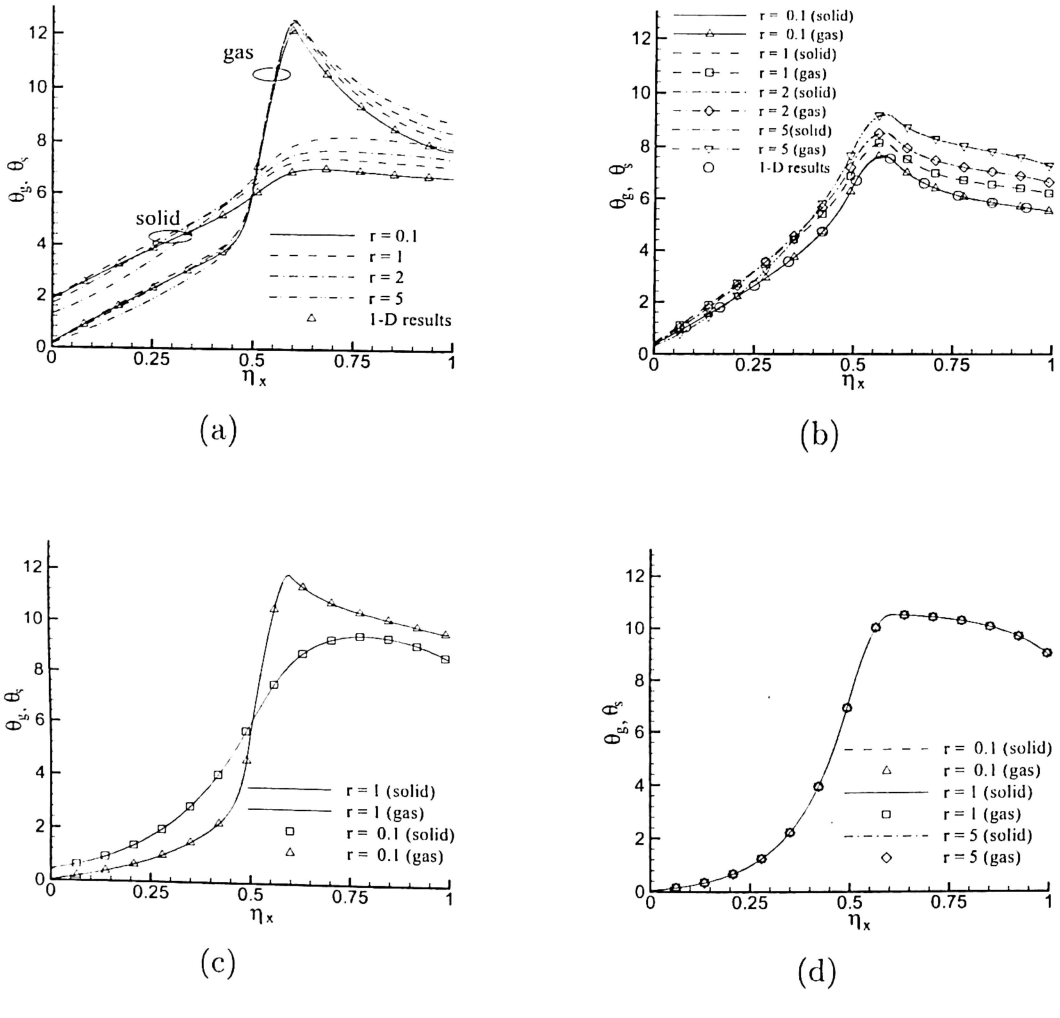


Figure 10.2: Effect of aspect ratio r on centerline ($\eta_y = 0.5$) temperature for (a) $P_2 = 1$, $\beta = 10$ (b) $P_2 = 500$, $\beta = 10$, (c) $P_2 = 1$, $\beta = 0$ and (d) $P_2 = 500$, $\beta = 0$ for $\omega = 0.0$ and $\epsilon_S = \epsilon_N = 1$.

this case, the problem is essentially a 1-D case. Since the boundaries are insulated (Eq. (10.6)), the temperature does not vary along y-direction when radiation is absent. But with radiation, this behavior changes as seen from Fig. 10.2(a)-(b) due to the radiative contribution from the boundaries. In the presence of radiation ($\beta = 10$), however when $r = 0.1$ ($L_y = 10L_x$), the effects of the south and north boundaries are negligible and the centerline temperature results of the 2-D code

TH-1868_004301

from the present work can be seen to match correctly the 1-D planar porous burners results generated by the author. The author's code for the 1-D planar porous burners was benchmarked against the results of Tong and Sathe [110].

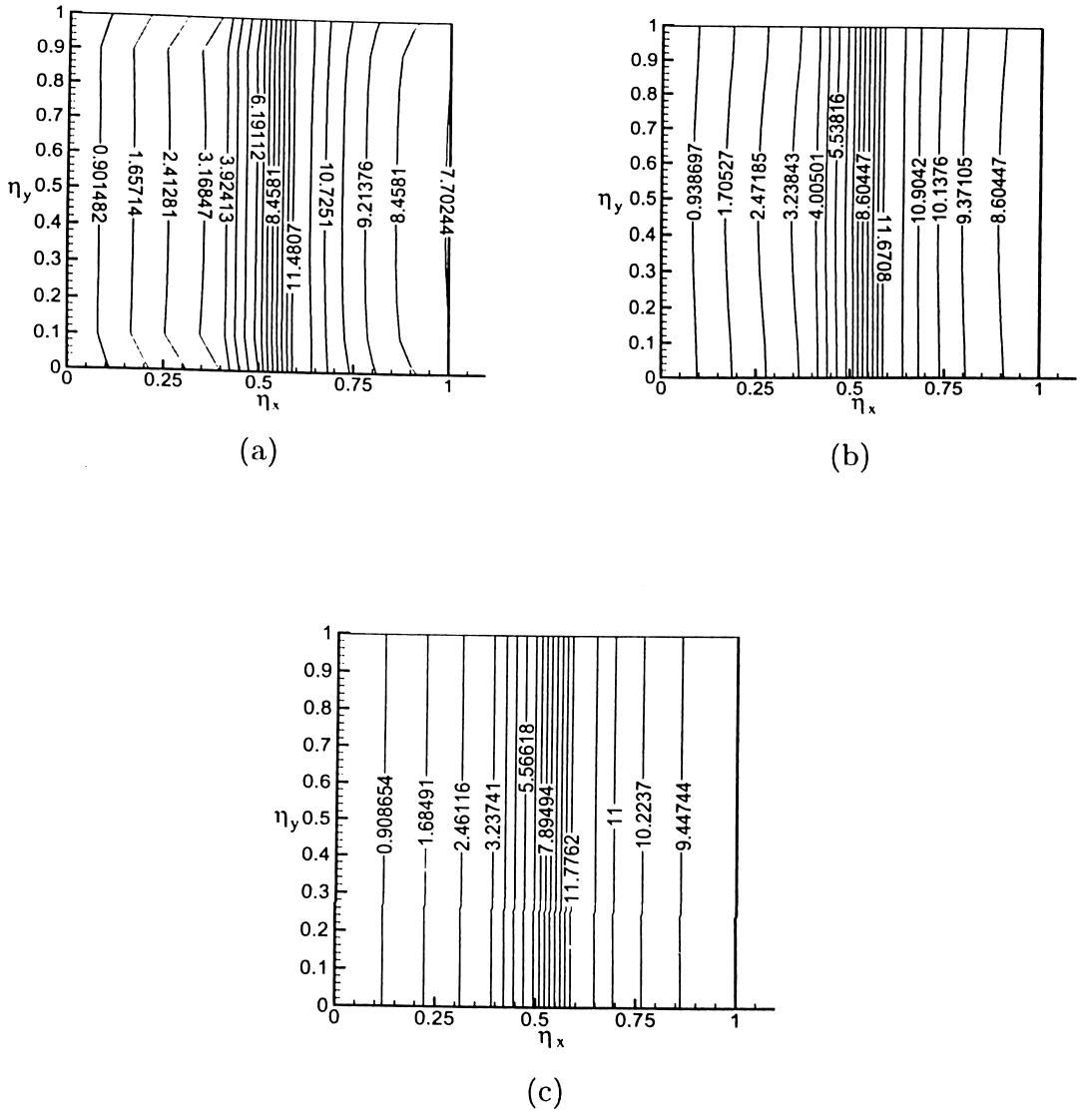
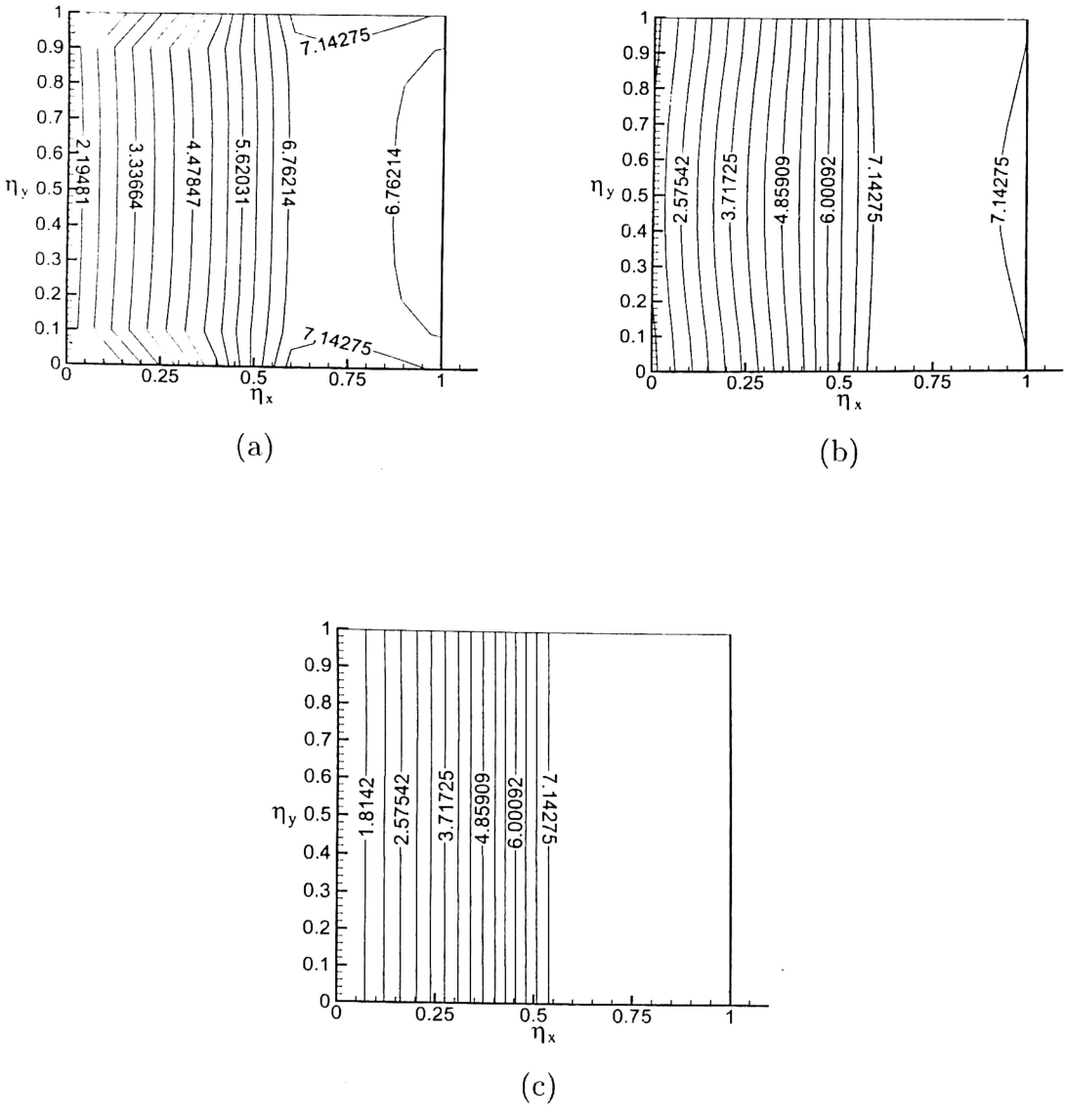


Figure 10.3: Isotherms of gas temperature for different aspect ratio r. (a) $r = 0.1$, (b) $r = 1$ and (c) $r = 5$ for $P_2 = 1$, $\beta = 10$, $\omega = 0.0$ and $\epsilon_S = \epsilon_N = 1$.

TH-1868_004301

In Figs. 10.3 and 10.4, lateral temperature profiles are shown for the gas and the solid, respectively. For $\omega = 0.0$ and $\epsilon_S = \epsilon_N = 1$, these profiles are shown for $P_2 = 1$ and $\beta = 10$. In these figures, isotherms are shown for three different values of the



(a) (b)

(c)

Figure 10.4: Isotherms of solid temperature for different aspect ratio r. (a) $r = 0.1$, (b) $r = 1$ and (c) $r = 5$ for $P_2 = 1$, $\beta = 10$, $\omega = 0.0$ and $\epsilon_S = \epsilon_N = 1$.

TH-1868_004301

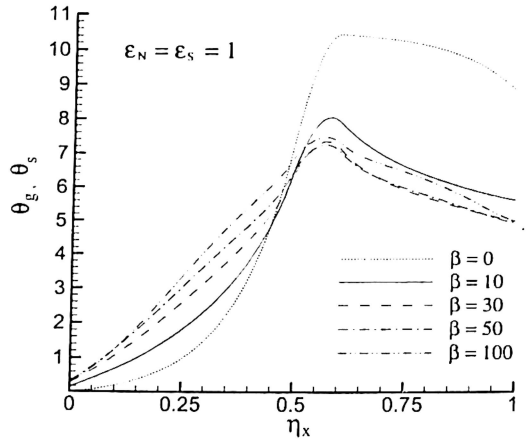
aspect ratio $r = 0.1$, 1 and 5.

It can be seen that for low r ($r = 0.1$, which is considered as a 1-D case), the temperatures near the boundaries (north and south) are not the same as the centerline temperature. Temperatures near the boundaries are higher than the temperatures in the bulk portion. However, this difference vanishes when r becomes high ($r = 5$) (Fig. 10.3(c)), and in this case for all x locations, an almost uniform temperature distribution is seen along the y-direction. A similar trend is also observed for the solid phase (Fig. 10.4(a)-(c)). It is interesting that for low r (Fig. 10.4(a)), in the region downstream of the heat generation zone, θ_s becomes high near the boundaries. This is because of the strong radiation from the boundaries. It is evident from Figs. 10.3(a) and 10.4(a) that for a low r (1-D case), in the presence of radiation, the temperature near the boundary is not the same as that in the bulk region.

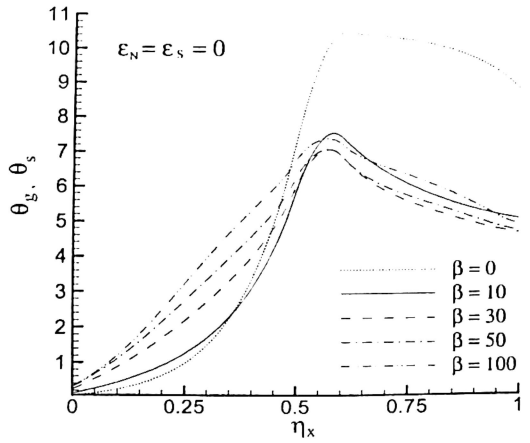
For an aspect ratio $r = 1$ and scattering albedo $\omega = 0.5$, in Fig. 10.5(a) and (b) steady-state centerline ($\eta_y = 0.5$) solid temperature θ_s and gas temperature θ_g distributions are shown for five different values of the extinction coefficient β ranging from 0.0 to 100. In Fig. 10.5(a), the north and the south boundaries are considered black ($\epsilon_N = \epsilon_S = 1.0$), whereas in Fig. 10.5(b) the two boundaries are purely reflecting ($\epsilon_N = \epsilon_S = 0.0$). These results are shown for a high value of the convective energy coupling, $P_2 = 500$. It should be noted that for a high value of P_2 as shown in Fig. 10.2, the gas and the solid temperatures are the same. Therefore, in Fig. 10.5 only one plot is shown for both θ_s and θ_g.

It can be seen from Fig. 10.5(a) and (b) that the peak temperature is highest in the absence of radiation ($\beta = 0.0$) from the solid matrix. In the absence of radiation, there is no heat removal by radiation from the heat generation zone and hence the temperature downstream of the heat generation zone increases. Since even for $\beta = 0.0$ radiation from the boundaries is present, there is some radiation loss and as a result the temperature decreases downstream of the heat generation zone. If radiation is not considered from the boundary, for $\beta = 0.0$, this curve becomes horizontal after it reaches the peak temperature in the heat generation zone (not shown). For $\beta = 0.0$, this observation is similar to the 1-D planar medium results

TH-1868_004301



(a)



(b)

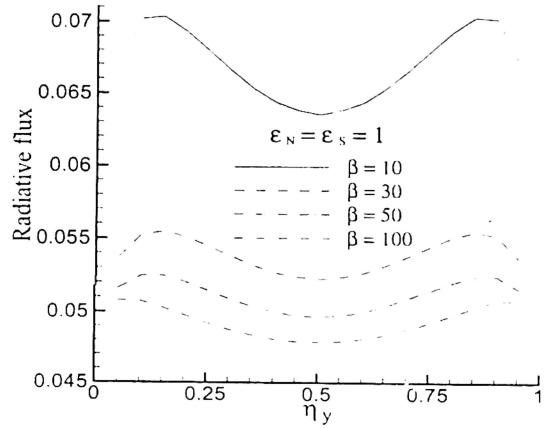
Figure 10.5: Effect of extinction coefficient β on centerline ($\eta_y = 0.5$) temperature for (a) black wall $\epsilon_S = \epsilon_N = 1$. (b) $\epsilon_S = \epsilon_N = 0.0$ for $r = 1$, $P_2 = 500$ and $\omega = 0.5$.

of Tong and Sathe [110].

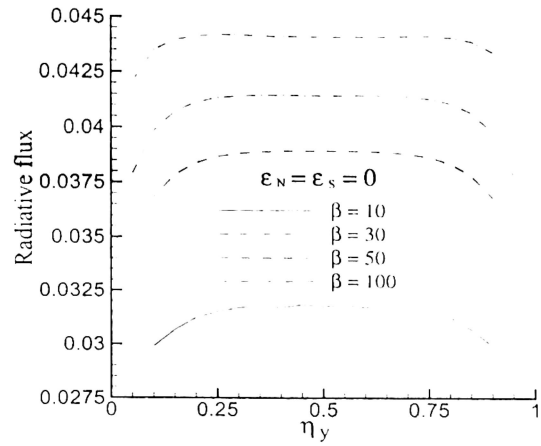
It can also be seen from Fig. 10.5(a) and (b) that in the region upstream of the heat generation zone ($\eta_x < 0.5$), the temperature is higher for higher β. This indicates that for higher β, both the solid and gas receive more heat by radiation

TH-1868_004301

and therefore become preheated. The temperature distribution in the downstream region ($\eta_x > 0.5$) has almost the same trend in both figures. In this region it first decreases with increase in β and then increases again when $\beta > 30$. This behavior is consistent with the 1-D results of Tong and Sathe [110].



(a)



(b)

Figure 10.6: Effect of extinction coefficient β on radiative heat flux at exit for (a) black wall $\epsilon_S = \epsilon_N = 1$. (b) $\epsilon_S = \epsilon_N = 0.0$ for $r = 1$ $P_2 = 500$, $\omega = 0.5$.

Variations of the radiative heat flux Ψ_R at the exit ($\eta_x = 1$) are shown in Fig. 10.6(a)

TH-1868_004301

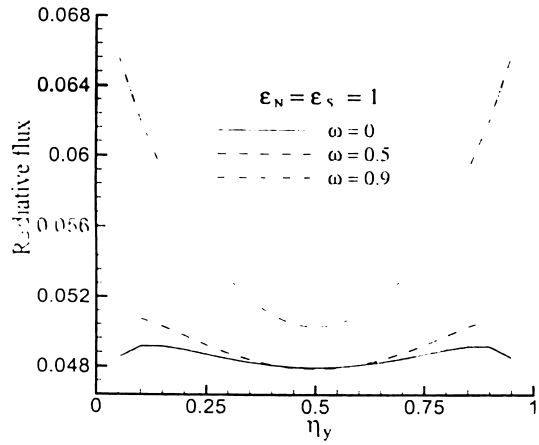
and (b). These results are shown for the same set of parameters as considered for Fig. 10.5. It can be seen that for black north and south boundaries ($\epsilon_N = \epsilon_S = 1$), Ψ_R at the exit decreases with increase in the extinction coefficient β. The value of Ψ_R is minimum in the center ($\eta_y = 0.5$), it increases towards the two boundaries and then it decreases when it reaches the boundaries. However, in the case of purely reflecting wall ($\epsilon_N = \epsilon_S = 0.0$) (Fig. 10.6(b)), an opposite trend is found. The radiative heat flux Ψ_R increases with increase in β. For the 1-D burner, a similar trend was also observed by Tong and Sathe [110].

When the north and the south boundaries are black, because of high emissions from these boundaries, the trend of radiative heat flux Ψ_R variations at the exit becomes opposite to the case when these boundaries are reflecting. Further, because of the high temperature of the boundaries, a significant amount of radiation comes from them and when the extinction coefficient β is low, an increased amount of radiation is able to rea h the exit plane. This observation is contrary to the 1-D planar medium case [109, 110], in which, the radiant output was found to increase with increase in β. In the case of a 2-D burner, with other parameters fixed, the maximum radiant output depends both on β and on the emissivities of the boundaries.

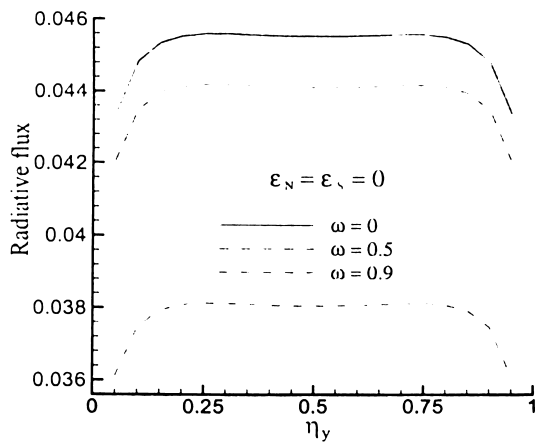
In Fig. 10.7(a) and (b), the effects of the scattering albedo ω on the radiative heat flux Ψ_R at the exit ($\eta_x = 1$) are shown. Here these results are presented for $P_2 = 500$, $r = 1$ and $\beta = 100$. The south and north boundaries are considered to be black ($\epsilon_S = \epsilon_N = 1$) in Fig. 10.7(a), whereas they are perfectly reflecting ($\epsilon_S = \epsilon_N = 0.0$) in Fig. 10.7(b). For black boundaries, Ψ_R increases with increase in ω (Fig. 10.7(a)). The opposite trend is observed when the boundaries are reflecting (Fig. 10.7(b)). Therefore, when the boundaries are black, a higher ω is desirable to obtain the maximum radiant output, but when they are reflecting, maximum radiant output is obtained when the solid matrix is only absorbing and emitting ($\omega = 0.0$).

To show the contributions of different terms of the energy equation to the total flux, in Fig. 10.8(a)-(c) results are shown at the centerline ($\eta_y = 0.5$) in the flow direction η_x. These results are shown for $P_2 = 500$, $\beta = 100$, $\omega = 0.5$ and $\epsilon_S = \epsilon_N = 1$.

TH-1868_004301



(a)

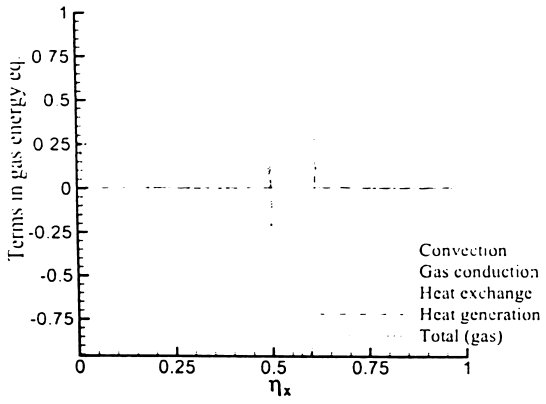


(b)

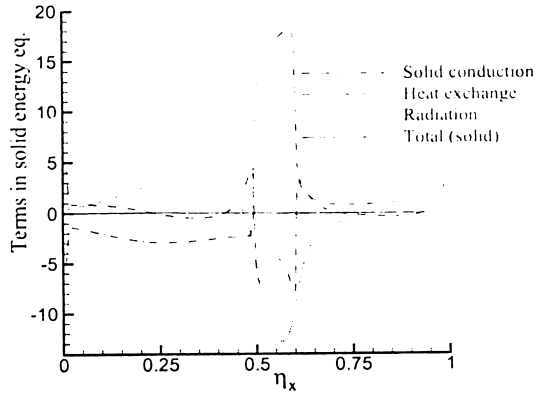
Figure 10.7: Radiative flux at the exit ($\eta_x = 1.0$) with the effect of scattering albedo for (a) black wall , $\epsilon_S = \epsilon_N = 1$. (b) $\epsilon_S = \epsilon_N = 0.0$ for $P_2 = 500$, $r = 1.0$, $\beta = 100$ and $\omega = 0.5$.

For $r = 1$, in Fig. 8(a) and (b) contributions are given for the gas and solid phase, respectively. In Fig. 10.8(c), contributions of conduction, convection and radiation to the total (gas and solid) heat flux are shown. Here results are presented for three different aspect ratios.

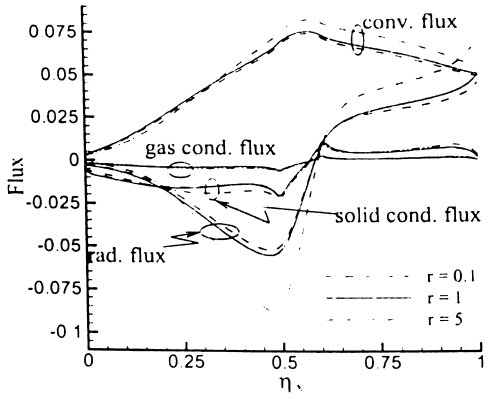
TH-1868_004301



(a)



(b)



(c)

Figure 10.8: (a) Different terms in gas energy equation for aspect ratio $r = 1$, (b) Different terms in solid energy equation for aspect ratio $r = 1$ (c) Centerline ($\eta_y = 0.5$) fluxes along x direction for different aspect ratio for $P_2 = 500$, $\beta = 100$ $\omega = 0.5$ and $\epsilon_S = \epsilon_N = 1$.

It can be seen from Fig. 10.8(a) that in the combustion region, heat generation is mainly balanced by the heat exchange term. Upstream of the combustion region, the heat exchange term is positive, meaning that the gas is being preheated and is balanced by the convective term. In the downstream portion, the heat exchange

TH-1868_004301

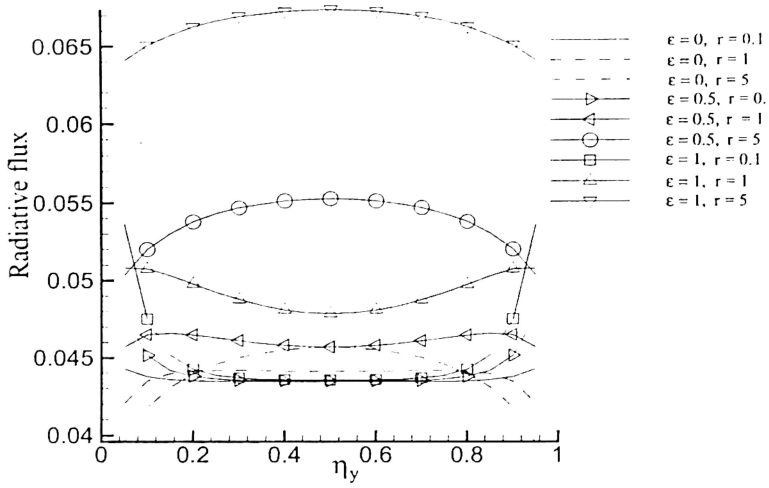
term is negative, implying that the gas loses heat to the solid and it is balanced by the positive convective term. The gas conduction term is important only in the combustion zone and it contributes to the heat exchange term.

In Fig. 10.8(b), various terms of the solid-phase energy equations (Eq. (10.4)) are analyzed. In the combustion zone and in the region upstream to this zone, the heat transferred from the gas to the solid is mostly balanced by the radiative term. On the upstream side, the radiation term is positive, implying that the solid is being heated by radiation and it is balanced by the heat loss to preheat the gas. The solid conduction term has a high negative value in the middle portion and along with radiation it balances the heat transfer from the hot gas to the solid. However, most of the heat transferred from the gas to the solid is lost to the environment by the radiation starting from the middle to the downstream side. It can be seen from Fig. 10.8(a) and (b) that all along η_x, energy is completely balanced and the total flux is zero.

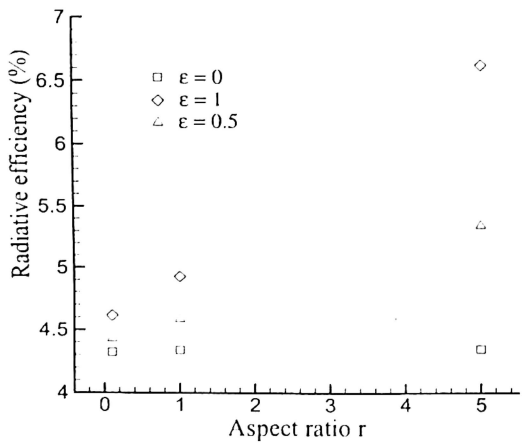
In Fig. 10.8(c), variations of fluxes due to solid conduction, gas conduction, convection and radiation are plotted for aspect ratios $r = 0.1, 1$ and 5. It can be seen that the gas conductive flux has a negligible contribution compared with other heat fluxes. Solid conduction has some contribution, but compared with radiation its effect is small. Near the combustion zone, the effect of the aspect ratio r on the radiative heat flux is greater. This indicates that the temperature profile changes with aspect ratio mainly due to radiation and the higher the aspect ratio, the higher is the radiant output. Convective flux is dominant everywhere and in the combustion zone and the region downstream of this zone, it increases with increase in the aspect ratio r.

In Fig. 10.9(a) at the exit ($\eta_x = 1$), the effects of the emissivity ϵ of the south and the north boundaries on the radiative output are shown. The emissivities of both the boundaries are considered to be the same. For $r = 1$, these results are presented for $P_2 = 500$, $\beta = 10$, $\omega = 0.5$ and $r = 1$. It can be seen that as the south and the north boundaries become more and more reflecting, the radiative output decreases. Further, for a given value of ϵ, the higher the aspect ratio r, the higher

TH-1868_004301



(a)



(b)

Figure 10.9: (a) Radiative flux at the exit ($\eta_x = 1.0$) with the effect of emissivity of the north and south boundaries and (b) Radiative efficiency at the exit for different aspect ratio r for $P_2 = 500$, $\beta = 100$ and $\omega = 0.5$.

is the radiative output.

TH-1868_004301

In Fig. 10.9(b), radiative efficiency is calculated for different values of r and ϵ. The values of the different parameters considered in this figure are the same as in Fig.

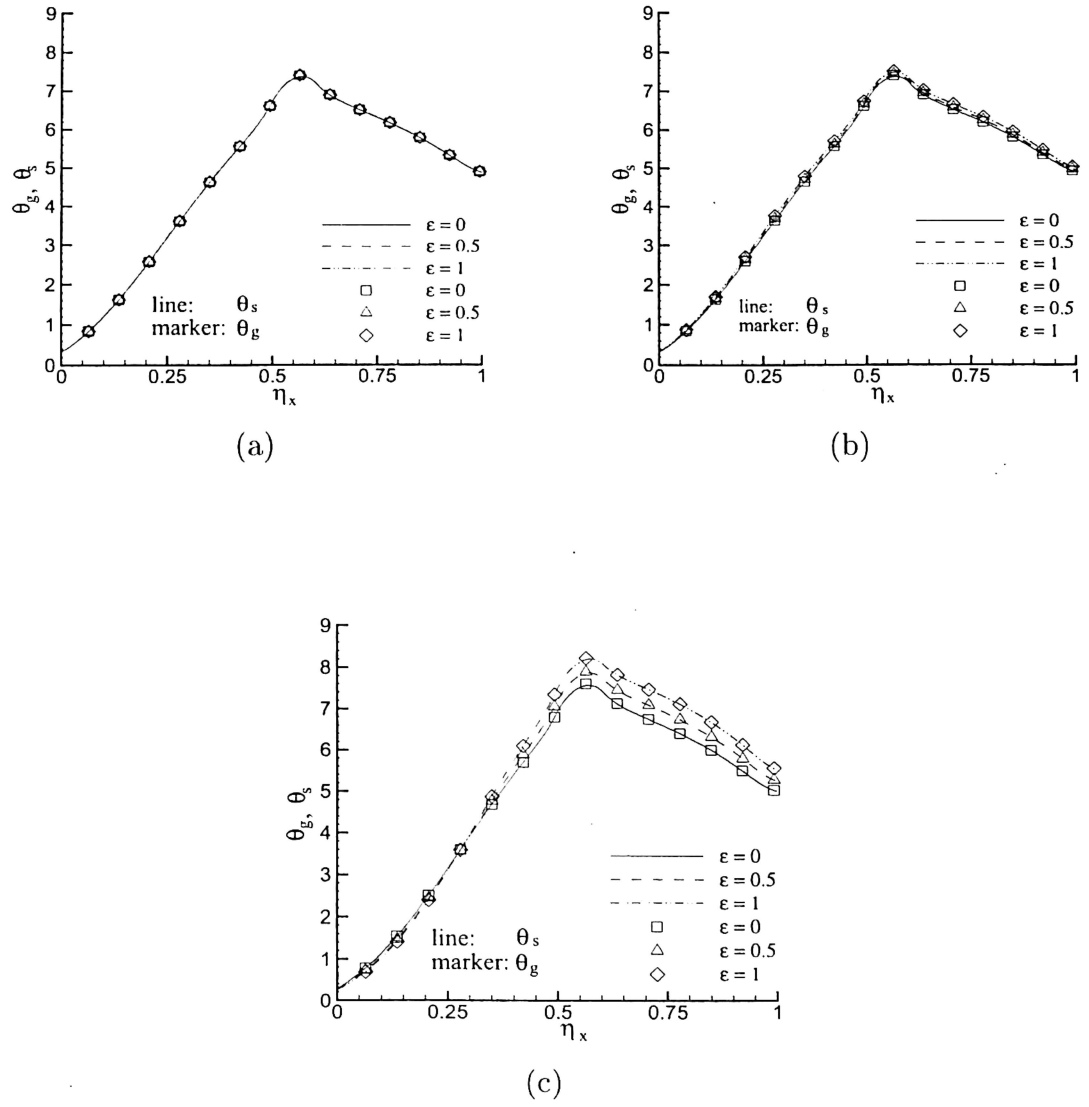


Figure 10.10: Effect of emissivities of the south and the north boundaries on centerline ($\eta_y = 0.5$) temperature for different aspect ratio r (a) $r = 0.1$, (b) $r = 1$ and (c) $r = 5$ for $P_2 = 1$, $\beta = 100$ and $\omega = 0.5$.

TH-1868_004301

10.9(a). Radiative efficiency is calculated as $\frac{\int_0^{L_y} \Psi_R dy}{\int_0^{L_y} dy} \times 100$. It can be seen that when the south and north boundaries are reflecting less ($\epsilon = 0.5$ or 1), the radiative efficiency increases with increase in the aspect ratio r. At high r, the distance between the south and the north boundaries becomes smaller, and in this case the radiation contribution from these boundaries increases, which in turn increases the radiative efficiency. When both boundaries are perfectly reflecting ($\epsilon = 0$), the radiative efficiencies for different values of r are very close to each other.

The corresponding temperature θ_g and θ_s profiles for the case considered in Fig. 10.9 are plotted in Fig. 10.10(a)-(c) where results are presented for $r = 0.1$, 1 and 5, respectively. It can be seen from Fig. 10.10(a) that for a low aspect ratio ($r = 0.1$) the centerline temperature profile does not change much with the side boundary emissivities. However, for a high aspect ratio ($r = 5$), as seen from Fig. 10.10(c), the temperature profile changes in the downstream region. With increase in the emissivities of the boundaries, in the downstream region, the temperature increases. This trend is consistent with the results presented in Fig. 10.9(a).

Some transient results are shown in Fig. 10.11. The convective, radiative, gas conductive and solid conductive heat fluxes are shown in Fig. 10.11(a)-(d), respectively at different time levels. For $r = 1$, these results are presented for $P_2 = 500$, $\beta = 100$, $\omega = 0.5$ and $\epsilon_S = \epsilon_N = 1$. It can be seen that the convective heat flux increases steadily with time, whereas the radiative heat flux increases only in the later period when the temperature of the solid becomes high. Initially the radiative heat flux remains very low and the solid conductive flux is more dominant than the radiative heat flux in that period. However, as it reaches a steady state, the solid conductive heat flux decreases and the radiative heat flux becomes more dominant. The gas conductive flux is always negligible compared with other fluxes.

TH-1868_004301

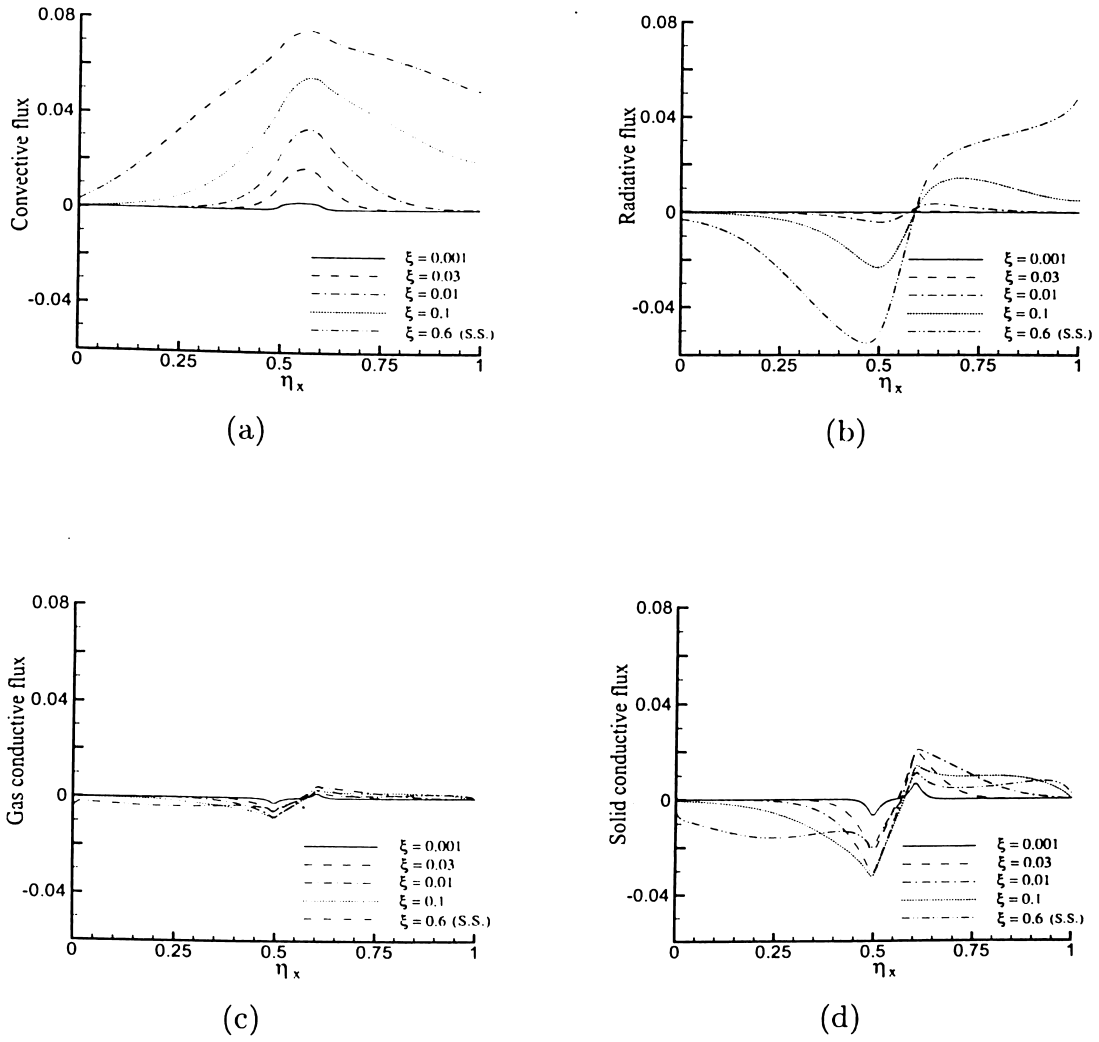


Figure 10.11: Transient centerline ($\eta_y = 0.5$) fluxes along x-direction (a) convective heat flux, (b) radiative heat flux, (c) gas conductive heat flux and (d) solid conductive heat flux for $r = 1$, $P_2 = 500$, $\beta = 100$ and $\omega = 0.5$.

10.4 Conclusions

Heat transfer analysis of a 2-D rectangular porous burner was carried out. Non-local thermal equilibrium between the gas and solid phases was accounted by considering

TH-1868_004301

separate energy equations for the two phases. Combustion was modeled by considering a uniform heat generation zone inside the porous medium. The collapsed dimension method was used to solve the radiative part of the energy equation. The transient energy equations for the gas and solid phases were solved using the alternating direction implicit scheme. Results for the centerline temperature and heat flux distributions were obtained for different parameters such as the aspect ratio, the extinction coefficient, the boundary emissivity and the scattering albedo. The contributions of various terms in the gas-phase and solid-phase energy equations to the heat flux were also analyzed. In comparison with radiation and solid conduction, gas conduction was found to be negligible.

For the insulated boundary conditions considered in this work, in the absence of radiation, for all values of the aspect ratio, the centerline temperature was found to be the same, implying that the problem could be considered as a 1-D case. With radiation, however, this was not the case. The radiation from the side boundaries was found to have a considerable effect on the total radiative output at the exit. For the 2-D case, the effects of β and ω on the total radiant output were found to depend on the emissivities of the side boundaries.

TH-1868_004301

Chapter 11

Conclusions and Recommendations

11.1 Summary

Interaction of radiation with conduction and/or convection is a subject of major interest due to its potential applications in variety of problems. In the present work, analyses of radiation, conduction and/or convection heat transfer were carried out for different situations. Either the collapsed dimension method (CDM) or the discrete transfer method (DTM) was used to solve the radiative component of the energy equation. Both the methods were developed to handle different situations. Effects of various optical properties were investigated.

The present work is summarized in the following lines:

In the first chapter, a brief review of thermal radiation and its importance were presented. To justify the works carried out in the thesis, research in the area of

TH-1868_004301

Indian Institute of Technology Guwahati

interaction of radiation with conduction and/or convection was reviewed.

In the second chapter, a general formulation of the radiative transfer equation was presented in conjunction with the energy equation. The DTM and the CDM were discussed and formulations for both were given.

The problems solved in Chapters 3-7 dealt with 1-D planar geometry whereas Chapters 8-10 dealt with 2-D Cartesian geometry.

In most of the practical cases, boundary conditions other than the temperature boundary conditions are also required. For applying a method to such problems, it is important to check the performance of a method in various types of boundary conditions. Looking at this aspect, in Chapter 3, the applicability of the CDM was tested for a conduction-radiation problem with flux boundary condition. Its accuracy was found to be very good for the cases considered. The effects of enclosure optical thickness, conduction-radiation parameter, scattering albedo, boundary emissivity, temperature of the cold boundary and the imposed heat flux were studied on the variations of medium temperature and conductive and radiative fluxes.

Transient behavior of heat transfer is of interest in many situations. Further, there are some cases where consideration of internal heat generation is required. To test how well the CDM worked for this class of problems, an analysis of transient conduction and radiation with heat generation was carried out in the the fourth chapter. The investigation was done for a 1-D planar geometry. Transient and steady state temperature and heat flux distributions were found for various radiative parameters. Heat generation was found to have effect on temperature and heat flux results. The results showed very good agreement with the results available in the literature

In most of the cases, thermal conductivity is assumed to be constant. But in certain situations, thermal conductivity varies with temperature. If accurate prediction of temperature and heat flux in the medium are important, one has to include the effect of variable thermal conductivity. To analyze this situation, conduction and radiation heat transfer in a planar geometry was considered in Chapter 5. Thermal

TH-1868_004301

conductivity was assumed to be vary linearly with temperature. The effects of variable thermal conductivity were found to be significant in some cases. The time to reach the steady state was found to increase with the decrease in the value of coefficient of thermal conductivity variation γ. The effect of γ was found to increase for radiation dominated situation.

The packed bed is considered to be a porous medium made of some regular patterns. From the literature review it was found that for a packed bed, analysis of transient conduction combined with radiation had not been done. Further, it was found that for dependent scattering, researchers were using Kamiuto's correlated scattering theory and Kaviany's scaling factor independently, and no works had been reported for the comparative study of the two scattering theories. Thus the work contained in Chapter 6 analysed transient conduction-radiation heat transfer in a planar packed bed with a comparison between the two theories. Both constant and variable porosity distributions were assumed. The models with variable porosity distribution were found to be matching with the available experimental results. With increase of the ratio of the conductivities of the dispersed phase to the continuous phase, κ and bed to particle diameter ratio, L/D_p, mean effective thermal conductivity and the total heat flux were found to decrease. For all values of κ, for the three porosity models, the values of total heat flux were found almost close to one other. However, for the lower values of L/D_p, total heat flux from model 1 (constant porosity with Kamiuto's correlated scattering theory) was found more than that from model 2 (variable porosity with Kamiuto's correlated scattering theory) and 3 (constant porosity with Kaviany's theory). Similar trends were also observed for the mean total effective thermal conductivity. Time to reach the steady state was found to increase with the increase of κ, L/D_p and conduction-radiation parameter N.

A porous matrix can be effectively used for the enhancement of heat transfer in a channel flow. The consideration of radiation in heat transfer analysis of this type of flow had not been investigated before. Therefore, in Chapter 7, the effect of radiation along with convection was studied in case of a channel flow bounded by two isothermal parallel plates. It was seen that the effect of radiation significantly changed the Nusselt number behavior along the flow direction. The effect of porous

TH-1868_004301

media shape parameter (PMSP) γ was found to be important in both cases (hot or cold) of plate conditions. Both the radiation Nusselt number and the convection Nusselt number increased with increase in PMSP γ. The behavior of the total Nusselt number for all values of PMSP γ was found to be the same as that for the combined radiative and convective heat transfer in Poiseuille flow. For the hot-plate condition, the Nusselt number decreased along the axial length, reached a minimum value and then increased again. The effect of γ on the radiation Nusselt number was smaller near the entrance, but it increased along the axial length. The opposite was the case with the convection Nusselt number. However, for the cold-plate condition, the total Nusselt number decreased along the axial length and reached an asymptotic value. In the presence of radiation, a fully developed temperature field was not obtained.

In previous works, the accuracy of the DTM and the CDM have been reported for several cases. But their computational ability had not been tested before. In case of a 1-D medium, computations are very fast and comparison between the two methods bears no real meaning. So, before solving any 2-D problem with the DTM and the CDM, it was important to compare their computational abilities. In Chapter 8, performance of both the methods was compared. Three different benchmark problems were considered. For same level of accuracy, the CDM was found computationally efficient.

Chapter 9 was devoted to study the effect of variable thermal conductivity on 2-D transient conduction-radiation heat transfer. Like 1-D case (Chapter 5), variable thermal conductivity was found to have significant effect on temperature and heat fluxes. The effect of variable thermal conductivity parameter γ on total heat flux at the boundaries was found to be greater for high aspect ratio. The effect of γ on total heat flux at the boundaries and centerline temperature were comparable for all extinction coefficients. However, its effect on total heat flux at the boundaries and centerline temperature was found to be greater for low conduction-radiation parameter.

After testing the applicability of the CDM in different situations and knowing its

TH-1868_004301

advantages over the DTM for a 2-D problem, in Chapter 10, it was used in the analysis of a 2-D rectangular porous radiant burner. Combustion was modeled as a spatially dependent heat generation source. The porous solid phase and the gas phase were considered to be not in local thermal equilibrium. The optimum condition to get maximum radiant output was analyzed. In comparison with radiation and solid conduction, gas conduction was found to be negligible. For the insulated boundary conditions considered in this work, in the absence of radiation, for all values of the aspect ratio, the centerline temperature was found to be the same, implying that the problem could be considered as a 1-D case. However, this was not the case when radiation was present. The radiation from the side boundaries was found to have a considerable effect on the total radiative output at the exit. For the 2-D case, the effects of extinction coefficient and scattering albedo on the total radiant output were found to depend on the emissivities of the side boundaries.

11.2 Recommendations and Future Works

In this work, the DTM and the CDM were used for many practical problems. From the present work, it is obvious that the CDM and the DTM can be used for any combined mode problems with a greater degree of accuracy. The CDM is, however, recommended as a better tool for a 2-D problem because of its computational economy.

In the present work, the CDM and the DTM were applied to heat transfer problems involving thermal radiation in 1-D planar absorbing, emitting and anisotropic scattering media. In those problems, anisotropy was approximated by linear anisotropic phase function. Moreover, in Chapter 6, the DTM was formulated to use the phase functions of diffuse gray spheres. The DTM can be extended to include other types of phase functions. The use of the CDM to different scattering phase functions other than the linear anisotropic scattering has not yet been developed. The development of the CDM for other scattering phase functions can be taken up for generalization of this method.

TH-1868_004301

Indian Institute of Technology Guwahati

In Chapter 10, heat transfer analysis was done for a porous burner. In that work, combustion was modeled as a constant heat generation source. The next step of this work can be to apply the actual combustion instead of a constant heat source. As a first step, one step global reaction given by Arrhenius equation can be applied. Then, detailed chemical kinetics can be used to model combustion more accurately.

In simulation of porous burner (Chapter 10), the velocity field was assumed constant. The momentum equation was not solved. With combustion, this is a very rude estimation. The high temperature gradient near the combustion zone changes the density of the gas mixture which eventually changes the velocity. So, simultaneous solution of the momentum equation with the energy equation is also recommended for the future work.

Since the porous burners are of different geometries, viz. cylindrical, cubic etc., the development of the CDM or the DTM codes for different geometries is recommended for the future research.

In simulation of a porous burner for calculating the radiative part, it is very important to know the optical properties like extinction coefficient, scattering albedo etc. It is a challenging task to find out the values of these optical properties for a foam like porous structures which are generally used for a porous burner. Either experiments or inverse methods may be the solution for calculating these properties. A great potential is seen for a research work in this area.

TH-1868_004301

Bibliography

[1] R. Siegel and J. R. Howell. *Radiative Heat Transfer*. Hemisphere, Washington DC, 4th edition, 2002.

[2] R. D. Cess. Radiation effects upon boundary layer flow of an absorbing gas. *J. Heat Transfer*, 86:469–475, 1964.

[3] R. Pitz-Pall, B. Hoffschmidt, M. Bohmer, and M. Becker. Experimental and numerical evaluation of the performance and flow stability of different types of open and volumetric absorbers under non-homogeneous irradiation. *Solar Energy*, 60(3/4):135–150, 1997.

[4] S. Andre and A. Degiovanni. A theoretical study of the transient coupled conduction and radiation heat transfer in glass: Phonic diffusivity measurements by flash technique. *Int. J. Heat Mass Transfer*, 38(18):3401–3412, 1995.

[5] L. Glicksman, M. Schuetz, and M. Sinofsky. Radiation heat transfer in foam insulation. *Int. J. Heat Mass Transfer*, 30(1):187–197, 1987.

[6] V. A. Petrov. Combined radiation and conduction heat transfer in high temperature fiber thermal insulation. *Int. J. Heat Mass Transfer*, 40(9):2241–2247, 1997.

[7] T. W. Tong and C. L. Tien. Radiative heat transfer in fibrous insulations-part 1: Analytical study. *J. Heat Transfer*, 105(1):70–75, 1983.

[8] R. Viskanta and M. P. Menğuç. Radiation heat transfer in combustion systems. *Prog. Energy Combust. Sci.*, 13:97–160, 1987.

TH-1868_004301

[9] P. F. Hsu, W. D. Evans, and J. R. Howell. Experimental and numerical study of premixed combustion within nonhomogeneous porous ceramics. *Combust. Sci. and Tech.*, 90:149-172, 1993.

[10] J. R. Howell. The Monte Carlo method in radiative heat transfer. *J. Heat Transfer*, 120:547-560, 1997.

[11] H. C. Hottel and H. S. Cohen. Radiant heat exchange in a gas filled enclosure: Allowance for nonuniformity of gas temperature. *A.I.Ch.E. Journal*, 4:3-14, 1958.

[12] A. C. Ratzel III and J. R. Howell. Two-dimensional radiation in absorbing-emitting -scattering media using the P_N approximation. *ASME Paper No. 82-HT-19*, 1982.

[13] Fengshan Liu, G. S. Garbett, and J. Swithernbank. Effect of anisotropic scattering on radiative heat transfer using the P_1-approximation. *Int. J. Heat Mass Transfer*, 35(10):2491–2499, 1992.

[14] Y. Bayazitoglu and J. Higenyi. The higher-order differential equations of radiative transfer: P_3 approximation. *AIIA Journal*, 17:424–431, 1979.

[15] K. D. Lathrop. Use of discrete ordinate methods for solution of photon transport problems. *Nuclear Science and Engineering*, 24:381–388, 1966.

[16] D. J. Hyde and J. S. Truelove. The discrete ordinate approximation for radiative heat transfer. Technical Report AERE-R 8502, 1977.

[17] Tae-Kuk Kim. *Radiation and Combined Mode Heat Transfer Analysis in Absorbing, Emitting, and Mie-Anisotropic Scattering Media Using S-N Discrete Ordinate Method.* PhD thesis, University of Minnesota, 1990.

[18] J. C. Henson and W. M. G. Malalasekara. Comparison of the discrete transfer and Monte Carlo methods for radiative heat transfer in three-dimensional nonhomogeneous scattering media. *Numer. Heat Transfer, Part A*, 32:19-36, 1997.

TH-1868_004301

[19] M. M. Razzaque, D. E. Klein, and J. R. Howell. Finite element solution of radiative heat transfer in a two-dimensional rectangular enclosures with gray participating media. *J. Heat Transfer*, 105:933–936, 1983.

[20] C. N. Sokman and M. M. Razzaque. Finite element analysis of conduction radiation heat transfer in an enclosure with heat flux boundary conditions. In *Radiation, Phase Change Heat Transfer, and Thermal Systems*, volume 81, pages 17–23. ASME HTD, 1987.

[21] R. Fernandes, J. Francis, and J. N. Reddy. A finite element approach to combined conductive and radiation heat transfer in a planar medium. In *Heat Transfer and Thermal Control*, pages 93–109. AIAA, 1981.

[22] G. D. Raithby and E. H. Chui. A finite volume method for predicting a radiant heat transfer in enclosures with participating media. *J. Heat Transfer*, 112:415 423, 1990.

[23] E. H. Chui, P. M. J. Hughes, and G. D. Raithby. Implementation of the finite volume method for calculating radiation transfer in a pulverised fuel flame. *Combust. Sci. and Tech.*, 92(4-6):225–242, 1993.

[24] N. G. Shah. *New Method of Computation of Radiation Heat Transfer Combustion Chambers.* PhD thesis, Imperial College, University of London, England, 1979.

[25] F.C. Lockwood and N. G. Shah. An improved flux model for the calculation of radiation heat transfer in combustion chambers. In *Proceedings of the 16th National Heat Transfer Conference, St. Louis*, pages 2–7. ASME, August 1976.

[26] P. Talukdar and S. C. Mishra. Transient conduction and radiation heat transfer with variable thermal conductivity. *Numer. Heat Transfer, Part A*, 41:851–867, 2002.

[27] P. Rath, S. C. Mishra, P. Mahanta, U. K. Saha, and K. Mitra. Discrete transfer method applied to transient radiative transfer problem in participating medium. *Numer. Heat Transfer, Part A*, 44(2):183–197, 2003.

TH-1868_004301

[28] P. Talukdar, S. C. Mishra, D. Trimis, and F. Durst. Combined radiation and convection heat transfer in a porous channel bounded by isothermal parallel plates. *Int. J. Heat Mass Transfer*, 47(5):1001–1013, 2004.

[29] P. Talukdar and S. C. Mishra. Analysis of conduction-radiation problem in absorbing, emitting and anisotropically scattering media using the collapsed dimension method. *Int. J. Heat Mass Transfer*, 45:2159–2168, 2002.

[30] P. Mahanta and S. C. Mishra. Collapsed dimension method applied to radiative transfer problems in complex enclosures with participating medium. *Numer. Heat Transfer, Part B*, 42(4):367–388, 2002.

[31] P. Mahanta and S. C. Mishra. Radiative transfer analysis in axisymmetric enclosures using collapsed dimension method. In *paper No. NHTC2000-12125, 34th National Heat Transfer Conference Pittsburgh, PA, USA*, August 2000.

[32] P. Talukdar, S. C. Mishra, D. Trimis, and F. Durst. Heat transfer characteristics of a porous radiant burner under the influence of a two-dimensional radiation field. *J. Quant. Spectros. Radiat. Transfer*, 84(4), 527-537, 2004.

[33] S. C. Mishra, P. Talukdar, D. Trimis, and F. Durst. Effect of temperature dependent thermal conductivity on two-dimensional conduction and radiation heat transfer. In *Eurotherm Seminar 73, Computational Thermal Radiation in Participating Media, Mons, Belgium*, 15-17 April, 2003.

[34] S. C. Mishra, P. Talukdar, D. Trimis, and F. Durst. Computational efficiency improvements of the radiative transfer problems with or without conduction-a comparison of the collapsed dimension method and the discrete transfer method. *Int. J. Heat Mass Transfer*, 46(16):3083–3095, 2003.

[35] M F. Modest. *Radiative Heat Transfer*. McGraw-Hill, Inc, 1993.

[36] R. Viskanta. Radiation transfer: Interaction with conduction and convection and approximate methods in radiation. In *Proceedings of the 7th International Heat Transfer Conference*, volume 1, pages 102–121. Munich, 1982.

[37] S. C. Mishra and M. Prasad. Radiative heat transfer in participating media - a review. *Sadhana*, 23(2):213–232, 1998.

TH-1868_004301

[38] J. R.. Howell. Radiative transfer in multi-dimensional enclosures with participating media. *ASME, 83-HT-32*, 1983.

[39] K. T. Yang. Numerical modeling of natural convection-radiation interactions in enclosures. In *Proceedings of the 8th International Heat Transfer Conference*, volume 1, pages 131–140. San Francisco, CA, August 18-23 1986.

[40] David A. Blank. The Cartesian collapsed-dimension method for use in numerical 2-D radiative calculations in absorbing-emitting media. *Int. J. Numer. Methods in Engineering*, 37:3023–3036, 1994.

[41] David A. Blank and S. C. Mishra. Use of the 2-D collapsed dimension method in gray enclosures with absorbing-emitting-isotropic scattering media in radiative equilibrium. *Numer. Heat Transfer, Part B*, 30(4):469–481, 1996.

[42] S. C. Mishra and M. Prasad. Radiative heat transfer in absorbing-emitting-scattering gray media inside 1-D Cartesian enclosure using collapsed dimension method. *Int. J. Heat Mass Transfer*, 45(3):697–700, 2002.

[43] P. Mahanta and S. C. Mishra. Solution of radiative heat transfer problems in long-cylindrical enclosures with participating media. In *proceedings of the fourth ISHMT-ASME Heat Transfer Conference and 15 th National Heat and Mass Transfer Conference, Pune, India*, January 2000.

[44] S. C. Mishra, P. Mahanta, and P. Talukdar. Collapsed dimension method applied to radiative transfer problems with inhomogeneous medium. In *proceedings of the 5th ISHMT-ASME Heat Transfer Conference and 16 th National Heat and Mass Transfer Conference, Kolkata, India*, January 2002.

[45] P. Talukdar and S. C Mishra. Analysis of conduction-radiation problem in absorbing-emitting media using collapsed dimension method. In *Paper No. NHTC2000-12129*. 34th National Heat Transfer Conference, Pittsburgh, PA, USA, 2000.

[46] P. Talukdar and S. C. Mishra. Transient conduction and radiation heat transfer with heat generation in a participating medium using the collapsed dimension method. *Numer. Heat Transfer, Part A*, 39:79–100, 2001.

TH-1868_004301

[47] Edward U. Condon. Radiative transport in hot glass. *J. Quant. Spectros. Radiat. Transfer*, 8(1):369–385, 1968.

[48] S. H. K. Lee and Y. Jaluria. Effects of variable properties and viscous dissipation during optical fiber drawing. *J. Heat Transfer*, 118:350–358, 1996.

[49] L. P. Kadanoff. Radiative transport within an ablating body. *J. Heat Transfer*, 83(2):215–225, 1961.

[50] M. A. Boles and M. N. Özişik. Simultaneous ablation and radiation in an absorbing, emitting and isotropically scattering medium. *J. Quant. Spectros. Radiat. Transfer*, 12:838–847, 1972.

[51] L. K. Matthews, R. Viskanta, and F. P. Incropera. Combined conduction and radiation heat transfer in porous materials heated by intense solar radiation. *J. Solar Energy Engineering*, 107(1):29–34, 1985.

[52] U. Heinemann, R. Caps, and J. Fricke. Radiation-conduction interaction: An investigation on silica aerogels. *Int. J. Heat Mass Transfer*, 39(10):2115–2130, 1996.

[53] H. M. Shafey, A. M. Abd El-Ghany, and A. M. Nassib. An analysis of the combined conductive-radiative heat transfer between a surface and a gas fluidized bed at high temperature. *Int. J. Heat Mass Transfer*, 36(9):2281–2292, 1993.

[54] R. Viskanta and R. J. Grosh. Heat transfer by simultanous conduction and radiation in an absorbing medium. *J. Heat Transfer*, 84:63–72, 1962.

[55] R. Viskanta. Heat transfer by conduction and radiation in absorbing and scattering materials. *J. Heat Transfer*, 87(1):143–150, 1965.

[56] W. W. Yuen and L. W. Wong. Heat transfer by conduction and radiation in a one-dimensional absorbing, emitting and anisotropically-scattering medium. *J. Heat Transfer*, 102:303–307, 1980.

[57] A. C. Ratzel III and J. R. Howell. Heat transfer by conduction and radiation in one dimensional planar medium using differential approximation. *J. Heat Transfer*, 104:388–391, 1982.

TH-1868_004301

[58] C. H. Ho and M. N. Özişik. Combined conduction and radiation in a two layer planar medium with flux boundary condition. *Numer. Heat Transfer*, 11(3):321, 1987.

[59] W. W. Yuen and E. E. Takara. Development of a generalized zonal method for analysis of radiative transfer in absorbing and anisotropically scattering media. *Numer. Heat Transfer, Part B*, 25:75–96, 1994.

[60] H. S. Chu and C. J. Tseng. Conduction-radiation interaction in absorbing, emitting, and scattering media with variable thermal conductivity. *J. Thermophys. Heat Transfer*, 6(3):537–540, 1992.

[61] C. C. Lii and M. N. Özişik. Transient radiation and conduction in an absorbing, emitting, scattering slab with reflective boundaries. *Int. J. Heat Mass Transfer*, 15:1175–1179, 1972.

[62] K. C. Weston and J. L. Hauth. Unsteady, combined radiation and conduction in an absorbing, scattering and emitting medium. *J. Heat Transfer*, 95(3):357–364, 1973.

[63] J. R. Tsai and M. N. Özişik. Transient, combined conduction and radiation in an absorbing, emitting and isotropically scattering solid sphere. *J. Quant. Spectros. Radiat. Transfer*, 38(4):243 251, 1987.

[64] R. Siegel. Transient radiative cooling of an absorbing and scattering cylinder. *J. Heat Transfer*, 111(1):199 203, 1989.

[65] C. Y. Wu and N. R. Ou. Transient two-dimensional radiative and conductive heat transfer in a scattering medium. *Int. J. Heat Mass Transfer*, 37(17):2675–2686, 1994.

[66] H. Tan, L. Ruan, X. Xia, Q. Yu, and T. W. Tong. Transient coupled radiative and conductive heat transfer in an absorbing, emitting and scattering medium. *Int. J. Heat Mass Transfer*, 42(15):2967–2980, 1999.

[67] C. Yao and B. T. F. Chung. Transient heat transfer in a scattering-radiating-conducting layer. *J. Thermophys. Heat Transfer*, 13(1):18–32, 1999.

TH-1868_004301

[68] P. D. Jones and Y. Bayazitoglu. Radiation, conduction, and convection from a sphere in an absorbing, emitting, gray medium. *J. Heat Transfer*, 114:250–254, 1992.

[69] I. H. Cho, S. W. Baek, and S. H. Han. Unsteady cooling of a solid sphere in a radiatively active medium. *Numer. Heat Transfer, Part A*, 34:119–133, 1998.

[70] T. K. Kim and T. F. Smith. Radiative and conductive transfer for a real gas in a cylindrical enclosure with gray walls. *Int. J. Heat Mass Transfer*, 28(12):2269 2277, 1985.

[71] B. Sunden. Transient conduction in a cylindrical shell with a time-varying incident surface heat flux and convective and radiative surface cooling. *Int. J. Heat Mass Transfer*, 32(3):575–584, 1989.

[72] J. A. Hariss. Solution of the conduction/radiation problem with linear-anisotropic scattering in an annular medium by the spherical harmonics method. *J. Heat Transfer*, 111:194–197, February 1989.

[73] D. K. Pandey. Combined conduction and radiation heat transfer in concentric cylindrical media. *J. Thermophys. Heat Transfer*, 3(1):75–82, 1989.

[74] T. M. Shih and Y. N. Chen. A discretized-intensity method proposed for two-dimensional systems enclosing radiative and conductive media. *Numer. Heat Transfer*, 6:117 -134, 1983.

[75] M. M. Razzaque, J. R. Howell, and D. E. Klein.. Coupled radiative and conductive heat transfer in a two-dimensional enclosure with gray participating media using finite elements. *J. Heat Transfer*, 106(3):613–619, 1984.

[76] W. W. Yuen and E. E. Takara. Analysis of combined conductive-radiative heat transfer in a two-dimensional rectangular enclosure with a gray medium. *J. Heat Transfer*, 110:468–474, 1988.

[77] Tae-kuk Kim and Haeok Lee. Effect of anisotropic scattering on radiative heat transfer in two-dimensional rectangular enclosures. *Int. J. Heat Mass Transfer*, 31(8):1711–1721, 1988.

TH-1868_004301

[78] H. C. Ho and M. N. Özişik. Combined conduction and radiation in a two-dimensional rectangular enclosure. *Numer. Heat Transfer*, 13(2):229–239, 1988.

[79] S. W. Baek and T. Y. Kim. The conductive and radiative heat transfer in rectangular enclosure using the discrete transfer method. In *Ninth International Heat Transfer Conference*, volume 6, pages 433–438. Washington, D. C., Hemisphere, 1990.

[80] T. Y. Kim and S. W. Baek. Analysis of combined conductive and radiative heat transfer in a two-dimensional rectangular using the discrete ordinate method. *Int. J. Heat Mass Transfer*, 34(9):2265–2273, 1991.

[81] M. Kaviani and B. P. Singh. Radiative heat transfer in porous media. *Advances in Heat Transfer*, 23:133–185, 1993.

[82] B. P. Singh and M. Kaviany. Independent theory versus direct simulation of radiation heat transfer in packed beds. *Int. J. Heat Mass Transfer*, 34(11):2869–2882, 1991.

[83] C. L. Tien. Thermal radiation in packed and fluidized beds. *J. Heat Transfer*, 110:1230–1242, 1988.

[84] L. A. Dombrovsky. *Radiation Heat Transfer in Disperse Systems.* Begell House, New York, 1996.

[85] J. R. Howell. Radiative transfer in porous media, Chapter 7 in K. Vafai (ed.). In *Handbook of Porous Media.* Marcel Dekker, New York, 2000.

[86] K. Kamiuto, S. Saito, and K. Ito. Combined conduction and correlated-radiation heat transfer in packed beds. *J. Thermophys. Heat Transfer*, 7(3):496–501, 1993.

[87] K. Kamiuto, S. Saito, and K. Ito. Numerical model for combined conductive and radiative heat transfer in annular packed beds. *Numer. Heat Transfer, Part A*, 23:433–443, 1993.

TH-1868_004301

[88] K. Kamiuto. Radiative transfer through a randomly-packed bed of spheres. *J. Quant. Spectros. Radiat. Transfer*, 41(1):23-27, 1989.

[89] R. D. Cess. The interaction of thermal radiation with conduction and convection heat transfer. *Advances in Heat Transfer*, 1:1-50, 1964.

[90] R. Viskanta. Radiation transfer and interaction of convection with radiation heat transfer. *Advances in Heat Transfer*, 3:175 251, 1966.

[91] R. Viskanta. Interaction of heat transfer by conduction convection and radiation in a radiating fluid. *J. Heat Transfer*, 85:318-328, 1963.

[92] Y. Kurosaki. Heat transfer by simultaneous radiation and convection in an absorbing and emitting medium in a flow between parallel plates. In *Proceedings of the 4th International Heat Transfer Conference*, volume 3. New York, 1970.

[93] R. Echigo, K. Kamiuto, and S. Hasegawa. Analytical method on composite heat transfer with predominant radiation-analysis by integral equation and examination on radiation slip. In *Proceedings of the 5th International Heat Transfer Conference*, volume 1, pages 103–107. Japan. JSME, 1974.

[94] V. N. Timofeyev, F. R. Shklyar, V. M. Malkin, and K. H. Berland. Combined heat transfer in an absorbing steam moving in a flat channel. Parts I, II, III. *Heat Transfer, Soviet Research*, 1(6):57 93, 1969.

[95] C. C. Lii and M. N. Özişik. Heat transfer in an absorbing, emitting and scattering slug flow between parallel plates. *J. Heat Transfer*, 95C:538-540, 1973.

[96] T. C. Chawla and S. H. Chan. Combined radiation convection in thermally developing Poiseuille flow with scattering. *J. Heat Transfer*, 102:297 307, 1980.

[97] M. P. Menğuç, Y. Yener, and M. N. Özişik. Interaction of radiation in thermally developing laminar flow in a parallel plate channel. *ASME Paper No. 83-HT-35*, 1983.

TH-1868_004301

[98] Y. Yener, B. Shahidi-Zandi, and M. N. Özişik. Simultaneous radiation and forced convection in thermally developing turbulent flow through a parallel plate channel. *J. Heat Transfer*, 108(4):985–987, 1986.

[99] T. H. Einstein. Radiant heat transfer to absorbing gases enclosed in a circular pipe with conduction, gas flow, and internal heat generation. *NASA TR R-156*, 1963.

[100] M. Kassemi and B. T. F. Chung. Two-dimensional convection and radiation with scattering from a poiseuille flow. *J. Thermophys. Heat Transfer*, 4(1):98–105, 1990.

[101] J. C. Y. Koh and R. Colony. Analysis of cooling effectiveness for porous material in a coolant passage. *J. Heat Transfer*, 96:324–330, 1974.

[102] K. Y. Wang and C. L. Tien. Thermal insulation in flow systems: Combined radiation and convection through a porous segment. *J. Heat Transfer*, 106:453–459, 1984.

[103] M. Kaviany. Laminar flow through a porous channel bounded by isothermal parallel plates. *Int. J. Heat Mass Transfer*, 28(4):851–858, 1985.

[104] A. F. Sarofim and H. C. Hottel. Radiative transfer in combustion chambers: Influence of alternative fuels. In *Proceedings of the 6th International Heat Transfer Conference*, volume 6, pages 199–217. Washington, D. C., 1978.

[105] D. Trimis and F. Durst. Combustion in a porous medium - advances and applications. *Combust. Sci. and Tech.*, 121:153–168, 1996.

[106] O. Pickenäcker, K. Pickenäcker, K. Wawrzinek, D. Trimis, W. E. C. Pritzkow., C. Müller, P. Goedtke, U. Papenburg, J. Adler, G. Standke, H. Heymer, W. Tauscher, and F. Jansen. Innovative ceramic materials for porous-medium burners I - II. *Interceram*, 48(5):326–330, 1999.

[107] Y. Yoshizawa, K. Sasaki, and R. Echigo. Analytical study of the structure of radiation controlled flame. *Int. J. Heat Mass Transfer*, 31(2):311–319, 1988.

TH-1868_004301

[108] S. W. Baek. The premixed flame in a radiatively active porous medium. *Combst. Sci. and Tech.*, 64:277–287, 1989.

[109] S. B. Sathe, R. E. Peck, and T. W. Tong. A numerical analysis of heat transfer and combustion in porous radiant burners. *Int. J. Heat Mass Transfer*, 33(6):1331 1338, 1990.

[110] T. W. Tong and S. B. Sathe. Heat transfer characteristics of porous radiant burners. *J. Heat Transfer*, 113:423 428, 1991.

[111] Pei-feng Hsu, Zhiqiang Tan, and J. R. Howell. Radiative transfer by the YIX method in nonhomogeneous scattering, and nongray media. *J. Thermophys. Heat Transfer*, 7(3):487–495, 1993.

[112] C. H. Ho and M. N. Özişik. An inverse radiation problem. *Int. J. Heat Mass Transfer*, 32:335–341, 1989.

[113] N.J. McCormick. Inverse radiative transfer problems: a review. *Nuclear Science and Engineering*, 112:185–198, 1992.

[114] P. J. Coelho, J. M. Goncalves, M. G. Carvalho, and D. N. Trivic. Modelling of radiative heat transfer in enclosures with obstacles. *Int. J. Heat Mass Transfer*, 41(4-5):745–756, 1998.

[115] P. S. Cumber, M. Fairweather, and H. S. Ledin. Application of wide band radiation models to non-homogeneous combustion systems. *Int. J. Heat Mass Transfer*, 41(11):1573 1584, 1998.

[116] S. C. Mishra, P. Talukdar, and L. R. Patbhare. Transient radiation and conduction heat transfer with heat generation in an inhomogeneous medium using the discrete transfer method. In *Paper No. NHTC2201-20232.* 35th National Heat Transfer Conference, Anaheim, California, USA, 2001.

[117] S. C. Mishra. *A Novel Computational Approach for the Solution of Radiative Heat Transfer Problems in Participating Media.* PhD thesis, IIT Kanpur, India, 1997.

TH-1868_004301

[118] R. Fernandes and J. Francis. Finite element analysis of planar conductive and radiative transfer with flux boundary. In *Paper No. 82-0910.* 3rd AIAA/ASME Joint Thermophysics, Fluids, Plasma and Heat Transfer Conf., Saint Louis, MO, June 7-11, 1992.

[119] J. D. Lin and J. H. Tsai. Radiation-conduction interaction in a planar, anisotropically scattering medium with flux boundary. *Numer. Heat Transfer, Part A*, 16:119–128, 1989.

[120] C. Barker and W. H. Sutton. The transient radiation and conduction heat transfer in a gray participating medium with semi-transparent boundaries. In *ASME Radiation Heat Transfer*, volume HTD-49, pages 25–36. B. F. Armaly and A. F. Emery, eds, 1985.

[121] W. H. Sutton. A short time solution for coupled conduction and radiation in a participating slab geometry. *J. Heat Transfer*, 108(2):465–466, 1986.

[122] P Mahanta and S. C. Mishra. Modified collapsed dimension method for radiative heat transfer problems. *J. Thermophys. Heat Transfer*, 15(2):246–248, 2001.

[123] T. W. Tong, D. L. McElroy, and D. W. Yarbrough. Conduction and radiation heat transfer in porous thermal insulations. *J. Thermal Insulation*, 9:13–29, 1985.

[124] C. F. Tsai and G. Nixon. Transient temperature distribution of a multilayer composite wall with effects of internal thermal radiation and conduction. *Numer. Heat Transfer*, 10(1):95-101, 1986.

[125] J. H. Tsai and J. D. Lin. Transient combined conduction and radiation with anisotropic scattering. *J. Thermophys. Heat Transfer*, 4(1):92–97, 1990.

[126] R. Siegel. Finite difference solution for transient cooling of a radiating-conducting semitransparent layer. *J. Thermophys. Heat Transfer*, 6(1):77–83, 1992.

TH-1868_004301

[127] S. W. Back, T. Y Kim, and J. S. Lee. Transient coling of a finite cylindrical medium in a rarefied cold environment. *Int. J. Heat Mass Transfer*, 36(16):3949 3956, 1993.

[128] C. E. Siewert. An improved iterative method for solving a class of coupled conductive radiative heat transfer problems. *J. Quant. Spectros. Radiat. Transfer*, 54(4):599 605, 1995.

[129] O. Hahn, F. Raether, M. C. Arduini-Schuster, and J. Fricke. Transient coupled conductive/radiative heat transfer in absorbing, emitting and scattering media: application to laser-flash measurements on ceramic materials. *Int. J. Heat Mass Transfer*, 40(3):689–698, 1997.

[130] C. Yao and B. T. F. Chung. Transient heat transfer in a scattering-radiating-conducting layer. *J. Thermophys. Heat Transfer*, 13(1):18-32, 1999.

[131] Zhiqiang Tan. Radiative heat transfer in multidimensional emitting, absorbing, and anisotropic scattering media - mathematical formulation and numerical method. *J. Heat Transfer*, 111:141-147, 1989.

[132] W. W. Yuen and M. Khatami. Transient radiative heating of an absorbing, emitting and scattering material. 4(2):193–198, 1990.

[133] R. Siegel. Transient thermal analysis for heating a translucent wall with opaque radiation barriers. *J. Thermophys. Heat Transfer*, 13(3):277 291, 1999.

[134] H. S. Chu and C. J. Tseng. Thermal performance of ultra-fine powder insulation at high temperatures. *J. Thermal Insulation*, 12:298–312, 1989.

[135] C. K. Krishnaprakas. Combined conduction and radiation heat transfer in a cylindrical medium. *J. Thermophys. Heat Transfer*, 12(4):605-608, 1998.

[136] C. K. Chan and C. L. Tien. Radiative transfer in packed spheres. *J. Heat Transfer*, 96:52–58, 1974.

[137] J-W Wu and H-S Chu. Combined conduction and radiation heat transfer in plane-parallel packed beds with variable porosity. *J. Quant. Spectros. Radiat. Transfer*, 61(4):443–452, 1999.

TH-1868_004301

[138] B. L. Drolen and C. L. Tien. Independent and dependent scattering in packed sphere systems. *J. Thermophys. Heat Transfer*, 1:63–68, 1987.

[139] B. P. Singh and M. Kaviany. Modelling radiative heat transfer in packed beds. *Int. J. Heat Mass Transfer*, 92:1397–1405, 1992.

[140] K. Nasr, R. Viskanta, and S. Ramadhyani. An experimental evaluation of the effective thermal conductivity of packed beds at high temperatures. *J. Heat Transfer*, 116:829 837, 1994.

[141] K. Ridgway and K. J. Tarbuck. Radial voidage variation in randomly packed beds of spheres of different sizes. *J. Pharm. Pharmacol*, 18:168S–175S, 1966.

[142] H. Yoshida, J. H. Yun, and R. Echigo. Transient characteristics of combined conduction, convection and radiation heat transfer in porous media. *Int. J. Heat Mass Transfer*, 33(5):847 857, 1990.

[143] S. Maruyama, T. Aihara, and R. Viskanta. Transient behaviour of an active thermal protection system. *Int. J. Heat Mass Transfer*, 34(3):625–632, 1991.

[144] M. A. Hossain, M. A. Alim, and D. A. S. Rees. Effect of radiation on free convection from a porous vertical plate. *Int. J. Heat Mass Transfer*, 42:181–191, 1999.

[145] A. A. Mohammadien and M. F. El-amin. Thermal dispersion-radiation effects on non-Darcy natural convection in a fluid saturated porous medium. *Transport Porous Media*, 40:153–163, 2000.

[146] G. Brenner, K. Pickenäcker, O.Pickenäcker, D. Trimis, K. Wawrzinek, and T. Weber. Numerical and experimental investigations of matrix-stabilized methane/air combustion in inert porous media. *Combust. Flame*, 123(1/2):201–213, 2000.

[147] J. C. Y. Koh and R. L. Stevens. Enhancement of cooling effectiveness by porous material in coolant passages. *J. Heat Transfer*, 97:309–311, 1975.

[148] M. Hirano, T. Miyauchi, and Y. Takahira. Enhancement of radiative heat transfer in the laminar channel flow of non-gray gases. *Int. J. Heat Mass Transfer*, 31(2):367–374, 1988.

TH-1868_004301

[149] T. K. Kim and H. S. Lee. Two-dimensional anisotropic scattering radiation in a thermally developing Poiseuille flow. *J. Thermophys. Heat Transfer*, 4(3):292 298, 1990.

[150] Yan. W. M. and H. Y. Li. Radiation effects on mixed convection heat transfer in a vertical square duct. *Int. J. Heat Mass Transfer*, 44(7):1401–1410, 2001.

[151] J. S. Chiou. Combined radiation-convection heat transfer in a pipe. *J. Thermophys. Heat Transfer*, 7(1):178 180, 1993.

[152] C. K. Krishnaprakas, K. Badari Narayana, and P. Dutta. Combined convective and radiative heat transfer in turbulent tube flow. *J. Thermophys. Heat Transfer*, 13(3):390–394, 1999.

[153] F.H.Azad and M.F. Modest. Combined radiation and convection in absorbing, emitting and anisotropically scattering gas-particulate tube flow. *Int. J. Heat Mass Transfer*, 24:1681 1698, 1981.

[154] S. H. Kim and K. Y. Huh. Assessment of the finite-volume method and the discrete ordinate method for radiative heat transfer in a three-dimensional rectangular enclosure. *Numer. Heat Transfer, Part B*, 35:85–112, 1999.

[155] S. C. Mishra and M. Prasad. Radiative heat transfer in absorbing-emitting-scattering gray media inside 1-D Cartesian enclosure using the collapsed dimension method. *Int. J. Heat Mass Transfer*, 45(3):697–700, 2002.

[156] J. R. Howell, M. J. Hall, and J. L Ellzey. Combustion of hydrocarbon fuels within porous inert media. *Prog. Energy Conbust. Sci.*, 22:121 145, 1996.

[157] P. F. Hsu, J. R. Howell, and R. D. Matthews. A numerical investigation of premixed combustion within porous inert media. *J. Heat Transfer*, 115:744 750, 1993.

[158] P. H. Bouma and L. P. H. D Goey. Premixed combustion on ceramic foam burners. *Combust. Flame*, 119:133 143, 1999.

[159] S. A. Leonardi, R. Viskanta, and J. P. Gore. Analytical and experimental study of combustion and heat transfer in submerged flame metal fiber burners/heaters. *J. Heat Transfer*, 125:118–125, 2003.

TH-1868_004301

[160] D. J. Diamantis, E. Mastorakos, and D. A. Goussis. Simulations of premixed combustion in porous media. *Combust. Theory Modelling*, 6:383 411, 2002.

[161] C. L. Hackert, J. L. Ellzey, and O. A. Ezekoye. Combustion and heat transfer in model two-dimensional porous burners. *Combust. Flame*, 116:177–191, 1999.

[162] J. Norbury and H. Byrne. The effects of radiation on combustion in porous media. *Mathl. Comput. Modelling*, 24:89 94, 1996.

[163] I. Malico and J. C. F. Pereira. Numerical study on the influence of radiative properties in porous media combustion. *J. Heat Transfer*, 123:951–957, 2001.

[164] S. A. Leonardi, R. Viskanta, and J. P. Gore. Radiation and thermal performance measurements of a metal fiber burner. *J. Quant. Spectros. Radiat. Transfer*, 73:409 501, 2002.

TH-1868_004301

Appendix

Collapsing coefficient (CC) Results For Radiative Equilibrium Case [117]

Expression of the collapsing coefficient, Γ*, for the case of absorbing-emitting media at radiative equilibrium,* $0.0001 \leq \tau_L \leq 5.0$.

$$\Gamma = \begin{cases} 1.27276 - 1.22505\,\tau_L + 23.6226\,\tau_L^2 - 136.935\,\tau_L^3 \\ \quad - 22.2416\,\tau_L^4 \\ \qquad\qquad\qquad\qquad \text{for } 0.0001 \leq \tau_L \leq 0.1 \\ 1.25684 - 0.108915\,\tau_L + 0.075431\,\tau_L^2 - 0.028079\,\tau_L^3 \\ \quad + 0.005164\,\tau_L^4 - 0.000363\,\tau_L^5 \\ \qquad\qquad\qquad\qquad \text{for } 0.1 < \tau_L \leq 5.0 \end{cases}$$

TH-1868_004301

CC Results For Non-radiative Equilibrium Case [117]

Expression of the collapsing coefficient, Γ, for the case of absorbing, emitting, isotropically scattering ($\omega \neq 0.0$, $a_1\omega = 0.0$) media at non-radiative equilibrium, $0.0001 \leq \tau_L \leq 5.0$.

$$
\Gamma = \begin{cases}
7.2638 - 5.33231\, e^{\tau_L} - 0.24256\, e^{\omega} - 6.15798\, e^{2\tau_L} \\
+ 0.00118\, e^{2\omega} + 0.23927\, e^{(\tau_L+\omega)} + 5.50250\, e^{3\tau_L} \\
\qquad\qquad \text{for } 0.0001 \leq \tau_L < 0.05 \\
\\
1.26384 - 0.25003\,\tau_L + 0.05515\,\omega + 0.65438\,\tau_L^2 \\
- 0.128667\,\omega^2 + 0.122951\,\tau_L\,\omega - 1.14301\,\tau_L^3 \\
+ 0.12475\,\omega^3 - 0.10899\,\tau_L^2\,\omega + 0.03722\,\tau_L\,\omega^2 \\
+ 0.78499\,\tau_L^4 + 0.037331\,\omega^4 \\
\qquad\qquad \text{for } 0.05 \leq \tau_L < 0.6 \\
\\
0.99729 + 0.39907\, e^{\tau_L} - 0.01500\, e^{\omega} - 0.30004\, e^{2\tau_L} \\
+ 0.01286\, e^{2\omega} + 0.04399\, e^{(\tau_L+\omega)} + 0.08583\, e^{3\tau_L} \\
- 0.00450\, e^{3\omega} - 0.00466\, e^{(2\tau_L+\omega)} - 0.00299\, e^{(\tau_L+2\omega)} \\
- 0.00869\, e^{4\tau_L} + 0.00037\, e^{4\omega} \\
\qquad\qquad \text{for } 0.6 \leq \tau_L < 1.2 \\
\\
1.17601 - 0.04592\, e^{\tau_L} + 0.08810\, e^{\omega} + 0.00464\, e^{2\tau_L} \\
- 0.02700\, e^{2\omega} + 0.01813\, e^{(\tau_L+\omega)} - 0.00020\, e^{3\tau_L} \\
+ 0.00394\, e^{3\omega} - 0.00063\, e^{(2\tau_L+\omega)} - 0.00252\, e^{(\tau_L+2\omega)} \\
\qquad\qquad \text{for } 1.2 \leq \tau_L < 1.7 \\
\\
1.20500 - 0.01958\,\tau_L + 0.03500\,\omega - 0.00692\,\tau_L^2 \\
+ 0.05273\,\omega^2 + 0.04568\,\tau_L\,\omega + 0.00247\,\tau_L^3 \\
- 0.06107\,\omega^3 - 0.00322\,\tau_L^2\,\omega - 0.00971\,\tau_L\,\omega^2 \\
- 0.00021\,\tau_L^4 + 0.02524\,\omega^4 \\
\qquad\qquad \text{for } 1.7 \leq \tau_L \leq 5.0
\end{cases}
$$

TH-1868_004301

Expression of the collapsing coefficient, Γ, for absorbing-emitting media (without scattering, $\omega = 0.0$) at non-radiative equilibrium, $0.0001 \leq \tau_L \leq 5.0$.

$$\Gamma = \begin{cases} 1.27338 - 1.34631\,\tau_L + 26.78364\,\tau_L^2 - 159.953\,\tau_L^3 \\ \qquad\qquad \text{for } 0.0001 \leq \tau_L < 0.1 \\ 1.26002 - 0.145619\,\tau_L + 0.125726\,\tau_L^2 - 0.067566\,\tau_L^3 \\ + 0.006472\,\tau_L^4 - 0.006152\,\tau_L^5 \\ \qquad\qquad \text{for } 0.1 \leq \tau_L \leq 1.0 \\ 1.2376 - 0.068275\,\tau_L + 0.018395\,\tau_L^2 - 0.002886\,\tau_L^3 \\ + 0.000185\,\tau_L^4 \\ \qquad\qquad \text{for } 1.0 < \tau_L \leq 5.0 \end{cases}$$

Expression of the collapsing coefficient, Γ, for absorbing, emitting and, forward scattering ($a_1\omega = 0.5$, $\omega = 0.5$ and $a_1 = +1.0$) media at non-radiative equilibrium, $0.0001 \leq \tau_L \leq 5.0$.

$$\Gamma = \begin{cases} 1.27355 - 2.22853\,\tau_L + 0.192067\,(a_1\omega) - 0.00537\,\tau_L^2 \\ + 0.107663\,(a_1\omega)^2 - 0.451894\,\tau_L(a_1\omega) - 0.000004\,\tau_L^3 \\ - 0.018215\,(a_1\omega)^3 - 0.000735\,\tau_L^2(a_1\omega) + 0.098177\,\tau_L(a_1\omega)^2 \\ \qquad\qquad \text{for } 0.0001 \leq \tau_L \leq 1.0 \\ 1.27127 - 0.857938\,\tau_L + 0.186669\,(a_1\omega) + 9.81455\,\tau_L^2 \\ + 0.121449\,(a_1\omega)^2 + 0.297198\,\tau_L(a_1\omega) + 0.675137\,\tau_L^3 \\ - 0.049495\,(a_1\omega)^3 + 0.986318\,\tau_L^2(a_1\omega) - 0.349831\,\tau_L(a_1\omega)^2 \\ + 0.04401\,\tau_L^4 + 0.061678\,(a_1\omega)^4 + 0.059332\,\tau_L^3(a_1\omega) \\ - 1.60615\,\tau_L^2(a_1\omega)^2 + 0.751796\,\tau_L(a_1\omega)^3 \\ \qquad\qquad \text{for } 0.1.0 < \tau_L \leq 5.0 \end{cases}$$

TH-1868_004301

Expression of the collapsing coefficient, Γ, for absorbing, emitting and, backward scattering ($a_1\omega = -0.5$, $\omega = 0.5$ and $a_1 = -1.0$) media at non-radiative equilibrium, $0.0001 \leq \tau_L \leq 5.0$.

$$\Gamma = \begin{cases} 0.7857617 + 0.569860\, e^{\tau_L} + 0.637736\, e^{(a_1\omega)} + 0.203843\, e^{2\tau_L} \\ + 0.165533\, e^{2(a_1\omega)} + 0.123876\, e^{(\tau_L + a_1\omega)} - 0.142041\, e^{3\tau_L} \\ + 0.046964\, e^{3(a_1\omega)} - 0.378914\, e^{(2\tau_L + a_1\omega)} - 0.357473\, e^{(\tau_L + 2(a_1\omega))} \\ - 0.460442\, e^{4\tau_L} + 0.019614\, e^{4(a_1\omega)} \\ \qquad\qquad \text{for } 0.0001 < \tau_L \leq 1.0 \\ \\ 1.27539 - 0.9223\, \tau_L + 0.1568052\, (a_1\omega) + 9.8065\, \tau_L^2 \\ + 0.17896722\, (a_1\omega)^2 + 0.0123934\, \tau_L (a_1\omega) + 0.6176416\, \tau_L^3 \\ + 0.0275371\, (a_1\omega)^3 + 1.50584\, \tau_L^2 (a_1\omega) + 0.0631003\, \tau_L (a_1\omega)^2 \\ + 0.0325394\, \tau_L^4 \\ \qquad\qquad \text{for } 1.0 < \tau_L \leq 5.0 \end{cases}$$

****

THESIS
Lakshminath Bezbaroa Central Library
Indian Institute of Technology Guwahati
ACC. No. TH..1868.....
Date.....28/3/19.....

620
TH-1868
P03

TH-1868_004301

Acknowledgement

I am grateful to Dr. Subhash C. Mishra, Associate Professor, Department of Mechanical Engineering, IIT Guwahati for permitting me to use Figs. 2.6 to 2.9.

TH-1868_004301